THE UNIVERSITY *of* EDINBURGH

Raman-Active Chemical Probes for Cancer Cell Imaging and Medicinal Chemistry

THE UNIVERSITY *of* EDINBURGH

Craig Forrest Steven

A thesis submitted for the degree of
Doctor of Philosophy

The University of Edinburgh
2024

Declaration

This thesis is submitted in part fulfilment of the requirement for the degree of Doctor of Philosophy at the University of Edinburgh. Unless otherwise stated, the work described in this thesis is original and has not been submitted previously in whole, or in part for any degree or qualification at this, or any other university. Any work performed by others has been clearly indicated by acknowledgement or reference in the text. In accordance with the dissertation regulations as specified by The University of Edinburgh, this thesis does not exceed 100,000 words in length.

Craig F. Steven
May 2024

Components of Chapters 1–3 of this thesis have been published in:

C. F. Steven, E. Chiarparin, A. N. Hulme, V. G. Brunton, in *Stimulated Raman Scattering Microscopy: Techniques and Applications*, ed. J. Cheng, W. Min, Y. Ozeki, D. Polli, Elsevier, 2022, pp. 403–419.

C. F. Steven, M. Lee, Gary S. Nichol, Paul R. J. Davey, E. Chiarparin, A. N. Hulme, V. G. Brunton, *Eur. J. Org. Chem*., 2022, **30**, e202200393.

C. F. Steven, M. P. Ravindra, M. Lee, Paul R. J. Davey, E. Chiarparin, A. N. Hulme, V. G. Brunton, *Proc. SPIE*, 2023, 123570G.

Acknowledgements

Firstly, I would like to thank my supervisors Professors Alison Hulme and Valerie Brunton. Alison – thank you for affording me all of the opportunities that have arisen since I started this PhD. I am so grateful that you have allowed me to explore my own ideas and have supported me throughout. Val – thank you for your kind patience as I became a (part-time) biologist and for all the invaluable support and guidance you have given which has allowed me to do so. I would also like to thank AstraZeneca for providing funding and support for this project, especially to Paul for facilitating my placement and organising all of the assays. Thanks also to the rest of the placement team at AZ – Elisabetta, Nic, Derek, Pam, Poppy, Lotte, Chris and Marianne.

Thank you to Andrei for assistance with spontaneous Raman spectroscopy and all other technical staff at the SoC and IGC who have provided essential support behind the scenes.

A huge thanks goes out to members of the Hulme group, past and present, for friendship and support over the years. A special thanks goes out to Connor for insightful and thought-provoking discussions during the days and stress-relieving pints afterwards. To Maria, for bringing both practical support in the early stages of my project, and for so much laughter. To Edith, for listening to me complain about almost everything, your incomparable analytical expertise, and your 'quirkiness' which always lit up the office. Hector, you were instrumental in inspiring me to pursue organic chemistry and I am very grateful for the time you spent teaching me. Ander, thanks for your support, especially during the writing process, and for always trying to convert my negativity into something positive (even when I did not want to hear it). Ellen, thanks for the support as we embarked on this (sometimes bumpy) journey together and for being my sounding board for anything vaguely biology-related. Manasa, my thesis would be a very different document without your hard work and essential contribution to the project; thanks for all of your support, you were an unbeatable 52 labmate! Thank you to Marie for help with DFT Raman calculations. Thanks to my project students, Spyros and Kenneth, for being textbook examples of great students.

Thanks to every biologist I have pestered with silly chemist curiosities – especially to Giovana. I am so grateful for the endless support you have given me, both practical and emotional, from Western blot 1 to 87! Thank you to my other friends and

colleagues at the ECRC and Frame-Brunton group, especially to Marianna and Alex for help with IP and IF, Molly for help with imaging assays, John for ImageXpress support and the AvK group for running proteomics samples. Thanks to Martin for expertise and support with the many microscope troubles.

Thanks to all my friends, both old and new, for making this PhD as enjoyable as it could ever be. To Justinas, thank you so much for everything; there's no one I would have rather had by my side over these last few years. Finally, I extend the greatest thank you to my family: Mum, Dad, Rachel, and of course Mick, for your boundless love and support. I will be forever indebted to you for the time you have spent encouraging me to pursue my goals.

To Nanna,

Abstract

Interest in stimulated Raman scattering (SRS) cellular imaging as a tool to aid preclinical drug testing has grown in recent years. **Chapter 1** discusses the fundamental principles of SRS, examples of its utility in intracellular drug imaging and challenges within the field. One major challenge is that the complex nature of intracellular biological environments complicates drug tracking by SRS, frequently necessitating attachment of small chemical tags to aid visualisation. Unfortunately, poor signal intensity and solubility have hampered the widespread use of these tags.

The poor solubility and high lipophilicity of Raman tags was addressed in **Chapter 2**. New molecules were synthesised using an optimised cross-coupling method. These tags were designed with greater consideration of medicinal chemistry parameters such as solvent partition coefficients (log*P* and log*D*) and fraction of sp^3-hybridised carbons (Fsp^3). The relative propensity of the tags to engage in intermolecular stacking, which is known to confer poorer solubility, was analysed by mass-spectrometry (MS) and X-ray crystallography. Whilst MS analysis found that tags with higher log*P* formed stronger associative interactions, determination of X-ray crystal structures revealed changes in tag crystal packing when Fsp^3 was increased. These results suggest a combined analysis of log*P* and Fsp^3 should guide future tag design. SRS imaging revealed that the tags were cell permeable, Raman activity was unaffected by structural modification and changes in physicochemical parameters did not significantly affect tag biodistribution.

In **Chapter 3**, the new tags were attached to the PARP inhibitor olaparib to allow intracellular drug tracking. Rigorous *in vitro* testing of the new drug analogues was carried out to investigate their physicochemical properties, target protein inhibition and binding kinetics, and biological stability. It was determined that olaparib activity was retained after tagging, providing the necessary prerequisites for the transition to *in cellulo* testing. SRS imaging allowed determination of drug biodistribution and discrimination of the compounds based on their relative Raman activity and physicochemical properties. An unexpected cellular distribution was observed with no drug detected within the nucleus by SRS, inconsistent with the known nuclear localisation of PARP and previous fluorescence imaging of olaparib. This warranted further study to confirm the biological effects of Raman tagging.

The effects of tagged drug analogues on cancer cells were studied in **Chapter 4**. The drug analogues were found to reduce cell viability in a range of cancer cell lines and a 3D cell model. Using a live-cell phenotypic readout, this loss of viability was shown to correlate with increased DNA damage when compared to olaparib, thus suggesting enhanced PARP inhibition. The origin of the increased potency was explored by identifying new biological pathways activated in response to exposure of the drug analogues. It was determined by protein expression analysis, gene profiling and proteomics that Raman tagging of olaparib induced degradation of PARP and activation of the unfolded protein response, which could be linked to cell death.

These studies have allowed the intracellular tracking of a PARP inhibitor by Raman microscopy for the first time and provide foundations for the future development of 2-in-1 theranostic Raman probes.

Lay summary

Millions of medications are prescribed each year. Before these can be given to patients, each new drug molecule undergoes, on average, 10–15 years of laboratory and clinical testing. This is essential to ensure the safety and effectiveness of the treatment. The complex nature of biology means that there are many considerations during this process. Even before testing in the human body, we must understand what happens in a single cell, the most basic unit of life.

However, drug molecules are around 100,000 times smaller than a human cell, which poses challenges for studying them in such a crowded biological environment. Complicating things further, drugs move around quickly and interact with many different parts of the cell. To track them effectively and study their behaviour, new methods are needed. A key technique used in this project for tracking molecules is Raman spectroscopy, which relies on the fact that, when we shine laser light on molecules, they vibrate in unique ways that allow us to determine their chemical makeup. We can improve the visibility of these molecules by chemically attaching small ‘tags’ which give very intense signals in a Raman spectrum. Unfortunately, these tags have not been well-optimised for biological applications, which limits their applicability for studying drugs in cells. This project aimed to improve tags by making changes to their chemical properties, e.g., to improve solubility. This was investigated by chemical analysis techniques that probe the interactions between molecules.

The new tags were then attached to an anti-cancer drug called olaparib which works by selectively blocking a protein involved in the repair of damaged cells, allowing it to kill cancerous tumours. Uncertainties in olaparib’s mode of action make it an interesting target for Raman tagging. Important properties of the new drug-tag compounds were then determined, including how they interact in environments mimicking those found in the cell, their effectiveness as anti-cancer drugs and how easy it is to see them in cancer cells using Raman tagging. In general, the new compounds behaved similarly to olaparib thus were suitable for further testing. A range of new, unexpected effects were uncovered when these tagged drugs were studied biologically. For example, the drug-tag compounds were more effective in killing ovarian cancer cells, prompting a detailed exploration of these effects and their implications in cancer biology. It was revealed that the attachment of Raman tags enhanced the effects of olaparib by changing its mechanism of action and initiating a series of stress responses which cause the cell to shut down.

Abbreviations

a.u.	arbitrary units
ANOVA	analysis of variance
Ar	aromatic
ATRI	alkyne-tagged Raman imaging
BADY	bis(aryl)-1,3-butadiyne
BafA	bafilomycin A1
BODIPY	boron-dipyrromethene
BRCA	breast cancer susceptibility protein
Bu	butyl
CSR	cell silent region
DFT	density functional theory
DIPEA	*N*-ethyl-*N*-(propan-2-yl)propan-2-amine
DMSO	dimethyl sulfoxide
DSB	double-stranded break
EdU	5-ethynyl-2′-deoxyuridine
ePSA	experimental polar surface area
Equiv.	equivalents
ER	endoplasmic reticulum
ESI	electrospray ionisation
Et	ethyl
Fsp^3	fraction of sp^3-hybridised carbons
GSEA	gene set enrichment analysis
HD	helical domain
HDX	hydrogen-deuterium exchange
HR	homologous recombination
HRMS	high resolution mass spectrometry
Hsp	heat shock protein
HyT	hydrophobic tagging
IC_{50}	half-maximal inhibitory concentration

KD	knockdown
LC	liquid chromatography
LOD	limit of detection
Me	methyl
MS	mass spectrometry
(N)IR	(near) infrared
NMR	nuclear magnetic resonance (spectroscopy)
Ola	olaparib
PARP	poly(adenosine diphosphate-ribose) polymerase
PARPi	PARP inhibitor
PBS	phosphate-buffered saline
Ph	phenyl
PhDY	phenyl-diyne
R_f	retention factor
RIE	relative intensity vs EdU
RT	room temperature
RT-qPCR	reverse transcription-quantitative polymerase chain reaction
SNR	signal-to-noise ratio
SPR	surface plasmon resonance
spRS	spontaneous Raman scattering
SRS	stimulated Raman scattering
SSB	single-stranded break
TKI	tyrosine kinase inhibitor
TLC	thin layer chromatography
TMS	trimethylsilyl
TPF	two-photon fluorescence
UPR	unfolded protein response
UPS	ubiquitin-proteasome system
WT	wild type

Table of Contents

Chapter 1 Introduction

1.1 Biomedical imaging

Imaging forms an essential component of scientific research and medicine. Biomedical imaging integrates principles from a range of disciplines – including biology, engineering, physics and medicine – to provide insight on the complexity of biological systems. With such a wide variety of modalities optimised for every stage of biomedical research, from the single cell to whole body level, imaging techniques are essential in modern life. Within the context of drug development, imaging has played a key role in all aspects from discovery to clinical testing.[1, 2] These studies have provided information on drug biodistribution, metabolism, and pharmacokinetics; information which may aid in reducing high drug attrition rates.[3] In recent years, interest in molecular imaging as a tool within the drug discovery industry has grown greatly and the development of new and varied methods for drug imaging is a strong driving force for increasing its uptake within the pharmaceutical industry.[4]

An opportunity exists within biomedical imaging for the development and application of new imaging modalities for intracellular drug analysis. Drug imaging techniques require high chemical specificity, detection sensitivity and spatiotemporal resolution to allow accurate and informative analysis. Raman imaging can fulfil these requirements and will be discussed within the context of biological imaging and the drug discovery industry.

1.1.1 Overview of techniques in drug imaging

Commonly used molecular imaging modalities include positron emission tomography (PET), whole-body autoradiography (WBA), mass spectrometry imaging (MSI), and magnetic resonance imaging (MRI) (**Figure 1.1**). Whilst such techniques are generally well-suited to the imaging of biological samples, inadequate spatiotemporal resolution can preclude their use in cellular imaging.[5] Comparing the above techniques, PET boasts excellent sensitivity and penetration depth; but with spatial resolution limited to 2–5 mm, single cell-scale imaging is unattainable.[6] WBA has been used extensively in preclinical tissue distribution studies and exhibits better spatial resolution than PET but is impractical due to long acquisition times (days to weeks).[7] Importantly, common to WBA and PET imaging techniques is the necessity to involve radioactive labels. As such, the information obtained reflects the concentration of radioactivity, as opposed to drug concentration directly, which limits

quantitative analysis.[8] MRI does not require radioactive labels and overcomes some of the issues with PET yet still cannot achieve sufficiently high spatial resolution, and has a broad requirement of 1-100 mM drug concentration in a tissue volume of greater than 1 mm^3.[9] MSI also does not require a radioactive label, offers unrivalled molecular specificity, and can operate on a 50 nm resolution scale with secondary ion MSI, however, is a destructive technique and is limited by the necessity for extensive sample preparation.[5, 10] Together, these imaging tools have provided a deep understanding of drugs in biological samples, however, it is clear that the intricacies of drug interactions at the cellular level alter their therapeutic effect.[11] Microscopic imaging is capable of detecting subtle nuances in drug delivery that would otherwise be overlooked.

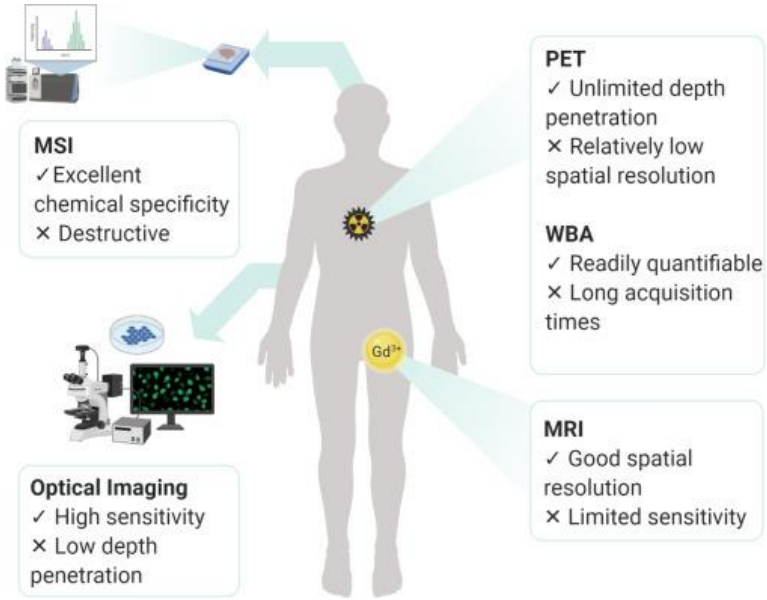

Figure 1.1. Overview of commonly used techniques in biomedical (drug) imaging, detailing their respective advantages and disadvantages. Reproduced with permission from Elsevier.[12]

1.1.2 Optical imaging

Optical imaging methods involve the use of light to visualise compounds of interest non-destructively in cells. Fluorescence microscopy has been employed extensively in cellular imaging. With a spatial resolution of up to 150 nm, confocal fluorescence imaging is capable of delineating individual cell organelles.[13] Fluorescence microscopy also often underpins the development and application of new chemical probes which facilitate chemical biology research.[14] The use of fluorescence technologies in drug imaging is regularly reported, revealing details of drug distribution, uptake and pharmacokinetics.[15-18] *In vivo* fluorescence imaging in

preclinical models has provided detail of drug processes, e.g., elucidation of drug pharmacokinetics to overcome taxane-resistant cancers.[19] Such diverse applications of fluorescence microscopy highlight its utility within the field of cellular imaging. However, with some exceptions for intrinsically fluorescent molecules, a notable shortcoming in using fluorescence for small molecule imaging is the requirement to attach a large fluorogenic tag. This is not generally problematic for targeting large biomolecules such as antibodies and proteins, however, small molecule drug imaging requires smaller tags for less perturbation. Common fluorophores often contain multiple fused ring moieties which aid in creating a delocalised electron system for fluorescence, but significantly increase molecular size. As a result, physicochemical properties can be affected, e.g., drug-target interactions and intracellular transport of the compound, rendering the system non-biocompatible. Label-free optical imaging modalities, specifically those relying on vibrational contrast, have been developed which avoid such issues. Label-free vibrational techniques circumvent photobleaching and phototoxicity issues associated with fluorescent labels and can theoretically offer better depth penetration due to longer laser excitation wavelengths.[20, 21]

The most common vibrational imaging techniques are near infrared (NIR) and Raman microscopy. NIR imaging exploits the dipole moment in chemical bonds to give characteristic vibrational bands for specific molecular features without the need for external labels. However, NIR imaging is not best suited to aqueous samples (e.g., cells), since the IR absorption cross-section of water is large. Raman imaging techniques such as stimulated Raman scattering (SRS) microscopy offer a range of unique benefits to facilitate drug imaging.[12]

1.2 Stimulated Raman scattering (SRS) microscopy

In recent years, interest in SRS microscopy as a tool to study biological systems, including those related to drug imaging, has grown considerably (**Figure 1.2**). The combined effects of advancements in microscope technology and the interest in using chemical biology techniques to gain insight on living systems has seen a shift in Raman scattering from a purely spectroscopic phenomenon to a practical life science technique. However, the fundamental principles remain unchanged.

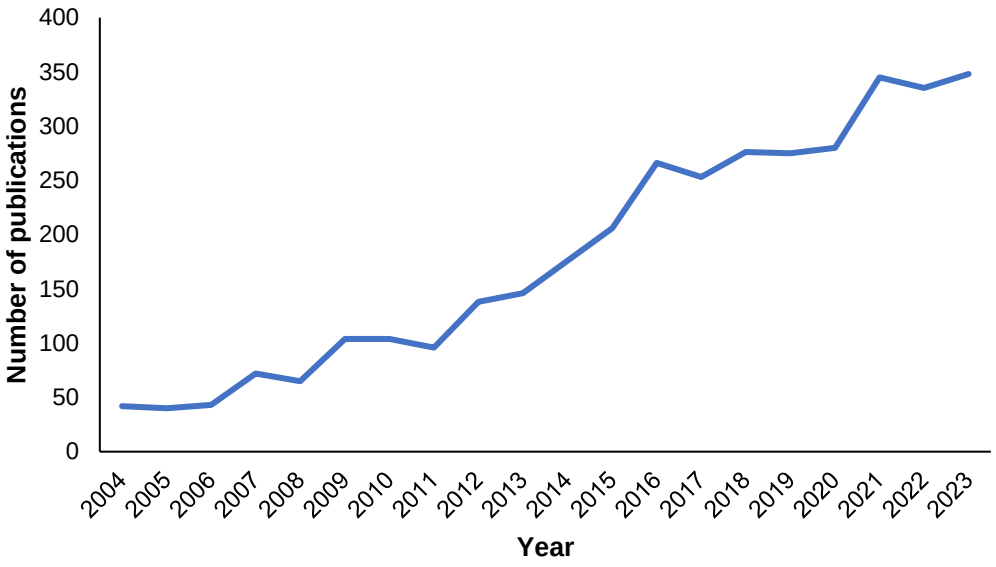

Figure 1.2. Publications on 'SRS imaging' over time, as determined by a Web of Science keyword search.

1.2.1 Background

The Raman effect refers to the inelastic scattering of light upon interaction with a molecular system. Depending on the system in question, this light may scatter at a higher energy (Anti-Stokes scattering) or lower energy (Stokes scattering), allowing information on the vibrational bands in the molecule to be determined (**Figure 1.3**). Specifically, Raman vibrational bands are generated when an associated change in the polarizability of a chemical bond is present. As such, highly electron-rich bonds (i.e., double and triple bonds) induce a high degree of polarizability and give intense Raman signals, relative to electron-deficient bonds.[22] This separates Raman spectroscopy from the frequently compared technique infrared (IR) spectroscopy, which is reliant on a change in dipole moment of a single bond. These fundamental principles form the basis of spontaneous Raman scattering (spRS) spectroscopy.

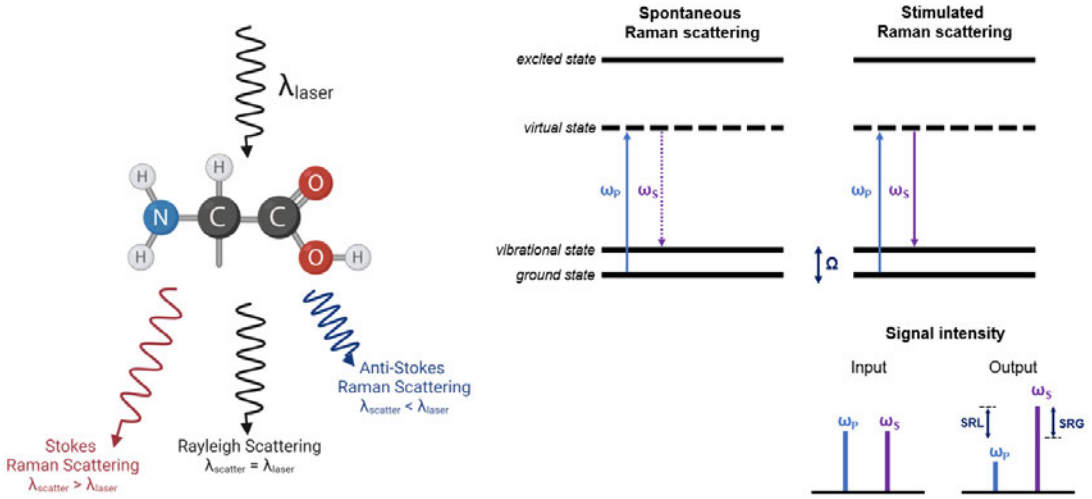

Figure 1.3. Schematic representations of Raman scattering. ω_P = pump beam, ω_S = Stokes beam, Ω = molecular vibration, SRG = stimulated Raman gain, SRL = stimulated Raman loss.

Raman scattering is an inherently weak effect, with only 1 in 10^7 photons absorbed scattered inelastically. Thus, spRS requires long acquisition times and generates spectra at relatively low signal-to-noise ratios (SNR). Several approaches, including the use of coherent Raman scattering techniques, overcome these sensitivity issues by the use of two laser light sources known as pump and Stokes beams (**Figure 1.3**).[23] By tuning the frequency difference between these two beams to the energy of a molecular vibration, stimulated excitation occurs. The result is a gain in the intensity of the Stokes beam or 'stimulated Raman gain' (SRG) and a loss in intensity of the pump beam or 'stimulated Raman loss' (SRL). The change in beam intensity (typically from the pump beam) is measured in SRS microscopy which allows generation of contrast.[24, 25]

SRS allows signal amplification by several orders of magnitude and reduces acquisition times when compared to spRS. Both SRS and coherent anti-Stokes Raman scattering (CARS) are examples of coherent Raman scattering techniques which have been applied in microscopy. Although CARS has been employed in biomedical imaging,[26] SRS imaging boasts some distinct advantages.[27, 28] For example, SRS does not suffer from the non-resonant background associated with CARS. In addition, quantitation and analysis is less complicated using SRS, with linear concentration dependence and ability to directly compare spectra with spRS spectra. SRS microscopy is a relatively new technique, with the first SRS microscope reported in 2007.[29] Since then, a number of technical developments and increased interest in the field has rendered SRS imaging an important tool in biomedical

research with a number of applications including label-free cell and tissue imaging, small-molecule imaging and even *in vivo* and *in situ* medical imaging.[30-32]

1.2.2 Generating contrast in SRS imaging

Several key features of Raman microscopy render it a particularly useful tool in cellular imaging. The selection rules for Raman spectroscopy allow a high degree of chemical specificity, with small changes in the chemical makeup of a sample giving distinguishable Raman vibrational bands. This factor allows contrast to be generated between cells and the analyte in biological Raman imaging. Containing millions of endogenous chemical compounds, cells are naturally Raman-active (**Figure 1.4**).

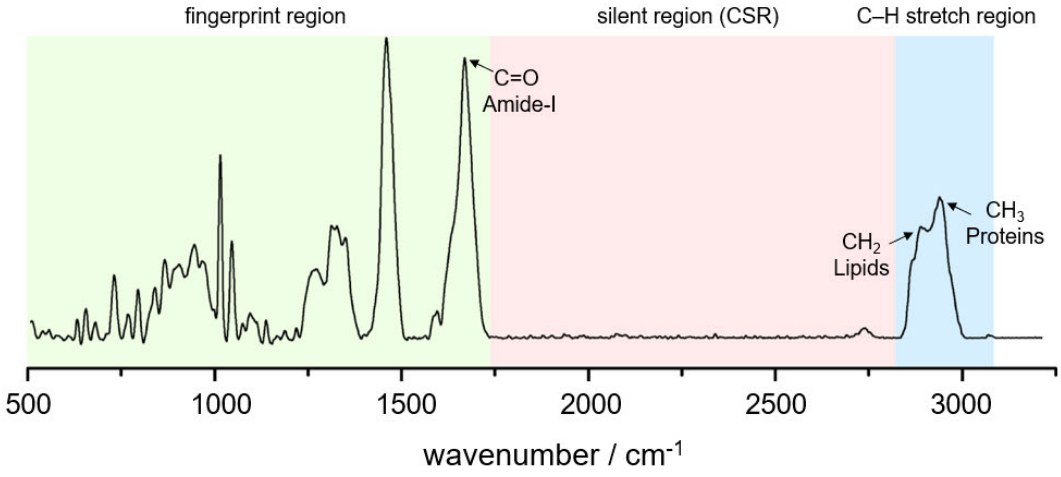

Figure 1.4. Raman spectrum of a cell. Adapted with permission from Elsevier.[33] CSR = cell silent region.

Accordingly, distinctive features of the fingerprint region and C–H stretch regions of the cellular spectrum can be used to obtain label-free cell images with SRS. For example, protein and lipid-rich regions of the cells can be identified by tuning to C–H bonds in CH_3 and CH_2 moieties, respectively, to visualise cellular structures; alongside identification of the amide-I stretch ubiquitous in proteins (**Figure 1.5**). The aforementioned high SNR and fast acquisition times of SRS also facilitate live cell imaging, which is essential to probe the dynamics of the cell.[34] Since SRS is a non-destructive and highly spatiotemporally resolved technique, time lapsed *in vitro* and *in vivo* imaging can be carried out.[35, 36] In addition, the linear relationship between SRS intensity and the concentration of the probed species allows real-time quantitative data to be obtained.[37] Ratiometric imaging has also complemented advances in quantitative SRS imaging.[38-40] Whilst SRS imaging is often performed to

view the distribution of a drug in a cellular sample laterally, depth profiling has also been achieved, allowing acquisition of 3D information.[41, 42]

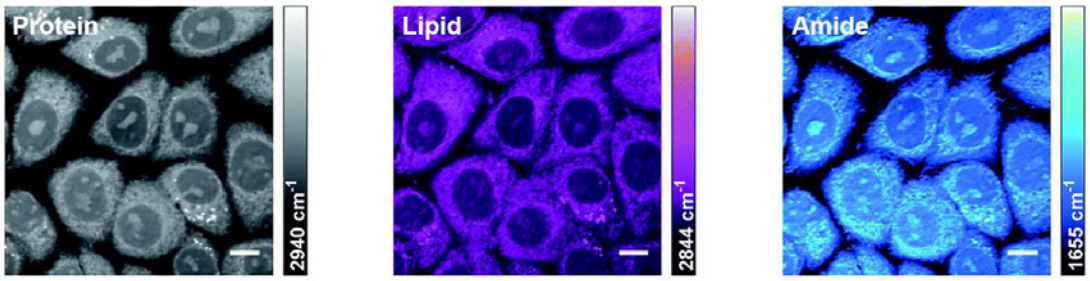

Figure 1.5. Examples of label-free SRS imaging of cell structures by tuning to protein, lipid or amide frequencies. Reproduced under Creative Commons public use license from Royal Society of Chemistry.[43] Scale bars 10 µm.

In some cases, such as for the biological components mentioned above, the Raman signal originates from an inherent feature of the probed molecule. Avoiding the attachment of tags is ideal when applicable. Advances in hyperspectral 'hsSRS' imaging have been fruitful in achieving label-free molecular imaging. hsSRS refers to the acquisition of Raman spectrum at a single pixel by rapidly tuning to multiple frequencies, as opposed to detecting a single Raman-active frequency. This has allowed delineation of individual spectral features ca. 10 cm^{-1} apart, with > 600 cm^{-1} spectral coverage.[44] hsSRS has enabled label-free imaging of a variety of analytes, including plant tissue, insulin fibrils and drugs within cells (see **Section 1.2.5.1**).[44-47] However, the need for rapid tuning between spectrally resolved Raman shifts in hsSRS requires advanced laser technology or complicated spectral unmixing, which is often not readily accessible.[48] Moreover, label-free SRS imaging is often more suited to the visualisation of biomolecules and cellular components, whose Raman-active bonds are in plentiful supply. For drugs and other exogenous small molecules, label-free technologies are not without limitations. Firstly, the molecule of interest may not contain distinguishable Raman bands. Molecular vibrations occurring within the fingerprint region (600–1800 cm^{-1}, **Figure 1.4**) can be lost in the noise of endogenous cellular signals. Moreover, since drugs are likely to accumulate at significantly lower concentrations than biomolecules, even if a distinct characteristic band is available, its Raman intensity may be insufficient in comparison to ubiquitous cellular protein and lipid signals.[22] Albeit more invasive, the attachment of highly Raman-active tags which resonate at frequencies distinct from the cellular background, i.e., within the cell silent region (CSR) (1800–2800 cm^{-1}, **Figure 1.4**), can be advantageous.[49]

1.2.3 Raman tags

The choice of tag is pertinent to not only the observable SRS signal but also the intracellular behaviour of the molecule-tag compound. In other words, the tag must be designed to exhibit Raman activity at high intensity and at a distinct wavenumber whilst remaining bioorthogonal to the cell. Tags for Raman imaging used to date can broadly be grouped into two categories: isotopologous and triple bonded.

Isotopologues (chiefly replacement of C–H bonds with C–D bonds) have been used to facilitate visualisation of small molecules in cells using SRS. Since isotopic substitution inevitably results in less, or no, disruption to the biochemistry of the system being studied, heavy atom tags may be advantageous over triple bonded tags. Several deuterated drugs have been investigated since they generally retain full potency and selectivity and have even been shown to confer benefits in drug action.[50] As probes, deuterated compounds have provided detail on drug pharmacokinetics both *in vitro* and *in vivo*.[51] According to the classical mechanics relationship $\bar{\nu} \propto \sqrt{k/\mu}$, the change in reduced mass (μ) when a C–H bond is replaced with a C–D bond results in a red-shifted Raman signal ($\Delta\bar{\nu}$ ~ 800 cm^{-1}). This, combined with the very low natural abundance of deuterium, makes for easily identifiable vibrational signatures for intracellular imaging. However, the Raman signal produced from the incorporation of deuterium labels tends to be more convoluted (from multiple vibrational modes) than the sharp band of alkyne moieties and also less intense, which may limit its applicability in some cases.[52] Nevertheless, the C–D bond has been used to visualise phospholipids, sterol, fatty acids, and amino acids.[5] Whilst small molecule drugs are not often directly deuterated for SRS cellular imaging, related examples do exist, e.g., deuterated nanomedicines for investigation of squalenoylation,[53] CARS imaging of deuterium-tagged docosanol,[54] and visualisation of deuterated nanoparticles for drug delivery.[55]

Nitrile (-C≡N), isonitrile (-N≡C), and metal carbonyl (-C≡O) tags on small molecule drugs have been used in spRS and SRS cellular imaging.[56-60] However, alkyne (C≡C) tags are most prevalent and have been used in both spRS and SRS for the study of cellular membrane biophysics, lipid metabolism and behaviour of various small (bio)molecules including drugs.[5] Alkynes exhibit intense, distinct (full width at half maximum (FWHM) = 10–15 cm^{-1}) Raman scattering peaks within the CSR (~2100–2300 cm^{-1}, depending on substitution).[61] Alkynes offer the additional benefit over other Raman-active bonds (e.g., nitriles) of being capable of substitution at either side of

the bond to allow generation of extended delocalised systems. Alkyne-tagged Raman imaging (ATRI) was first carried out by Yamakoshi *et al.* in 2011 using the alkyne-modified thymidine analogue EdU (**Figure 1.6**) to visualise cell proliferation,[62] and later for the localisation of coenzymeQ (coQ) analogues.[52] ATRI creates an interesting parallel with other alkyne chemistry in bioorthogonal imaging, for example attachment of fluorogenic moieties via Click chemistry.[63] However, direct ATRI is an undoubtedly less complicated tagging technique. Yamakoshi's seminal studies provided evidence of the expected increased Raman intensity of diynes over simple alkynes thus sparking interest in their use in ATRI. A diyne tag was used to probe the localisation and mechanism of action of ferrostatins using SRS.[64] Conjugation with 1 or 2 aromatic rings saw an expected stepwise intensity increase in Raman signals; capping alkynes with (aromatic) bulky groups also benefits the shelf life of the compounds.[65, 66]

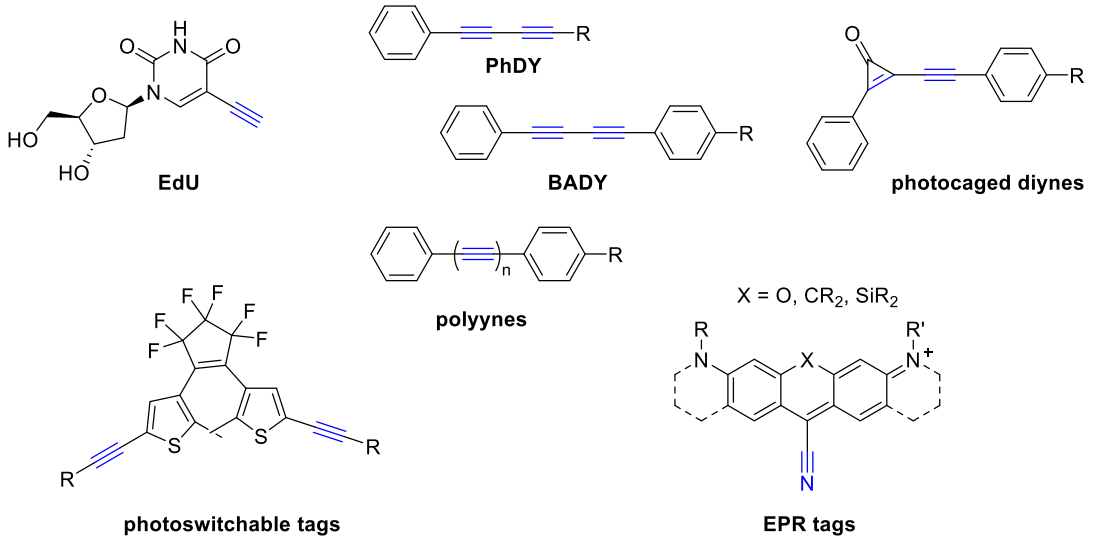

Figure 1.6. Examples of Raman tags for SRS imaging, highlighting Raman reporters in blue.

Following their initial development, these so-called BADY (bisaryl butadiyne) and PhDY (phenyl butadiyne) tags (**Figure 1.6**) were utilised for the visualisation of anisomycin in cells (see **Section 1.2.5.2**).[43] Aside from direct drug attachment, diyne tags have been readily used in the development of new chemical probes, including organelle markers and photocaged versions for dynamic cell studies (**Figure 1.6**).[67, 68] Likewise, organelle dynamics have been probed by photoswitchable alkyne-based tags (**Figure 1.6**).[69, 70] The design of conjugated alkyne tags (**Figure 1.6**) was taken further by Min *et al.*, who constructed chains containing up to 6 alkynyl groups for supermultiplexed cellular imaging (**Figure 1.7**),[71] which has since seen new applications including Raman-based cytometry.[72] Multiplex imaging offers the

possibility of imaging different molecules simultaneously which may be practical in investigating combination therapies, or alternatively, for imaging both a drug and a target organelle or protein. The sharp peaks obtained in the Raman spectra of alkyne moieties compared to the overlapping spectra for fluorescent dyes provides clear advantages for SRS supermultiplexed imaging (**Figure 1.7**).

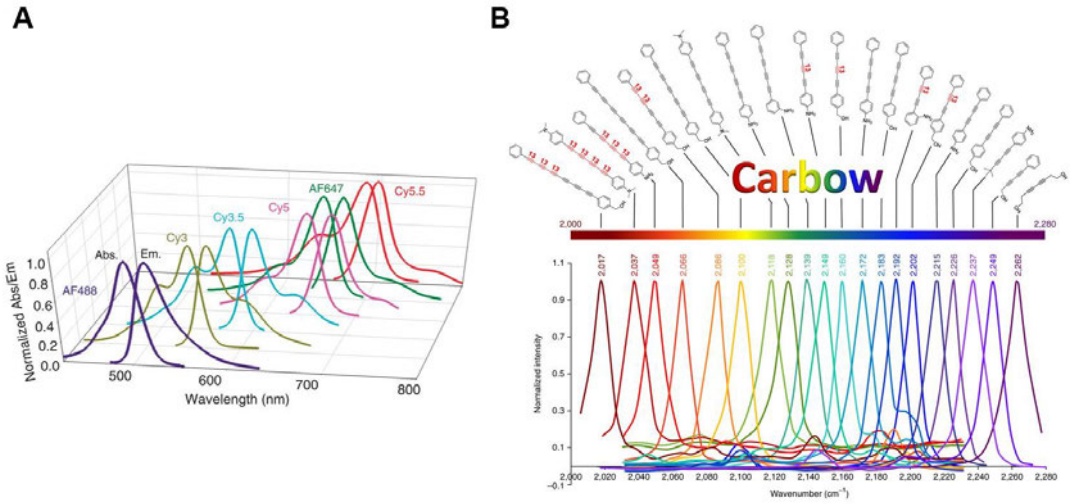

Figure 1.7. Comparison of spectral overlap between **A)** common fluorescent dyes and **B)** supermultiplexed polyyne Raman tags. Adapted with permission under the Creative Commons public use license **(A)**[73] and arranged license agreement **(B)**[71] from Springer Nature.

Although efforts are often made to separate Raman imaging from fluorescence due to its many benefits, the techniques are undoubtedly complementary. The intertwined nature of the two techniques has recently become more evident with the development of so-called electronic pre-resonance (EPR) SRS.[74-76] This technique relies on excited electronic states (c.f. fluorescence microscopy) as well as excited vibrational states. When incident light is close in energy to the excitation energy of an analyte, the partial excitation of the molecule confers a concurrent enhancement of Raman activity. This means that high wavelength fluorophores with excitation energies close to pump beam frequencies, such as NIR dyes, can act as highly Raman-active probes. This has led to the development of new, primarily xanthene-based, Raman reporters which can be partially multiplexed through isotopic substitution of C or N atoms in a nitrile moiety (**Figure 1.6**). These advances have pushed the limit of detection (LOD) of SRS microscopy closer to that of fluorescence microscopy, however, the larger size of these tags and their lability in aqueous solution emphasises the need for further optimisation for application in drug imaging.[77] A more detailed understanding of the origins of EPR will also aid in the computational design of new tags.[78]

In order to harness the potential of SRS as a widespread technique for drug imaging, new Raman probes must be developed which comprehensively address the requirements of an effective tag. Computational chemistry studies, namely density functional theory (DFT) calculations, have been used to assess the suitability of tags in a rational, efficient manner. DFT calculations have accurately predicted the Raman intensity of compounds of interest e.g., tags for anisomycin imaging.[43] Whether experimentally or computationally predicted, Raman tag intensity values are often represented as their relative intensity to EdU (RIE), since its activity in SRS imaging is well reported.[52] More recent studies have also reported a computationally predicted Raman shift value, greatly reducing the time required to assess banks of potential tag compounds. Sepp *et al.* found that DFT calculations could predict the Raman frequency of the alkyne moiety in ponatinib as 2217 cm^{-1} vs a corresponding experimental value of 2221 cm^{-1}.[79] In addition, Aljakouch *et al*. found strong correlation between the DFT calculated Raman frequencies of drug metabolites and those observed experimentally.[58] *A priori* assessment of the Raman vibrational profile of a tag allows confirmation of its activity in the CSR.

Computational chemistry also allows for the prediction of physicochemical properties that are relevant to cellular imaging. For example, considering most existing Raman tags (**Figure 1.6**) are generally rigid, carbon-rich structures with poor solubility, it is prudent to consider cLog*P*/cLog*D* in tag design. As more complex tags are developed, it will be important to confirm that biocompatibility with the cellular system being imaged is retained, e.g., in terms of molecular biodistribution. A thorough analysis of cLog*P* was carried out in the development of new BADY tags by Punaha-Ravindra *et al*.[80] Nitrogen and sulfur-containing heteroaromatic diynes were synthesised which, for the first time, addressed improvement of BADY tag solubility. In making changes to the aromatic endcaps, changes in the diyne Raman shift were achieved, allowing generation of tags which may be later used for multiplexing. These studies are particularly important because changes in lipophilicity can negatively affect drug distribution. Calculation of the change in partition coefficient log*P* with variation in coQ alkyne tags was carried out in the study by Yamakoshi *et al.*, allowing insight into cellular uptake.[52] Assessment of the tagged drug's target engagement must also be confirmed by assaying the compound, and could be probed by prior computational modelling.

1.2.4 Multimodal imaging

The unique mode of analyte visualisation in SRS imaging allows its combination with other modalities.[81] An imaging platform can thus be created which merges the benefits of other techniques and alleviates their shortcomings. This presents the exciting opportunity of being able to concurrently follow the transport of drugs through cells and monitor cell functions.[82] As most SRS imaging platforms are also designed for fluorescence imaging, fluorescent stains have been used to carry out multimodal cellular imaging of drugs. This allows small molecule drugs to be tagged with appropriately sized labels, whilst diffuse macromolecular lipids and proteins can be attached to bulky fluorophores. For example, anisomycin was imaged in fluorescently stained endoplasmic reticulum (ER)[43] and fluorescent lysosomes allowed the localisation of Raman-tagged ferrostatins[64] and, later, ponatinib (see **Sections 1.2.5.1 –1.2.5.2**).[79] Similarly, 2-in-1 bimodal probes have been developed which allow simultaneous SRS and fluorescence *in situ* detection.[83-85]

SRS-correlated multimodal imaging systems need not be limited to optical imaging techniques. A study involving the combination of matrix-assisted laser desorption/ionization (MALDI)-MSI and SRS investigated the pharmacokinetics and pharmacodynamics of erlotinib in brain tissue (**Figure 1.8**).[86] Although this was the first example of erlotinib imaging by SRS microscopy, it has been previously targeted for spRS imaging by Mashtoly *et al.*[87] The spRS study illustrated label-free detection and monitoring of drug metabolism in colon cancer cells. Erlotinib is a tyrosine kinase inhibitor and known epidermal growth factor receptor (EGFR) inhibitor; therapeutically, it has been licenced for the treatment of non-small cell lung and pancreatic cancers and has been investigated for treatment of a number of other tumour types including glioblastoma.[88] In this SRS study, a patient-derived xenograft model of glioblastoma, the high spatial and molecular resolution of MALDI-MSI allowed the distribution of erlotinib across the entire brain sample to be visualised (**Figure 1.8a**), whilst SRS provided a multicolour readout of the chemical composition of the tissue (lipids, proteins, and haem) (**Figure 1.8b**). This permitted analysis of drug accumulation in the differing tissue micro-architectures (**Figure 1.8d**). Interest in MALDI-SRS has continued to grow, with new examples describing simultaneous multimodal detection using the same tissue sample, at least partially overcoming the destructive nature of MSI.[89, 90]

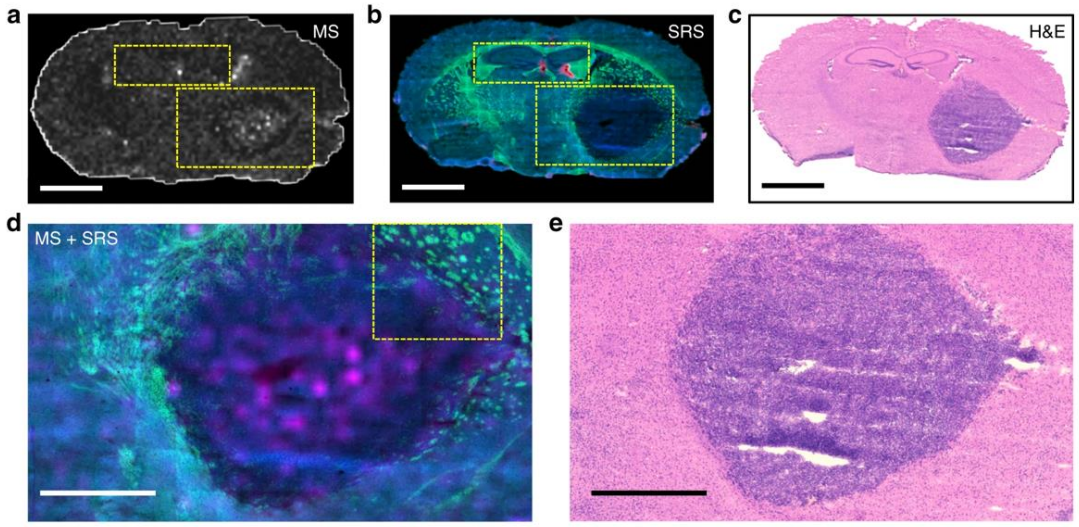

Figure 1.8. Multimodal imaging of drug distribution and brain tissue morphology. Reproduced under the Creative Commons public use license from Springer Nature.[86] **a)** MALDI-MS imaging shows erlotinib distribution across whole brain section. **b)** SRS imaging, green = lipid, protein = blue, heme = red. **c)** Haematoxylin and eosin (H&E) staining of a separate brain slice from same sample. **d)** Magnification of large rectangle area shown in **b** showing erlotinib detection in pink. **e)** H&E staining of area in **d**. Scale bars for **a**–**c** 1 mm and **d** & **e** 0.5 mm.

The nature of SRS allows imaging to pinpoint drugs by their unique chemical makeup, which, upon combination with well-established imaging modalities, allows for a comprehensive insight into their behaviour in cells. New and innovative multimodal imaging techniques will inevitably increase the applicability of SRS imaging. In practice, advancements will allow facile, holistic analysis of drugs at the cellular level and will underpin the translation of findings into pharmacological applications e.g., combination therapies.[91]

1.2.5 Examples of SRS-based drug imaging

As discussed, SRS imaging can be carried out in a label-free manner, permitted the structure of the drug allows this and/or hsSRS is used. In cases when this is not possible, Raman tags have been useful in facilitating drug visualisation. A range of drug types have been targeted for SRS imaging, primarily with a focus on anti-cancer therapies, dermatological drugs, nanoparticle-encapsulated drugs and formulation studies. Although this section will focus on only the study of drugs in biological environments, this does not diminish the significance of materials science-based study of drug formulations.[12] With the continuous exemplification of SRS microscopy as a quantitative, chemically specific and highly spatiotemporally resolved technique, its further integration into the drug discovery pipeline may be possible (**Figure 1.9**).[92]

The amenability to intracellular imaging means that application of SRS microscopy may be best placed in early stages of drug discovery (generally before clinical trials). Conversely, approved drugs may be re-examined by SRS imaging to uncover new drug functions or resistance mechanisms, examples of which will be discussed.

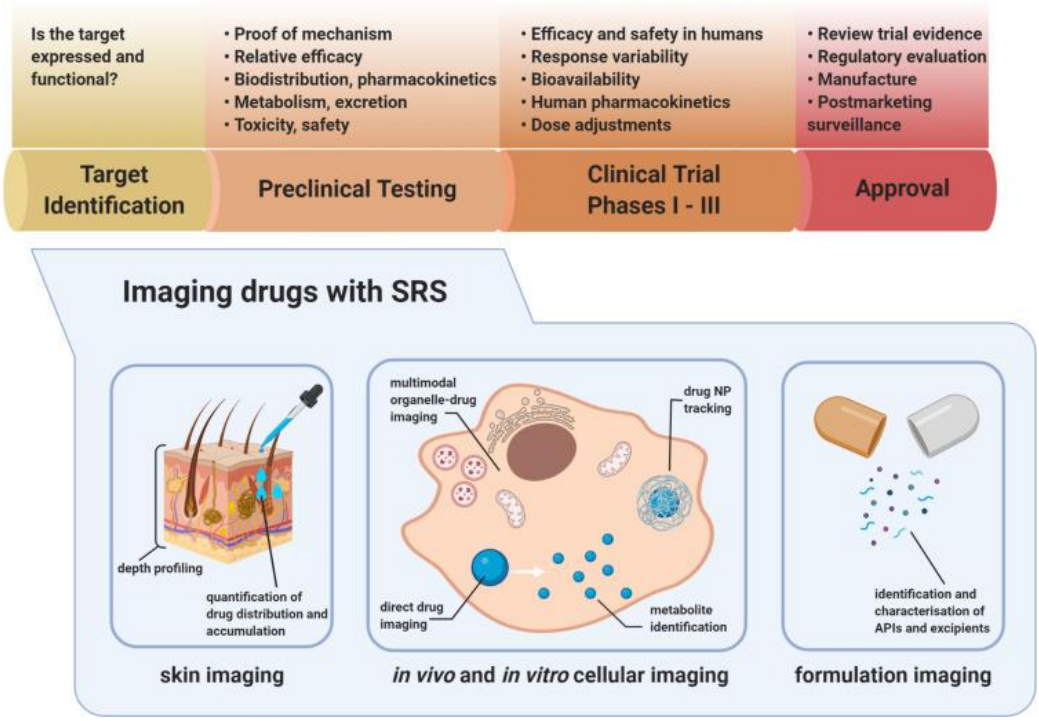

Figure 1.9. Examples of the utility of SRS imaging within the context of the drug discovery pipeline with explanation of steps involved in the process. Reproduced with permission from Elsevier.[12]

1.2.5.1 Label-free

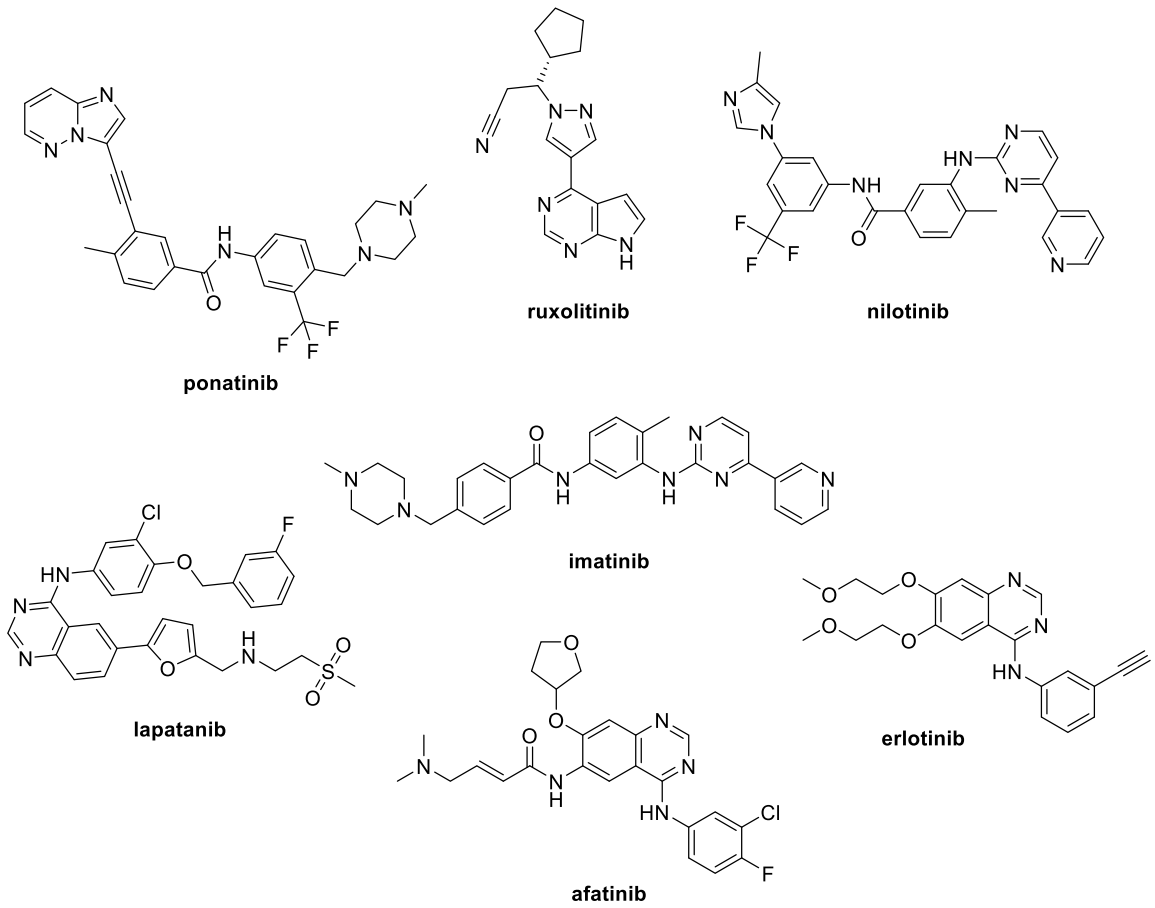

Figure 1.10. Examples of drugs targeted for label-free SRS imaging. Erlotinib and ponatinib were detected by tuning to the alkyne frequency, ruxolitinib using its nitrile group and all others were imaged by hyperspectral scanning in the CSR.

As discussed, label-free drug imaging sets SRS imaging aside from other modalities and has allowed a range of compounds to be visualised in cells (**Figure 1.10**). Although some examples do exist where drugs contain highly Raman-active reporters (C≡C, C≡N), many of these studies rely on hsSRS imaging. Tyrosine kinase inhibitors (TKIs) have been studied most frequently by SRS imaging. The lysosomotropic properties of imatinib and nilotinib were probed in a study by Fu *et al.* using hsSRS.[46] Indeed, the fact that such drugs accumulate in punctate organelles such as the lysosomes greatly facilitates SRS detection since a very high local concentration of drug signal is achieved. Both imatinib and nilotinib contain a pyridinyl pyrimidine ring moiety which allowed visualisation of the molecules via the C–C stretching frequency of the ring linker bond. The drugs were detected as puncta in chronic myeloid leukaemia (CML) cells.[46] Correlation with fluorescence imaging allowed drug localisation to be pinpointed within the lysosomes of the cells; a distribution pattern

that is not unanticipated, considering weakly basic drugs tend to be protonated in acidic environments such as the lysosomes. Moreover, the linear intensity-concentration relationship of SRS allowed quantification of the lysosomal accumulation, revealing more than 1,000-fold enrichment of the drugs in the lysosomes. The cells were then incubated with chloroquine, a known lysosomotropic agent, which saw a ca. 900-fold and 2,500-fold increase in cytosolic concentration of imatinib and nilotinib, respectively. This may provide evidence for the sensitising effect of chloroquine observed in CML patients treated with some TKIs, including imatinib.[93] Although autophagy inhibition has been proposed as the mechanism behind the synergistic effect of chloroquine and its analogue hydroxychloroquine in TKI drug therapy, Fu *et al.* found this was not the case for the drugs used. The cells were incubated with a known autophagy inhibitor, which saw no significant change in drug accumulation.[46] Interestingly, a recent study found that clinically achievably doses of hydroxychloroquine failed to give the plasma concentrations required to inhibit autophagy, emphasising the need for further investigations.[94] hsSRS imaging of other TKIs (lapatinib and afatinib) was carried out more recently by Wong *et al.*[47] This study revealed important new information on drug uptake through cell membrane transporters and sought to link dysregulation of drug influx and efflux to TKI-resistance mechanisms.

Sepp *et al.* also studied a TKI in KCL22 CML cells using SRS microscopy (**Figure 1.11**).[79] Ponatinib naturally contains two aromatic moieties bridged by an alkyne bond, giving rise to a strong, distinct Raman signal. Importantly, ponatinib was visualised at a physiologically active concentration of 500 nM, an impressive feat considering the detection sensitivity of SRS had hitherto precluded the imaging of such low drug concentrations. Lysosomal trapping was again explored by use of a multimodal SRS-fluorescence imaging platform. Colocalisation of the SRS and two-photon fluorescence signal of a fluorescent dye for acidic organelles was observed, reaffirming the sequestration of basic TKIs in the lysosomes. Since lysosomal trapping of TKIs is thought to reduce interaction with their target receptors, the distribution of ponatinib in ponatinib-resistant CML cells was investigated. The resistant cells had a higher concentration of ponatinib in the cytoplasm and a 1.9-fold and 2.5-fold increased mean and maximum Raman signals over the sensitive CML cells, respectively. [79] As in the study by Fu *et al.*, the addition of chloroquine reduced the concentration of ponatinib within lysosomes in both the sensitive and resistant CML cells. Greater inhibition of BCR-ABL, the cytosolic tyrosine kinase targeted by

ponatinib in CML, was observed in the chloroquine-treated cells.[79] In other words, the prevention of lysosomal trapping by chloroquine allowed a higher cytosolic concentration of ponatinib for interaction with BCR-ABL. Notably, this did not vary in ponatinib-resistant CML cells, consistent with a reported BCR-ABL-independent mechanism of resistance to ponatinib.[95] This contrasts with studies of imatinib by Fu *et al.*, which suggested that target engagement (i.e., BCR-ABL-dependent resistance) could be improved with combined TKI and chloroquine treatment. These studies highlight the ability of SRS imaging to provide important information on drug-target engagement.[46, 93]

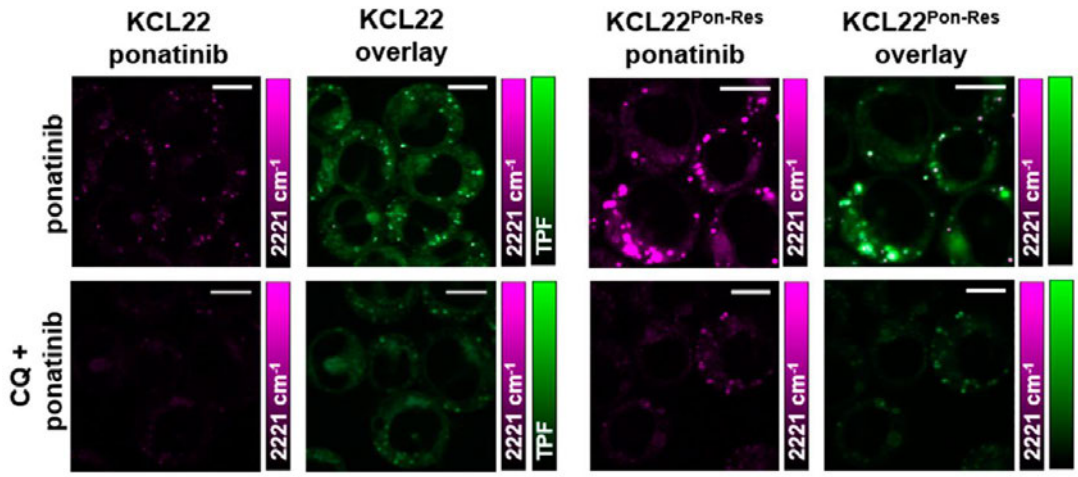

Figure 1.11. Label-free SRS imaging of ponatinib in live KCL22 and KCL22 ponatinib-resistant (Pon-Res) cells for investigation of resistance mechanisms. Reproduced under Creative Commons public use license from the American Chemical Society.[79] Contrast achieved by tuning to the alkyne frequency in ponatinib or two-photon fluorescence (TPF) from Lysotracker Green. CQ = chloroquine. Scale bars 10 µm.

Feizpour *et al.* studied the delivery of ruxolitinib to murine skin by SRS imaging (**Figure 1.12**).[41] The linear relationship between signal intensity and drug concentration again facilitated quantitative measurements such that pharmacokinetic data could be obtained. Time-lapsed depth-profile imaging, tuning into the nitrile vibration in ruxolitinib, revealed a build-up of the drug at the stratum corneum. This is expected; the lipophilicity of ruxolitinib is likely to have resulted in oversaturation of the transcutol formulation as the solvent permeated the skin, which was previously reported using SRS microscopy.[96] Deeper in the skin, the drug was detected initially at high concentrations which tapered off rapidly, suggesting a shunt mechanism of drug delivery.[97] Lipid- and water-rich areas in the stratum corneum, sebaceous glands, adipocytes and subcutaneous fat were probed by SRS, indicating higher

concentrations of ruxolitinib in the lipidic regions in all cases.[41] The study continued with an investigation into the effect of the formulation solvent on drug delivery. A low-pH gel formulation containing various solvents, excipients, and penetration enhancers was used to solubilise ruxolitinib and increase skin penetration.[41] Compared to ruxolitinib in transcutol, which initially accumulated at the skin surface over time, the gel formulation exhibited the opposite trend with drug concentration decreasing at the surface over time. The work by Feizpour *et al.* suggested that the gel had disrupted the skin structure, allowing for increased transdermal flux of drug. Despite the superior penetration of ruxolitinib in the gel, no translation to increased drug uptake could be found within the timeframe of the experiment. Interestingly, deuterated betamethasone dipropionate was studied to investigate how its higher lipophilicity (log*P* of 3.6 vs 2.1 for ruxolitinib) affects partition factors in lipidic cell regions. Despite their differing lipophilicities, SRS imaging revealed statistically similar partition factors for both drugs in the adipocyte and SCF layers. This highlights the capability of SRS to quantitatively probe and allow deduction of the physicochemical parameters of drugs, which is essential for further implementation in the drug discovery industry.[92]

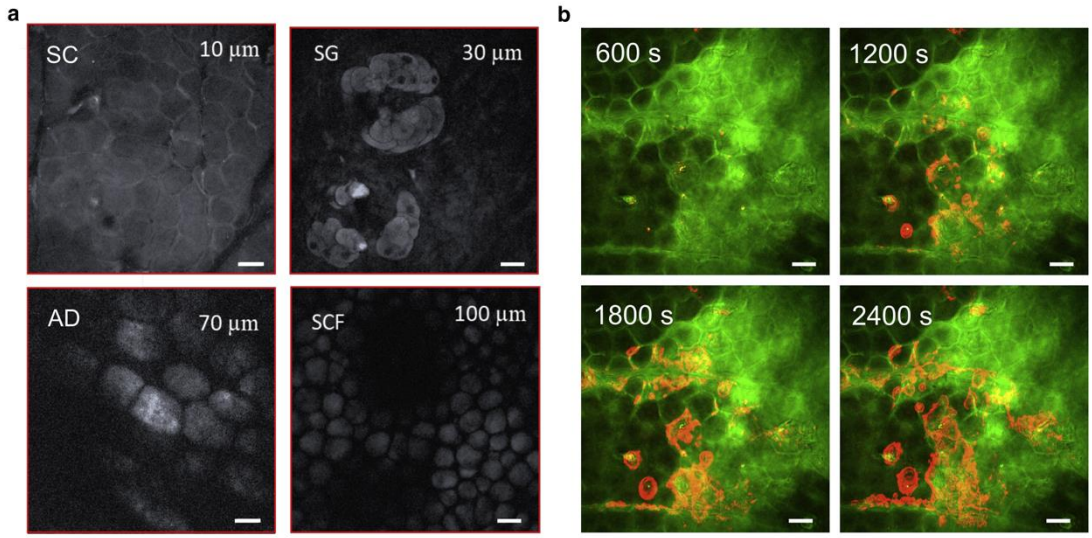

Figure 1.12. Label-free imaging of ruxolitinib in mouse skin. Reproduced with permission from Elsevier.[41] **a)** Examples of SRS images showing the distinct tissue morphology of different skin regions, acquired by tuning to the lipid CH_2 frequency. SC = stratum corneum, SG = sebaceous gland, AD = adipocyte, SCF = subcutaneous fat. **b)** Drug deposition in the SC layer (green) after treatment with ruxolitinib (red). Scale bars 20 µm.

1.2.5.2 Raman-tagged

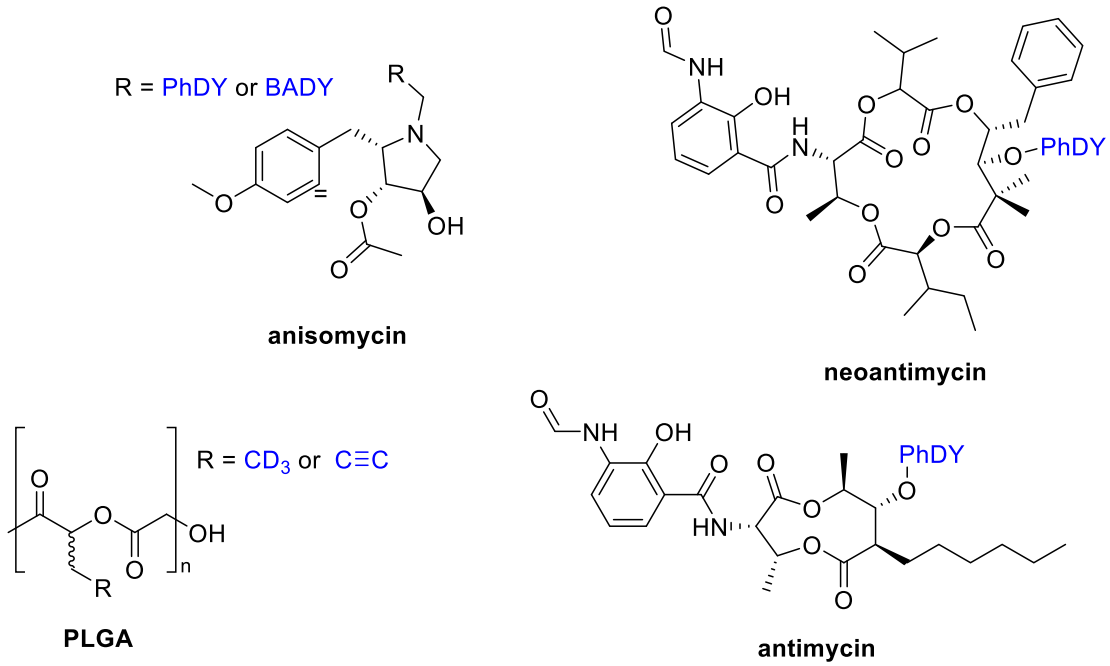

Figure 1.13. Examples of drugs and drug-related structures targeted for Raman-tagged SRS imaging. Tags used are highlighted in blue.

Albeit less frequently published, which reflects the associated challenges and greater interest in label-free imaging, examples of drugs/drug delivery systems targeted for Raman tagging do exist (**Figure 1.13**). Alkyne-tagged anisomycin was visualised in human breast cancer cells using SRS by Tipping *et al.* (**Figure 1.14**).[43] Anisomycin is known to inhibit protein synthesis by activation of stress-activated protein kinase (SAPK) pathways and its derivatives have been shown to have good activity against MDA16 triple negative breast cancer cells.[98, 99] A detailed knowledge of its structure-activity relationship allowed selection of the pyrrolidine nitrogen as a site for attachment to the alkyne tags; biocompatibility was further confirmed by carrying out a biological assay on the tagged compounds. Whilst no cytotoxicity was observed, the tags did exhibit some effect on drug activity, highlighting the need for further optimisation of tag design. BADY and PhDY tags were used in the study, since their structure allows for strong, distinct alkyne signals.[65, 66] BADY-tagged anisomycin provided a clearer SRS image at lower drug concentration compared to the PhDY-tagged compound. DFT calculations carried out prior to the experimental findings successfully predicted the higher signal intensity of BADY. Tipping *et al*. found that anisomycin accumulated in the cytoplasm of the cell, specifically in the perinuclear space. This distribution pattern is consistent with findings from a fluorescence

microscopy study of anisomycin.[100] Multimodal SRS-fluorescence imaging further pinpointed the localisation of anisomycin; the drug was colocalised with a fluorescent ER stain, consistent with anisomycin's known ribosomal binding site.[98]

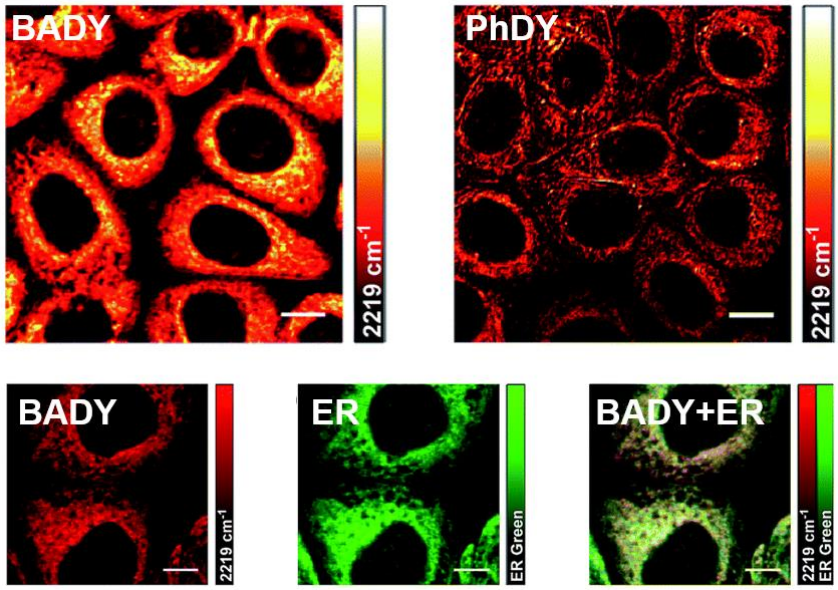

Figure 1.14. SRS imaging of BADY- and PhDY-labelled anisomycin in fixed SKBR3 cells. Reproduced under Creative Commons public use license from Royal Society of Chemistry.[43] Multimodal imaging allowed determination of colocalisation with ER tracker green. Scale bars 10 µm.

Diyne tags were also used to tag depsipeptide anti-cancer agents for intracellular SRS imaging.[101] The large molecular size and hydrophobicity of natural products such as these depsipeptides mean that tagging with BADY and PhDY is less likely to alter drug properties. PhDY tagged-antimycin and neoantimycin were visualised by SRS and their relative distribution was determined in cells. SRS imaging was again correlated with the subcellular localisation of known target proteins and further confirmed using multimodal imaging of the ER. The tagging methodology allowed information on structure-activity relationship to be obtained, revealing optimal sites for structural modification on the antimycin structures. The study revealed differences in the subcellular localisation of antimycin and neoantimycin, which was proposed to be driven by both their different protein targets and lipophilicity profiles.

Raman imaging has been used to study nanoparticles (NPs) for drug delivery in cells and presents advantages over other common imaging methods, e.g., incorporation of fluorescent dyes.[102, 103] Macromolecules such NPs are more amenable to Raman tagging than small molecules since modification is more likely to be bioorthogonal. In

addition, NPs are often formed of polymeric structures, thus many Raman reporters can be incorporated in a sequence to generate high local Raman activity. Vanden-Hehir *et al.* synthesised Raman-tagged polymeric NPs and visualised their uptake in *ex vivo* murine brain.[55] Alkyne- and deutero-analogues of the FDA-approved polymer, poly(lactic acid-*co*-glycolic acid) (PLGA), were synthesised and fabricated into NPs, giving rise to distinct Raman signals in the CSR. The NPs were first visualised in primary rat microglia and were found to distribute throughout the cytoplasm. Whilst drugs were not loaded into the NPs, rhodamine was encapsulated and its fluorescence signal was found to colocalise with the NP signal in microglia, demonstrating that PLGA NPs could successfully deliver material to the cells. NPs can cross the blood-brain barrier and thus offer the possibility of facilitating drug delivery to the brain.[104] The alkyne-tagged PLGA NPs were visualised in mouse brain slices to determine whether the *in vitro* findings could be translated to *ex vivo* imaging. The NPs were indeed distributed throughout the brain tissue; depth-profile images revealed internalisation by the microglia. Since the Raman-active PLGA directly reports its intracellular location via bond vibrations in its molecular structure, this study by Vanden-Hehir *et al.* may be inherently advantageous over fluorescence methods. For fluorescently tagged NPs to report accurately, they must not undergo photobleaching or leaching of the dye from its carrier, which would contaminate the signal. Notwithstanding the many benefits of labelled NPs, SRS has also recently been used to carry out label-free imaging of NPs for drug delivery.[105]

1.2.6 State of the art

The latest research in the SRS microscopy field has primarily focused on the development of new technologies for label-free and ultrasensitive imaging. For example, considerable efforts have been made in the advancement of hyperspectral imaging which coincides with the development of new laser sources and technology upgrades.[48] Hyperspectral imaging is complemented by the development of new data processing and denoising methods, and has been facilitated by new sparse spectral sampling approaches.[106, 107] Improvements in sensitivity through electronic pre-resonance or plasmon enhancement continue to lower the LOD of SRS.[108, 109] Moreover, recent examples of super-resolution SRS microscopy have broken the barriers of spatial resolution and will allow Raman detection to compete with fluorescence methods.[110-112] These technological advances set the precedent for a bright future within the SRS microscopy field and will expand its range of applications.

However, new practical developments also continue to emerge which may allow SRS microscopy to reach a broader audience. For example, high-throughput multi-well plate and flow cytometry offer new opportunities for SRS in biochemical testing and provide the necessary efficient, parallelised analysis for integration into biomedical research.[113, 114] Likewise, the tangible advantages of SRS imaging have been showcased in recent examples of intraoperative SRS imaging, providing real-time analysis of diseased tissue.[115]

It is important to note that the relative 'novelty' of SRS microscopy over other better characterised or more commonplace techniques greatly complicate its use. This is especially relevant for custom built SRS microscope setups (which represented the only option for researchers until recent commercial systems became available). For example, fluctuations in laser alignment through all portions of the microscope set up can occur and are not always possible to detect, leading to variation in signal intensity between samples. Variations between samples are also highly likely when detector misalignment occurs. Finally, electronic components such as the lock-in amplifier, which is involved in signal detection, are sensitive to thermal drift and decomposition over time. These factors are particularly challenging when attempting to obtain quantitative data, which is essential for bolstering the utility of SRS microscopy for drug imaging.[116] However, as interest in SRS microscopy continues to grow and further advances are made, these problems may become obsolete.

1.3 Conclusions

SRS microscopy continues to undergo advancements which move it to the forefront of biomedical imaging. The unique advantages of SRS imaging as a highly spatially and temporally resolved technique, with exquisite chemical specificity, have allowed important information on the intracellular behaviour of drugs to be determined. Facilitated by new label-free imaging modalities and improvement in microscope technology, the range of compounds targeted by SRS imaging is expanding. However, whilst larger super-Raman-active tags may continue to find utility in the labelling of macromolecules, there is an unmet need for the development of small, bioorthogonal tags. Generation of new, highly Raman-active tags which have been optimised for biological imaging will allow new drugs to be targeted, without relying on inherent Raman activity in the CSR which is so rarely available. Raman tags also offer a practical circumvention of the inherently high LOD of SRS microscopy, without the need for advanced microscope/laser setups. The ability to visualise drugs in this

manner may open up new avenues for the integration of SRS imaging into the drug discovery industry, where unique information on uptake, distribution and metabolism can be acquired.

1.4 Project summary

This project aimed to develop new Raman tagging methodology for the visualisation of drugs in living cells. A key focus was made on the improvement of existing Raman tags, which have been hampered by poor solubility, to broaden the application of Raman tagging in drug imaging. Guided by medicinal chemistry principles, in **Chapter 2**, new diyne tags were developed which aimed to improve tag solubility and retain high Raman activity. These new tags were analysed by mass spectrometry, X-ray crystallography and SRS microscopy to quantitate the effects of structural modification. **Chapter 3** focused on attachment of newly developed Raman tags to an anti-cancer drug of interest. It was envisaged that this would allow intracellular drug tracking and new information to be acquired on drug uptake, distribution and associated phenotypic responses. The new drug-tag analogues were characterised using physicochemical and biophysical analyses to determine tag bioorthogonality and imaged in a cancer cell line by SRS. In **Chapter 4**, the biological effects of drug tagging were explored in detail.

Chapter 2 Design, Synthesis and Analytical Evaluation of Raman Tags

2.1 Introduction

BADY was chosen as a starting point for the development of new Raman tags. The primary goal was to generate new molecules with increased aqueous solubility, thus expanding the applications of Raman-tagged drug imaging to include more complex targets. A design-synthesis-test approach was taken, guided by computational predictions of both physicochemical and Raman properties of the tags (**Figure 2.1**). Importantly, the DFT calculations provided information on both Raman intensity – which should be high enough to be able detect the molecule of interest at physiologically relevant concentrations – and Raman shift – which must exist in the CSR and provides information on tag multiplexability. BADY and related molecules are known to engage in intermolecular π-π stacking,[117-119] which was proposed to contribute to their poor solubility and intracellular distribution. An approach was taken to reduce the planarity of BADY by increasing the fraction of sp^3-hybridised carbons (Fsp^3). The concept of Fsp^3 has seen increased interest in recent years as a parameter for predicting the likely success of drugs and other biomolecules.[120,121] Moreover, disruption of planarity with the increase of Fsp^3 has been shown to result in improved molecular solubility.[122, 123] Considering these factors, BADY analogues with increased Fsp^3 character were designed, synthesised, and analysed. This element of tag design was carried out in parallel to ongoing studies in the group targeting specifically heteroaromatic tags with low log*P*, which will be discussed in **Section 2.6**.

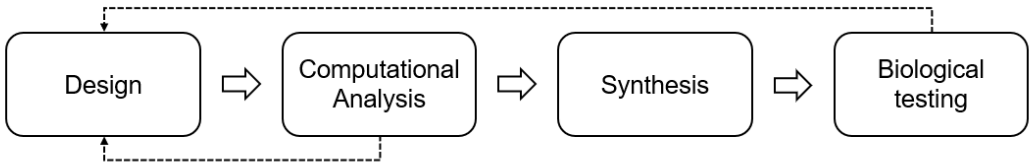

Figure 2.1. Workflow for the design, synthesis and evaluation of new Raman tags for cellular imaging.

2.2 *A priori* computational analysis

Whilst Fsp^3 was the main focus of this tag design campaign, log*P* was also taken into account considering its importance in medicinal chemistry. The parameter log*P* represents the logarithm of the partition coefficient of a species between *n*-octanol and water. Whilst log*P* considers the hydrophobicity a neutral species, log*D* also considers ionised forms of a molecule and is calculated at a specific pH. Unfortunately, increasing Fsp^3 generally also increases log*P* so the two parameters must be considered collectively. A range of diyne-containing molecules (**Figure 2.2**) were designed and analysed to determine their relative Raman activity (**Figure 2.3**). Calculations were based upon tags featuring the BADY or PhDY motif, containing a hydrolysable ester handle which provides a site for attachment to a compound of interest. In general, tags were designed that included a greater number of sp^3 carbons, whilst attempting to retain, or improve, Raman activity of the tag. A number of interesting observations can be drawn from the data. Theoretically, complete removal of an aromatic ring from the BADY motif to generate PhDY would disrupt π-π stacking, however, this significantly reduces diyne signal intensity. Accordingly, bicyclic aromatic motifs (A, B, O, U) were examined which retained Raman activity whilst still addressing Fsp^3. Similar compounds can be grouped together on the plot, *e.g.,* cyclic alkenes D, Q, and N gave similar shifts and intensities to the BADY tag. This indicates that a bis-aryl capped diyne may not be absolutely necessary to achieve high Raman activity. However, tags which showed increased Raman intensity over BADY all contained aromatic rings on both sides of the diyne. Furthermore, tags containing aromatic rings with additional groups allowing extended delocalisation (R, S, U) expectedly showed very high RIE values. RIE refers to the Raman intensity of a given bond relative to 5-ethynyl-2'-deoxyuridine (EdU), the chemical structure of which is shown in **Figure 2.2**. Each of the PhDY analogues were calculated to have greater Raman intensity over unsubstituted PhDY. The ability to accurately predict Raman shifts is also useful in the design of tags for multiplexing, whereby modifications in chemical structure allows series of molecules to be developed with stepwise changes in Raman shift. For example, C has a lower cLog*P*, higher Fsp^3 and is significantly blue-shifted compared to A, so was later taken forward for multiplexing studies (**Section 2.5**). **Figure 2.3** also indicates the cLog*P* value for each tag compound. Expectedly, positive correlation between the presence of heteroatoms and cLog*P* is evident, with piperidine (E) and piperazine (F) tags calculated as least lipophilic. Unfortunately, tag F is an unsuitable candidate since such ynamines are

highly susceptible to hydrolysis.[124] Compounds E, F and S exhibited very low cLog*P* as they feature multiple polar functional groups. Amine and sulfonic acid groups present in these molecules would also be charged at physiological pH, presumably resulting in a lower log$D_{7.4}$ value. Although this may improve aqueous solubility, these tags were not prioritised due to concern over unwanted sequestration into cell organelles.[125, 126] This does, however, highlight the opportunities for new Raman probes deliberately designed for organelle targeting. The compounds tested in this study constitute a very small portion of the tags available for synthesis. DFT calculations were carried out regularly throughout the tag design and optimisation process and will continue to guide future tag development.

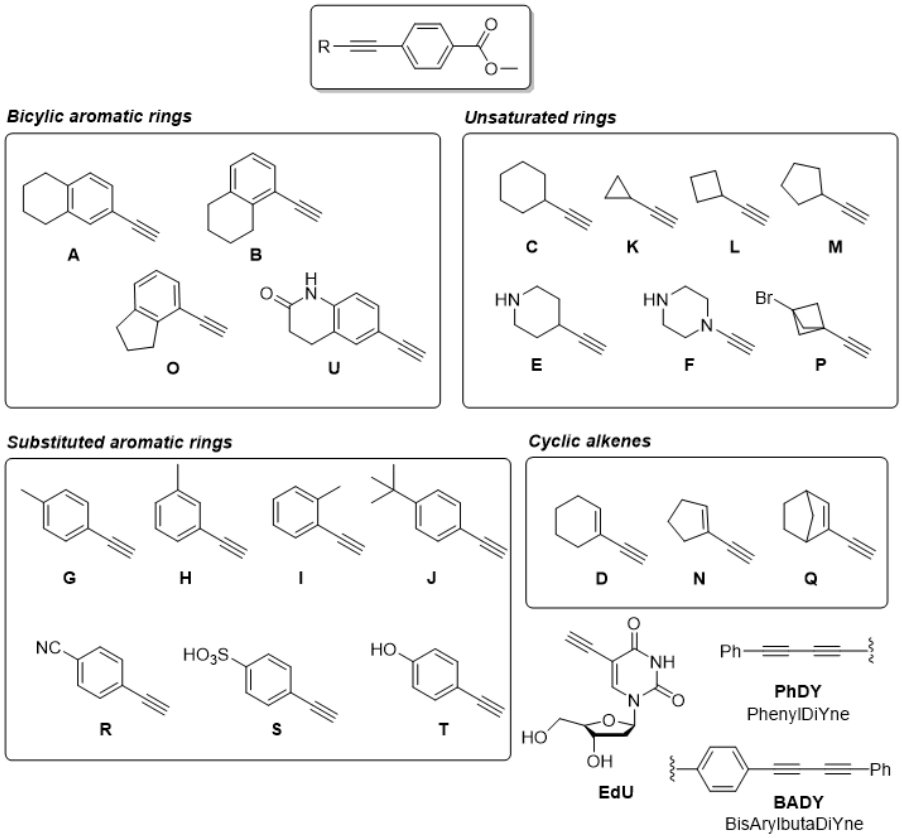

Figure 2.2. Chemical structures of new Raman tags A–T taken forward for computational analysis. Structures of 5-ethynyl-2'-deoxyuridine (EdU), PhDY and BADY are shown for comparison.

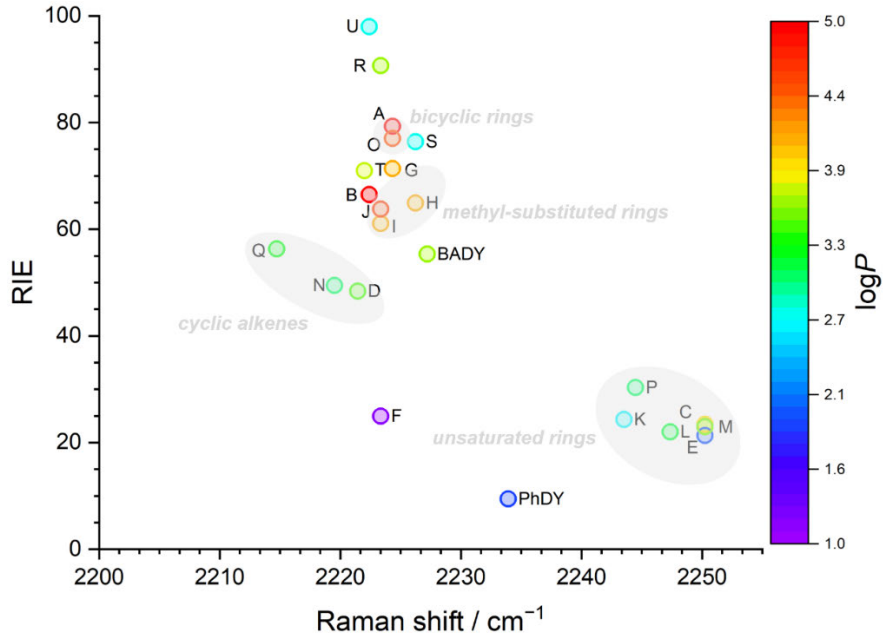

Figure 2.3. Results of computational analysis of methyl ester tags A–T. Full structures are provided in in **Figure 2.2**. Raman intensities are expressed relative to the calculated intensity of the alkyne in EdU (relative intensity vs EdU, RIE).

With computational data in hand, a series of synthetically accessible BADY analogues were taken forward to probe the physicochemical effects of changes in Fsp^3-character (**Figure 2.4**). Tetralinyl, (*p*-Me)-substituted, and (*p*-^{t}Bu)-substituted BADY analogues (**1b** and **1d**–**1e**, respectively) provide an increased Fsp^3 value, potentially disrupting π-π stacking.[122] Completely removing aromaticity in the alkyne end cap gives cyclohexyl PhDY analogue **1c**; a tag with an Fsp^3 value which falls within the typical range for a fragment library (>0.36).[120] A naphthalene-containing tag **1f** was included in the design process as a positive control; this has a very similar Fsp^3 value to **1a**, but with an added planarity which might be expected to increase stacking interactions.[127, 128]

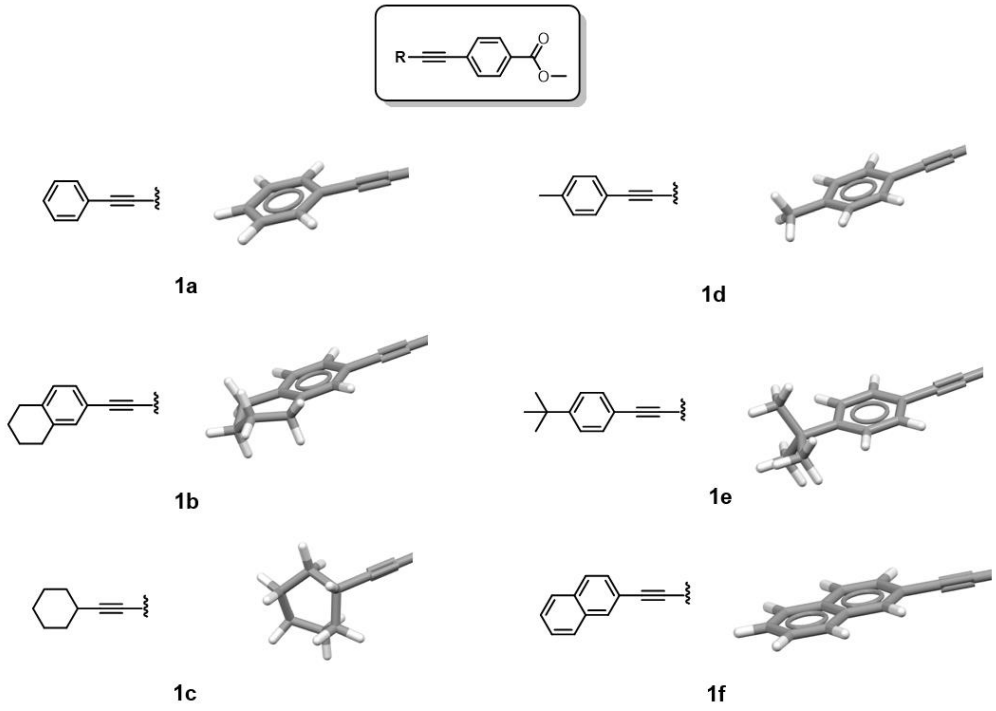

Figure 2.4. General chemical structure of BADY analogues and energy-minimised molecular structures of **1a**–**1f**. In each structure the methyl 4-ethynylbenzoate moiety remains unaltered and is therefore omitted for clarity.

2.3 Synthesis of mono- and bis-alkynes

In general, diyne-containing molecules such as BADY are synthesised via coupling of two alkynes. Synthesis of these mono-alkyne groups can be achieved through a number of synthetic routes, primarily via the Sonogashira reaction of aromatic halides with silyl-protected terminal alkynes, or via homologation such as in the Corey-Fuchs or Seyferth-Gilbert reactions. In this particular study, all but one of the alkyne starting materials for **1a**–**1f** were commercially available. For **1b**, where an aromatic halide starting material was not available for direct Sonogashira coupling, the alkyne was formed via Seyferth-Gilbert reaction with Ohira-Bestmann modification (**Scheme 2.1**). The carboxylic acid in **2** was reduced cleanly with $LiAlH_4$ to afford **3** in excellent yield. This was followed by the conversion to aldehyde **4**, which reacted with the Ohira Bestmann Reagent **5** to form **6**. This homologation reaction was later proven to be successful for the synthesis of more exotic, previously untargeted, heteroaromatic alkynes.[80]

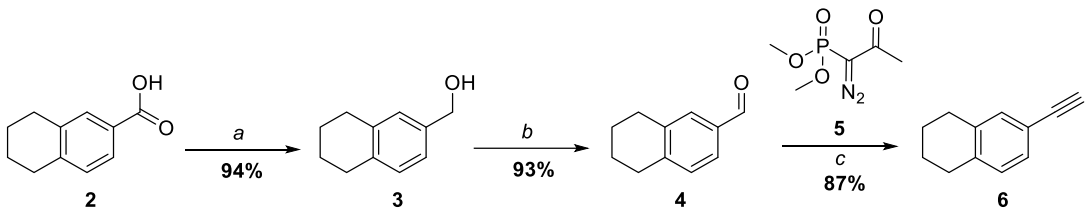

Scheme 2.1. Synthesis of tetralinyl starting material **6** required for the synthesis of **1b**. Reagents and conditions: a) $LiAlH_4$ (4 equiv.), THF, 0 °C→RT, 3 h. b) Dess-Martin periodinane (1.1 equiv.), DCM, 0 °C→RT, 16 h. c) Ohira-Bestmann reagent **5** (1.2 equiv.), MeOH, K_2CO_3 (1.1 equiv), 0 °C→RT, 4 h.

The synthesis of non-symmetrical bisaryl butadiynes is non-trivial, primarily due to competitive homocoupling of the starting materials. Limited synthetic routes are available, with the majority of published methods focusing on Cu-based Glaser-type coupling. A major limitation of this route is the need for a superstoichiometric amount of one of the coupling partners. A Cadiot-Chodkiewicz (CC)-type coupling was employed in attempts to synthesise BADY analogues in an efficient, cost-effective and green manner. In the early stages of the project, cross coupling yields were consistently hampered by the generation of by-products such as **9** and **10** (**Scheme 2.2**).

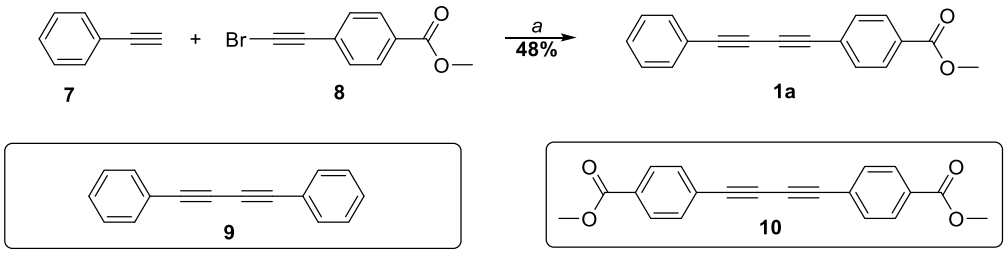

Scheme 2.2. Synthesis of **1a** using unoptimised CC-coupling, forming by-products **9** and **10**. Reagents and conditions: a) $Pd_2(dba)_3$ (0.04 equiv.), CuI (0.02 equiv.), Et_3N (2 equiv.), PPh_3 (0.04 equiv.), THF, RT, 4 h.

The appearance of impurities **9** and **10** can be rationalised considering the mechanism of Pd-catalysed CC coupling (**Scheme 2.3**).

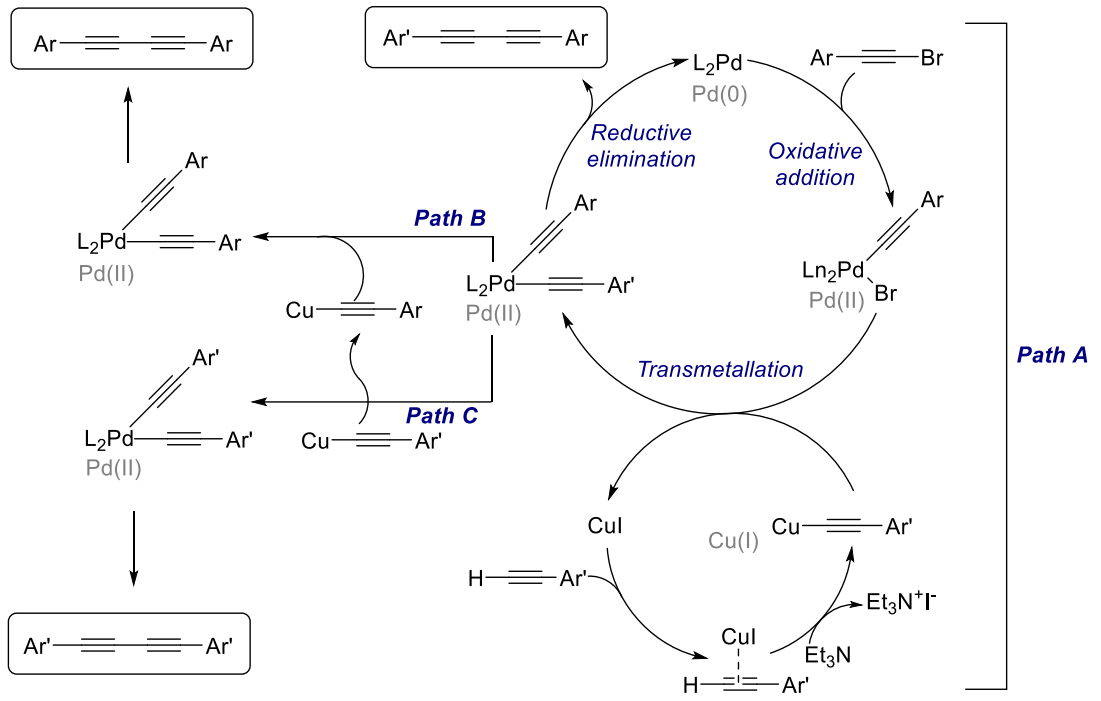

Scheme 2.3. Catalytic cycle of the Pd/Cu-catalysed CC coupling reaction with possible routes (paths B and C) to homocoupled side products. L = phosphine ligand and R = modified group in diyne tag structure.

After the transmetallation step, the alkyne-bound Pd intermediate may engage in a second transmetallation with a Cu-bound acetylide, forming homocoupled diynes (paths B and C in **Scheme 2.3**). Both phenylacetylene homodimer **9** and *para*-methyl ester phenylacetylene homodimer **10** were formed. Such side products, where extended delocalisation is available throughout the molecule, are likely formed in higher amounts than in reactions involving just one terminal alkyne or aliphatic R groups. A yield of 12% of compound **10** (*vs* 60% **1a**) was previously obtained in a Pd-catalysed cross coupling reaction.[129] With this information, attention was drawn to possible modifications to supress side product formation.

The phosphine ligand used in the reaction was identified as a component which may be modified to supress homocoupling.[130] For example, increased steric bulk is known to facilitate the transmetallation step, and electron rich phosphines increase the rate of reductive elimination.[131] As such, combining both these effects, the tri(*o*-tolyl)phosphine ligand was used. In addition, tri-*tert*-butylphosphine was trialled, which is substantially more electron rich than the aryl phosphines. Unfortunately, neither ligand appeared to have a significant impact on the yield of the reaction with homocoupled products still being formed. To determine whether by-product formation

would be a consistent issue in the reaction, alkyne **6** was subjected to the same reaction conditions in attempts to form the desired diyne **1b** (**Scheme 2.4**). Homocoupled products were again observed, with full starting material conversion but only a modest 39% yield of the desired heterocoupled product.

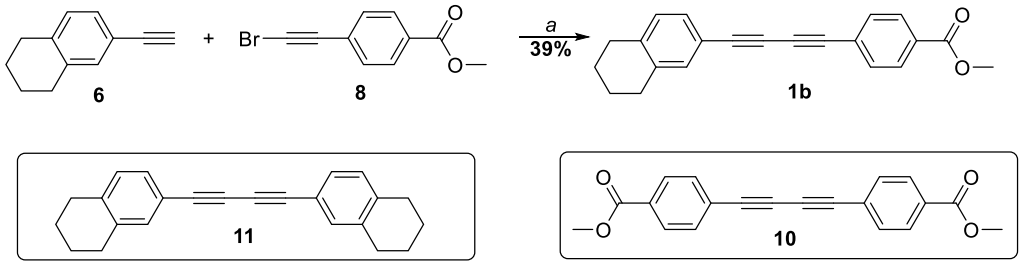

Scheme 2.4. Synthesis of **1b** using unoptimised CC-coupling, forming by-products **10** and **11**. Reagents and conditions: a) $Pd_2(dba)_3$ (0.04 equiv.), CuI (0.02 equiv.), Et_3N (2 equiv.), PPh_3 (0.04 equiv.), THF, RT, 4 h.

Shi *et al*. reported the use of phosphine ligand **12** (**Scheme 2.5**) in the synthesis of unsymmetrical diynes.[132] Therein, mechanistic studies provided evidence for reductive elimination as the rate limiting step, with phosphine **12** facilitating the formation of the reactive *cis* Pd complex. Both the bidentate nature and the π-acceptor ability of **12** were thought to accelerate the reductive elimination step.

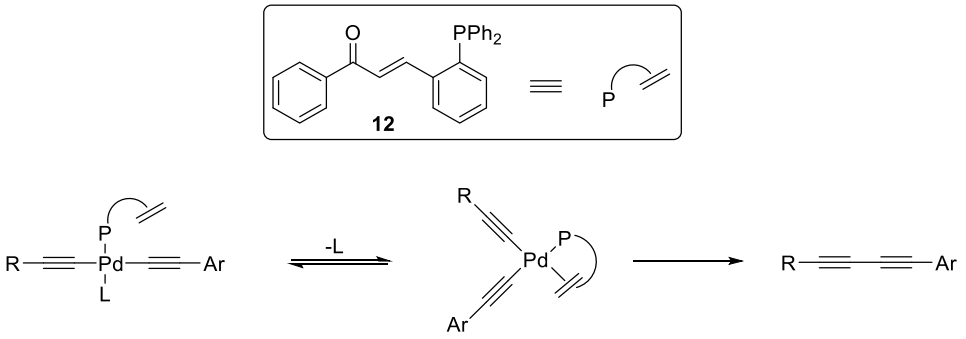

Scheme 2.5. Postulated mechanism of action of phosphine ligand **12** in supressing side product formation.[132]

Gratifyingly, replacement of the phosphine ligand with **12** improved reaction yield to 73%, providing more than 2-fold increase in formation of the heterocoupled product. (**Table 2.1**).

Table 2.1. Optimisation of the Pd-catalysed CC-type coupling reaction.

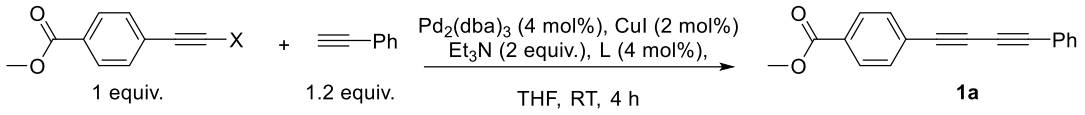

Entry	L	Yield
1	PPh_3	41% [a]
2	P(*o*-tol)$_3$	47%
3	P(^{t}Bu)$_3$	34%
4	**12**	73%

[a]Similar yields were obtained with alkynyl iodides, however, challenging workups prompted the use of alkynyl bromides which gave cleaner crude products.

Using the optimised conditions reported in **Table 2.1**, compounds **1b**–**1f** were also obtained in very good to excellent yields, reinforcing the utility of **12** (**Table 2.2**). However, it should be noted that for more complex molecules (including those with additional heteroatoms) **12** did not always afford heterocoupled products in high yields.

Table 2.2. Synthesis of compounds **1a**–**1f** via Pd-catalysed cross-coupling.

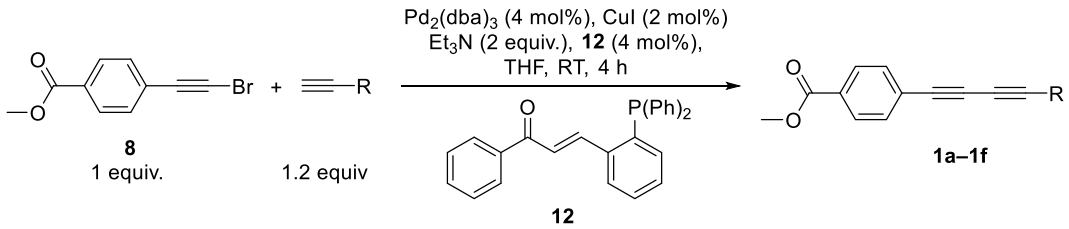

Compound	R	Yield
1a	phenyl	73%
1b	tetralinyl	71%
1c	cyclohexyl	69%
1d	(*p*-Me)-phenyl	76%
1e	(*p*-^{t}Bu)-phenyl	67%
1f	naphthyl	66%

2.4 Analytical evaluation of Fsp^3-inspired tags

The physicochemical properties of the newly synthesised tags were then probed; particularly their relative propensities to engage in intermolecular stacking, as this is known to affect solubility.[122, 123] Mass spectrometry (MS) has previously been used to provide information on both inter- and intra-molecular π-π stacking.[133, 134] ESI-MS analysis of **1a** revealed both its monomeric and dimeric sodiated molecular ion (**Figure 2.5**). The relationship between dimeric and monomeric species was confirmed by isolation of the dimer, which fragmented to the monomeric form under normal ESI conditions. It was postulated that, if the proportion of monomer and dimer could be regulated, a readout of molecular aggregation could be obtained. By increasing the collision voltage, which controls the fragmentation of ions in the collision cell, concomitant reduction in the intensity of dimer peak and augmentation of the monomer peak was observed (**Figure 2.6**).

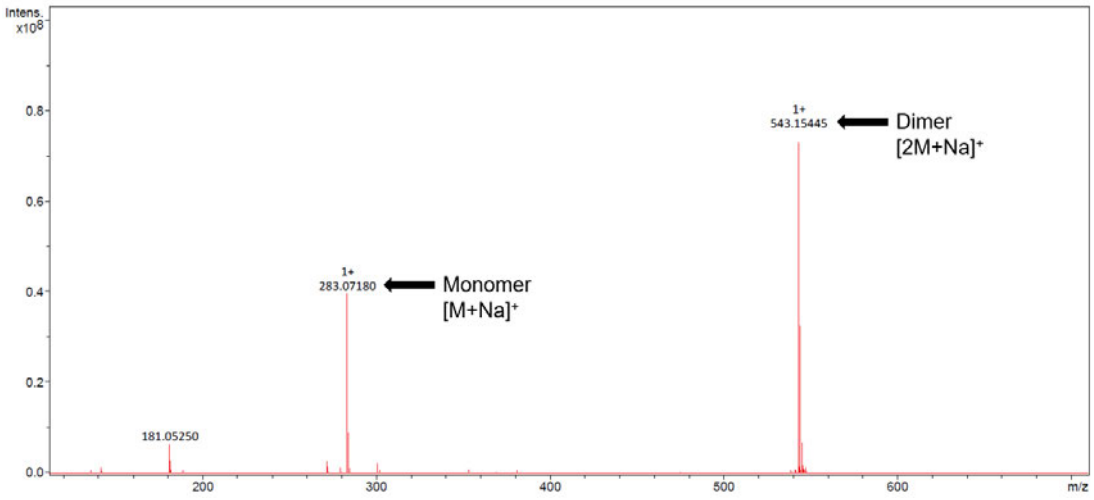

Figure 2.5. Mass spectrum of **1a** acquired at collision voltage = 0 V, *m/z* = 283.07 $[M+Na]^+$, 543.15 $[2M+Na]^+$.

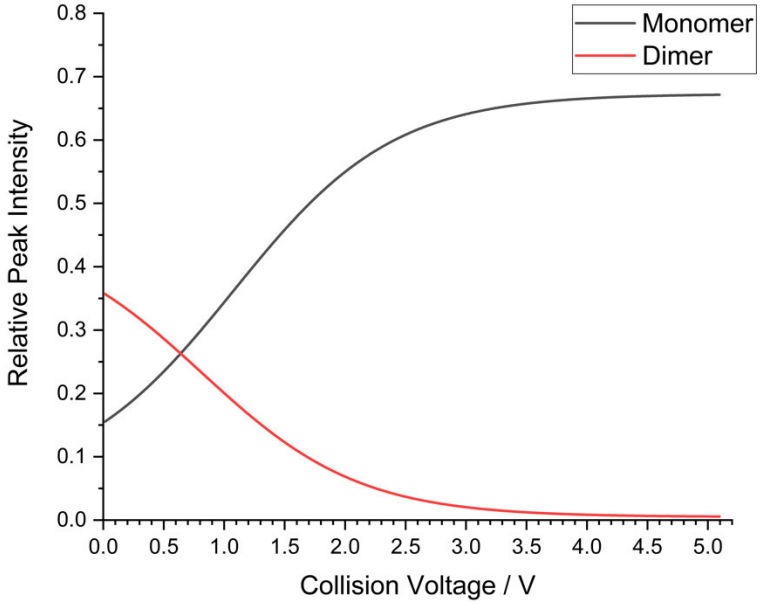

Figure 2.6. Change in peak intensity (normalised to the total ion count) for monomer (*m/z* = 283.07) and dimer (*m/z* = 543.15) species with increasing collision energy as identified in the mass spectrum of **1a**.

Performing the same experiment on tags **1b**–**1f** revealed similar reductions in the relative proportion of dimer at higher collision voltages (**Figure 2.7**). However, by determining the half-wave collision voltage (HWCV, collision voltage at which the dimer fraction represents half its original value), the tags could be distinguished. This indicated that the strength of the interaction holding together each molecule was different. Attempts to correlate HWCV with Fsp^3 were unsuccessful (**Figure 2.8**), suggesting that either the tags used or the MS protocol conducted, were not useful in comparing compounds based on Fsp^3. As previously noted, introducing a higher Fsp^3 to the BADY molecule gives a consequential increase in cLog*P*. Interestingly, a significant correlation between cLog*P* and HWCV was observed (**Figure 2.9**). This finding suggests that cLog*P* is a more useful parameter in predicting the strength of non-covalent interactions by MS.

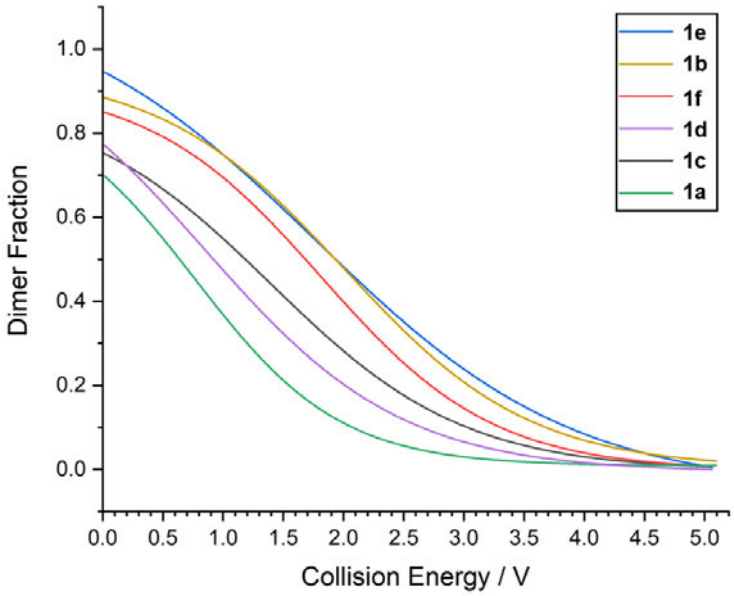

Figure 2.7. Change in fraction of **1a**–**1f** dimer with increasing collision energy, as determined by ESI MS. Dose-response curves were fitted to extracted ion chromatogram data normalised to the total ion count.

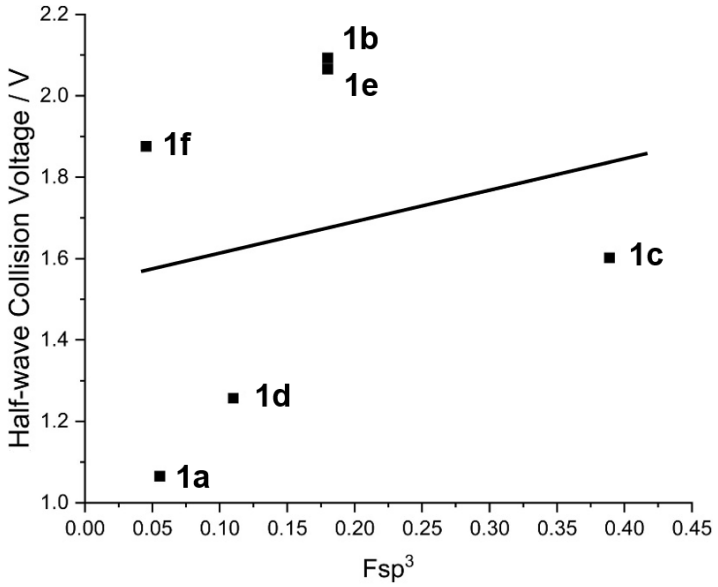

Figure 2.8. HWCV data obtained from ESI MS experiments plotted against Fsp^3 for **1a**–**1f**. $r = 0.40$, $p > 0.4$.

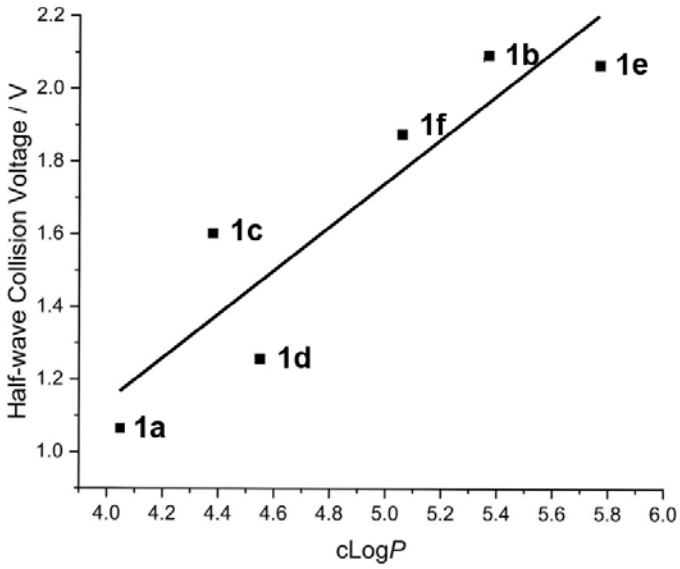

Figure 2.9. HWCV data obtained from ESI MS experiments plotted against cLog*P* for **1a**–**1f**. $r = 0.91$, $p = 0.01$.

Soft ionisation techniques such as ESI have been shown to preserve non-covalent interactions in small molecules, peptides, and proteins.[135, 136] However, since this MS data is obtained from a high energy gas-phase state, it was important to gauge the propensity of each tag to engage in non-covalent interactions which might affect crystal stability and dissolution. Unfortunately, attempts to study these molecules in solution, e.g., by DOSY NMR were unsuccessful. Nevertheless, the tags were investigated in the solid state. The crystal structure of 1,4-diphenyl-1,3-butadiyne has been solved,[137] however, **1a**–**1f** have hitherto never been investigated by X-ray crystallography. Crystals of **1a** and **1b** were obtained by slow evaporation from methanol and a 1:1 mixture of ethyl acetate and hexane, respectively, allowing their molecular structures to be determined (**Figure 2.10** and **Figure 2.11**).

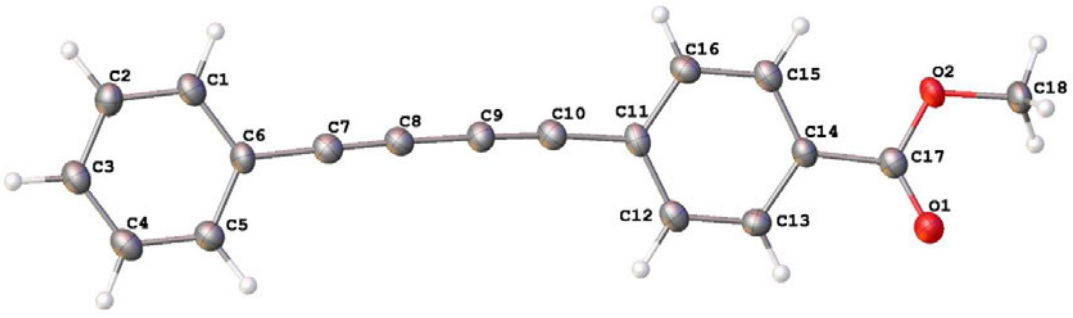

Figure 2.10. X-ray crystallography structure of **1a**. Displacement ellipsoids are at the 50% probability level.

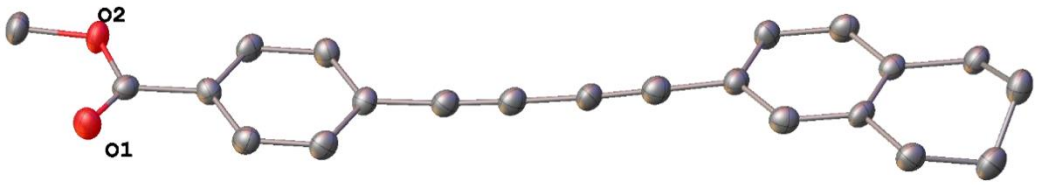

Figure 2.11. X-ray crystallography structure of **1b**. Displacement ellipsoids are at the 50% probability level. Hydrogen atoms omitted for clarity.

X-ray crystallography revealed differences in the crystal structure of tags with varying Fsp^3 (**Figure 2.12**). Whilst **1a** exhibits a regular end to end stacked structure, with the distance between aromatic rings (3.4–3.8 Å) within the typical range for π-π aromatic interactions (3.3–3.8 Å),[138] the same observations could not be made for **1b**. This suggests the asymmetry of the molecule and/or replacement of the phenyl diyne cap with the tetralinyl functionality impacted its ability to stack under the conditions used in X-ray analysis. Attempts to crystallise cyclohexyl derivative **1c** from a range of solvents including hexane, dichloromethane, ethyl acetate, ethanol, methanol, and combinations thereof were unsuccessful. Although this has not allowed any conclusions to be drawn about the stacking of this molecule, it does indicate that **1c** has improved solubility over **1a**.

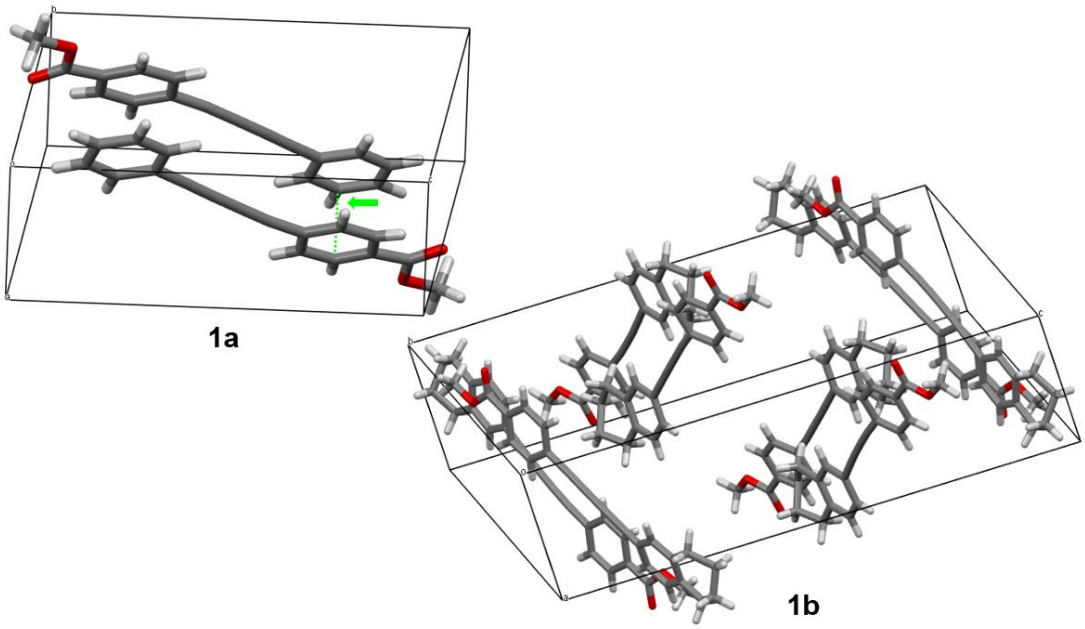

Figure 2.12. X-ray crystallography structures of **1a** (top) and **1b** (bottom). Green dashed line/arrow denotes the distance measured between aromatic rings (3.4–3.8 Å).

2.5 Raman activity of Fsp^3-inspired tags

The relative Raman activity of tags **1a**–**1f** in solution was then determined by spRS. Direct equimolar comparison with the signal intensity of EdU was unsuccessful due to the poor solubility of tag compounds in DMSO at higher concentrations which are required to observe EdU (**Figure 2.13**).

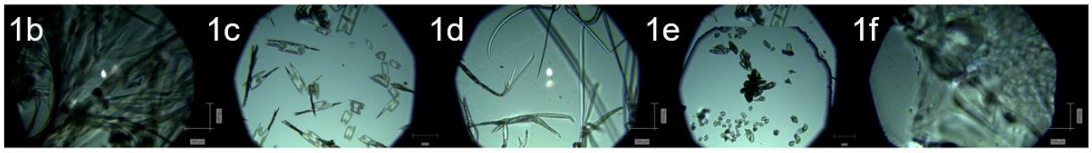

Figure 2.13. Microscope images of **1f**–**1c** (L–R) crystallising out of DMSO solution (100 mM tag + 100 mM EdU) after 20–30 s laser exposure.

However, on mixing at a 1:10 ratio, the BADY analogues (10 mM) exhibited a significantly greater Raman intensity than EdU (100 mM), as predicted by DFT calculations (**Figure 2.14**). Importantly, Fsp^3-based structural modifications to the BADY motif had no negative effect on the signal intensity of the diyne peak, excluding **1c** which, as a PhDY analogue, is known to exhibit lower Raman activity.[43]

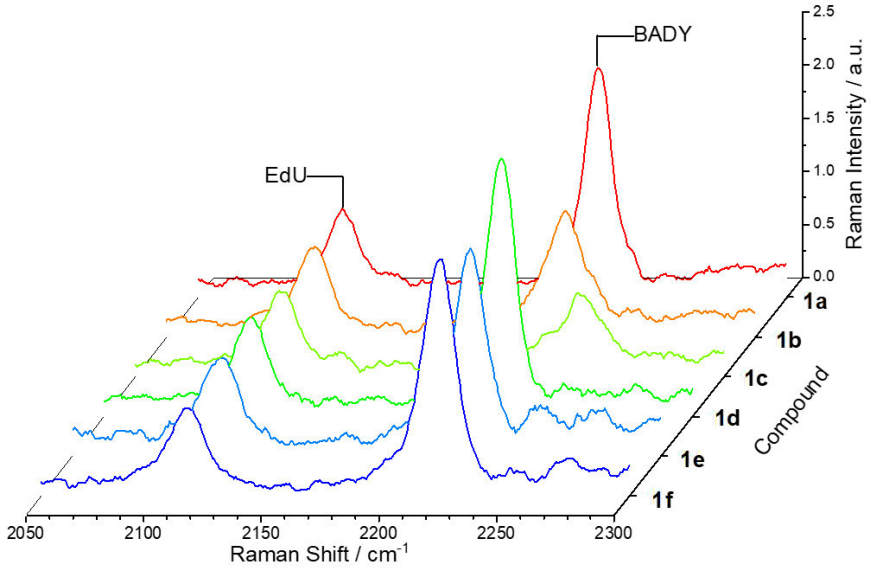

Figure 2.14. Spontaneous Raman spectra acquired from solutions of **1a**–**1f.** Tag samples were prepared in DMSO (10 mM) and mixed (1:1 v/v) with solutions of EdU in DMSO (100 mM). Intensities normalised to EdU at ca. 2112 cm^{-1}. The diyne peak in the spectrum of **1b** is anomalously low due to partial insolubility in DMSO.

Table 2.3 reports the experimentally obtained Raman parameters to those predicted in **Section 2.2**. Comparing predicted and experimental values (**Figure 2.15)**, Raman

shifts generally matched well. However, RIE values were much lower than predicted and did not correlate well. Variable and poor solubility of the tags leading to lower effective concentrations in solution may be partly responsible for these discrepancies.

Table 2.3. Calculated and experimental (**Figure 2.14**) Raman properties of tags **1a**–**1f**. RIE = relative intensity vs EdU. Predicted values were obtained via density functional theory (DFT) calculations (B3LYP/6-31G (d)).

Compound	Predicted		Experimental	
	Raman shift / cm^{-1}	RIE	Raman shift /cm^{-1}	RIE
1a	2225	63	2220	26
1b	2222	82	2220	14
1c	2248	23	2238	10
1d	2223	74	2219	26
1e	2223	79	2219	21
1f	2221	102	2220	27

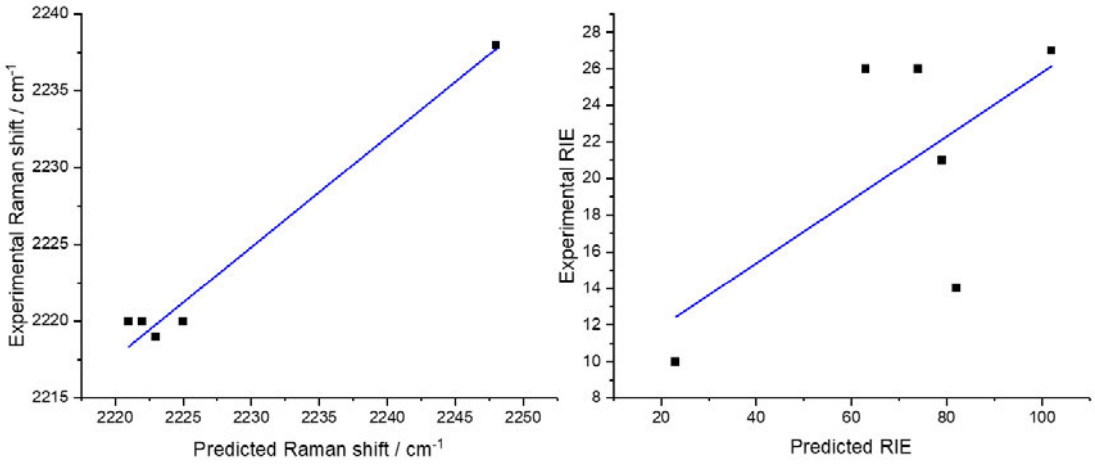

Figure 2.15. Correlation analysis of predicted and experimental Raman properties listed in **Table 2.3**. Left: Raman shift; $r = 0.98$, $p < 0.001$. Right: RIE (relative intensity vs EdU); $r = 0.64$, $p = 0.08$.

Having confirmed Raman activity in the CSR with spRS, **1a**–**1f** were taken forward for intracellular SRS imaging. When imaging a new compound, it was considered important to confirm the exact wavelength at which the maximum Raman intensity is observed via a hyperspectral scan. This accounts for any small differences in the

wavenumber obtained by spRS vs SRS and any changes when the compound is detected in cells vs pure solid/solution. ES-2 human ovarian cancer cells were used in this study as they are a robust, relatively easy to culture cell line. By tuning to wavelengths around 2220 cm^{-1}, and plotting the average intensity values in a region of interest within the cells, **1a** was shown to localise inside cells and exhibit maximum intensity at ca. 2213 cm^{-1} (**Figure 2.16**). As discussed, SRS is unique in the field of live cell microscopy in providing label-free delineation of cellular structures. Protein and lipid-rich regions of the cell were identified by their unique vibrational profile (**Figure 2.17 A** and **B**, respectively). This is achieved by tuning to the C–H bond in CH_3-rich moieties for proteins and CH_2-rich moieties in lipids. The alkyne image acquired is generally processed by subtracting an image taken at an off-resonance frequency to account for non-specific background signal. The on-resonance, off-resonance, and subtracted images are shown in **Figure 2.17 C**–**E**. **1a** was found to localise within the cytoplasm of the cell, notably absent from the nucleus. By overlaying the alkyne and lipid images, it became apparent that **1a** was concentrated in lipid-rich regions of the cell, which is consistent with theoretical and experimental analyses of the lipophilic BADY structure. The biodistribution of tag (specifically its absence from the nucleus) prompted further investigation into whether the physicochemical properties of BADY prevented nuclear penetration. If true, this may hamper future drug-tag imaging through disruption of the drug's natural cellular distribution.

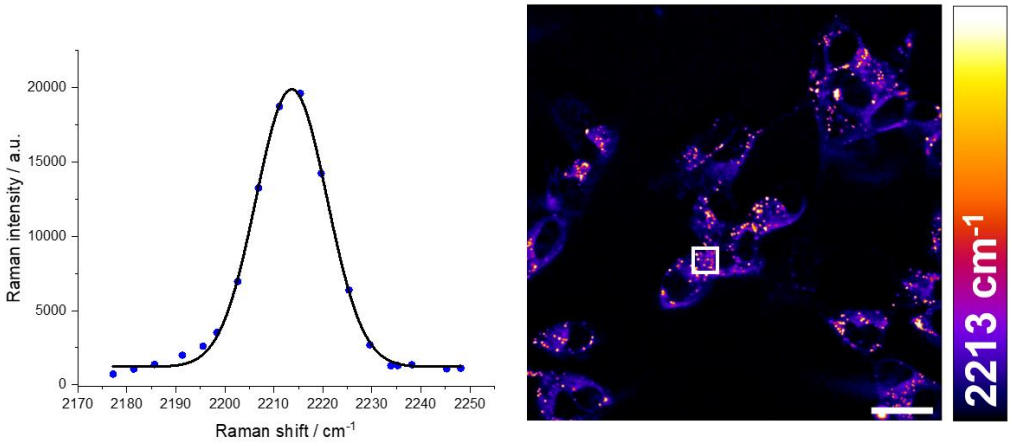

Figure 2.16. Hyperspectral scan of the alkyne vibrational window obtained from live SRS imaging of ES-2 cells after incubation with **1a** (10 µM, 1.5 h). Gaussian curve fitted using Origin 9.6.0.172. Region of interest within the cell used for intensity measurement is highlighted with a white box. Scale bar 25 µm.

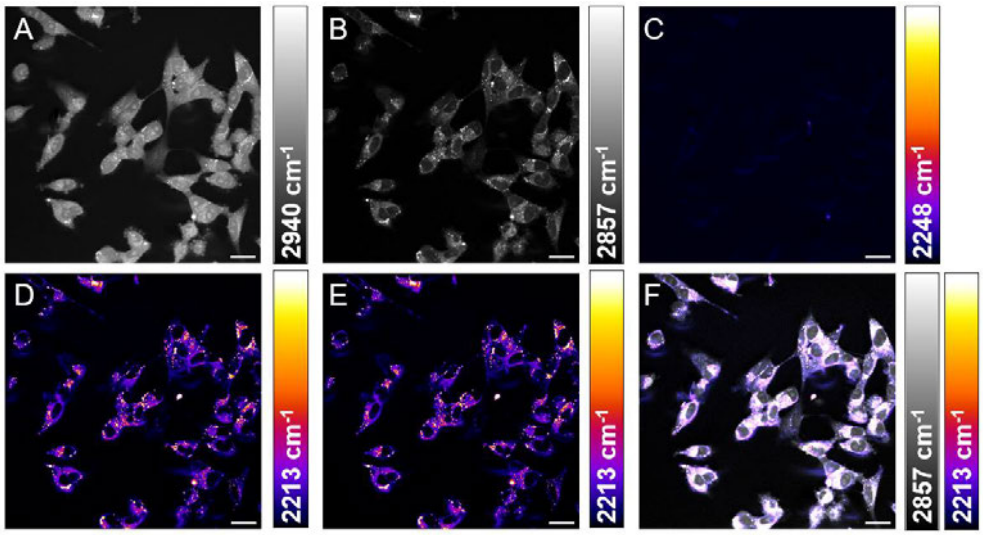

Figure 2.17. SRS imaging of **1a** in live ES-2 cells (10 µM, 1.5 h). Contrast achieved by tuning to the indicated wavenumbers for: **A)** CH_3 (proteins), **B)** CH_2 (lipids), **C)** C≡C (alkyne off-resonance), **D)** C≡C (alkyne on-resonance) **E)** subtraction of **D**-**C**, **F)** overlay of **B** & **E**. False colouring applied to **C**–**F** for clarity. Scale bars 25 µm.

Given that the exact relationship between physicochemical properties (cLog*P*, Fsp^3) and tag aggregation remained uncertain, differences in the biodistribution of **1a**–**1f** were assessed. Comparing images acquired upon incubation of ES-2 cells with tags **1a**–**1f** (**Figure 2.18**), showed a general similarity in the distribution of each tag. The tags appeared to be accumulating in lipid droplets and were not diffuse throughout the cell. At the incubation concentration, no compound signal was apparent in the cell media, suggesting no major issues with tag solubility. The images show no significant change in the cellular distribution of the tags was achieved upon structural modification, despite changes in physicochemical properties.

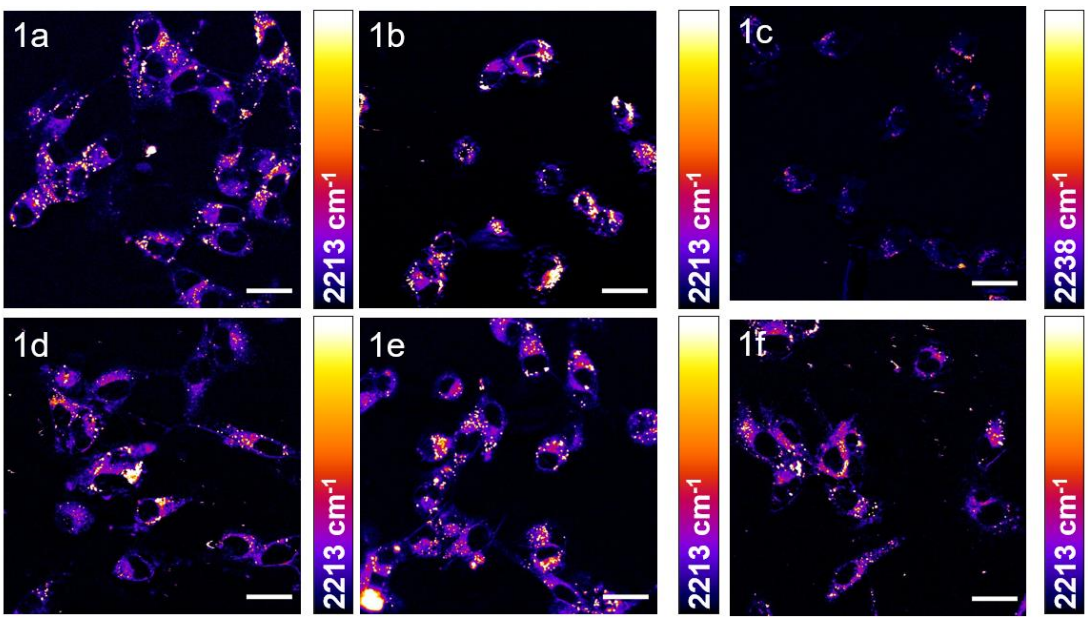

Figure 2.18. SRS imaging of **1a**–**1f** in ES-2 cells (10 µM, 1.5 h). Contrast achieved by tuning the indicated wavenumbers for the alkyne frequency. False colouring applied for clarity. Off-resonance frequency image subtracted from each alkyne image to account for background signal. Scale bars 25 µm.

With the knowledge that each of the tags were visible in cells at relatively high SNR, the possibility of simultaneous detection, i.e., multiplexing was explored. The blue-shifted signal of cyclohexyl tag **1c** highlighted it as an obvious candidate for multiplexing. In addition, its relatively low cLog*P* and high Fsp^3 made it an interesting target as a compound theoretically less prone to lipophilic accumulation. Direct comparison of tag distribution within the same cell environment allows for a richer investigation than independent analysis of the tags. Thus, HeLa cells were incubated with a mixture of tetralinyl tag **1b** and cyclohexyl tag **1c** and subjected to SRS imaging. By spanning a range of Raman shifts that encompassed the predetermined alkyne frequencies of both **1b** (2213 cm^{-1}) and **1c** (2238 cm^{-1}), two maxima could be clearly distinguished (**Figure 2.19**). Initial incubation of HeLa cells with **1b** and **1c** in a 1:1 ratio at 10 µM concentration, gave only low signal intensity for compound **1c** (**Figure 2.19** purple) reflecting its lower relative Raman vibrational intensity (**Table 2.3** and **Figure 2.18**) at the same intracellular concentration. However, increasing the concentration of **1c** 10-fold augmented its observed intensity (**Figure 2.19** blue), allowing both compounds to be imaged concurrently within the cells.

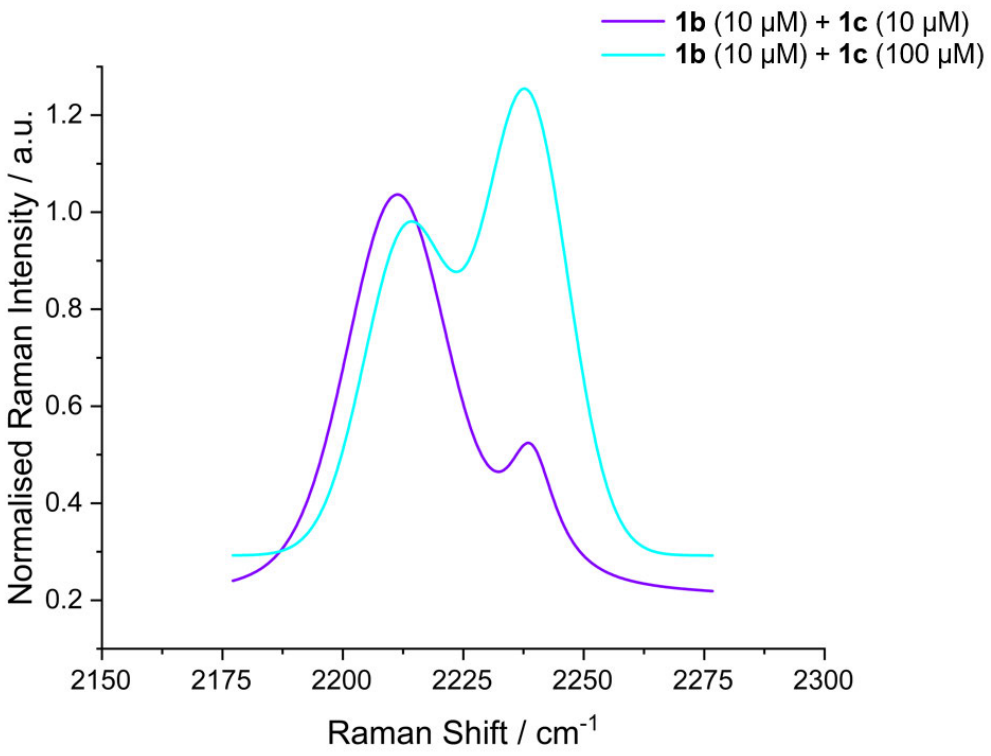

Figure 2.19. Simultaneous detection of **1b** and **1c** at the indicated concentrations in HeLa cells (2.5 h) via hyperspectral scanning of the CSR by SRS microscopy. Gaussian curves fitted using Origin 9.6.0.172 (OriginLab Corporation).

Incubation of HeLa cells with a mixture of **1b** and **1c** allowed their simultaneous detection within the cytoplasm (**Figure 2.20**). No significant differences in the distribution of the tags could be observed; although partial overlap of the signal resulted in some bleed through of signal between frequencies, as demonstrated in **Figure 2.19**. Moreover, when **1b** and **1c** were imaged independently, their subcellular localisation appeared to be similar (**Figure 2.18**). In future work, it may be interesting to install different organelle-targeting moieties to **1b** and **1c** in order to maximise the opportunity for multiplexing.

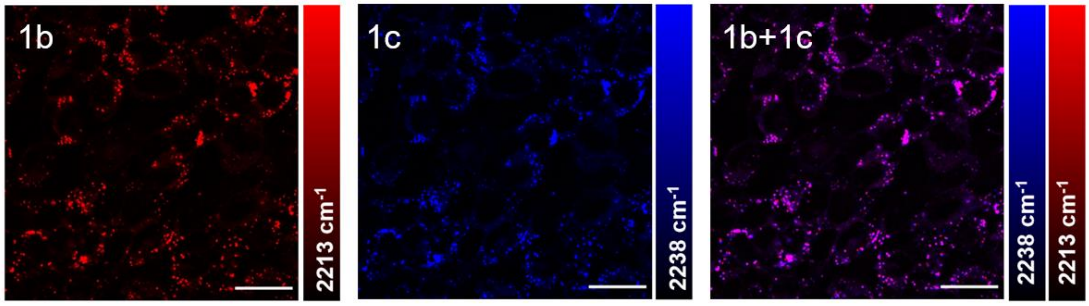

Figure 2.20. Multiplexed SRS imaging of **1b** and **1c** in HeLa cells. Cells were incubated with a mixture of **1b** (10 µM) and **1c** (100 µM) for 2.5 h. Contrast achieved by tuning to the indicated frequencies. Off-resonance frequency image subtracted from each alkyne image to account for background signal. Scale bars 50 µm.

Together, the study of compounds **1a**–**1f** highlight several important points. Firstly, it appeared that, whilst some effect of modulating Fsp^3 were observed in the solubility and intermolecular interactions of the tags, this did not translate to differences in their propensity to form dimers. Moreover, all tags were cell permeable and differences in the Fsp^3 did not change their apparent intracellular distribution. With MS data suggesting cLog*P* may be an important factor in tag association and these high cLog*P* compounds demonstrating punctate signal in lipid-rich regions of the cell and absent from the nucleus, attention was drawn to further reducing the cLog*P* of BADY tags.

2.6 Further addressing cLog*P* in tag design

Additional tags were designed with the hope of improving intracellular characteristics by further increasing tag solubility. Having assessed the signal intensity of the tags in cells, it was decided that further modification of the BADY (rather than PhDY) motif would be carried out.

2.6.1 Bicyclic low cLog*P* compounds

Tags **1g** and **1h** (**Figure 2.21**) were designed with iterative changes to the structure of tag **1b**. Benzolactam tag **1g** was included in the initial tag design phase (**Section 2.2**) and was shown to exhibit high calculated RIE, moderate Fsp^3 and low cLog*P* vs **1a** or **1b**. Fully substituting the lactam ring to generate quinazoline-2,4(1*H*,3*H*)-dione **1h** further reduces cLog*P*. Both of these bicyclic ring motifs have featured in medicinal chemistry development.[139, 140]

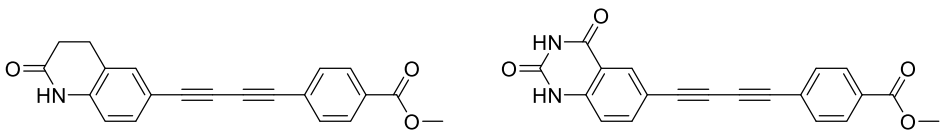

1g
cLog*P* = 2.75, Fsp^3 = 0.14

1h
cLog*P* = 2.01, Fsp^3 = 0.05

Figure 2.21. Structures of new Raman tags **1g** and **1h** and associcated calculated physiochemical properties.

Synthesis of the terminal alkyne precursors to **1g** and **1h** was carried out via microwave-assisted Sonogashira coupling of **13** or **14** to give **15** or **16** and subsequent silyl deprotection to terminal alkynes **17** and **18** (**Scheme 2.6**). This method avoided the long reaction times and high temperatures often associated with benchtop Sonogashira reactions. Diynes **1g** and **1h** were then synthesised using the Pd-catalysed cross coupling reaction conditions optimised in **Section 2.3**. Paradoxically, it was noted that **1g** and **1h** were very insoluble in common laboratory solvents (compared to other synthesised diynes) which may have been an early indication of their unsuitability. This may be due to intermolecular hydrogen bonding, which has previously been linked to the insolubility of quinazoline-2,4(1*H*,3*H*)-diones.[141, 142]

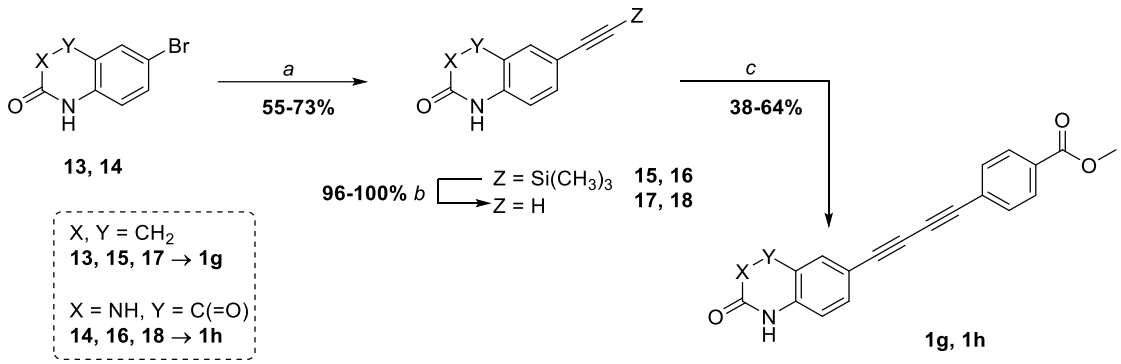

Scheme 2.6. Synthesis of **1g** and **1h**. Reagents and conditions: a) $PdCl_2(PPh_3)_2$ (0.02 equiv.) CuI (0.01 equiv.), Et_3N (2 equiv.), ethynyltri(methyl)silane (2 equiv.), pyridine:DMF (1:1 v/v), 90 °C, MW, 4 h, **15** (55%), **16** (73%). b) K_2CO_3 (0.1 equiv.), MeOH, RT, 24 h, **17** (96%), **18** (quant). c) **8** (0.83 equiv.), $Pd_2(dba)_3$ (0.04 equiv.), CuI (0.02 equiv.), Et_3N (2 equiv.), **12** (0.04 equiv.), DMF, RT, 4 h, **1g** (38%), **1h** (64%).

Interestingly, in addition to the expected Raman activity, **1h** exhibited fluorescent properties in solution (**Figure 2.22**). The quinazoline-2,4(1*H*,3*H*)-dione core has been used previously in fluorescent probes for biological applications.[143, 144] As discussed in **Chapter 1**, dual modality tags exhibiting both fluorescence and Raman activity are advantageous for a number of reasons and have previously been reported in the

field.[84] In this study, it was considered useful to utilise fluorescence detection mode to confirm the lack of signal (e.g., in the cell nucleus) was due to lack of compound rather than the high LOD of SRS vs fluorescence microscopy. Tags **1g** and **1h** were taken forward for attachment to a molecule of interest, alongside the Fsp^3 compounds.

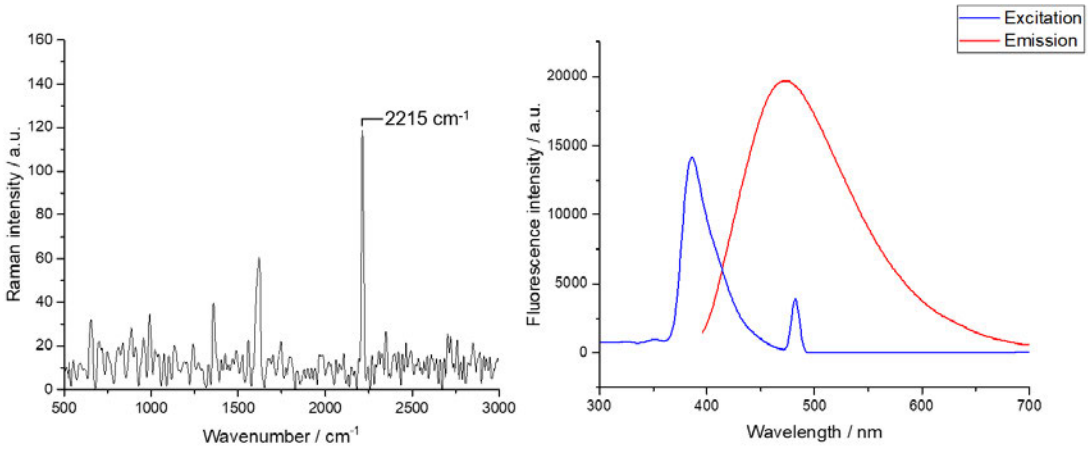

Figure 2.22. Raman and fluorescence properties of **1h**. Left: spontaneous Raman spectrum of a solid sample of **1h**, indicating the alkyne vibrational peak at 2215 cm^{-1}. Right: fluorescence excitation and emission profiles of **1h** (0.1 mg/mL in DMSO), λ_{ex} = 386 nm λ_{em} = 480 nm.

2.6.2 Heteroaromatic tags

The work presented thus far represents a small portion of the tag development carried out by the Hulme group. In parallel to the Fsp^3-focused work, new heteroaromatic tags were designed and synthesised, in collaboration with Dr Manasa Punaha-Ravindra.[80] These molecules offered a range of possible new opportunities in ATRI (**Figure 2.23**).

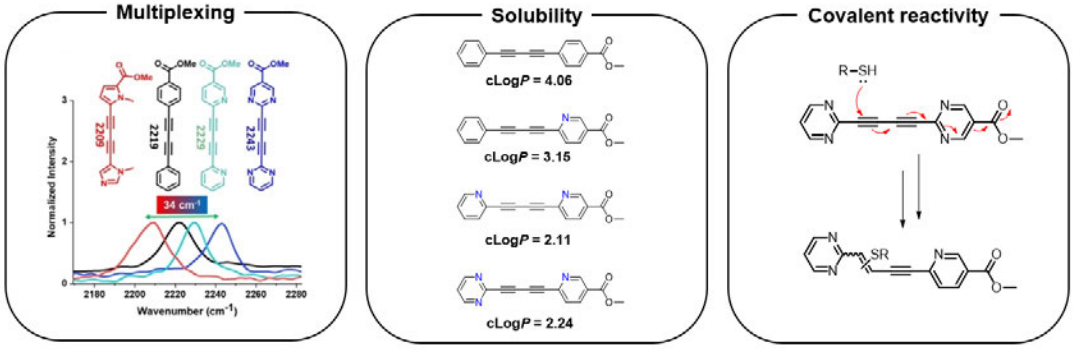

Figure 2.23. Opportunities for heteroaromatic BADY analogues. Reproduced under Creative Commons public use license from Wiley-VCH.[80]

An obvious advantage and the main focus of this study was the predicted improvement in solubility upon introduction of heteroatoms. Stepwise increase in the

number of nitrogen atoms in the BADY structure provides a consequential reduction in cLog*P*. With the commercial availability of alkyne precursors and widespread presence in medicinal chemistry, heteroaromatic rings appeared to be a sensible choice in the improvement of tag design. As noted in **Section 2.2**, small changes in the electronics of the aromatic rings flanking diynes changes their Raman shift considerably. By installing electron rich end-caps such as pyrrole and imidazole rings, red-shifted probes are generated. Conversely, *N*-containing 6-membered rings such as pyrazoles and pyrimidines result in blue-shifted probes. This allows for the relatively facile production of tags for multiplexing without the expensive and complicated synthesis of isotope-doped compounds, which are more commonly utilised in the field. Finally, a serendipitous but extremely important discovery was the covalent reactivity of some (primarily) heteroaromatic tags. Incubation of tags with glutathione resulted in the formation of glutathione-enyne adducts. Diyne reactivity with thiols has been reported, however, reactions generally require elevated temperatures/additives. The high reactivity of these tags at RT with a ubiquitous biological molecule may exclude them from general applicability in cellular ATRI, however, if reactivity could be modulated, this may represent an exciting new opportunity for covalent Raman probes. Recently, a ratiometric nitrile probe was developed for intracellular monitoring of the thia-Michael addition reaction.[145] If similar reactivity is observed, a diyne-to-enyne based reporter system offers distinct benefits in multiplexability and signal intensity (**Scheme 2.7**).

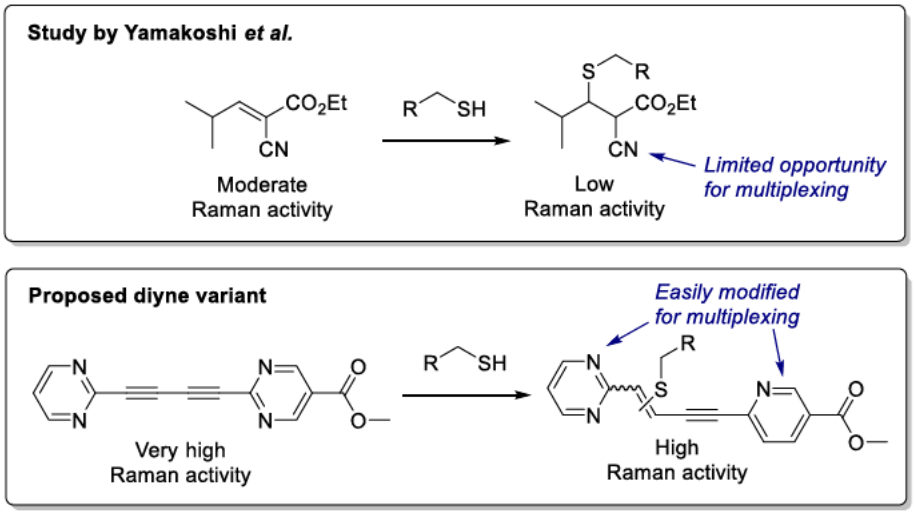

Scheme 2.7. Comparison of published and proposed covalent Raman probes.[145]

Three heteroaromatic probes (**1i**–**1k**, **Figure 2.24**) were selected for further testing. With up to 9× lower cLog*P* values than **1a** (cLog*P* = 4.10), these tags offered potential of improving tag solubility considerably.

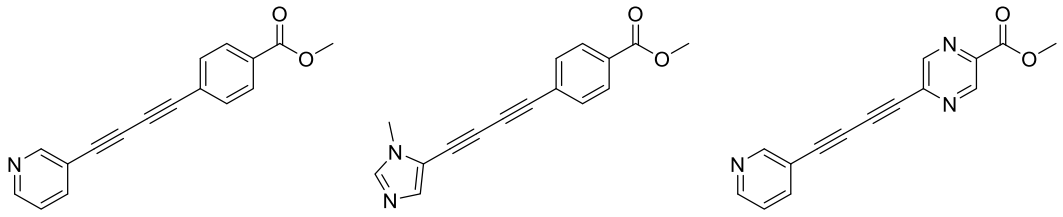

1i
cLog*P* = 2.28

1j
cLog*P* = 1.21

1k
cLog*P* = 0.46

Figure 2.24. Heteroaromatic tags **1i**–**1k** synthesised by Dr Manasa Punaha-Ravindra and carried forward for further analysis in this project.

2.7 Conclusions

This chapter discussed the design, synthesis and evaluation of new Raman tags for cellular imaging. By considering physicochemical properties such as cLog*P* and Fsp^3, tags were designed and their predicted Raman activity was calculated. Taking forward several tags designed to disrupt the planarity of BADY and thus improve solubility, intermolecular interactions were probed by MS and X-ray crystallography. Despite modifications to Fsp^3, these experiments determined that the propensity of tags to form dimers was largely unaffected. However, the MS results highlighted a significant correlation between cLog*P* and the strength of non-covalent interactions, suggesting the importance of cLog*P* in predicting tag association. The modifications made to BADY were shown not to negatively impact Raman activity, with each tag imaged inside cells at high SNR. Interestingly, it was possible to multiplex BADY analogue **1b** and PhDY analogue **1c**, allowing simultaneous intracellular detection. cLog*P* was further addressed in tag design and new bicyclic and heteroaromatic analogues were synthesised primarily to improve solubility but also offering numerous additional benefits e.g., multimodal imaging and easier multiplexing. These tags were next taken forward for use in the assessment of intracellular drug biodistribution by SRS imaging.

Chapter 3 Biochemical and Biophysical Evaluation of Raman-Active Drug Analogues

3.1 Introduction

Having generated a series of new Raman tags with modified physicochemical properties, attention was focused on their attachment to a drug of interest. The choice of drug was based on a) synthetic feasibility of tag attachment, b) amenability of drug to structural modification and c) interests of collaborators at AstraZeneca. Olaparib was investigated as a possible target for Raman-tagged drug imaging.

3.1.1 Olaparib

Olaparib is a small molecule poly(ADP-ribose) (PARP) inhibitor (PARPi) prescribed as maintenance therapy in the treatment of ovarian cancer (**Figure 3.1**).[146] The structural core of olaparib forms several key interactions within the amino acid residues in the PARP-1 active site, whereas its terminal cyclopropyl group does not participate in binding and confers only oral bioavailability.

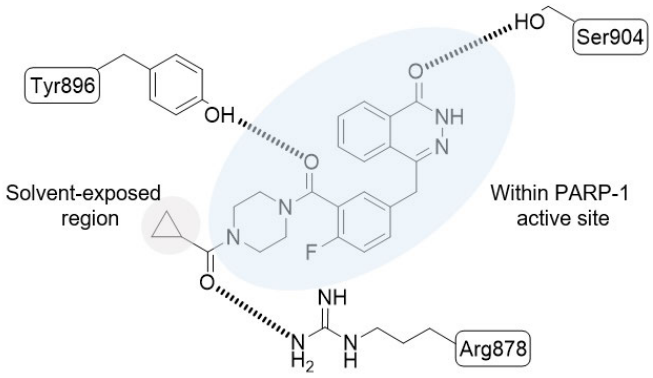

Figure 3.1. Structure of olaparib showing key hydrogen bond interactions with amino acids in the PARP-1 active site.[147]

Olaparib has been modified to generate a range of theranostic analogues, including radiotracers for positron emission tomography (PET) and single photon emission computed tomography (SPECT) imaging.[148] As discussed in **Chapter 1**, radiolabelled drugs are useful the assessment of drug distribution within larger scale biological environments and have even reached clinical trial phase.[149] However, PET and SPECT probes are generally not suitable for cellular imaging, which relies more commonly on the spatial resolution provided by fluorescence microscopy. Several

fluorescent imaging probes have previously been synthesised by replacement of the cyclopropyl group in olaparib (**Figure 3.2**). Probes **19**–**21** were used to visualise olaparib distribution directly,[150, 151] whereas **22** allowed fluorescent drug detection via an *in vitro* Click reaction.[152] There is a notable increase in both molecular weight (895 vs 640 g·mol^{-1}) and cLog*P* (6.0 vs 4.0) from **19** to **20**. This translated to slower uptake of drug to – and clearance from – the nucleus and mouse plasma, highlighting the importance of considering physicochemical properties in tag design. Retention of drug in the nucleus is important for a PARPi considering these drugs must be available to bind to PARP interacting with DNA. Although the cLog*P* of the Raman probes are lower than **20**, this factor could be expected to cause similar issues. Nevertheless, **20** was still shown to be a useful compound, and the precedent of tag attachment at the cyclopropyl site in these studies and others provided a sound rationale for Raman tagging in a similar way.

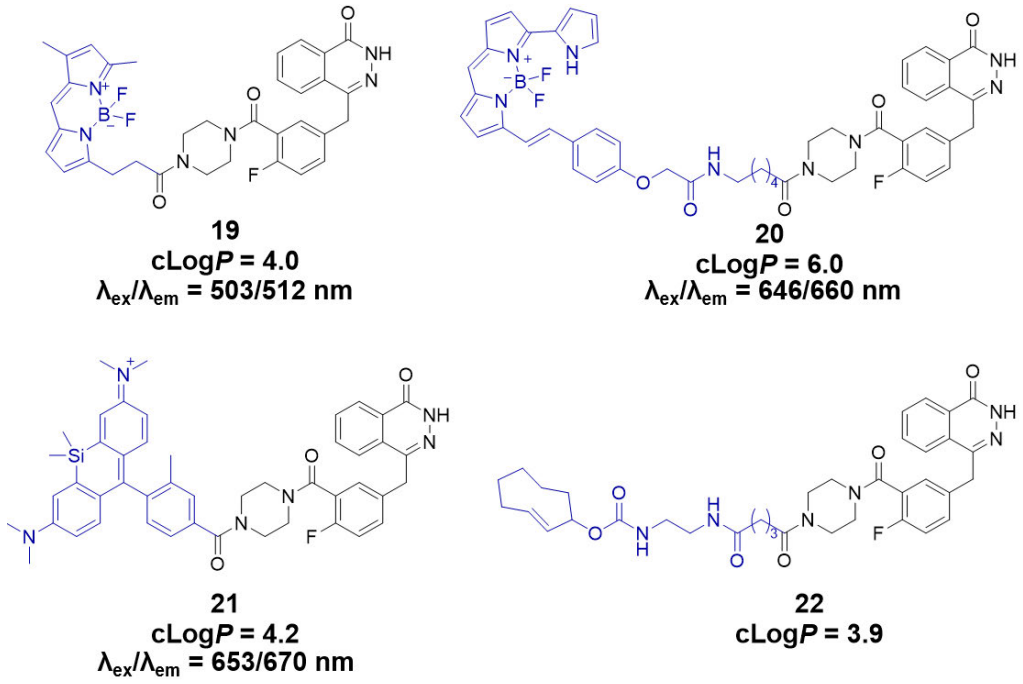

Figure 3.2. Previously reported olaparib analogues for optical imaging: BODIPY-labelled drugs **19** and **20**,[150] Si-rhodamine-labelled drug **21**,[151] and *trans*-cyclooctene (TCO) Click reagent **22**.[152] Calculated logP (cLogP) and fluorescence excitation/emission maxima are indicated.

3.1.2 Poly(ADP-ribose) polymerase (PARP)

The structure of olaparib was designed to mimic nicotinamide adenine dinucleotide (NAD^+), the natural substrate of PARP-1. PARP-1 is a member of the PARP family of proteins whose primary function is in the response to DNA damage (**Figure 3.3**).

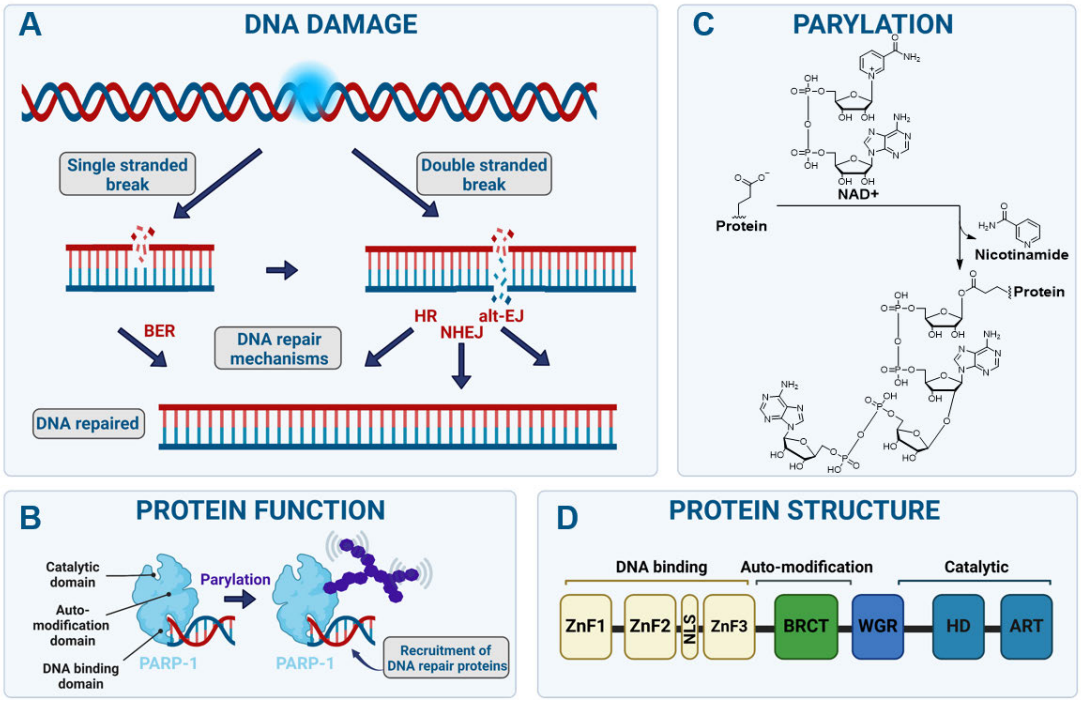

Figure 3.3. Overview of the structure, function and role in the DNA damage response of PARP-1. Abbreviations: ZnF = zinc finger, NLS = nuclear localisation sequence, BRCT = breast cancer type 1 susceptibility protein (BRCA1) C-terminus domain, WGR = tryptophan-glycine-arginine-rich domain, HD = helical domain, ART = ADP-ribosyl transferase fold, NAD = nicotinamide adenine dinucleotide, BER = base excision repair, HR = homologous recombination, NHEJ = nonhomologous end joining, alt-EJ = alternative end joining. Produced using Biorender.

DNA damage can occur through endogenous sources (reactive oxygen species, DNA replication errors, DNA base alkylation, etc.) or exogenous sources (radiation, chemicals, etc.).[153] This can result in both single- and double-stranded breaks (SSB/DSB) in DNA which must be repaired for the healthy function of the cell (**Figure 3.3A**). These breaks can be rectified through a number of pathways, e.g., base excision repair (BER), homologous recombination (HR), nonhomologous end joining (NHEJ) and alternative end joining (alt-EJ). PARP-1 plays a role in many of these DNA repair pathways, primarily to bind to damaged regions of DNA and act as a signalling protein (**Figure 3.3B**), forming chains of adenosine diphosphate (ADP) polymers in a process known as parylation (**Figure 3.3C**).[154] Parylation is then recognised by a series of DNA damage repair proteins which restore the DNA to its original form and retain viability of the cell. The structure of PARP-1 consists of 3 main domains: DNA binding, auto-modification and catalytic, which are each split into further subdomains (**Figure 3.3D**, **Figure 3.4**).[155] The DNA binding domain comprises three zinc finger motifs (ZnF1–ZnF3) and a nuclear localisation sequence (NLS). A

breast cancer type 1 susceptibility protein (BRCA1) C-terminus (BRCT) domain constitutes the main bulk of the auto-modification domain which is linked to the catalytic domain via a tryptophan-glycine-arginine-rich (WGR) domain. The catalytic domain comprises a helical domain (HD) and ADP-ribosyl transferase fold (ART). PARP-1 shares a high degree of sequence homology with other PARP proteins, including PARP-2, which retains much of the catalytic domain and a truncated DNA binding domain.[156] As such, olaparib binds strongly to both PARP-1 and PARP-2.[157]

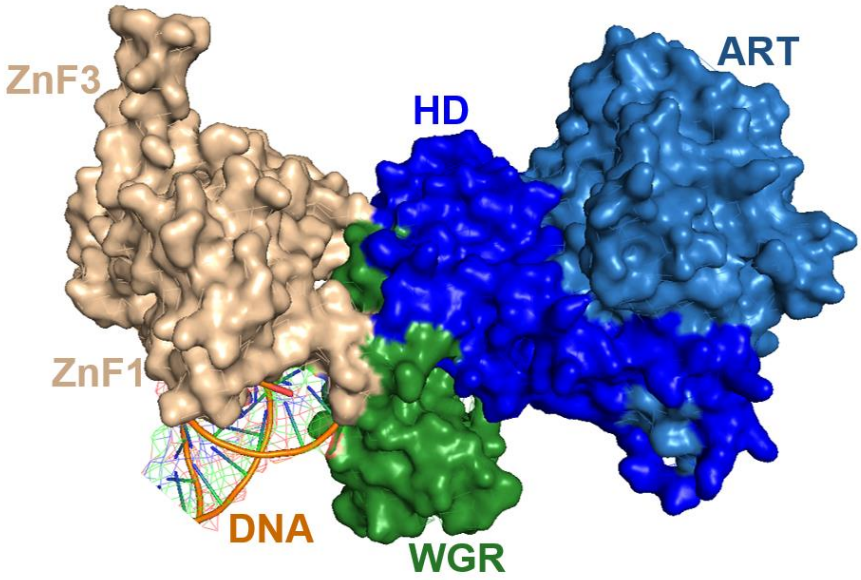

Figure 3.4. Structure of PARP-1 protein bound to double stranded DNA, highlighting various domains. PDB: 4DQY. ZnF = zinc finger, WGR = tryptophan-glycine-arginine-rich domain, HD = helical domain, ART = ADP-ribosyl transferase fold.

A range of PARPi have been developed, primarily for breast and ovarian cancers (**Figure 3.5**). PARPi are thought to induce cytotoxicity not only through the inhibition of DNA repair but by preventing the cleavage of PARP from DNA in a process known as PARP trapping. This leads to the accumulation of DNA lesions which cannot be repaired. PARPi have been particularly successful in certain cancers due to a phenomenon known as synthetic lethality.[158] Synthetic lethality refers to the situation where loss of two genes (or proteins) independently does not have a remarkable effect but their simultaneous loss is lethal to the cell. An important example of synthetic lethality involves the breast cancer susceptibility gene (*BRCA*). *BRCA1* and *BRCA2* genes are involved in the DNA damage repair pathway. Upon mutation (*BRCAm*), cells become deficient in HR, an aforementioned mechanism of repairing damaged DNA. This renders cells reliant on other repair pathways, which, when

inhibited, leads to synthetic lethality. PARPi like olaparib generally exhibit greater potency in reducing *BRCAm* cell viability than *BRCA* wild type (WT) due to this synthetic lethality.

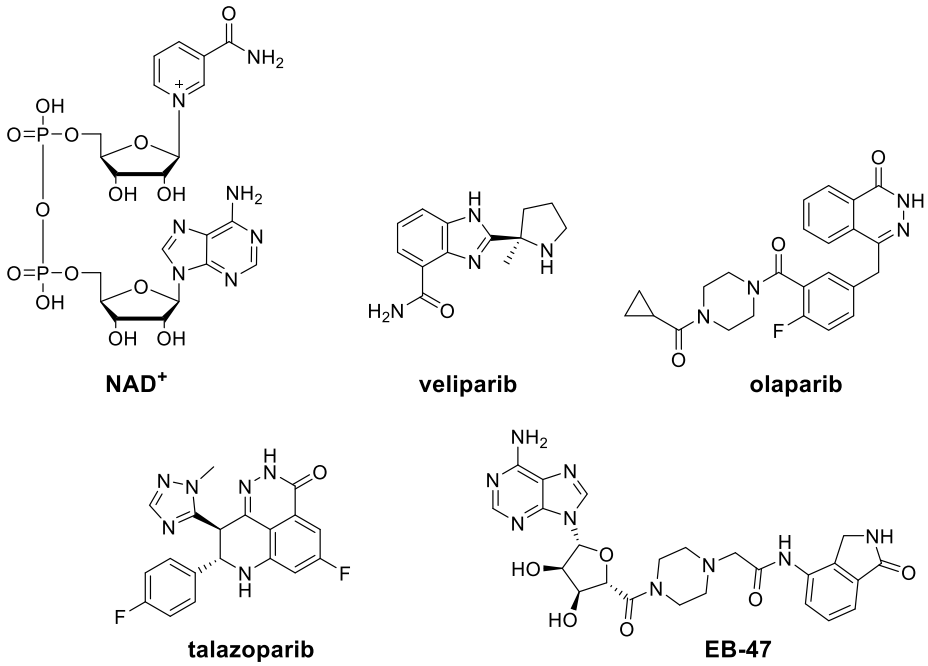

Figure 3.5. PARP inhibitors (PARPi) discussed in this chapter and nicotinamide adenine dinucleotide (NAD^+), the natural substrate of PARP-1.

The current relevance of PARPi in the latest cancer research make olaparib an attractive target for Raman tagging. The ability to track olaparib in cells was thought to offer new benefits in correlating biodistribution with other biological parameters and the phenotypic response to PARP inhibition. It was also considered that investigation of resistance mechanisms could be correlated with intracellular drug tracking, as has been previously carried out using SRS microscopy (**Section 1.2.5.1**). However, it is important to note that olaparib is a particularly challenging drug target for SRS imaging, due to the nuclear location of its protein target. Transport of molecules across the nuclear membrane is more tightly regulated than the cell membrane and drugs must avoid lysosomal/endosomal degradation to reach the nucleus.[159] Whilst designed to be bioorthogonal, changes in physicochemical properties and molecular size through Raman tagging has the potential to interrupt successful drug delivery to the nucleus. To date, no drugs for nuclear targets have been visualised by SRS microscopy.

3.2 Molecular docking

To confirm the Raman tags in the proposed olaparib analogues were indeed likely to protrude from the active site of PARP-1 as reported previously, molecular docking was carried out (**Figure 3.6**). BADY-tagged olaparib was shown to adopt the same lowest energy conformation within the active site, retaining key hydrogen bond interactions. The tag extended outwards into the solvent-exposed region as expected.

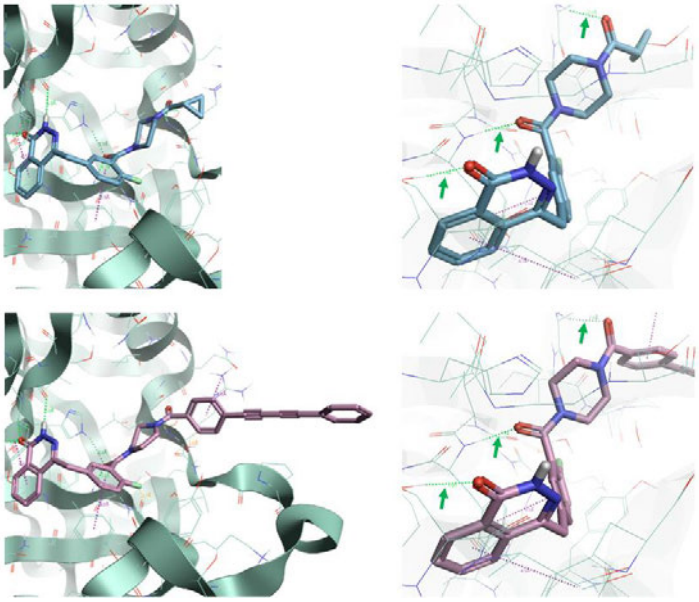

Figure 3.6. Ligand docking of olaparib (**top**) and **26a** (**bottom**) in the active site of PARP-1 (PDB: 7KK4) carried out using Flare v7 (Cresset). Key hydrogen bond interactions are indicated with green dashed lines/arrows.[147]

Although the docking study did not reveal any major concerns, these predictions do not consider the ability of the compound to navigate into the enzyme active site. Addressing the rigidity of the BADY tag, an additional linker was included in drug-tag design to generate 'BADY-linker-olaparib' compounds, envisaged to introduce more flexibility to facilitate entry into the active site (**Figure 3.7**).

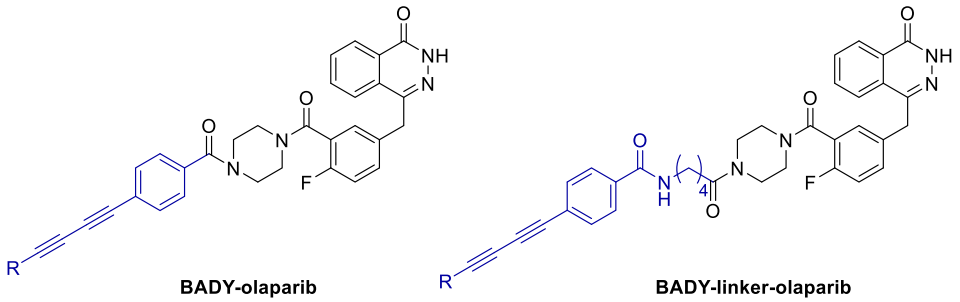

Figure 3.7. General structures of the proposed Raman-tagged olaparib analogues.

3.3 Synthesis

A commercially available des-cyclopropylcarbonyl analogue of olaparib **24** was used to synthesise the Raman-tagged compounds (**Figure 3.8**). Simple amide coupling of tags **1a–1c and 1g–1h** to **24** yielded directly coupled olaparib tags **26a–26c** and **26g–26k** in good yields. Likewise, inclusion of the linker **25** to generate tags **28a–28c** allowed coupling to **24** to generate tag-linker-olaparib compounds **29a–29c** and **29i**.

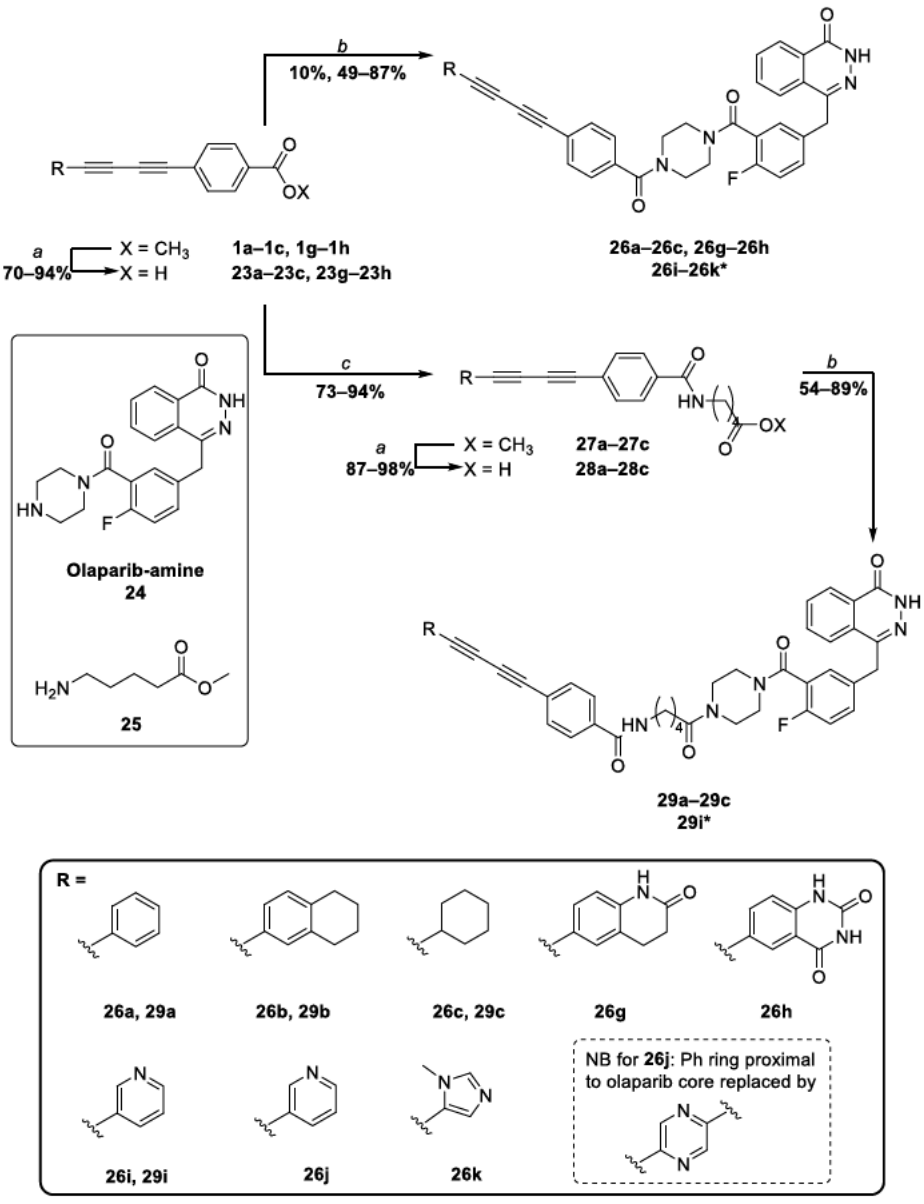

Figure 3.8. Synthesis of olaparib analogues. Reagents and conditions: **a)** NaOH (5 equiv.), CH_3CN, reflux, 16 h. (**23a**, 94%; **23b**, 82%; **23c**, 86%; **23g**, 70%; **23h**, 72%; **28a**, 90%; **28b**, 90%; **28c**, 87%) **b) 24** (1 equiv.), PyBOP or HATU (1.2 equiv.), DIPEA, (4 equiv.) CH_3CN, RT, 4 h. (**26a**, 73%; **26b**, 87%; **26c**, 74%; **26g**, 49%; **26h**, 61%; **29a**, 85%; **29b**, 89%; **29c**, 56%) **c) 25** (1 equiv.), PyBOP (1.2 equiv.), DIPEA (4 equiv.), CH_3CN, RT, 4–16 h. (**27a**, 82%; **27b**, 76%; **27c**, 94%). *Compounds **26i** (45%), **26j** (10%), **26k** (82%) and **29i** (84%) synthesised by Dr Manasa Punaha Ravindra.

3.4 Physicochemical analysis

The aim of this section of the project was to generate bioorthogonal drug-tag conjugates, i.e., to mimic as closely as possible the characteristics of olaparib. Whilst attachment of a tag such as BADY will undoubtedly change some drug properties, keeping these effects to a minimum was the main focus.

Physicochemical properties of olaparib and Raman-active analogues were predicted and are reported in **Table 3.1**. These show the expected trend of relatively high cLog$D_{7.4}$ and Fsp^3 for the all-carbon tag compounds and lower cLog$D_{7.4}$ values for heteroaromatic tag compounds. Although such predictions are often used in medicinal chemistry, it was clearly important to assess experimentally the physiochemical properties of the tags. Log$D_{7.4}$ and ePSA (experimental polar surface area) values were determined at AstraZeneca. A liquid chromatography method was utilised for log$D_{7.4}$ measurements, using a C18 stationary phase to distinguish compounds based on their hydrophobicity and hence lipophilicity. For ePSA measurements, a supercritical fluid chromatography system was employed. The use of a non-aqueous mobile phase enables the evaluation of compound affinity for the stationary phase without interfering with intramolecular hydrogen bonding, offering new information on drug properties.[160, 161]

Interestingly, whilst overall both cLog$D_{7.4}$ and cLog$P$ correlated well with log$D_{7.4}$, log$D_{7.4}$ correlated better with cLog$P$ (r = 0.98) than cLog$D_{7.4}$ (r = 0.95) (**Figure 3.9**). Replacement of all-carbon aromatic rings with nitrogen-containing heterocycles saw a stepwise reduction in log$D_{7.4}$ (4.8, 2.8 and 2.1 for **26a**, **26i**, and **26j**, respectively). The lowest log$D_{7.4}$ (1.8), notably similar to that of olaparib (1.1), was achieved by replacing the phenyl ring with an imidazole functionality in **26k**. Modification of **26b** to generate benzolactam **26g** resulted in a large reduction in log$D_{7.4}$ (6.9 vs 2.4). Inclusion of additional linker motifs (**29a**–**29c**, **29i**) reduced log$D_{7.4}$ relative to their directly linked analogues (**26a**–**26c**, **26i**), suggesting the additional amide moiety negates additional hydrophobicity introduced by the 4-carbon chain linker. All compounds were found to exhibit ePSA values below the accepted upper limit for passive membrane permeability (<140 $Å^2$).[162]

Table 3.1. Calculated and experimentally obtained physicochemical properties of olaparib and tagged olaparib analogues. cLog*P* and clog$D_{7.4}$ calculated using Marvin (Chemaxon).

	Compound	cLog*P*	cLog$D_{7.4}$	Fsp^3 vs 26a	log$D_{7.4}$	ePSA (Å^2)
	olaparib	1.2	1.9	-	1.1	89.9
Without linker	**26a**	4.2	4.4	-	4.8	100.9
	26b	5.8	5.5	1.57	6.9	105.2
	26c	5.3	4.8	2.14	5.8	98.2
	26g	3.4	3.6	1.29	2.4	120.7
	26i	2.7	3.5	1.01	2.8	100.9
	26j	2.2	3.1	1.07	2.1	99.3
	26k	2.1	2.9	1.02	1.8	105.2
With linker	**29a**	3.8	4.4	1.50	4.3	108.9
	29c	4.9	4.9	2.57	5.3	105.7
	29i	2.4	3.8	1.57	2.4	108.4

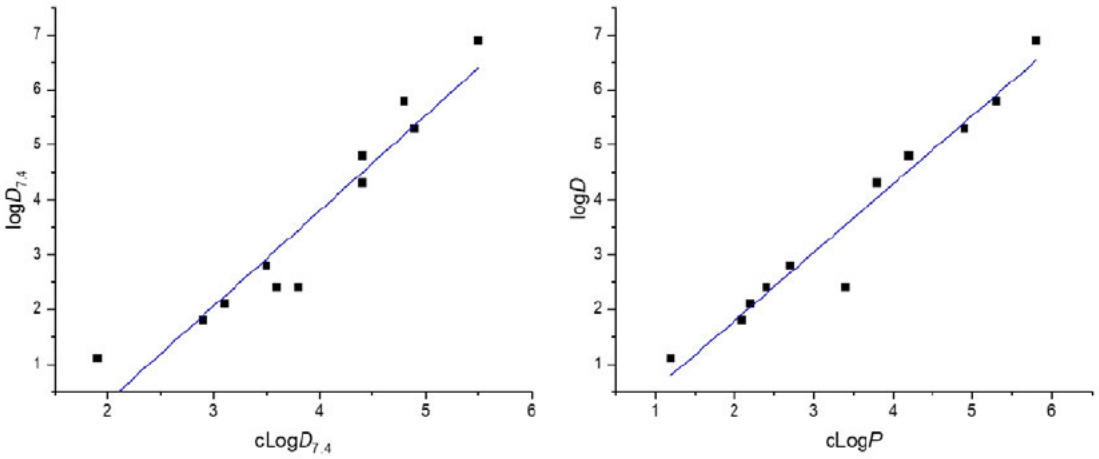

Figure 3.9. Correlation analysis of predicted physicochemical parameters and experimentally determined log$D_{7.4}$ values for the compounds in **Table 3.1**. Left: vs cLog$D_{7.4}$, r = 0.95, p < 0.0001. Right; vs cLog*P*, r = 0.98, p < 0.0001.

Whilst attachment of the tag through an amide functionality on olaparib mimics the unmodified drug structure, and the all-carbon BADY tag is generally considered to be unreactive, it was important to consider the stability of the compounds over time. An LC-MS stability assay was conducted to ensure compound suitability for future *in cellulo* studies (**Figure 3.10**). Compounds were incubated for 7 days in DMSO and

serum-containing cell culture media to account for chemical and biological instability, respectively. The *m/z* signal for each compound was identified and measured relative to an internal standard, clozapine, which is known to remain stable within the timescale of the assay.

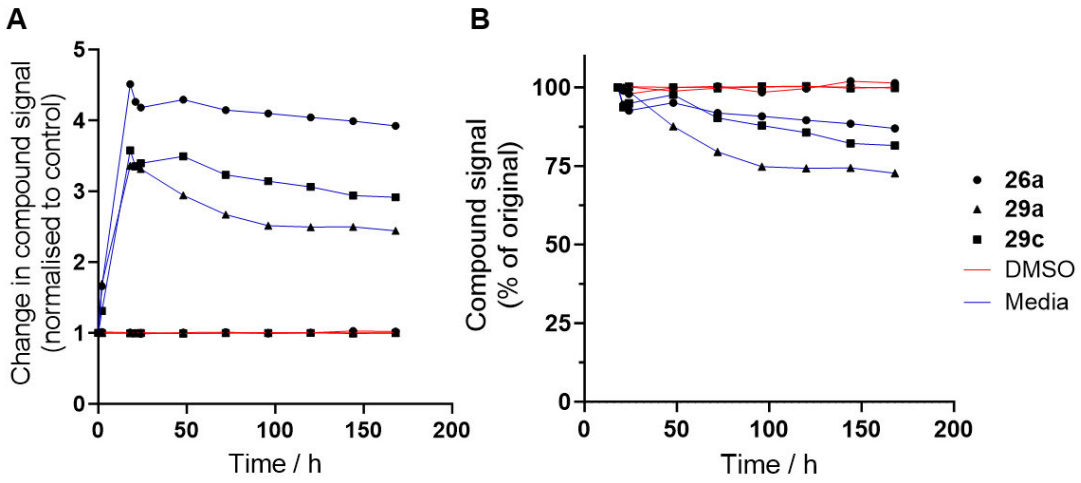

Figure 3.10. Stability of **26a**, **29a** and **29c** in DMSO and cell culture media over time. **A)** Compound signal intensity from LC-MS analysis measured over time relative to clozapine internal standard. **B)** Data from graph **A** expressed as a percentage of the signal at t_{max} = 18 h.

Figure 3.10A shows the change in compound signal from t = 0. An initial incubation period was evident, during which the LC-MS signal intensity increased over the first 18 h, presumably due to the increase in temperature from the laboratory bench to the LC-MS system which featured a temperature-controlled sampler. As such, **Figure 3.10B** shows the change in compound relative to the t_{max} = 18 h timepoint. Each compound remained stable over the 7-day period in DMSO, indicating no inherent structural lability. Some loss of compound signal in media was observed during the course of the assay, most markedly for **29a**. No trends could be drawn from such a small sample set; however, it was determined that the loss of signal was likely due to the observed precipitation of the compounds (**Appendix A**), which reflects their relatively high log$D_{7.4}$ values. No new compound peaks were observed in the chromatograms, suggesting the compounds were not decomposing within the timescale of this experiment. In future studies of this kind, it would be useful to incubate the compounds at 37 °C to mimic biological conditions (and retain solubility). It would also be sensible to include olaparib as a control in the stability assay to compare tagged vs untagged drug, which may allow change in drug concentration over time to be further correlated with log$D_{7.4}$ and solubility.

3.5 PARP protein studies

Having confirmed their general suitability, the olaparib analogues were taken forward for the next stage of testing. Using parent compounds **26a** and **29a**, studies were carried out with PARP-1 protein.

3.5.1 Surface plasmon resonance (SPR)

Surface plasmon resonance (SPR) is a useful tool in medicinal and biophysical chemistry for the investigation of protein-ligand interactions (**Figure 3.11**).[163] In SPR, light is shone onto a thin metal film upon which a protein immobilisation matrix is affixed. A flow cell allows solutions of protein, ligands etc. to pass across the matrix. The incident light is reflected and its magnitude can be used to determine the strength and dynamics of protein-ligand interactions on the surface of the matrix.

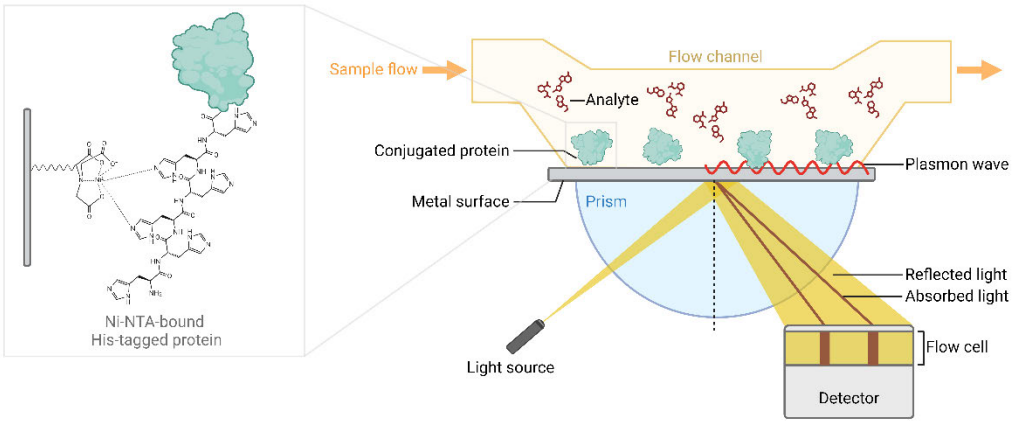

Figure 3.11. Schematic representation of the SPR experiment to determine ligand-protein binding. Produced using Biorender.

Olaparib, **26a** and **29a** were all found to bind to PARP-1 with low nanomolar affinity (**Figure 3.12**). The obtained equilibrium constant (K_D = 0.733 nM) for olaparib compared well to previously reported data (K_D = 0.24 and 1.1 nM).[157, 164] **26a** and **29a** exhibited considerably slower on rates/association constants (k_a = 4.87×10^4 and 2.06×10^4 $M^{-1}s^{-1}$, respectively) than olaparib (1.80×10^5 $M^{-1}s^{-1}$), which may reflect their increased rigidity or molecular size. However, their slower off rates/dissociation constants (k_d = 5.03×10^{-5} and 2.86×10^{-5} s^{-1} for **26a** and **29a**, respectively) led to K_D values in line with olaparib (K_D = 3.88 and 2.47 nM for **26a** and **29a**, respectively). Whilst slightly higher than that of olaparib, these K_D values are close to the PARP-1 inhibitor veliparib (4.4 nM)[165] and are lower than other related probes such as an olaparib-based Click reagent (22 nM)[166] and a radiolabelled analogue for imaging

(15 nM),[167] all of which were shown to be functional and potent. A recent study showed that PARPi dissociation values for olaparib, talazoparib and veliparib (**Figure 3.5**) obtained in isolated protein assays hold true in cells and that there is a direct link between k_d and PARP trapping.[168] As a result, with up to 5× slower dissociation from PARP-1 than olaparib, it is possible that the Raman-tagged compounds may increase PARP trapping in cells. Overall, the acquired K_D values suggested that the modifications made to olaparib did not significantly affect their affinity to bind to PARP-1.

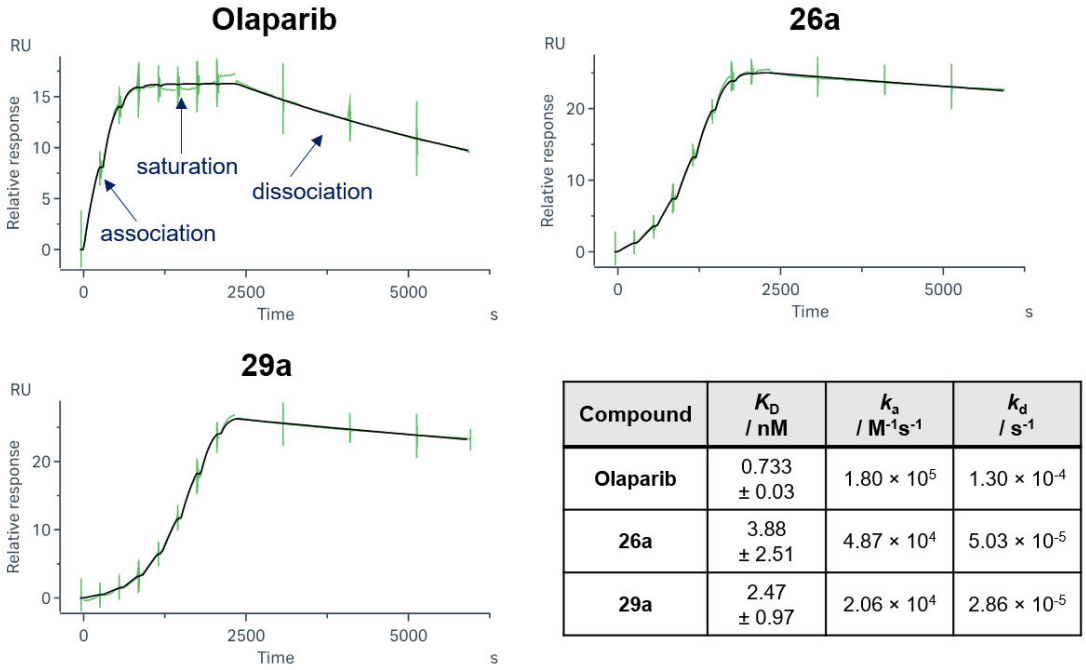

Compound	K_D / nM	k_a / $M^{-1}s^{-1}$	k_d / s^{-1}
Olaparib	0.733 ± 0.03	1.80×10^5	1.30×10^{-4}
26a	3.88 ± 2.51	4.87×10^4	5.03×10^{-5}
29a	2.47 ± 0.97	2.06×10^4	2.86×10^{-5}

Figure 3.12. SPR sensorgrams and summary kinetic data for binding of olaparib, **26a** and **29a** to PARP-1. K_D values are reported ± standard deviation of the mean across 3 independent experiments. Data acquired in collaboration with Dr Christopher Stubbs at AstraZeneca.

3.5.2 Hydrogen-deuterium exchange mass spectrometry (HDX-MS)

Hydrogen-deuterium exchange mass spectrometry (HDX-MS) is a technique which uses MS analysis to quantify the degree of HDX of a protein upon exposure to a deuterated solvent (**Figure 3.13**).[169] This allows information about the structure and dynamics of the protein to be determined, based on the fact that buried protein regions will exchange less readily with the deuterium in the solvent and exposed regions will exchange rapidly. Coupling this to MS allows quantitation of this exchange by first digesting the protein into unique peptide sequences which represent the different regions of the protein and determining their mass at fixed time points. HDX-MS has

previously been used to examine PARP-1 structure and dynamics, both with and without ligand binding.[170, 171]

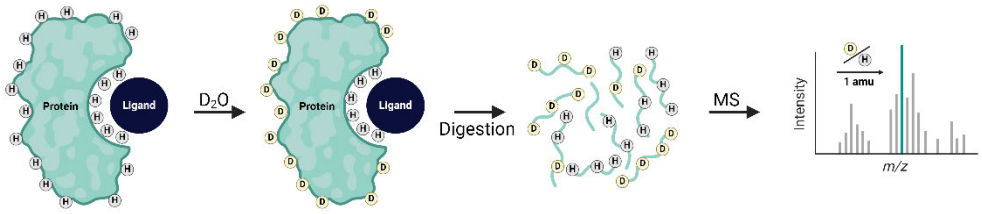

Figure 3.13. Schematic representation of the HDX-MS experiment. Produced using Biorender.

HDX-MS analysis revealed a range of information about the binding of olaparib, **26a** and **29a** (**Figure 3.14**). Importantly, the binding site of olaparib was identified within the ART domain, confirmed by its decreased exchange with the solvent (**A** in **Figure 3.14**). The region identified is consistent with previous reports of HDX-MS analysis of olaparib-bound PARP-1.[170] This region was also observed in **26a** and **29a**-treated protein, suggesting drug binding is retained after Raman tagging. An additional protected region within the catalytic domain was identified for all three compounds (significantly for **26a** and **29a**, **B** in **Figure 3.14**), as previously identified for various PARP-1 inhibitors, most markedly for talazoparib (**Figure 3.5**).[170] The decreased deuterium exchange of this region with **26a** and **29a** vs olaparib may be a result of the increased surface area of these larger tags. Interestingly, two new regions were found to experience increased exchange with deuterium only after treatment with **29a**. The first region (**C** in **Figure 3.14**) forms part of the HD region of PARP-1, whereas the second exposed region (**D** in **Figure 3.14**) is part of the WGR domain and is adjacent to the HD. Although not identified by the molecular docking, steric clash of the tag in **29a** may be responsible for these changes in protein structure upon binding.

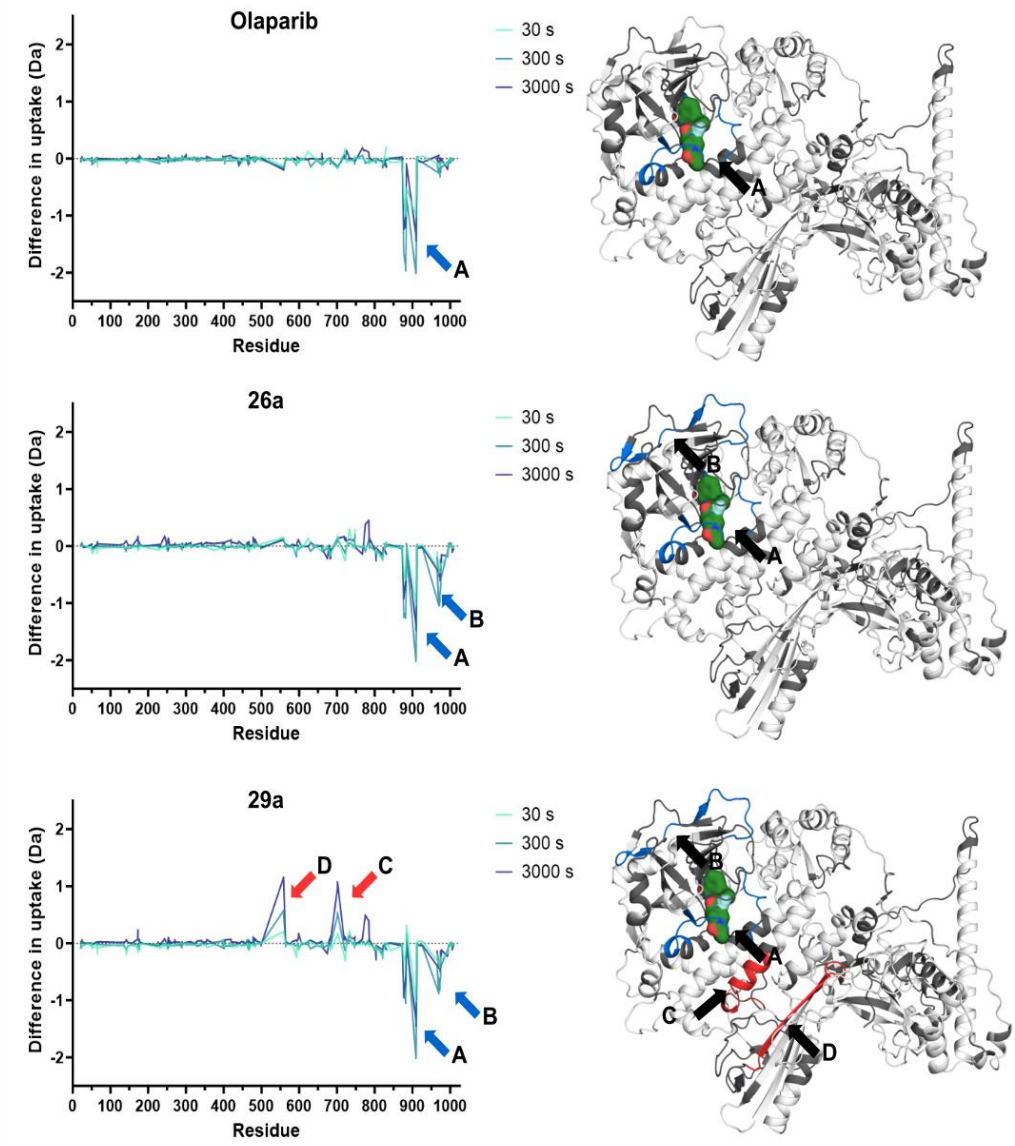

Figure 3.14. HDX-MS analysis of the indicated ligands bound to PARP-1. Left = graphs plotting relative changes in atom uptake. Right = PARP-1 protein structure (PDB: 4DQY) highlighting regions with significantly (p < 0.01 vs DMSO-treated, n=3) decreased exchange with deuterium (blue, labels **A** and **B**) and increased exchange with deuterium (red, labels **C** and **D**). Olaparib is shown bound to PARP-1 in each case. Individual peptide data provided in **Appendix B**. Data acquired in collaboration with Dr Christopher Stubbs at AstraZeneca.

This idea is further explained by examining the ligand-protein interactions in greater detail (**Figure 3.15**). Molecular modelling suggested that the Raman tag in **29a** could extend up to 15.8 Å from the piperazine ring of olaparib, introducing the possibility of a steric clash with the neighbouring HD in PARP-1. The proximity of the HD to the WGR domain may have also induced a resultant allosteric effect on this region, reflecting the changes observed in **Figure 3.14 D**. Although the magnitude and any possible consequences of this effect are difficult to quantify, these results may be

compared to previously reported studies. For example, the preclinical PARP inhibitor EB-47 (**Figure 3.5**), which is also larger in size than olaparib, has been shown by HDX-MS to disrupt the HD.[172] Local unfolding of HD in PARP-1 plays an important role in the regulation of DNA binding catalytic activity.[173] EB-47 is an example of a type-I PARPi, whose ability to disrupt the HD induces stronger DNA binding of PARP (i.e., PARP trapping) which has been linked to increased cellular toxicity.[174] On the other hand, olaparib is an example of a type-II PARPi, which are not known to significantly affect the HD domain.[175] It was considered important to later assess whether these new effects of **29a** upon binding to PARP-1, combined with its lower k_d from SPR, altered the function of PARP and the behaviour of **29a** in cells.

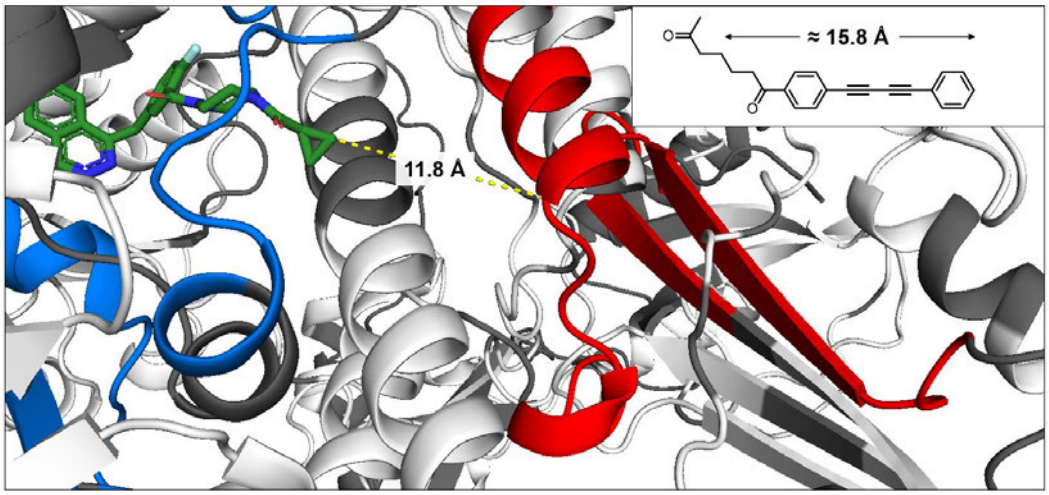

Figure 3.15. Magnified imaging showing the effects of **29a** binding to the structure of PARP-1 (PDB: 4DQY), as determined by HDX-MS analysis. Blue and red regions are those with significantly decreased or increased exchange with deuterium, respectively. The distance between the terminal piperazine ring in the olaparib core and a residue in the helical domain is shown. A measurement of the estimated diameter of **29a** is shown in the top right.

3.5.3 Inhibition assay

With the confidence that the tested compounds bind in the active site of PARP-1, the next step was to confirm that this translated to inhibition of PARP-1 activity (**Figure 3.16**). As discussed, PARPi bind competitively in the NAD^+ binding site of PARP-1, which is required for parylation. Measuring the amount of 'free' NAD^+ is thus a readout of PARP activity. Accordingly, a commercially available NAD^+/NADH assay was coupled to a reaction mixture of PARP-1 and olaparib and the synthesised drug analogues (**Figure 3.16A**). The PARPi veliparib (**Figure 3.5**) was used as a control compound in this assay and was incubated with PARP-1 at concentrations of 100 to 0.005 nM, giving an IC_{50} value of 2.18 nM (**Figure 3.16B**). The obtained IC_{50} value is

in good agreement with a previously reported value of 3.3 nM.[176] Unfortunately, olaparib and the analogues were incorrectly assumed to exhibit much lower PARP-1 inhibitory activity than veliparib and were incubated at 1000× higher concentrations of 100 to 0.005 µM. This resulted in complete inhibition of PARP-1 at even the lowest concentration, preventing determination of IC_{50} values. However, it could still be determined that each of the compounds tested had an IC_{50} value < 0.005 µM (5 nM), suggesting potent inhibitory activity of PARP-1. IC_{50} values for BODIPY-olaparib compounds **19** and **20** were previously reported as 14 ± 1.2 nM and 92 ± 25 nM, respectively, vs 4.4 ± 1.0 nM for olaparib),[150] suggesting improved activity of the Raman-tagged compounds vs these imaging probes. This may highlight the benefit of smaller Raman tags over larger fluorescence tags for drug imaging.

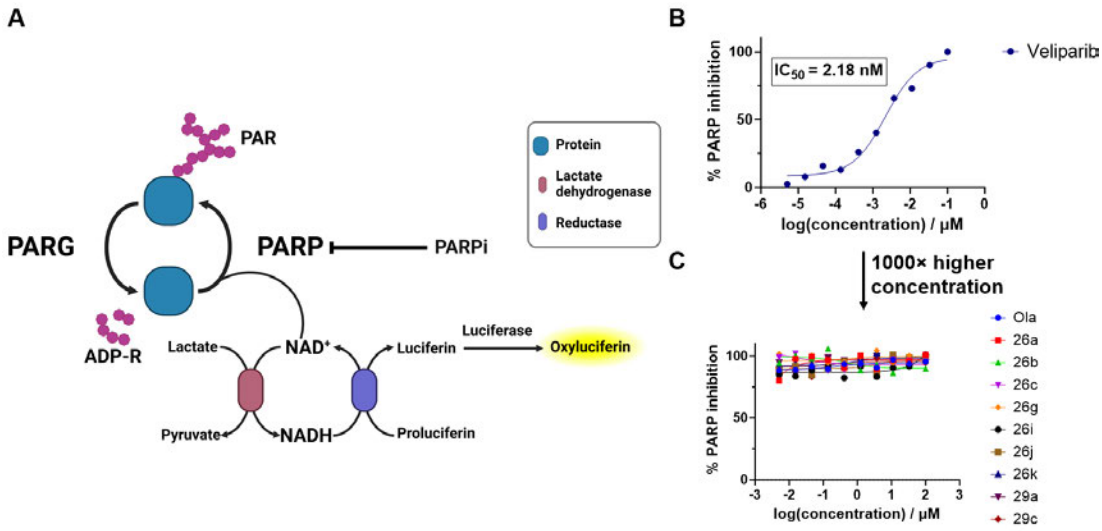

Figure 3.16. PARP enzyme activity assay. **A)** Schematic representation of PARP-1 activity using NAD^+ as a substrate. The NAD^+ cycle is coupled to a luciferase bioluminescence assay as a readout of PARP-1 enzyme inhibition. Produced using Biorender. **B)** Dose-response curve for PARP-1 inhibition in presence of veliparib. **C)** Dose-response curve for PARP-1 inhibition in presence of the compounds listed in **Table 3.1**. Data acquired in collaboration with Dr Derek Barratt at AstraZeneca.

3.6 Initial testing *in cellulo*

With the knowledge that the compounds tested were a) predicted to be cell permeable, b) stable over several days in media and c) shown to be biologically active against PARP-1, they were determined to be suitable for testing *in cellulo*. The primary aim of this study was to develop probes for SRS imaging of olaparib, thus it was important to determine how the variety of tags developed, with differing physicochemical properties, affected drug biodistribution.

3.6.1 SRS imaging

First, **26a** was incubated in ES-2 cells and subjected to SRS imaging (**Figure 3.17**). Consistent with its acceptable ePSA value, **26a** was found to be cell permeable and was detected in cells at good signal-to-noise ratio. Similar to the imaging results discussed in **Chapter 2**, no alkyne signal was detected in the nucleus. For a compound with strong binding affinity for PARP-1, which is located primarily in the nucleus, this result was unexpected. **26a** appeared to be distributed diffusely within the cytoplasm of the cell. Some areas of clustered signal were observed, however, the signal generally appeared less punctate than imaging of the unconjugated BADY tag **1a**, discussed in **Chapter 2**. The alkyne signal was overlayed with the lipid image (**Figure 3.17 C** & **F**), revealing some colocalisation but no accumulation of the drug into lipid droplets. Fixing the cells did not significantly impact compound signal intensity, indicating some degree of retention of the drug within the cells. Further confirmation of cell permeability of the compound was provided by carrying out depth profiling (i.e., analysing drug distribution throughout the cell in the *z* direction). (**Figure 3.17 D**). Compound signal was detected throughout the cytoplasm and was not found to accumulate on the cell surface, which would have indicated poor cell permeability.

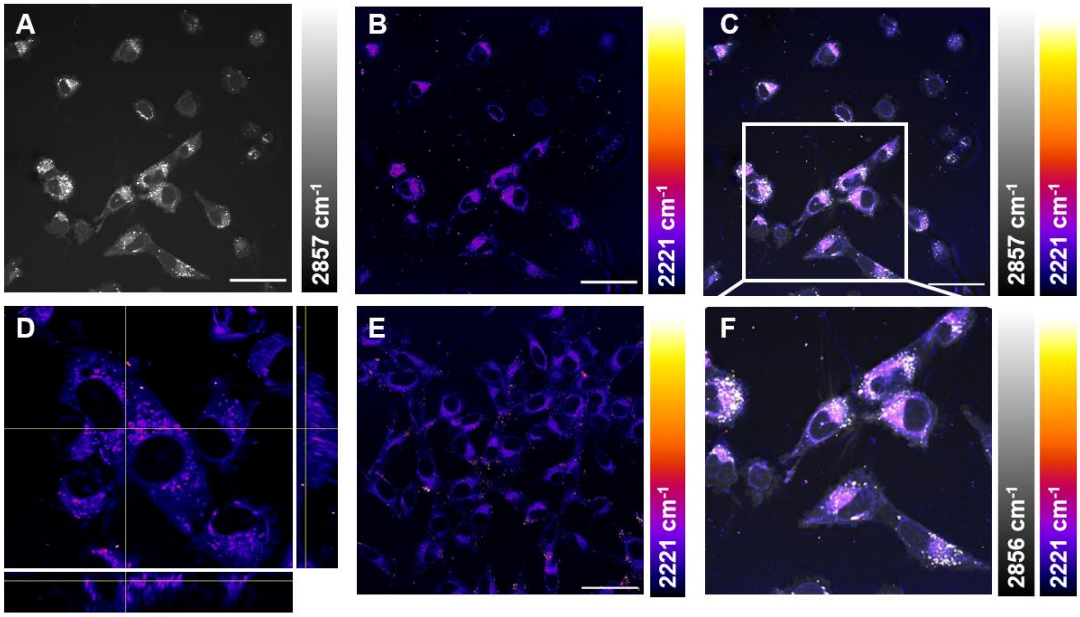

Figure 3.17. SRS imaging of **26a** (10 µM, 2 h) in live (**A**–**D** and **F**) and fixed (**E**, 4% formaldehyde in PBS, 15 min) ES-2 cells. Contrast achieved by tuning to the indicated wavenumbers for: **A)** CH_2 (lipids), **B**, **D**–**F)** C≡C (alkyne). **C)** Overlay of **A** & **B**. **D)** Z-stack orthogonal projection. **F)** Magnification of FOV indicated in **C**. Off-resonance frequency image subtracted from the alkyne images to account for background signal. False colouring applied to **B**, **D** & **E**. for clarity. Scale bars 50 µm.

Olaparib is known to accumulate in the nucleus (where PARP is concentrated) which is inconsistent with the subcellular localisation of **26a**. As such, there were concerns that the drug detected in the cytoplasm may be indicative of simple passive diffusion of the compound from the incubation rather than active drug uptake which would be expected to proceed to the nucleus. The lack of nuclear signal for the drug conjugate was envisaged to be caused by a number of possible factors: a) the compound was present in the nucleus at low concentrations possibly below the limit of detection (LOD) of SRS imaging b) there was shuttling of drug between the nucleus and cytoplasm or c) the tagging had affected the ability of olaparib to permeate the nuclear membrane.

Addressing first the possibility of a LOD issue, the drug incubation protocol was examined. The incubation concentration of **26a** was increased 10-fold to examine the effects on its signal intensity in cells (**Figure 3.18**, left). The diffuse signal within the cytoplasm appeared consistent with the lower concentration experiments and only some additional punctate signal around the cell membranes was observed. This likely indicates that drug flux had reached equilibrium and further increasing drug incubation concentrations would be futile. Although short incubation times were shown to be suitable for previously reported BODIPY-olaparib imaging,[150] a longer incubation time of 24 h was trialled to circumvent any slower association kinetics (as per the SPR results) of the Raman compounds compared to olaparib (**Figure 3.18**, right). For example, it is possible that the tagged drug compounds enter the cell rapidly (as determined by the high intracellular signal after a short incubation time) but take longer to cross the nuclear membrane. The nucleus is more difficult to permeate than the cell membrane and BODIPY-tagged olaparib conjugate **20** was shown to exhibit slower nuclear penetration than lower cLog*P* compounds in a fluorescence study.[159] Notwithstanding the longer incubation times, no significant differences in signal intensity were observed. Moreover, increased compound precipitation was evident, consistent with the LC-MS analysis of **26a** in solution (**Figure 3.10**) which showed a small decrease in compound concentration in solution over time. These results illustrated that a brief, low micromolar incubation allowed visualisation of **26a** in the cytoplasm and that drug could not be detected in the nucleus by increasing incubation concentration or time.

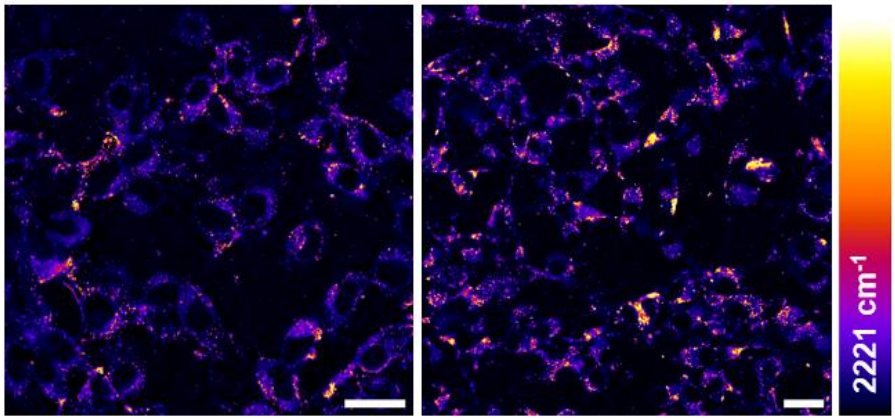

Figure 3.18. SRS imaging of **26a** in live ES-2 cells. **Left**: 100 µM, 3 h. **Right**: 100 µM, 24 h. Contrast achieved by tuning the indicated wavenumber for the alkyne frequency. Off-resonance frequency image subtracted to account for background signal. False colouring applied for clarity. Scale bars 25 µm.

The published BODIPY- and rhodamine-olaparib studies also reported the presence of a strong cytosolic fluorescence signal, rendering fluorescence signal in the nucleus difficult to identify. This issue was alleviated by a brief drug wash out period (ca. 5 min) for BODIPY-olaparib **19** which cleared cytosolic drug, leaving only nuclear-localised drug signal. However, higher log*P* BODIPY-olaparib compound **20** required > 1 h washout time. Repeating this washout experiment for **26a** did not allow visualisation of the drug in the nucleus but rather indicated a slow disappearance of signal from the cells (**Figure 3.19**), as expected for a non-covalent inhibitor during washout studies. Considering the similarity in distribution/signal of **26a** between 0 and 5 min washout, it is possible that the higher log*P* of **26a** matches more closely the behaviour of **20** than **19**. However, it would not be practical to further increase the washout time of **26a** considering the substantial loss of compound signal after just 45 min of washout. Although the fluorescent analogues are the only comparable olaparib imaging probes used to date, it is important to reiterate that the LOD of fluorescence microscopy is several magnitudes lower than SRS microscopy. As such, it is possible that **26a** was present in the nucleus after the washout period but was undetectable by SRS.

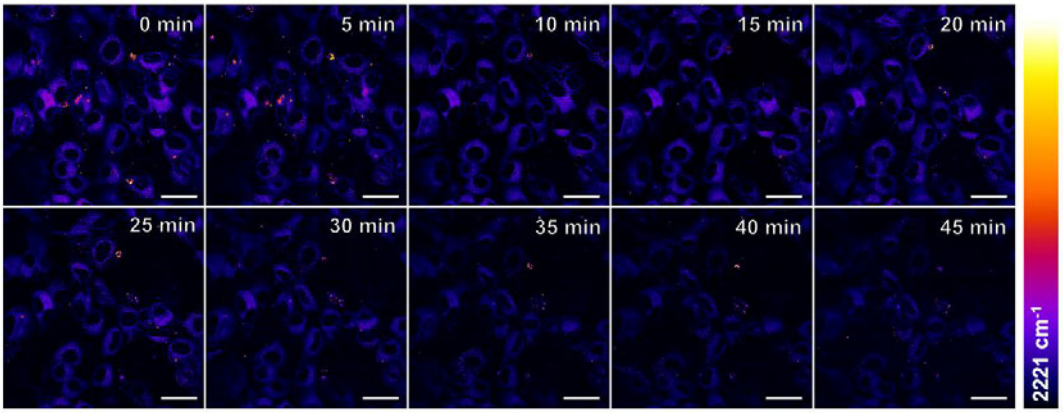

Figure 3.19. SRS imaging of **26a** in live ES-2 cells (10 μM, 2 h) after replacement of drug media with fresh culture media. Images acquired at 5-minute intervals from start of washout period. Contrast achieved by tuning to the indicated wavenumber for the alkyne frequency. Off-resonance frequency image subtracted to account for background signal. False colouring applied for clarity. Scale bars 25 μm. Imaging carried out by Dr Martin Lee.

To explore the idea that the Raman tag itself was preventing nuclear penetration of olaparib, the synthesised compounds with modified physicochemical characteristics were imaged in cells. For ease of comparison, **26b**, **26c**, **26g** and **29a**–**29c**, which do not feature heteroaromatic tags were first compared (**Figure 3.20**). **29a**, a variant of **26a** with an additional linker between the Raman tag and drug was shown to exhibit similar intracellular distribution. Likewise, tetralinyl BADY variants **26b** and **29b** were found to be distributed within the cytoplasm at similar signal intensity to the unmodified BADY drug-tag conjugates despite changes to Fsp^3 and log*D*. Images of PhDY tagged compounds **26c** and **29c** in cells also revealed diffuse cytoplasmic drug distribution (**Figure 3.20**). Interestingly, a significant difference in signal intensity between the two PhDY-tagged drug images was visible (**Figure 3.21**). This incubation should be repeated for further quantification to determine whether this is biologically significant. Considering both **26c** and **29c** contain the same PhDY Raman reporter, this suggests the apparent increased signal intensity may have been due to a difference in cell uptake between the two compounds, which is discussed in more detail in **Section 3.6.2**. The cellular signal intensity of **26c** was found to be similar to the BADY analogues, despite having a PhDY tag which was shown to exhibit ca. 2.6× lower spRS intensity than BADY (**Section 2.5**), further suggesting increased uptake.

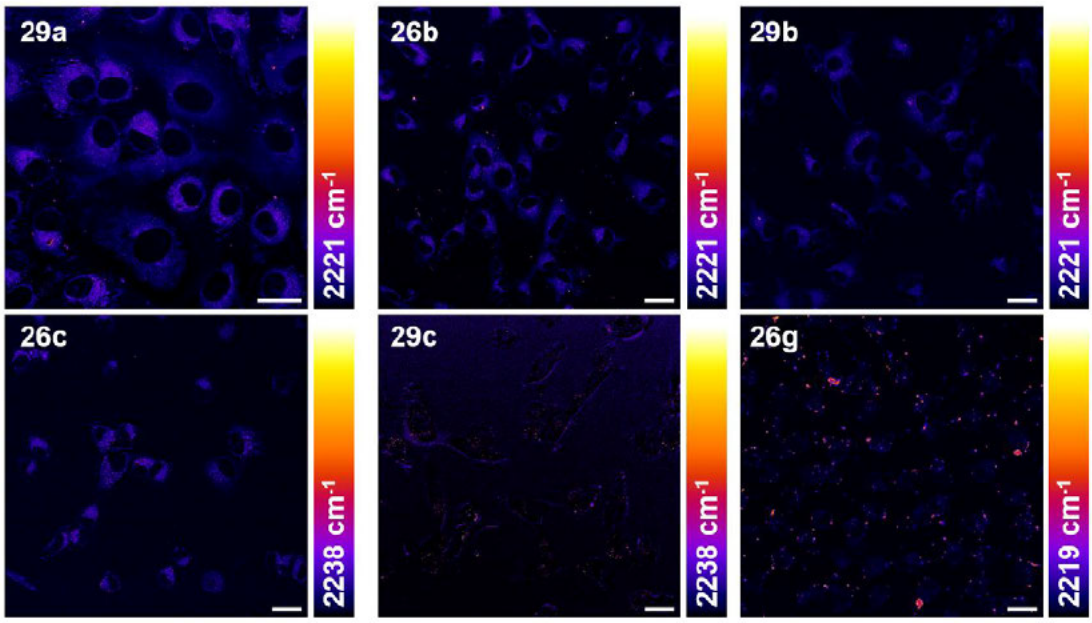

Figure 3.20. SRS imaging of **26b**, **26c**, **26g** and **29a–29c** in ES-2 cells (10 μM, 2 h). Contrast achieved by tuning the indicated wavenumbers for the alkyne. Off-resonance frequency image subtracted to account for background signal. False colouring applied for clarity. Scale bars 25 μm.

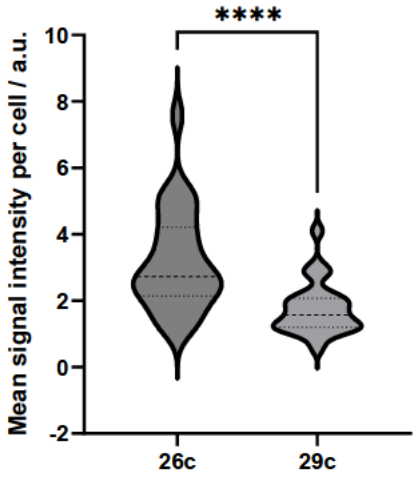

Figure 3.21. Quantification of the mean (across 25 cells) alkyne signal intensity normalised to the intensity of the protein (CH_3) signal for **26c** and **29c**, as shown in **Figure 3.20**. Raman intensity quantified using ImageJ. Mann-Whitney test **** $p < 0.0001$. Single biological repeat.

Finally, the intracellular distribution of **26g** was visualised (**Figure 3.20**). Poor solubility of **26g** was evident from both precipitated compound signal around the cell membranes and low signal intensity within the cell. This observation is more consistent with the relatively high ePSA value of **26g**, rather than its lower log$D_{7.4}$ which might be expected to facilitate cellular uptake.

Considering its similar structure to **26g**, the **26h** conjugate was next examined in cells (**Figure 3.22**). Although not included in the physicochemical testing, **26h** might be expected to further decrease the lipophilicity of BADY. Moreover, **26h** offered the opportunity to re-address the possibility of LOD issues with SRS imaging due to its fluorescence properties discussed in **Chapter 2**. Whilst colocalisation of the fluorescence and Raman signals of **26h** was observed, no additional fluorescence signal in the nucleus could be identified (**Figure 3.22C**). **26h** was observed to adopt a similar cellular distribution to **26g** punctate around cell membranes and was not diffuse throughout the cell, confirmed by examining distribution in the *z* direction (**Figure 3.22D** and **E**). As such, the fact that **26h** was not as cell permeable/soluble as the other compounds resulted in a fruitless attempt of signal detection the nucleus. If future studies require multimodal fluorescence-SRS tags, compounds must be designed that do not negatively affect intracellular distribution.

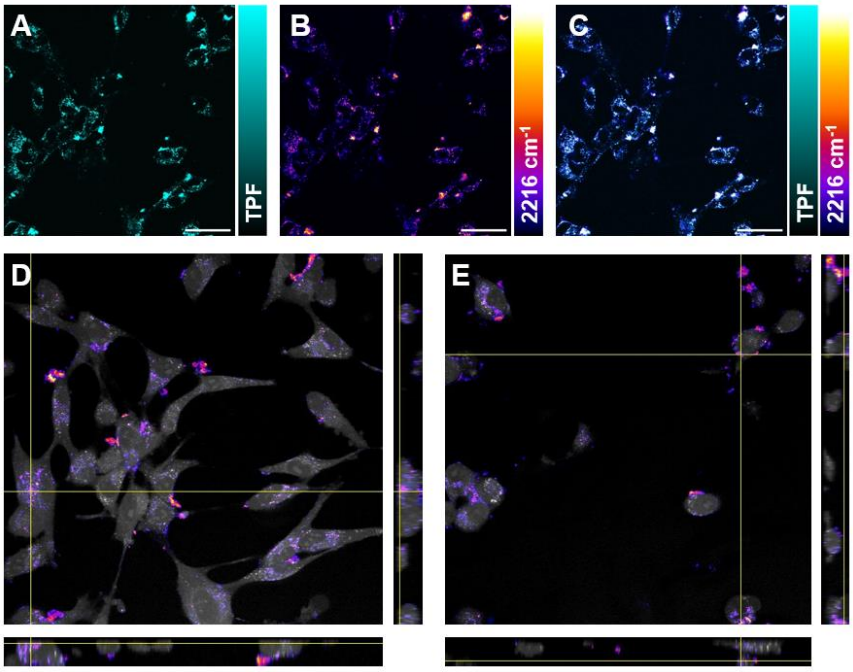

Figure 3.22. Multimodal imaging of **26h** in live ES-2 cells (100 μM, 2 h). **A**) Two-photon fluorescence (TPF) image acquired at 791.2 nm and **B**) SRS image acquired at 2216 cm^{-1}. **C**) overlay of **A** & **B**, **D**) and **E**) Z-stack orthogonal projections (overlay of CH_3 and alkyne signals). Off-resonance frequency image subtracted to account for background signal. False colouring applied to alkyne images for clarity. Scale bars 50 μm.

Finally, **26i–26k** were imaged (**Figure 3.23**). Despite offering the closest match of log$D_{7.4}$ and ePSA value compared to olaparib (e.g., log$D_{7.4}$ of **26k** = 1.8 vs 1.1 for olaparib), the distribution of **26i**, **29i** and **26k** remained visible only in the cytoplasm.

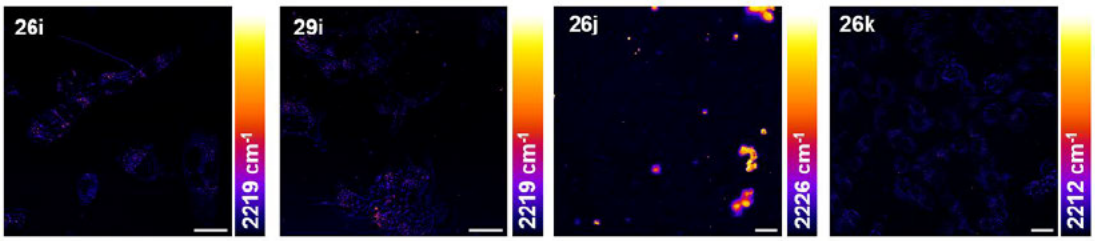

Figure 3.23. SRS imaging of **26i–26k** in ES-2 cells (10 μM, 2 h). Contrast achieved by tuning the indicated wavenumbers for the alkyne frequency in **26i–26k**. Off-resonance frequency image subtracted to account for background signal. False colouring applied for clarity. Scale bars 25 μm.

The signal intensity of these tags was lower than other all-carbon BADY compounds (e.g., **29a** vs **26i, Figure 3.21**), which is consistent with previous reports.[80] An unusual distribution of alkyne signal was observed from **26j**, which significant accumulation of the compound in the media. This was distinct from the images revealing compound precipitation (e.g., **Figure 3.20**) and did not appear to show compound signal within the cells (**Figure 3.25**). Although the exact tag structure in **26j** has not been shown to exhibit covalent reactivity, similar tags reacted rapidly with $^{-}$SH and $^{-}$OMe nucleophiles.[80] It is therefore possible that the unusual images obtained show compound that has reacted with components of the cell media.

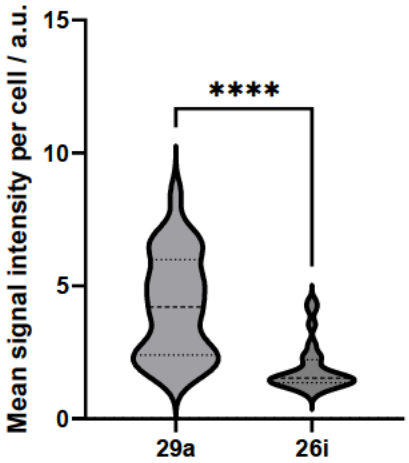

Figure 3.24. Quantification of the mean (across 25 cells) alkyne signal intensity normalised to the intensity of the protein (CH_3) signal for **29a** and **26i**, as shown in **Figure 3.23**. Raman intensity quantified using ImageJ. Mann-Whitney test **** $p < 0.0001$. Single biological repeat.

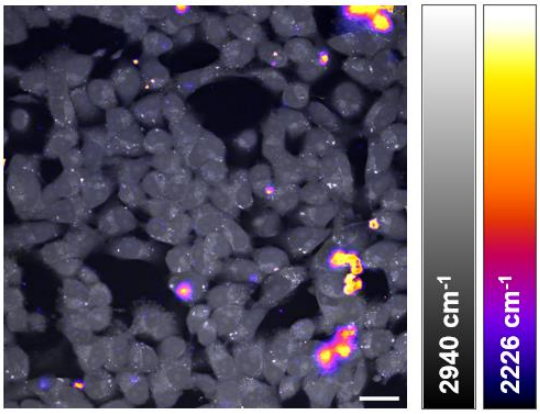

Figure 3.25. SRS imaging of **26j** in ES-2 cells (10 μM, 2 h) Overlay of alkyne image of **26j** shown in **Figure 3.23** with protein stretch to delineate cells. Contrast achieved by tuning the indicated wavenumbers. Off-resonance frequency image subtracted to account for background signal. False colouring applied to the alkyne image for clarity. Scale bars 25 μm.

Together, the lower signal intensity, lack of improvement in biodistribution and possibility of unwanted covalent reactivity, drove focus away from the heteroaromatic tag compounds. Focusing once again on the carbon-based tags, experiments were undertaken to clarify the unexpected cytoplasmic drug distribution.

3.6.2 Mass spectrometry

To determine whether drug was present in the nucleus at concentrations below the LOD of SRS, cells incubated (2 μM, 48 h) with tagged olaparib were analysed by MS at AstraZeneca. MS offers increased sensitivity over SRS and has previously been used for determination of intracellular drug concentrations within whole cells,[177, 178] and in specific organelles.[179] By separating cell compartments through fractionation, a readout of relative drug concentration in the nucleus could be determined. Validation of the nuclear fractionation protocol is provided in **Appendix A**, which shows clean separation of the cytoplasm and nucleus via Western blot analysis of organelle marker proteins.

Remarkably, **29c** was detected at considerably higher concentrations than olaparib across all cellular compartments (**Figure 3.26**, left). The question of whether attachment of the Raman tag prevented nuclear penetration of olaparib was also answered, with similar concentrations of olaparib and **29c** detected in the nucleus. However, at a concentration of 13.0 pmol/mg, **29c** would be undetectable by SRS imaging. Aside from the absolute concentrations of drug in the different organelles, the relative distribution between the cytoplasmic, perinuclear and nuclear

compartments was different for olaparib and **29c** (**Figure 3.26**, right). Consistent with the SRS imaging results, the majority of **29c** was shown to be in the cytoplasm. It is thus possible that the origin of increased **29c** nuclear concentrations is at least partly due to translocation of the high drug concentration from the cytoplasm, rather than having actively targeted the nucleus. It is also unclear why such a high percentage of olaparib was detected in the perinuclear region. The BODIPY-olaparib study by Thurber *et al*. also reported perinuclear staining of olaparib, however this was cleared with washing.[150] Drug may also have diffused out of the nucleus (or indeed other organelles) during the course of this long fractionation protocol. In general, it may have been prudent to allow a longer washout period after drug incubation and before starting the fractionation protocol. This would account for clearance of unbound drug localised in the cytoplasm and may have alleviated any issues with the increased lipophilicity of **29c** hindering its diffusion from the cell. Modification of the protocol to include these additional washout steps may explain the origins of increased intracellular concentrations of **29c**.

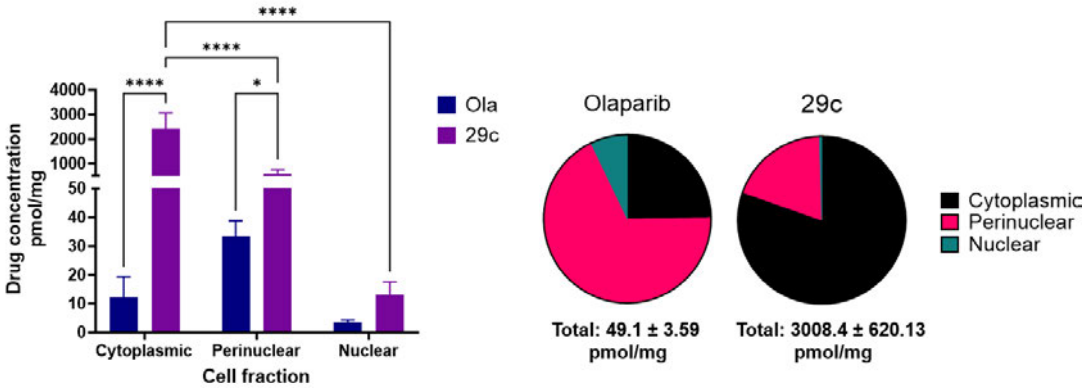

Figure 3.26. Quantitation of relative subcellular concentrations of olaparib and **29c** after treatment of ES-2 cells with the indicated compound (2 µM, 48 h). Error bars report the standard deviation of the mean from three independent experiments. (n=3, two-way ANOVA, * $p < 0.05$, **** $p < 0.0001$, only significant differences are reported). Mass spectrometry carried out at AstraZeneca by Paul Davey and Erin Braybrooke.

A second MS experiment was conducted in efforts to understand the relative cell permeability of the different compounds. Olaparib, **26a**, **26c**, **26k** and **29c** were incubated in cells and the whole cell lysate was subjected to MS quantitation (**Figure 3.27**, left). These compounds were chosen as they represent the diversity of physicochemical properties determined in **Table 3.1**. Each of the olaparib analogues tested were again detected at much higher concentrations than olaparib, with the highest concentration of 7222 pmol/mg for **26c** ca. 61× higher than olaparib. The

relative intracellular concentrations **26c** >> **26a** > **26k** > **29c** could be correlated with their increasing ePSA values quantitation (**Figure 3.27**, right). In addition, with **26c** detected at ca. 3× higher concentration than **29c**, this may explain the unusually high signal intensity of **26c** detected by SRS imaging (**Figure 3.20**). It is, however, important to note that the increased concentration of each of the compounds relative to olaparib does not necessarily indicate increased uptake by the cell. Instead, the compounds may have exhibited similar permeability profiles but differ in their ability to be cleared from the cell. For example, whilst **26c** has the lowest ePSA value of the tag compounds tested by MS, it was also reported to have the highest log*D*. As such, **26c** may have become trapped in lipophilic regions of the cell and not washed out efficiently due to poor aqueous solubility. Again, modifying the protocol to include a longer washout period may alleviate these issues. Aside from a purely physicochemical rationale for increased drug concentration, it may be interesting to further investigate these findings within the context of drug efflux. Olaparib is a known substrate of P-glycoprotein 1 (P-gp), a cell membrane protein which functions as a drug efflux pump.[180] Decreases in intracellular olaparib concentration through P-gp-mediated drug export hampers effective drug treatment and is a major cause of drug resistance in cancer.[181] It is unclear whether Raman tagging of olaparib affected drug efflux but it may be important to examine this in the future, especially considering structural modifications have previously been made to olaparib which decreased affinity for P-gp and improved efficacy in olaparib-resistant tumours.[182]

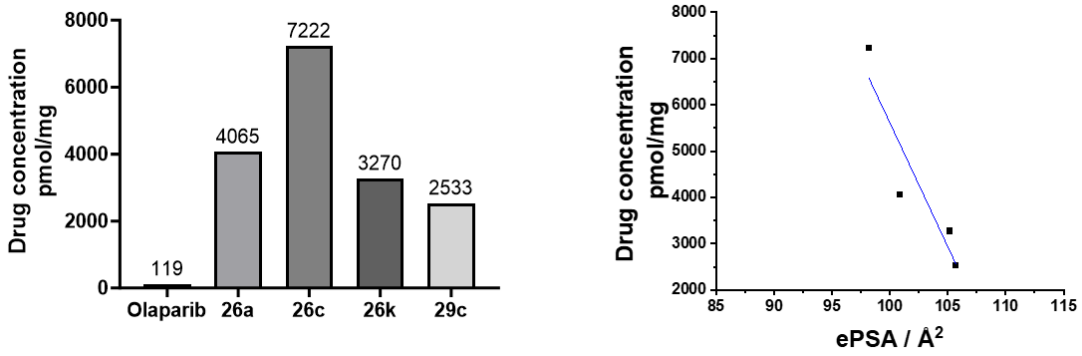

Figure 3.27. **Left:** Quantitation of relative intracellular concentrations of olaparib, **26a**, **26c**, **29c** and **26k** in whole cell lysates from a single experiment after treatment of ES-2 cells with the indicated compound (2 μM, 48 h). **Right:** Correlation analysis of ePSA and intracellular drug concentration for Raman-tag olaparib analogues. R^2 = 0.86, *r* = 0.92. Mass spectrometry carried out at AstraZeneca by Paul Davey and Erin Braybrooke.

Considering no significant difference in drug concentration between olaparib and **29c** was detected in the nucleus, it was expected that the function of olaparib was retained. However, it was important to determine whether the much higher cytoplasmic concentration of **29c** conferred any differences in other cell-based assays. In order to clarify whether the differences in apparent intracellular concentrations and relative organelle distributions correlated with a change in drug activity *in cellulo*, further testing needed to be carried out. It is also important to note that the nuclear fractionation protocol involved multiple consecutive washing and centrifugation steps spanning more than 1 hour, yet drug was still detected in the nucleus. Referring to **Figure 3.19**, this suggests that, whilst SRS imaging did not allow detection of drug in the nucleus, the compound was likely present below the LOD.

3.7 Conclusions

In this chapter, the PARP inhibitor olaparib was imaged in cancer cells using SRS microscopy. Attachment of the Raman tags discussed in **Chapter 2** allowed the generation of a series of drug analogues with varying physicochemical properties. To assess their suitability for biological applications, log$D_{7.4}$ and ePSA values were determined and these predicted that all compounds were likely to be cell permeable, despite being considerably more lipophilic than olaparib. SPR, HDX-MS, and enzyme activity assays revealed that tagging olaparib did not significantly affect binding to PARP-1, providing the necessary prerequisites for the transition to *in cellulo* testing. SRS imaging allowed the biodistribution of the olaparib analogues to be determined, revealing drug signal in the cytoplasm, generally consistent between all compounds tested. Heteroaromatic tags were generally not suitable for this application due to poor signal intensity and a risk of non-specific reactivity. To determine whether the compounds were present in the nucleus at low concentrations, approaches to address the LOD of SRS imaging were taken. Although attempts to optimise incubation conditions and application of multimodal imaging still did not allow nuclear drug detection, analysis by mass spectrometry revealed tagged olaparib in the nucleus at similar concentrations to unmodified olaparib. This highlights both the limitations of SRS microscopy and the challenges of targeting a nuclear drug. MS analysis also revealed much higher intracellular concentrations of the Raman-tagged drugs compared to unmodified olaparib, warranting further study to determine whether this translated into new biological activity. The intracellular activity of these compounds will be explored in **Chapter 4**.

Chapter 4 Effects of Raman Tagging on Drug Action in Cancer Cells

4.1 Introduction

For the development of a bioorthogonal tagging methodology, it is essential that the molecule of interest is not fundamentally changed by attachment of the tag. For example, the molecule should exhibit the same toxicity profile, retain activity and potency with its target and maintain the original mechanism of action. Having determined that all of the synthesised olaparib analogues retained PARP activity and most appeared to be cell permeable, the majority of compounds were deemed suitable for further analysis in cells. For ease of comparison, **26a**–**26c** and **29a**–**29c** were selected due to their similarity in chemical structure but slight differences in physiochemical properties. The unexpected biodistribution of these compounds revealed by SRS imaging in **Section 3.6.1** provoked further study to assess their drug activity in cells. To determine the bioorthogonality of the tags, the initial goal was to confirm that the analogues had a similar IC_{50} to olaparib and ensure retention of PARP inhibitor activity *in cellulo*.

4.2 Cell viability

Using the Alamar Blue cell viability reagent as a readout, the viability of ES-2 cells was measured after an incubation of 72 h with olaparib, **26a**–**26c**, **29a**–**29c** and BADY ester **1a** (**Figure 4.1**, left). The IC_{50} value of 11.52 µM obtained for olaparib compares well with published data for ES-2 cells (13.12 µM).[183] Strikingly, all of the olaparib tag conjugates exhibited much lower IC_{50} values than olaparib. Two groups of compounds were identified: those with ca. 250-fold lower IC_{50} values than olaparib (**29a**–**29c**) and those with ca. 15-fold lower IC_{50} values than olaparib (**26a**–**26c**). Interestingly, the compounds are also distinct in molecular structure. **26a**–**26c** contain tags attached directly to the piperazine ring in olaparib, whereas **29a**–**29c** are bonded via a 4-carbon chain linker. Later studies also found differences between these 2 groups of compounds and will be discussed in **Section 4.3**. A qualitative assessment of cell viability after incubation with **29c** vs olaparib was further illustrated by carrying out a crystal violet assay (**Figure 4.1**, right). Crystal violet non-specifically stains proteins thus allowing a quick assessment of cell density, a reduction of which was more evident with **29c** treatment. BADY tag ester **1a** was shown not to affect cell viability at any concentration, ruling out any possible toxicity of the Raman tag itself. These

results are in contrast to other olaparib-tag compounds, e.g., a PROTAC and BODIPY-labelled compound tested were not found to exhibit considerably lower IC_{50} values when compared to olaparib.[184, 185]

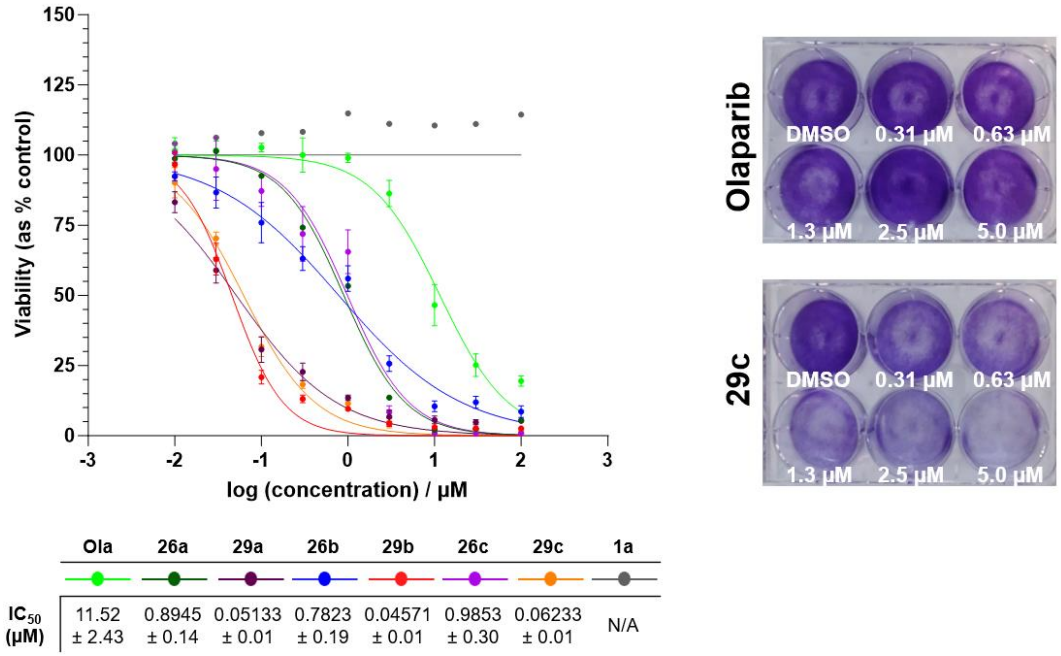

Figure 4.1. **Left**: Dose-response curves for olaparib (Ola), **26a**–**26c**, **29a**–**29c** and **1a** in ES-2 cells treated for 72 h. Viability was measured using the Alamar Blue reagent and expressed as percentage of DMSO-treated wells. Error bars report the standard deviation of the mean from three independent experiments. **Right**: Crystal violet assay to qualitatively assay cell density of ES-2 cells treated with Ola and **29c** at the indicated concentrations for 48 h.

Considering that the cause of the increased sensitivity to **26a**–**26c** and **29a**–**29c** over olaparib was unclear, it was important to determine whether it could be related to a drug-dependent mechanism. In order to confirm whether sensitivity was linked to the direct action of olaparib engagement with PARP, a viability assay was designed (**Figure 4.2A**) using ES-2 cells with a *PARP1* gene knockdown (KD). Cells were transfected with siRNA targeting *PARP1* for 24 h, reducing PARP-1 expression to ca. 40% vs control, as confirmed by Western blot (**Figure 4.2B, C**). The PARP-1 antibody used is known not to cross-react with other PARP family members. The cells were then replated and treated with compounds for 48 h. PARP-1 expression continued to decrease over the course of this incubation and was shown to reach ca. 4% vs the control.

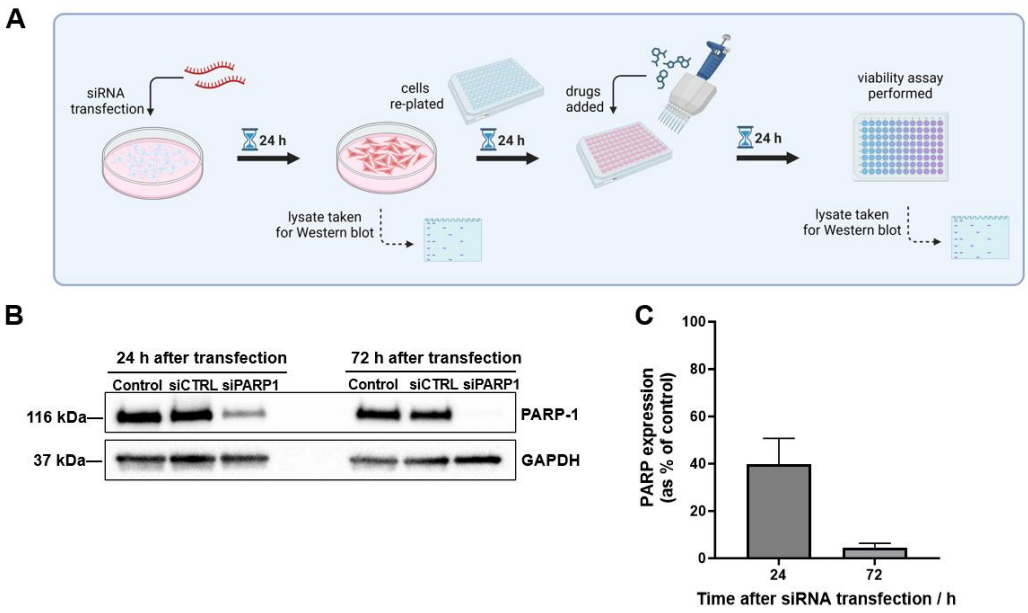

Figure 4.2. **A**) Schematic representation of siRNA-mediated knockdown of *PARP1* and subsequent viability assay. **B)** Validation of siRNA-mediated *PARP1* knockdown by Western blot analysis. Representative blot shown. **C)** Quantification of Western blot analysis (n=3). PARP-1 levels are expressed as a percentage of the siCTRL-treated cells. Error bars report the standard deviation of the mean from three independent experiments.

The extent of *PARP1* KD was further confirmed visually by carrying out immunofluorescence imaging (**Figure 4.3**). When compared to WT cells, *PARP1* KD cells (24 h after siRNA treatment) showed a significant decrease in the fluorescence signal from fluorophore antibody-conjugated PARP-1.

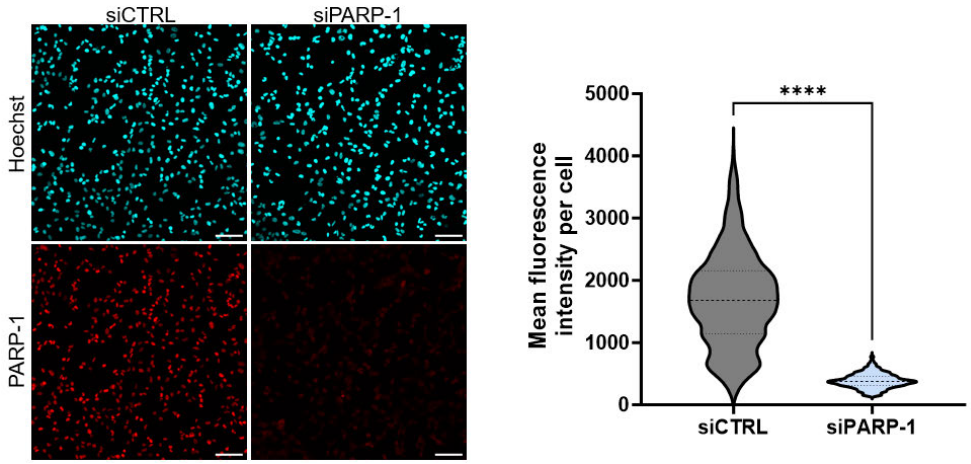

Figure 4.3. **Left**: immunofluorescence imaging of ES-2 cells after siRNA-mediated knockdown of PARP-1 (24 h after siRNA treatment). Hoechst-33342 was used to stain nuclei (blue) and PARP-1 primary antibody was coupled to Alexa Fluor 594 secondary antibody (red). **Right**: quantification of fluorescence signal across the FOV shown on the right. Fluorescence intensity quantified using ImageJ. (n=1, unpaired t-test **** $p < 0.0001$). Scale bars 100 µm.

Olaparib analogue **29c** was selected as representative compound for the olaparib-tag conjugates and was tested in the *PARP1*-KD viability assay with BADY ester **1a** as a negative control. Staurosporine and doxorubicin were selected as positive controls, which might be expected to kill cells irrespective of PARP status. As expected, sensitivity to olaparib was lost in *PARP1* KD cells (**Figure 4.4A**). The same observation was made for **29c** (**Figure 4.4B**, 10× lower concentrations than olaparib). BADY ester **1a** had no effect on cell viability, reiterating its inertness (**Figure 4.4C**). Both staurosporine and doxorubicin had a marked effect on cell viability in both WT and KD cells, confirming their ability to reduce cell viability is not strictly linked to PARP. However, a significant difference in the viability of WT vs KD cells was observed for doxorubicin, which is known to affect PARP-dependent processes.[186] The final objective of this assay was to determine the effect of co-incubation of olaparib and **29c**. It was hypothesised that, based on the lower k_a and k_d values of the tagged compounds (**Section 3.5.1**), olaparib may preferentially bind to PARP in the cells, partially blocking the effects of **29c**. A significant increase in viability was observed in cells treated with both olaparib and **29c** vs those treated with only **29c**, suggesting a competitive effect of the two compounds (**Figure 4.4D**). Together, these results indicated that the loss of viability is likely due to the interaction of the drug-tag analogue **29c** with PARP, however, further studies needed to be conducted to explain its increased activity vs olaparib. Considering the tagged compounds are similar in chemical structure and each exhibited increased potency in the viability assays, it may be assumed that the other olaparib analogues would have a similar PARP-dependent sensitivity profile. However, the *PARP1*-KD viability assay should be repeated with all compounds to confirm this.

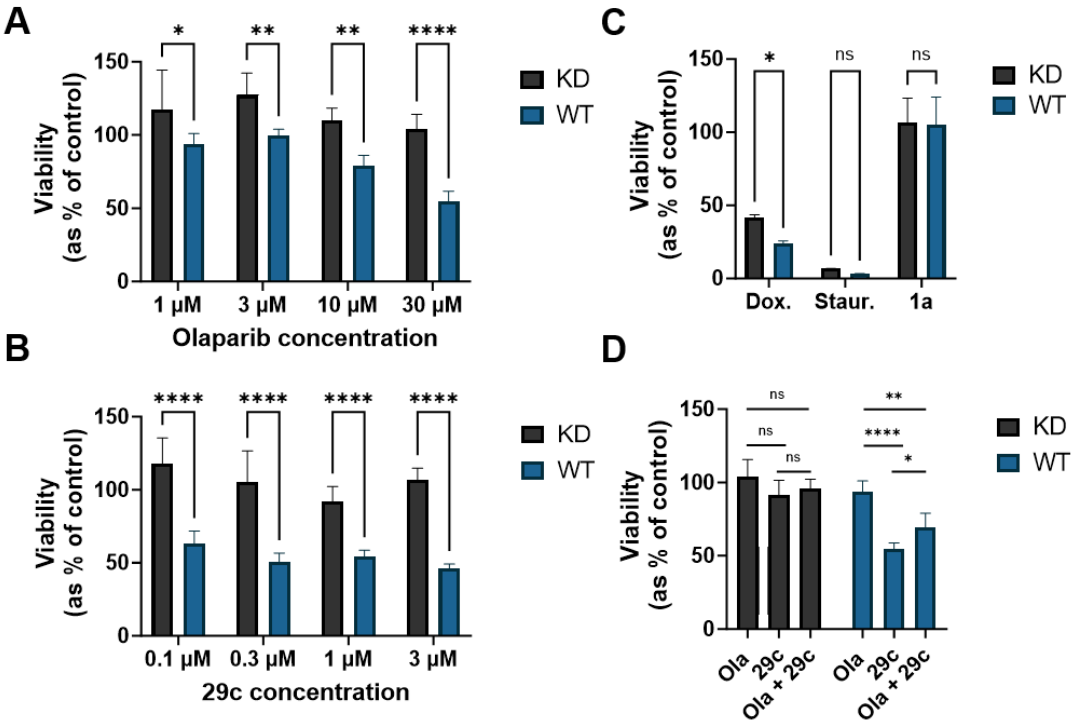

Figure 4.4. Viability data from wild type (WT) and *PARP1* knockdown (KD) ES-2 cells after 48 h drug treatment with **A)** olaparib (Ola), **B) 29c**, **C)** doxorubicin (Dox.), staurosporine (Staur.) or **1a**, and **D)** combinations of Ola/**29c**. Viability was measured using the Alamar Blue reagent and expressed as percentage of DMSO-treated wells. Error bars report the standard deviation of the mean from three independent experiments. (n=3, two-way ANOVA, ns not significant $p > 0.05$, * $p < 0.05$, ** $p < 0.01$, *** $p < 0.001$, **** $p < 0.0001$).

In efforts to further rule out general cytotoxicity of **26a**–**26c** and **29a**–**29c**, their effect on viability was studied in two non-cancerous cell lines: human embryonic kidney (HEK-293) cells and red fluorescent protein telomerase reverse transcriptase (TERT)-immortalised fibroblasts (RTIF)[187] generated from skin punch biopsies (**Figure 4.5**). When compared to ES-2, both cell lines showed decreased sensitivity to both olaparib and **29c**.

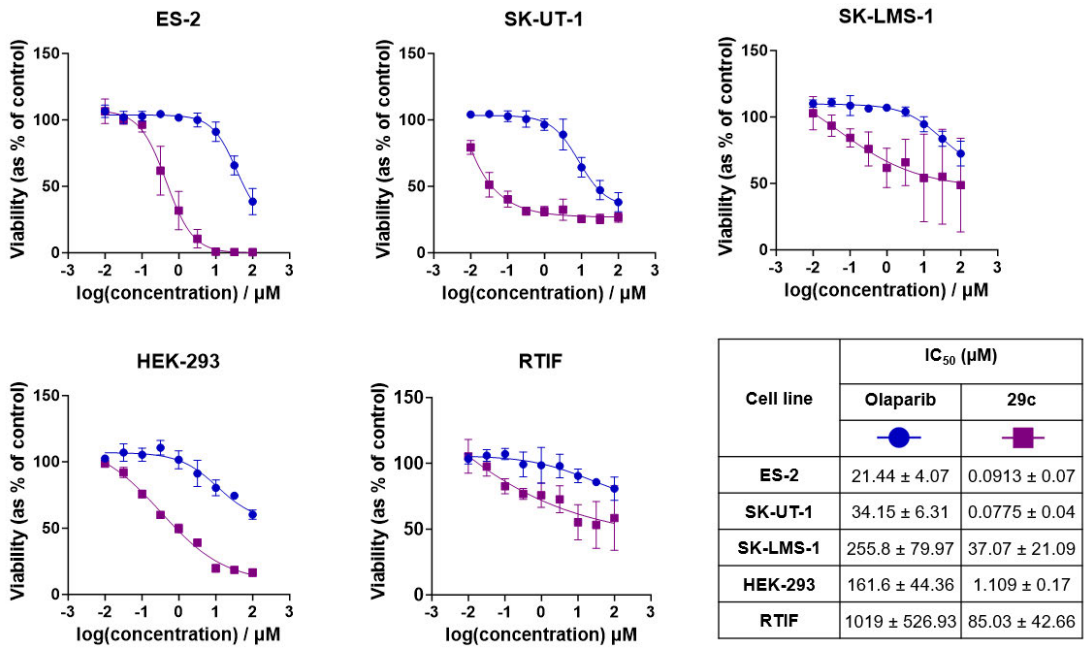

Cell line	IC_{50} (µM)	
	Olaparib	29c
ES-2	21.44 ± 4.07	0.0913 ± 0.07
SK-UT-1	34.15 ± 6.31	0.0775 ± 0.04
SK-LMS-1	255.8 ± 79.97	37.07 ± 21.09
HEK-293	161.6 ± 44.36	1.109 ± 0.17
RTIF	1019 ± 526.93	85.03 ± 42.66

Figure 4.5. Dose-response curves for olaparib and **29c** in the indicated cell lines treated for 72 h. Viability was measured using the Alamar Blue reagent and expressed as percentage of DMSO-treated wells. Error bars report the standard deviation of the mean from three independent experiments. Corresponding IC_{50} data is tabulated.

In HEK-293, both olaparib and **29c** gave IC_{50} values ca. 10× higher than in ES-2 cells. In RTIF, both compounds were shown to have even less effect on cell viability. These data may suggest that the compounds are more selective for cancer cells over non-cancer cells, however, without assessing this *in vivo* or screening a wide range of cell lines, no definite conclusions can be made. Since the ES-2 cell line is homologous recombination (HR)-proficient, it was expected to be less sensitive to PARP inhibition than a HR-deficient cell line. Uterine leiomyosarcoma model cell lines SK-LMS-1 and SK-UT-1 bearing *BRCA1* and *BRCA2* mutations, respectively, were also tested for sensitivity to olaparib and **29c** (**Figure 4.5**). *BRCA*-mutated (*BRCAm*) cell lines did not show increased sensitivity to either olaparib or **29c** when compared to ES-2 *BRCA* WT cells. It may be sensible to repeat this assay using longer incubation periods for a more reliable viability readout, since longer incubation times are usually required for the build-up of SSB/DSB in DNA before cell death occurs. However, it is difficult to compare between each of these cell lines as they each have unique genetic profiles aside from *BRCA* status. Ideally, isogenic cell lines would be used, modified only by a DNA damage response gene of interest.

Accordingly, colorectal cancer DLD-1 *BRCA2* WT and DLD-1 *BRCA2* -/- cells were incubated with olaparib, **26a–26c**, **29a** and **29c** over a 7-day period in a viability assay at AstraZeneca (**Table 4.1**). This type of assay is currently being used at AstraZeneca to determine the suitability of new DNA damage-related drugs. Expectedly, olaparib was shown to exhibit a ca. 400-fold lower IC_{50} value in *BRCA2* -/- cells vs WT and a similar trend was observed for the tagged compounds. However, **26a–26c**, **29a** and **29c** show much less of a difference between the two cell lines, indicating that, whilst a PARPi mechanism similar to that of olaparib may be occurring, they are exerting a cell death mechanism that cannot be overcome by the normal DNA damage response cell machinery.

Table 4.1. IC_{50} values obtained from cell viability data for olaparib and olaparib analogues in *BRCA* WT and *BRCA* -/- DLD-1 cell lines from three independent experiments. IC_{50} curves are provided in **Appendix A**. Data acquired with assistance from Dr Pamela Lochhead and Dr Poppy Winlow at AstraZeneca.

Compound	IC_{50} (nM)		Fold change WT vs -/-
	DLD-1 WT	DLD-1 *BRCA2* -/-	
Olaparib	7786	18.62	418
26a	417.8	5.927	70
29a	390.9	17.94	22
26b	925.0	50.02	18
26c	2062	15.34	134
29c	483.6	10.34	47

The increased use of PARPi such as olaparib has seen a concomitant increase in the cases of drug resistance. Although work is being done to understand the mechanisms of PARPi resistance, this was not the focus of the present study. However, it was hypothesised that the apparent increased potency of the olaparib-tag compounds may offer an opportunity to target olaparib-resistant cancers. An olaparib-resistant variant of the ES-2 cell line was previously developed and acquired for this assay.[188] Expectedly, olaparib was shown to exhibit a much higher (5×) IC_{50} in the olaparib-resistant cell line (**Figure 4.6**). **29c** was also much less active (27× higher IC_{50}) in the resistant cell line, further suggesting this analogue retains the biological properties of olaparib. However, the two compounds were again separated by their absolute IC_{50} values in the resistant cell line, i.e., **29c** is 85× more potent than olaparib, suggesting this compound may be useful in targeting olaparib-resistant cancers.

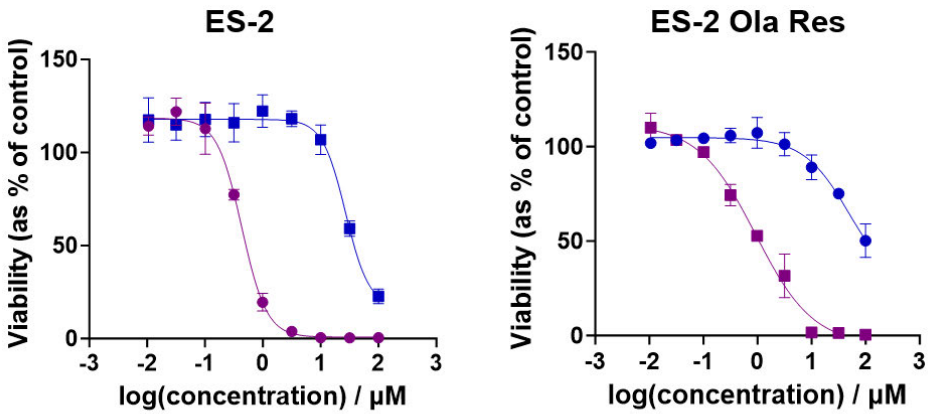

Cell line	IC_{50} (µM)	
	Olaparib	29c
ES-2	19.19 ± 1.26	0.0423 ± 0.01
ES-2 Ola Res	96.77 ± 28.24	1.134 ± 0.25

Figure 4.6. Dose-response curves for olaparib and **29c** in ES-2 and ES-2 olaparib-resistant (Ola Res) cell lines treated for 72 h. Viability was measured using the Alamar Blue reagent and expressed as percentage of DMSO-treated wells. Error bars report the standard deviation of the mean from three independent experiments. Corresponding IC_{50} data is tabulated.

Whilst absolute IC_{50} results varied, for each cell line tested throughout this study **29c** was shown to be much more potent than olaparib which clearly separates the two compounds. This was not expected and considering the apparent connection to PARP, rather than nonspecific toxicity (**Figure 4.4**), further testing was carried out to explain the origin of this effect.

4.3 Discovery of PARP protein degradation

It has been reported that replacement of the cyclopropyl ring of olaparib with a fluorenyl moiety to generate **HyTX** induced new effects on cancer cells.[189] This structural modification is an example of a technique known as hydrophobic tagging (HyT), whereby a small hydrophobic moiety, most commonly adamantane, is attached to a drug (**Figure 4.7**). This in turn destabilises the drug target either by mimicking or inducing a partially unfolded protein state, triggering the cell's natural protein folding machinery.

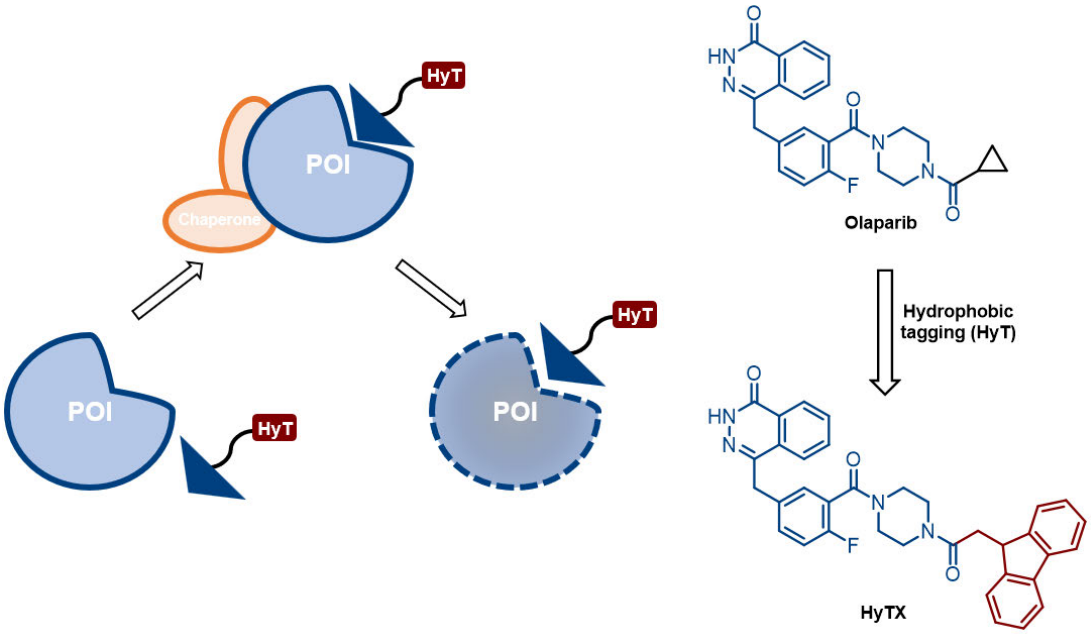

Figure 4.7. **Left**: Hydrophobic tagging (HyT) technology applied to a protein of interest (POI). A ligand containing a hydrophobic moiety binds to the POI causing destabilisation and activation of chaperone-assisted refolding. If the misfolding cannot be overcome, the protein is degraded. **Right**: HyT of olaparib to generate compound **HyTX**.

If the cell becomes overwhelmed with unfolded proteins, the unfolded protein response (UPR) is activated to avoid endoplasmic reticulum (ER) stress which activates a plethora of pathways and can result in cell death (**Figure 4.8**). If protein destabilisation cannot be rectified, the protein degradation process is activated, removing the damaged protein from the cell. The recognition and processing of ER-localised proteins for degradation is often referred to as endoplasmic reticulum-associated protein degradation (ERAD). As such, hydrophobic tagging can be classed as a form of targeted protein degradation (TPD), which is a burgeoning field in medicinal chemistry. Compound **HyTX** was reported to initiate the UPR, induce apoptosis and have an IC_{50} value ca. 16× lower than olaparib in MDA-MB-231 cells.[189] Considering the hydrophobicity of BADY and its analogues, and the increased potency of **26a**–**26c** and **29a**–**29c** in viability assays, it was hypothesised that a HyT-induced pathway may have been inadvertently activated.

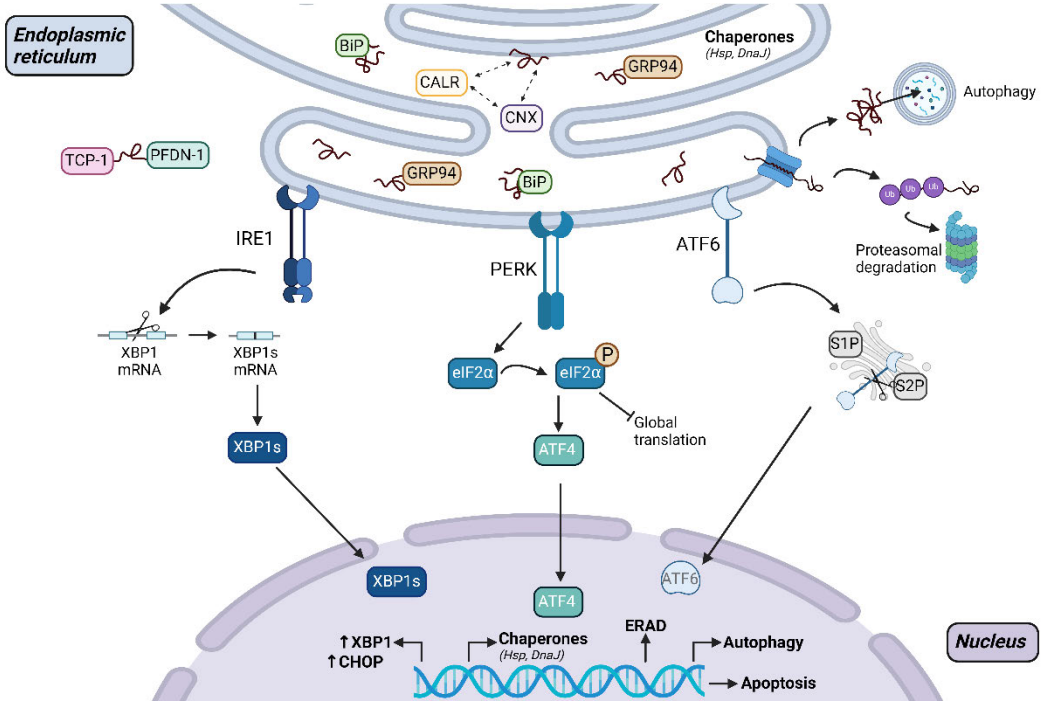

Figure 4.8. Diagram of proteins and pathways involved in the unfolded protein response (UPR) and endoplasmic reticulum (ER)-stress. ATF4 = activating transcription factor 4, ATF6 = activating transcription factor 6, BiP (HSPA5, GRP78) = binding immunoglobulin protein, CALR = calreticulin, CHOP = C/EBP homologous protein, CNX = calnexin , DnaJ = J-domain molecular chaperones, eIF2α = eukaryotic translation initiation factor 2α, ERAD = endoplasmic reticulum (ER)-associated protein degradation, GRP94 (HSP90B1) = glucose-regulated protein 94, Hsp = heat shock protein, PERK = protein kinase R (PKR)-like endoplasmic reticulum kinase, PFDN-1 = prefoldin subunit 1, S1P = site-1 protease , S2P = site-2 protease, TCP-1 = T-complex 1, XBP1 = X-box binding protein 1. Produced using Biorender.

Accordingly, **26a**–**26c** and **29a**–**29c** were incubated in ES-2 cells to assess any effect on the expression of PARP (**Figure 4.9**). Interestingly, every compound tested was shown to reduce the expression of PARP when compared to olaparib. Moreover, the compounds were again separated into two potency groups: **29a**–**29c** were active at 2.5 µM, whereas **26a**–**26c** generally required higher concentrations to reduce PARP expression. This is consistent with the two potency groups identified in **Figure 4.1**, where **29a**–**29c** exhibited lower IC_{50} values than **26a**–**26c**. For most compounds, ca. 50% PARP remained after 48 h at the effective concentration, with the most potent compound **29c** inducing 58% degradation at 5 µM ($p < 0.001$). The potency of **26a**–**26c** at 10 µM was very similar to the published PARP HyT compound **HyTX**, possibly reflecting their similar structures (no linker between tag and drug). Importantly, esters of tags **1a**–**1c** and **27a** (not conjugated to olaparib) did not show any degradation effect on PARP (**Appendix A**). In order to facilitate further investigation, **29c** was taken forward as a representative compound.

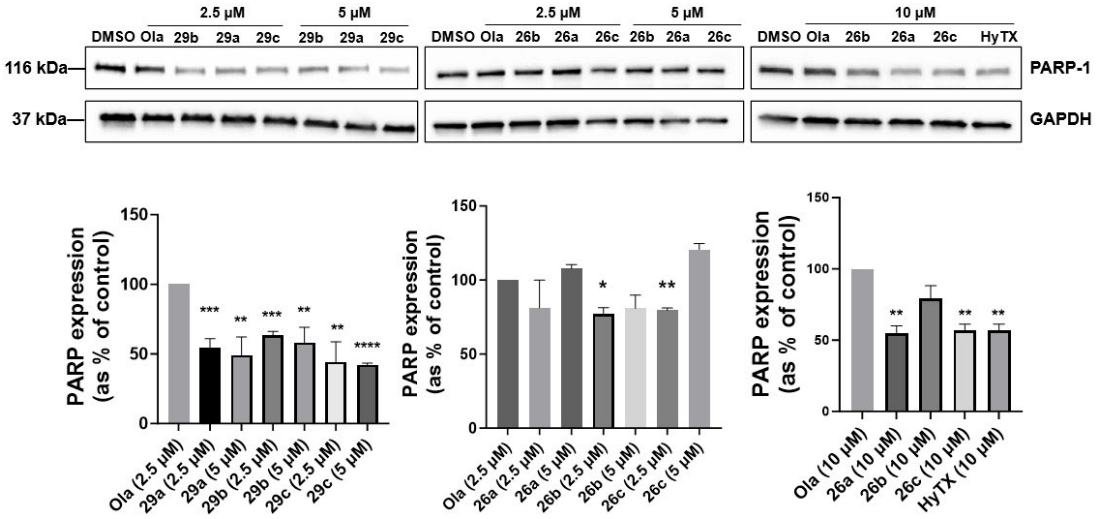

Figure 4.9. Representative Western blots (**top**) and corresponding quantification (**bottom**) after treatment of ES-2 cells with the indicated compound for 48 h. PARP expression is expressed as a percentage of olaparib control. Error bars report the standard deviation of the mean from three independent experiments (n = 3, one-way ANOVA vs olaparib, * $p < 0.05$, ** $p < 0.01$, *** $p < 0.001$, **** $p < 0.0001$).

Before further studies were conducted, it was confirmed that the **29c** was acting at the PARP protein level and not affecting *PARP* gene expression (**Figure 4.10**). No significant changes in *PARP1* gene expression were observed.

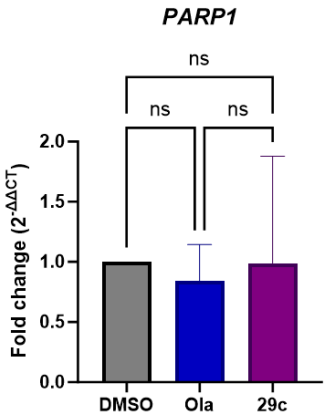

Figure 4.10. qPCR data for the expression of the *PARP1* gene after treatment with DMSO, olaparib (ola) or **29c** at 2.5 µM for 48 h. Fold change in expression vs *GAPDH* control is shown. Error bars report the standard deviation of the mean of the mean from three independent experiments. (n=3, one-way ANOVA, ns not significant $p > 0.05$)

Protein degrader compounds are often compared by degradation efficiency parameters such as D_{max} (maximum percentage degradation) and DC_{50} (concentration at which 50% degradation is achieved). These parameters were

obtained for **29c** (**Figure 4.11**), which gave a DC_{50} of 0.618 µM and D_{max} of 55%. This compares well to, or is an improvement on, many of the published examples of HyT degradation. DC_{50} values for **HyTX**-mediated degradation of PARP were not published, although **Figure 4.9** shows that **HyTX** exhibited similar potency to **26a** and **26c** in degrading PARP in this study. As discussed, the mechanisms of PROTAC-based degradation of PARP are not the same as HyT-based degradation, and published PARP-1 PROTACs have lower DC_{50} values (0.51, 36 & 82 nM).[185, 190]

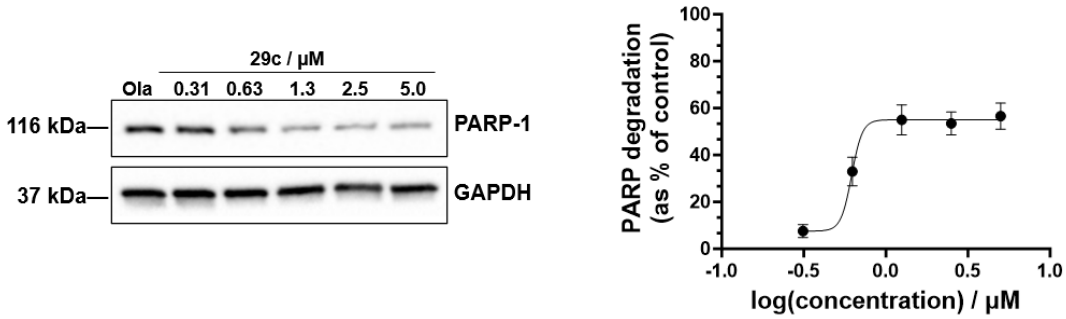

Figure 4.11. Representative Western blots (**left**) and corresponding quantification (**right**) after treatment of ES-2 cells with **29c** for 48 h at the indicated concentrations to quantify degradation parameters. PARP expression is expressed as a percentage of olaparib control. Error bars report the standard deviation of the mean from three independent experiments.

Next, the dynamics of protein degradation were explored through a series of experiments (**Figure 4.12**). An incubation time of up to 48 h was chosen based on previous reports; however, it was not clear how quickly these compounds elicited an effect on PARP expression. Accordingly, PARP expression was monitored over the 48 h period. Significant loss of protein expression was only observed after 12 h, after which the expression level appeared to plateau at around 24 – 48 h (**Figure 4.12A**). The relatively slow apparent onset of action of protein degradation is not unexpected for PARP, which has a half-life of over 60 h.[191] Similarly, performing a washout experiment did not recover the PARP protein level (**Figure 4.12B**), which was shown to restore expression of (shorter-lived) HyT-degraded Src1 and SMD1 proteins.[192, 193] Finally, with the knowledge that co-incubation of olaparib and **29c** partially recovered cell viability compared to **29c**-only treated cells (**Figure 4.4D**), a competition experiment was conducted. Although co-incubation of **HyTX** and olaparib was shown to prevent the degradation of PARP,[189] the same result was not obtained in this study (**Figure 4.12C**). Instead, no significant difference in PARP expression was observed after olaparib co-incubation. This may indicate a difference in the mode of action of

29c vs **HyTX**, however, the protocol may also be modified to further investigate competition, e.g., by pre-incubation with olaparib for a longer period to ensure saturation of PARP binding.

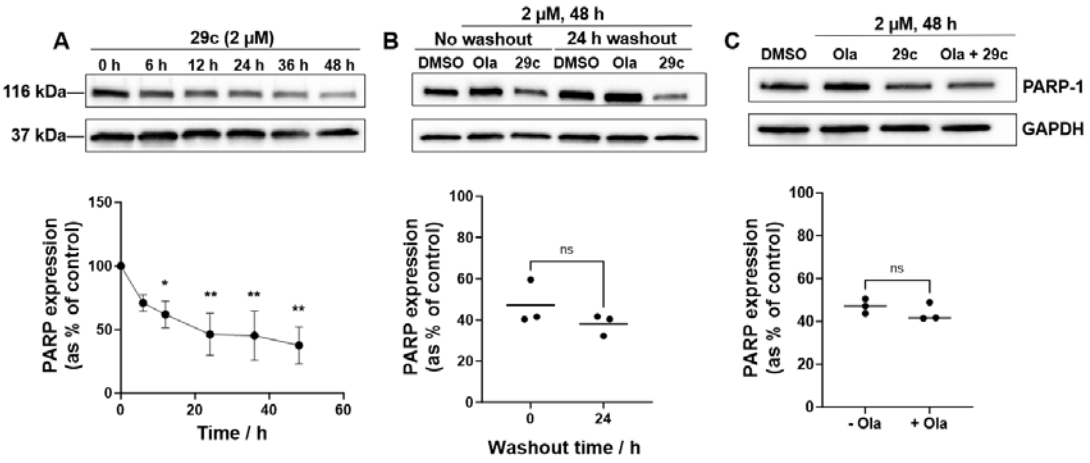

Figure 4.12. Representative Western blots (**top**) and corresponding quantification (**bottom**) after treatment of ES-2 cells under the indicted conditions: **A)** Effect of incubation time on **29c**-induced PARP degradation, **B)** Effect of washout (removal of drug-containing media and replacement with fresh media) on PARP degradation, and **C)** Competition experiment using either Ola, **29c** or both drugs. PARP expression is expressed as a percentage of olaparib control. (n = 3, unpaired t test, ns not significant $p > 0.05$, * $p < 0.05$, ** $p < 0.01$).

Attention was next drawn to the mechanism of degradation. Although no single conclusive mechanism has been determined to explain the effects of HyT, studies often demonstrate involvement of proteins related to the UPR (**Figure 4.8**) and ubiquitin-proteasome system (UPS).[194] Despite often found intertwined, activation of the UPR by HyT does not always end with degradation through the UPS, which separates it from TPD using PROTACs. Nevertheless, for many proteins the degradation caused by HyT has been shown to be blocked using the proteasome inhibitor MG-132. Extensive attempts were made to demonstrate the prevention of PARP degradation by MG-132, however, no consistent blocking of PARP degradation could be observed. (**Figure 4.13A**). Instead, an inconsistent effect on PARP expression was observed after MG-132 treatment (**Figure 4.13B**). Various incubation times and concentrations were trialled, however, the high toxicity of MG-132 combined with the slow onset of action of **29c** complicated these experiments. Also, MG-132 has been shown to be ineffective for blocking HyT degradation of other proteins in some cell lines.[195] Moreover, these proteasome inhibitor effects are often shown to only partially block HyT-induced protein degradation and/or are assessed

qualitatively.[192, 193, 196] Thus, while involvement of the UPS was not ruled out completely, other degradation routes were also considered.

Activation of autophagy has also been shown for a number of proteins targeted by HyT and its role in the UPR and ER stress has been studied.[197, 198] Autophagy has been indicated as the preferred route of degradation of long-lived proteins (such as PARP-1) and protein aggregates.[199] Indeed, increased expression of autophagy-related genes was confirmed after treatment with **HyTX** in the published PARP study,[189] however, autophagy was not linked directly to PARP degradation. To this end, the autophagy inhibitor bafilomycin-A1 (BafA) was co-incubated with **29c** (**Figure 4.13C**). LC3 expression was used as a marker for autophagy inhibition, which increased considerably after BafA treatment. Interestingly, expression of LC3 was also shown to increase upon treatment of **29c** in cells, even without BafA treatment (**Figure 4.13F**). This represented the first suggestion that **29c** may be inducing autophagy. When comparing **29c**-treated cells ± BafA, a significant increase in PARP expression was observed when autophagy was inhibited (**Figure 4.13D**). Together, these results implicate autophagy in the mechanism of **29c**-induced PARP degradation. It is also noteworthy that, considering the compensatory effect of increased UPS activation to combat decreases in autophagy (and vice versa),[200] proteasome inhibitors including MG-132 have been shown to upregulate autophagy.[199, 201] This indicates that, if autophagy is a major driver of HyT-induced PARP degradation, proteasomal inhibition may paradoxically exacerbate degradation.

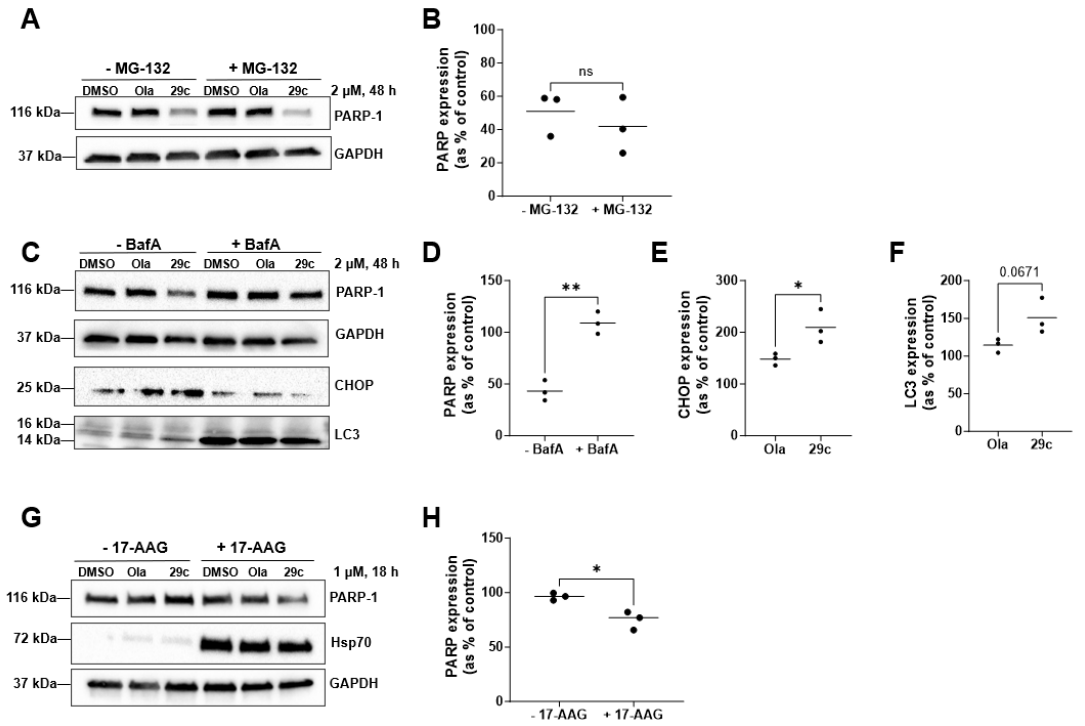

Figure 4.13. Representative Western blots (**A, C, G**) and corresponding quantification (**B, D–F, H**) after treatment of ES-2 cells with DMSO, olaparib (Ola) or **29c**. Cells were pre-treated with **A)** MG-132 (100 nM, 18 h), **C)** BafA (1 µM, 18 h) or **G)** 17-AAG (100 nM, 18 h). PARP expression is expressed as a percentage of olaparib control. CHOP/LC3 expression is expressed as a percentage of DMSO control. (n = 3, unpaired t test, ns not significant $p > 0.05$, * $p < 0.05$, ** $p < 0.01$).

To increase the robustness of these mechanistic findings, other proteins involved in the UPR and ER stress were probed (**Figure 4.8**). CHOP is a key component of the ER stress pathway with a multifaceted role. An increase in CHOP expression was observed after treatment with **29c** (**Figure 4.13E**). Interestingly, BafA decreased CHOP expression, especially in **29c**-treated cells. Before destabilised proteins reach the point of degradation and removal from the cell, chaperone proteins attempt to re-fold proteins or transport them to the ER for repair. A major class of chaperones are the heat-shock proteins (Hsp), e.g., Hsp40, Hsp70 and Hsp90. Interactions of the Hsp proteins are complex and intertwined, however, it is understood that inhibition of Hsp90 activates Hsp70.[202] The Hsp70 inhibitor 17-AAG has previously been used to augment HyT-mediated degradation of Src-1.[192] At shorter incubation times at low drug concentrations (1 µM, 18 h), PARP was not shown to be significantly degraded (**Figure 4.13G**). However, addition of 17-AAG significantly decreased PARP levels, promoting degradation at this lower incubation concentration/timepoint (**Figure 4.13H**). This indicates that that Hsp70 promotes PARP degradation.

4.4 Changes in gene expression

Although involvement of the UPR appeared likely and blocking autophagy prevented PARP degradation, since many intermediate pathways (**Figure 4.8**) may have been activated, it was important to further investigate the process. Using RT-qPCR, the effects of **29c** were studied at the genetic level (**Figure 4.14**). First, genes involved in autophagy were studied. Mirroring the increase of LC3 at the protein level, **29c** was shown to increase expression of *LC3A* and *LC3B*. A large increase in the expression of *SQSTM1* (which encodes for the p62 protein) was also observed. p62 has a multifaced role in the cell but is known to be a key component of the autophagy pathway which recognises toxic cellular waste (such as a misfolded protein) for removal.[203] A number of UPR/ER stress-related genes were probed for and most (*ATF4*, *DDIT3*, *DNAJB9*, *HSP90B1*, *XBP1s*) were shown to have increased with **29c** treatment. The large increase in *DDIT3* gene expression (which encodes for CHOP) correlates well with its increased expression on Western blot (**Figure 4.13E**). *EDEM1* and *HSPA5* (*BiP*/*GRP78*) did not show significant increases with **29c** treatment. *EDEM1* has been linked to proteasome-specific ER-associated protein degradation (ERAD) mechanisms so may not be as important in autophagy-based degradation.[204] *HSPA5* is involved primarily in the early stages of the UPR (**Figure 4.8**), thus its unaffected expression may suggest the progression to later stages in the pathway. These analyses suggested **29c** exhibited a marked effect on whole cell processes.

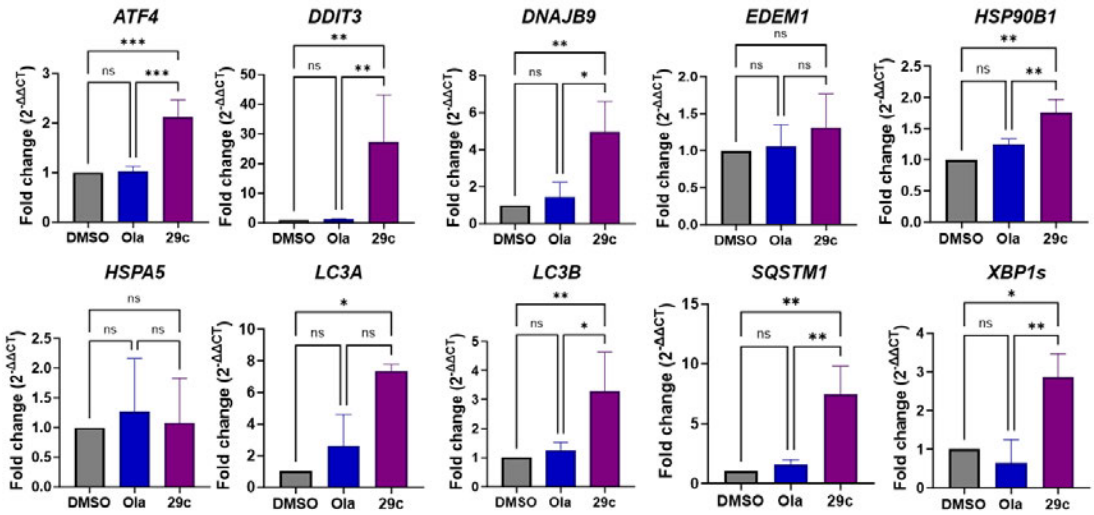

Figure 4.14. qPCR data of the indicated genes after treatment with DMSO, olaparib (ola) or **29c** at 2.5 μM for 48 h. Fold change in expression vs *GAPDH* control is shown. Error bars report the standard deviation of the mean from three independent experiments. (n=3, one-way ANOVA, ns not significant $p > 0.05$, * $p < 0.05$ ** $p < 0.01$ *** $p < 0.001$)

4.5 Monitoring DNA damage

Considering the evidence gathered hitherto that HyT activates a number of new pathways in cells, it was unclear how this affected the usual mechanism of action of olaparib. It was hypothesised that the new effects of tagging olaparib may a) prevent the normal PARP inhibitor action of olaparib due to sequestration into other cellular compartments, or b) augment the inhibitor effects due to additional degradation (and thus removal) of PARP from the cell. ES-2 cells were engineered to express a fluorescent reporter for DNA damage (**Figure 4.15A**), enabling an indirect phenotypic readout of PARP inhibition. Stable expression of the mApple fluorescent protein fused to 53BP1, a crucial component of DSB repair,[205, 206] was achieved in ES-2 cells by Dr Amy Davies. Use of this reporter obviated the need for fluorescent staining, thus allowing live cell imaging. The 53BP1-mApple reporter localises to sites of DSB on DNA and was initially validated against H2AX, an essential protein in DNA repair (**Figure 4.15B**). Using a confocal microscope at high magnification, delineation of individual 53BP1-mApple foci was possible, which colocalised well with the immunofluorescence signal from the γ-H2AX antibody. Counting the number of 53BP1-mApple foci thus enabled quantitative assessment of the extent of DNA damage. To increase the efficiency of these measurements, a high content imaging system was used, which allowed rapid screening and analysis using live cells. As shown in **Figure 4.15C**, the nuclear signal from DAPI was used to segment nuclei. A machine learning-based method was then used to identify foci within each nucleus, which could be quantified to give a readout of DNA damage.

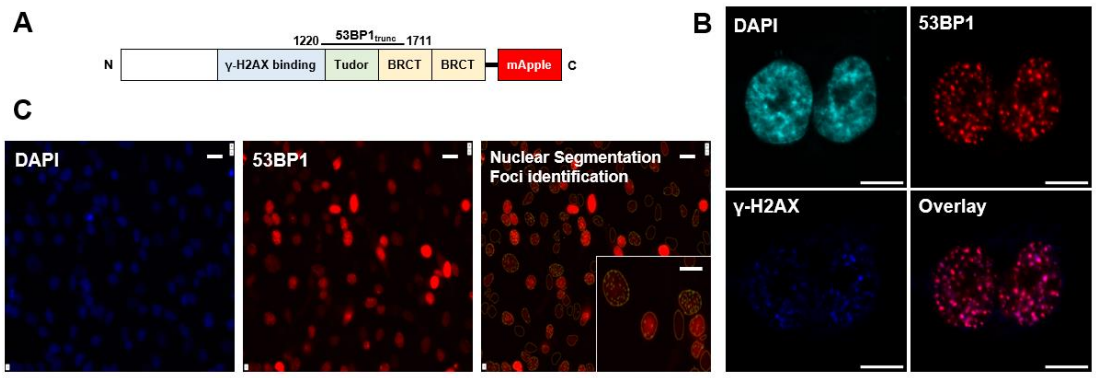

Figure 4.15. DNA damage imaging. **A)** 53BP1-mApple construct was expressed in the ES-2 cells (Dr Amy Davies). **B)** Representative image showing staining of the nucleus with DAPI (cyan), 53BP1 DNA damage foci (red) and colocalisation with γ-H2AX immunofluorescence signal (blue), scale bars 10 µm. **C)** Representative images showing segmentation and detection of DNA damage foci using ImageXpress imaging platform, scale bars 25 µm.

The DNA damage assay was designed to mimic the incubation conditions shown to cause PARP degradation, to determine whether these pathways may be linked. First, olaparib was incubated in cells at concentrations up to 1 μM (**Figure 4.16**). Since only a small increase in DNA damage foci was observed, higher concentrations up to 10 μM were used. The possible negative effect on viability were counteracted using higher cell densities in these assays to give a more reliable DNA damage readout. A dose-response relationship was thus obtained and the higher drug concentrations reduced the total cell number, presumably through DNA damage-induced cell death.

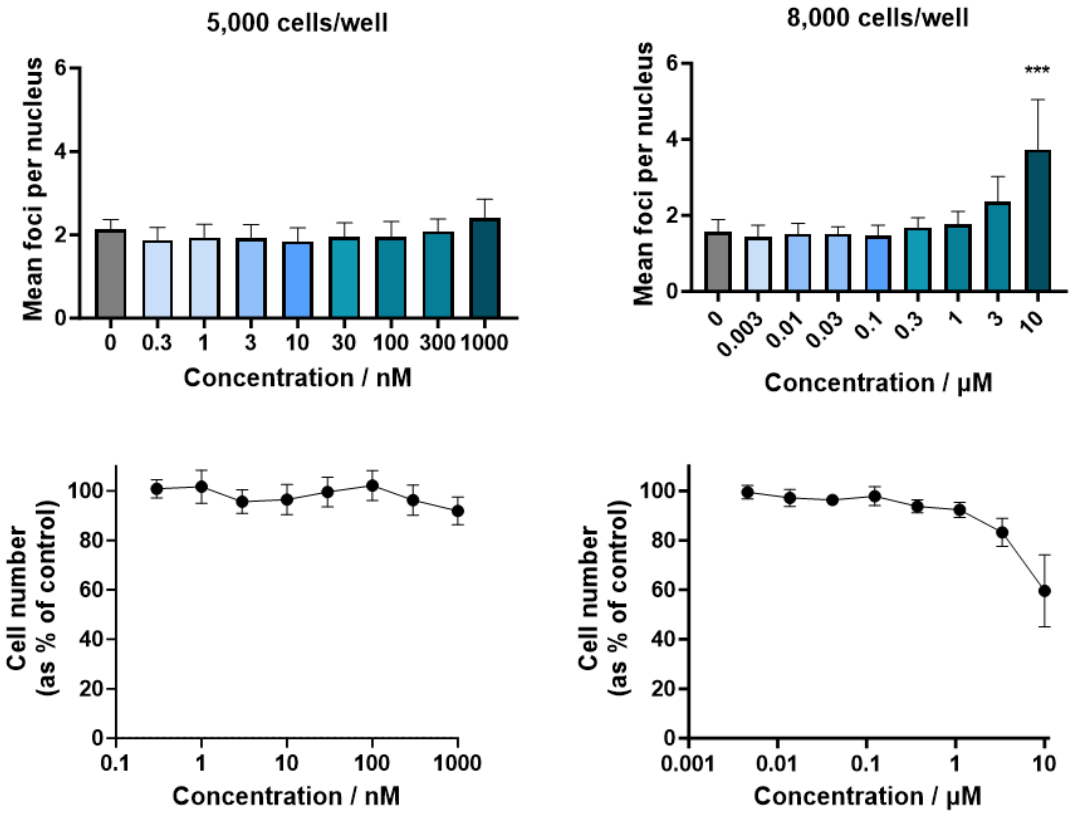

Figure 4.16. DNA damage analysis of olaparib-treated ES-2 cells at the indicated cell densities. Bar charts report the quantification of DNA damage foci and line graphs measure the corresponding number of cells at each drug concentration, expressed as a percentage of DMSO-treated cells. Error bars report the standard deviation of the mean from three independent experiments. (n=3, one-way ANOVA vs DMSO, *** $p < 0.001$).

Due to the relative ease of high throughput imaging, all of the olaparib-tag analogues could be analysed without relying on the use of only **29c** as a representative compound (**Figure 4.17**). It was clear that each compound (excluding **1a**, used as a negative control) increased the number of foci to some degree. Interestingly **29a**–**29c** once again emerged as more potent than **26a**–**26c**, both in terms of increased foci

number and decreased cell number. Treatment with **29c** resulted in the greatest number of foci, with significant increases vs DMSO from 30 nM. These results are strikingly different from olaparib (**Figure 4.16**), which only induced a significant increase in foci at 10 µM.

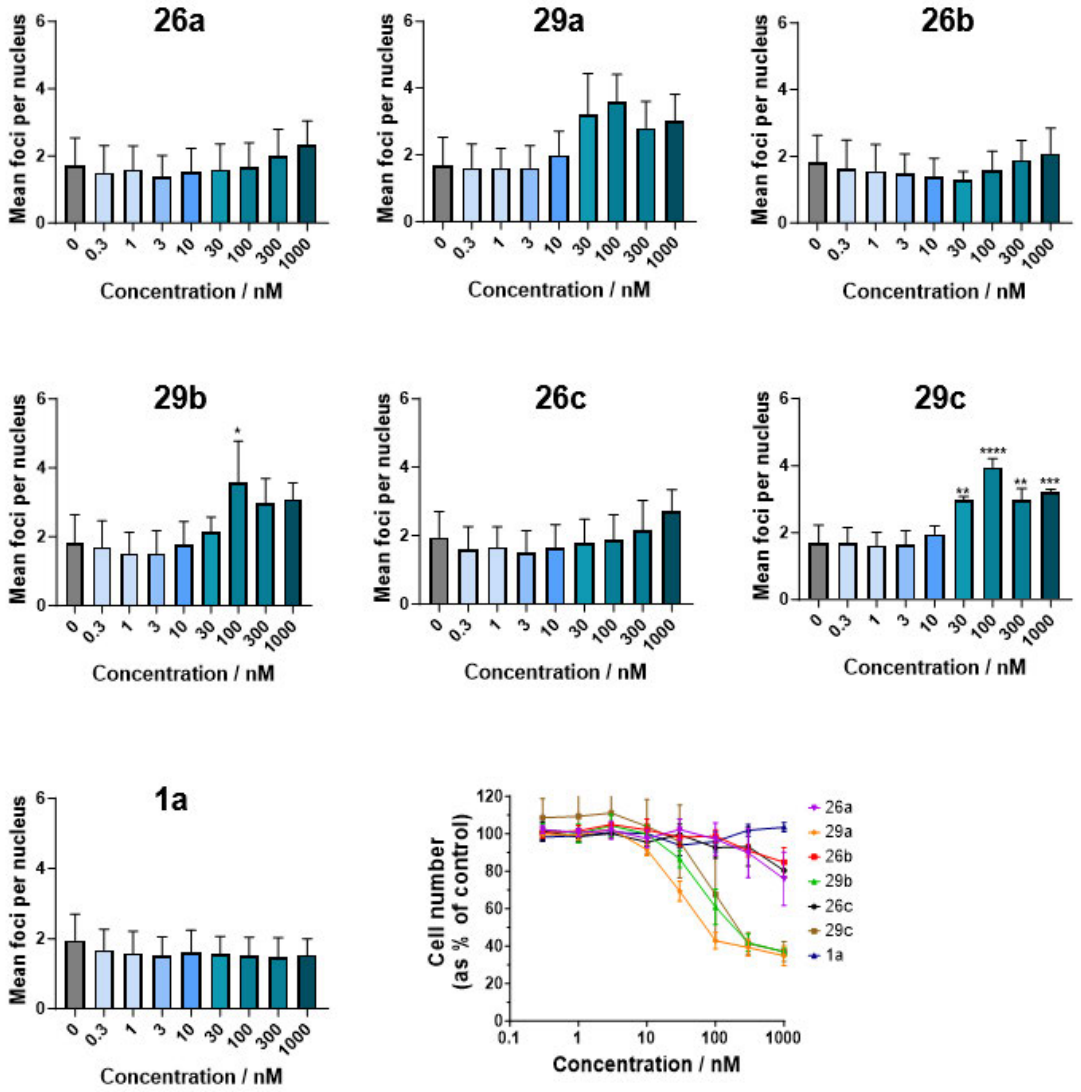

Figure 4.17. DNA damage analysis of drug-treated ES-2 cells (5,000 cells/well). Bar charts report the quantification of DNA damage foci and line graphs measure the corresponding number of cells at each drug concentration, expressed as a percentage of DMSO-treated cells. Error bars report the standard deviation of the mean from three independent experiments. (n=3, one-way ANOVA vs DMSO, * $p < 0.05$, ** $p < 0.01$, *** $p < 0.001$, **** $p < 0.0001$).

At higher compound concentrations, **29a**–**29c** still stood out as being more effective at increasing foci number (**Figure 4.18**). However, increased cell death occurred at the higher concentrations of all compounds, indicated by the reduction in cell number.

The DNA damage readout at these high concentrations, where the number of live cells is greatly reduced, is likely unreliable and may explain the drop-off in foci number. This additional loss of cell viability is likely due to additional cytotoxic effects of the compounds, rather than DNA damage-associated cell death. This is especially clear considering for some compounds e.g., **26a**–**26c**, no significant upward trend in foci was observed with increasing concentration.

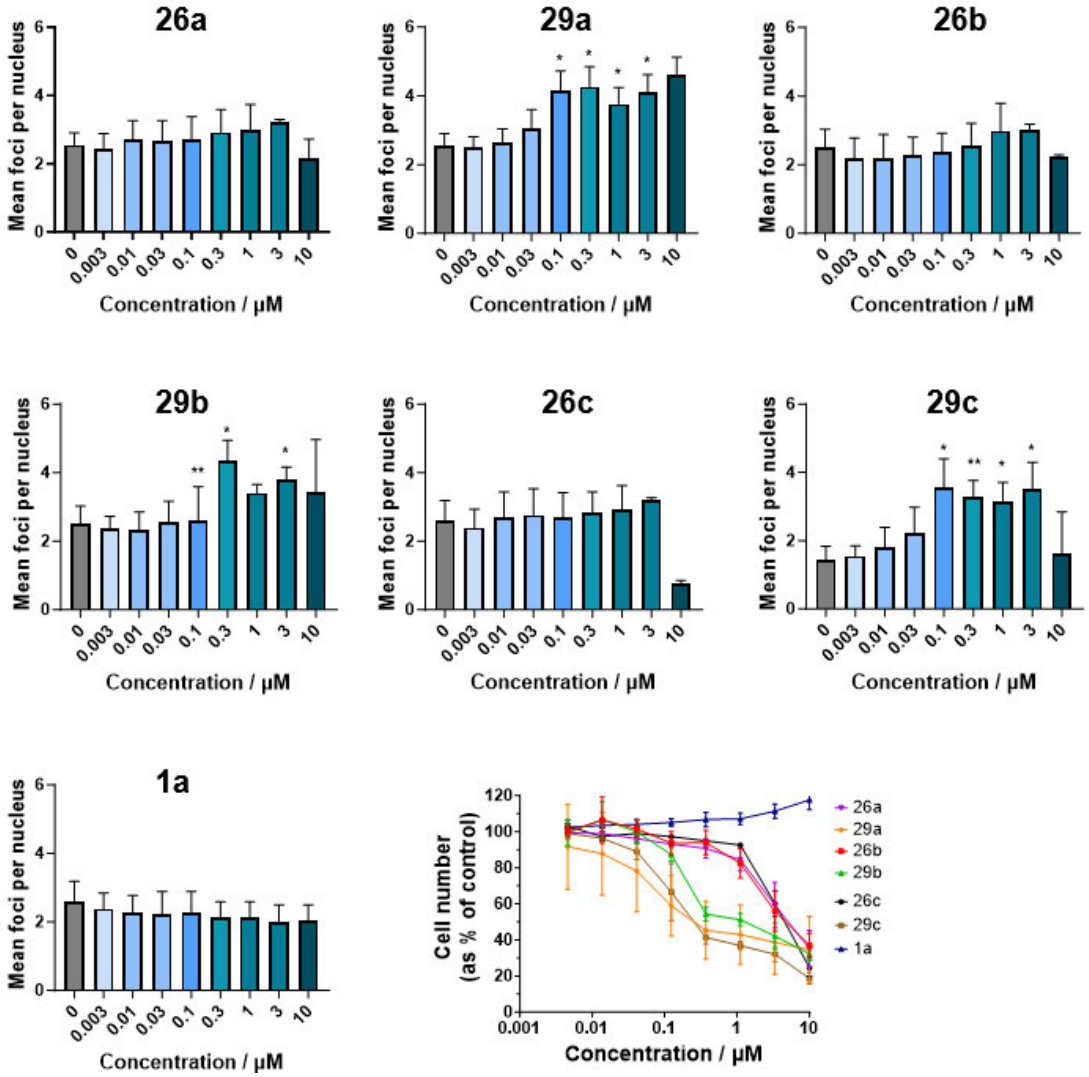

Figure 4.18. DNA damage analysis of drug-treated ES-2 cells (8,000 cells/well). Bar charts report the quantification of DNA damage foci and line graphs measure the corresponding number of cells at each drug concentration, expressed as a percentage of DMSO-treated cells. Error bars report the standard deviation of the mean from three independent experiments. (n=3, one-way ANOVA vs DMSO, * $p < 0.05$, ** $p < 0.01$)

In order to compare easily between the different compounds, the foci readout (as fold-change vs DMSO) for each compound at a fixed concentration of 100 nM is shown

(**Figure 4.19**). The lower cell density experiment shows clearly **29a**–**29c** as prominent compounds, each increasing the foci number by more than double vs DMSO. These three compounds were also the most potent in the higher cell density experiment, albeit with **29b** not showing a statistically significant increase in foci number at this concentration. **29c** consistently gave the most significant increase in foci number.

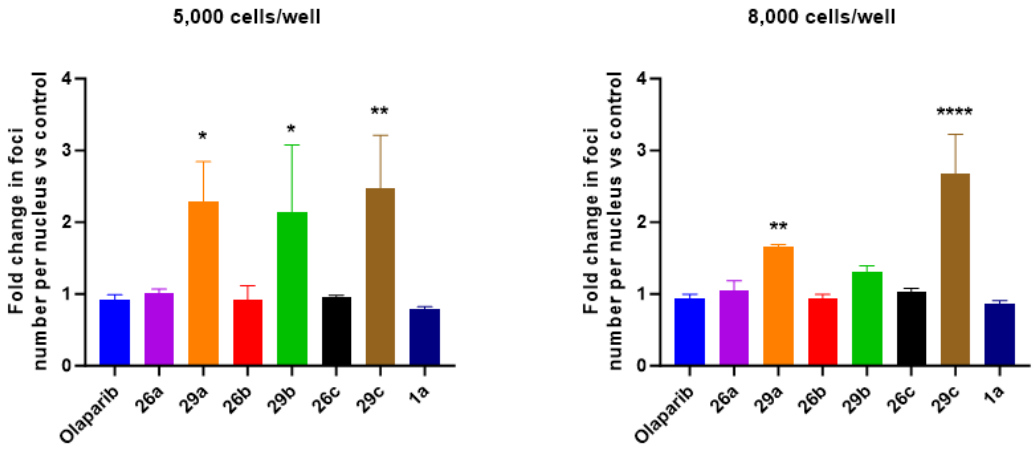

Figure 4.19. Summary of DNA damage foci quantification at 100 nM at the indicated cell densities. Error bars report the standard deviation of the mean from three independent experiments. (n=3, one-way ANOVA vs olaparib, * $p < 0.05$, ** $p < 0.01$, **** $p < 0.0001$).

Together, these data suggest the olaparib-tag compounds **29a**–**29c**, allow the accumulation of more DNA damage than olaparib. It may be important to repeat the DNA damage experiment over long incubation periods to determine whether this increased potency still holds true or whether the olaparib-tag compounds simply have a faster onset of action than olaparib. The latter argument may be rationalised by hypothesising the ability of the analogues to destabilise and remove PARP from the cell has a greater and faster effect on the build-up of DNA damage than PARP inhibition alone. Although previously reported changes in DNA damage associated with reduction in PARP expression have been shown to be variable (i.e., both increases and decreases in DNA damage foci have been observed dependent on the study), both PROTAC-mediated degradation and knockout of PARP-1 induced increases in H2AX foci.[185, 207]

4.6 Proteomics

In cases such as this study when new, unexpected pathways are activated upon drug incubation, it is useful to take a broad approach for deeper understanding. Proteomics allows a wealth of information to obtained from drug-treated cells using mass

spectrometry (MS) analysis. Furthermore, combining immunoprecipitation (IP, selective protein isolation from a cell lysate) with proteomics analysis can allow detection of protein binding partners. IP-MS was conducted in this study to clarify any additional binding partners of PARP which may help to explain the mechanisms of **29c** mediated PARP degradation. This study was also considered particularly useful for the detection of chaperone proteins which may be involved in the UPR process (**Figure 4.8**). Proteomics has seen limited use within the HyT field and has never been utilised for detection of binding partners until now.[193, 196]

4.6.1 Immunoprecipitation of PARP

Before carrying out immunoprecipitation-mass spectrometry (IP-MS) experiments, validation of the IP of PARP was first carried out by Western blot analysis (**Figure 4.20**).

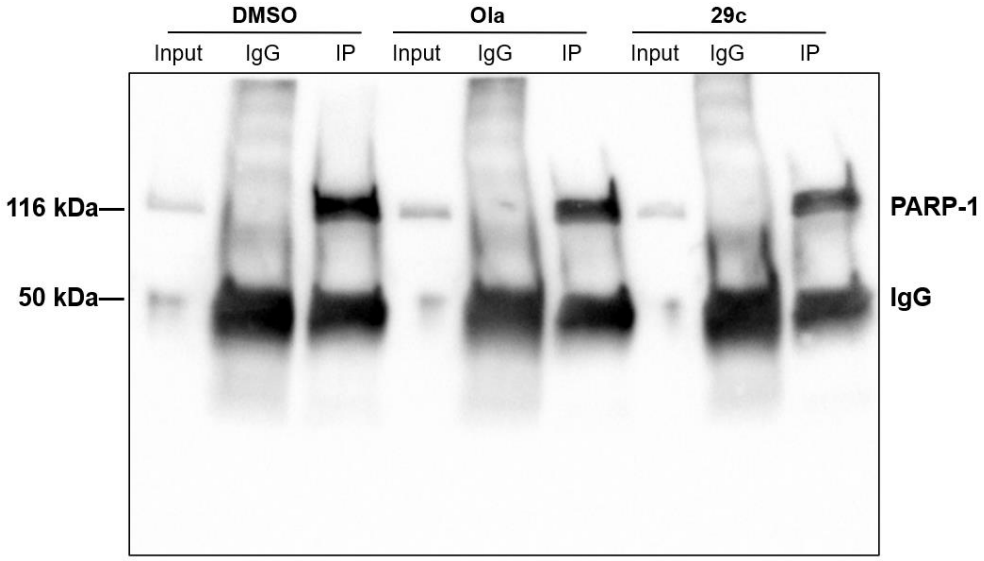

Figure 4.20. Representative Western blot after drug treatment (2.5 µM, 48 h) probing for PARP-1. Input lanes represent whole cell lysates, IgG lanes represent samples immunoprecipitated with an IgG control antibody and IP lanes represent samples immunoprecipitated with a PARP-1 antibody.

PARP-1 was successfully and cleanly immunoprecipitated from the cell lysate, showing 1 clear band from PARP-1 and detection of the IgG heavy chain (**Figure 4.20**). Importantly, no PARP-1 band was detected in the IgG lane, confirming no non-specific binding of PARP-1 to the IgG antibody.

Before assessing new binding partners related to the UPR following treatment with **29c**, the proteins identified from the PARP-1 IP were compared to the IgG control for DMSO-treated cells (**Figure 4.21A**). Significance and fold change (FC) cut-off values were determined as p = 0.05 and 1.5, respectively, based on the sample size and distribution of proteins.[208] Among the 544 significantly enriched proteins, PARP-1 was detected ($\log_2$(FC) = 4.36, $\log_{10}(p)$ = 4.42), confirming successful pulldown of the protein. As further validation, several key members of the PARP-1 interactome were identified,[209, 210] including those participating in each step of DSB repair (**Figure 4.21B** and **C**), as discussed in **Section 3.1.2**. All members of the MRN complex, which plays an essential role in HR and Alt-EJ, were identified (MRE11, RAD50, NBN). DNA repair proteins XRCC5 and PRKDC were detected which are needed for NHEJ with PARP. Finally, XRCC1, LIG3 and POLB, which constitute the main components of the complex responsible for Alt-EJ-mediated DNA repair were all identified. H2AX was also identified, which is required for the assembly of these DNA repair proteins at sites of damaged DNA, and was used in **Section 4.5** as marker for DNA damage.

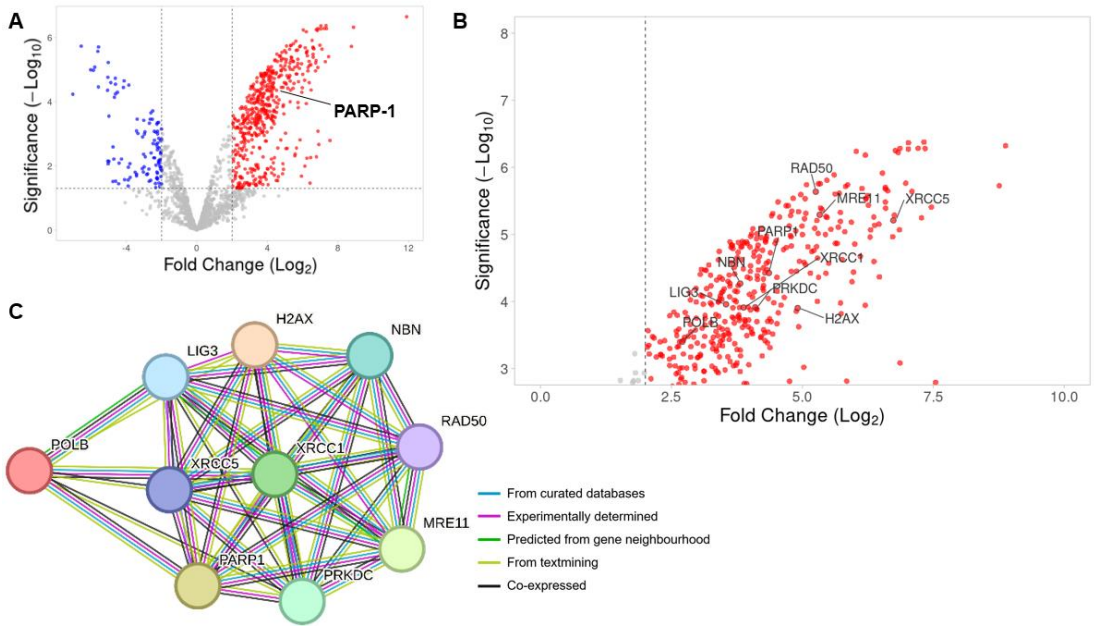

Figure 4.21. **A)** Volcano plot of differentially expressed proteins between ES-2 cells immunoprecipitated with PARP-1 antibody vs IgG isotype control antibody (red = increased in PARP-1 IP, blue = increased in IgG). Horizontal and vertical dashed lines indicate significance (p = 0.05) and fold change (1.5) cut-off values, respectively. **B)** Magnification of **A** with detected proteins in the PARP-1 interactome labelled. **C)** Network of significantly enriched PARP-1 interactome proteins, using PARP-1 as the seed protein.[209, 210] Visualised using STRING with 90% interaction confidence setting.[211]

Turning to the effects of **29c** treatment on the PARP-1 interactome, several new proteins were identified. Considerably more significantly differentially expressed proteins (100) were identified after **29c** treatment, compared to olaparib-treated cells (52), with only a small overlap (11), indicating possible new interactions (**Figure 4.22**).

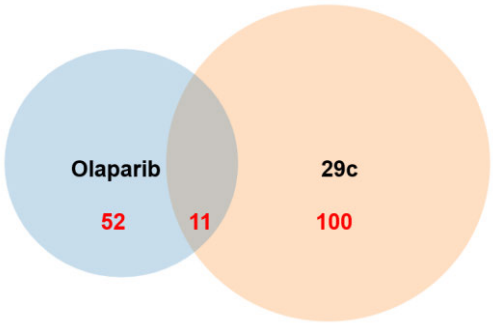

Figure 4.22. Venn diagram of the number of differentially expressed proteins ($p < 0.05$) from IP-MS data of olaparib or **29c**-treated cells. Protein count is indicated in red.

Data acquired from **29c**-treated cells was compared to olaparib-treated cells to examine only new hits related to HyT, rather than effects of PARP inhibition (**Figure 4.23**). STRING analysis was performed to identify clusters of related proteins which may indicate new mechanisms or pathways activated by **29c** treatment (**Figure 4.24**).

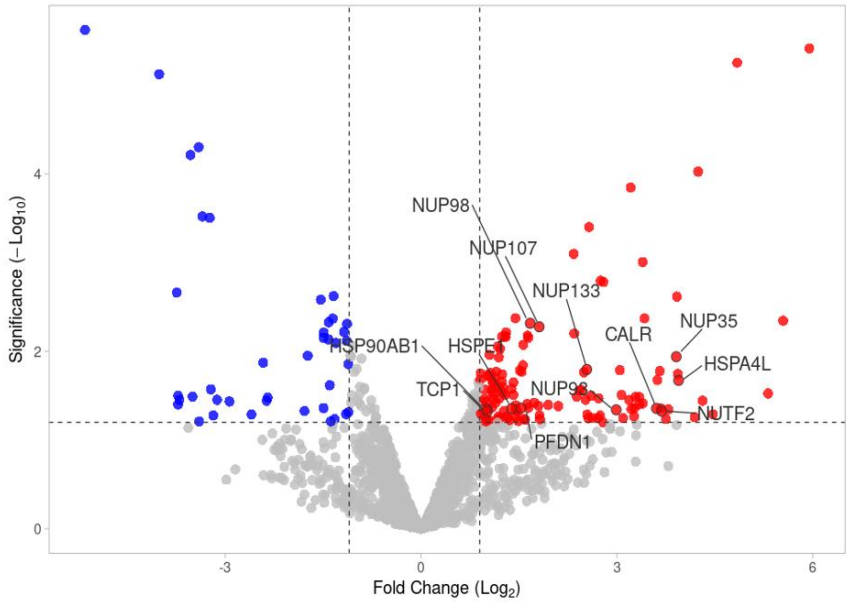

Figure 4.23. Plot of differentially expressed proteins between **29c** and olaparib-treated cells as identified by IP-MS analysis (red = increased in **29c** treated cells, blue = decreased in **29c** treated cells). Horizontal and vertical dashed lines indicate significance ($p = 0.05$) and fold change (1.5) cut-off values, respectively. Significantly enriched proteins of interest are labelled.

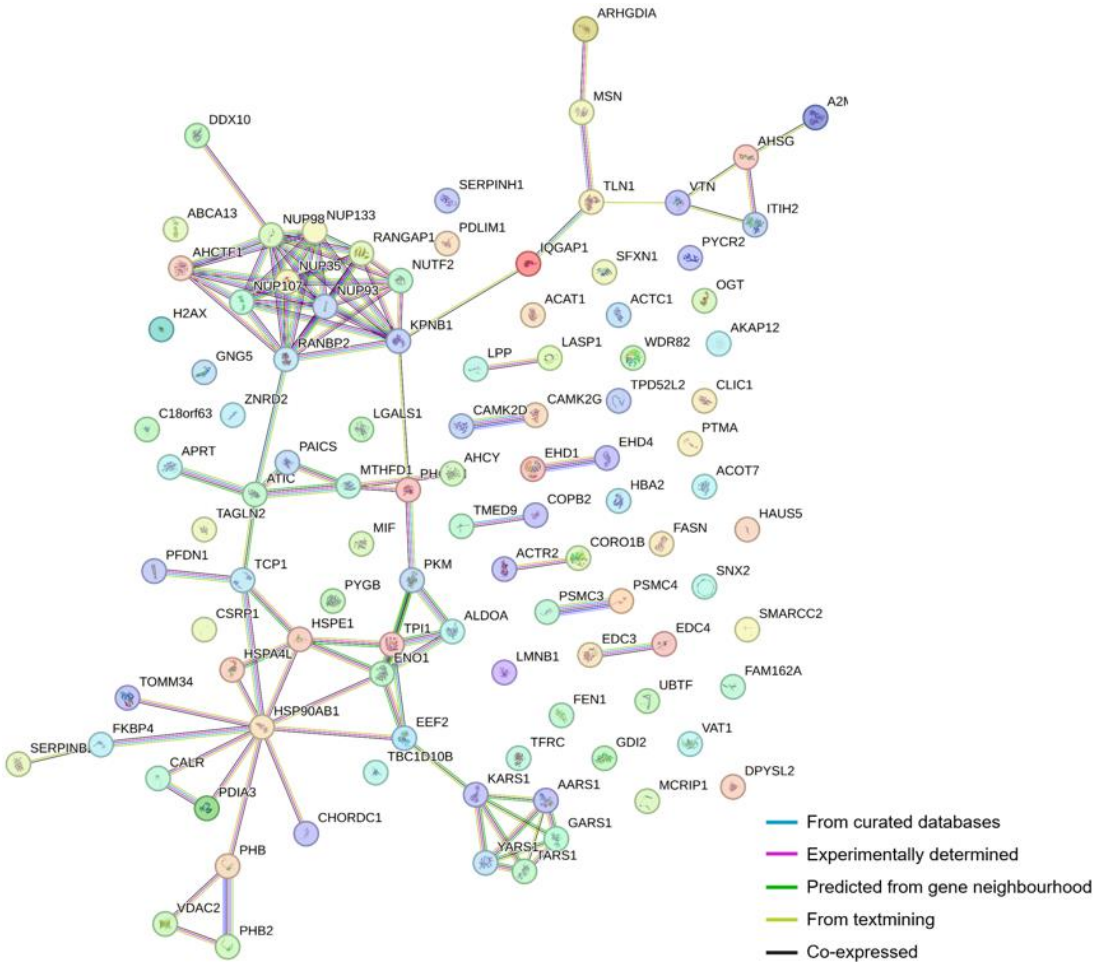

Figure 4.24. Networks of significantly enriched proteins from analysis shown in **Figure 4.23** (after **29c** vs olaparib treatment) visualised using STRING with 90% interaction confidence setting.[211]

Interestingly, several groups of proteins were identified as having significantly higher enrichment in **29c**-treated cells (**Figure 4.25A**). The first comprised NUP98, NUP107, NUP35, NUP93, NUP133, AHCTF1, RANGAP1, RANBP2, KPNB1 and NUTF2, which are all components of the nuclear pore complex. The presence of these proteins was not expected but it may be postulated that this is indictive of the nuclear-cytoplasmic transport of PARP-1. A recent study revealed important new information on the fate of misfolded nuclear proteins, identifying a spatial relationship between the cytosolic juxtanuclear quality control (JUNQ) and intranuclear quality control (INQ) compartments.[212] Upon protein misfolding, the INQ and JUNQ flank either side of the nuclear membrane, connected by nuclear pores, to remove the INQ from the nucleus. Thus, if the UPR is activated by PARP-1 HyT, PARP-1 may be exported from the nucleus through the nuclear pore complex via this mechanism. Unfortunately, attempts to validate this idea with immunofluorescence imaging were unsuccessful

and only nuclear PARP was detected. However, considering the PARP-1 antibody used in **Section 4.3** detected intact PARP only (since a loss of signal was observed indicating degradation) this may not be the optimal method for tracking the dynamics of PARP destabilisation/misfolding. It may be useful to generate a fluorophore-fused PARP-1 variant to allow live cell tracking in the future. The idea of cytosolic PARP localisation does, however, correlate with the observed cytosolic drug distribution discussed in **Section 3.6.1**.

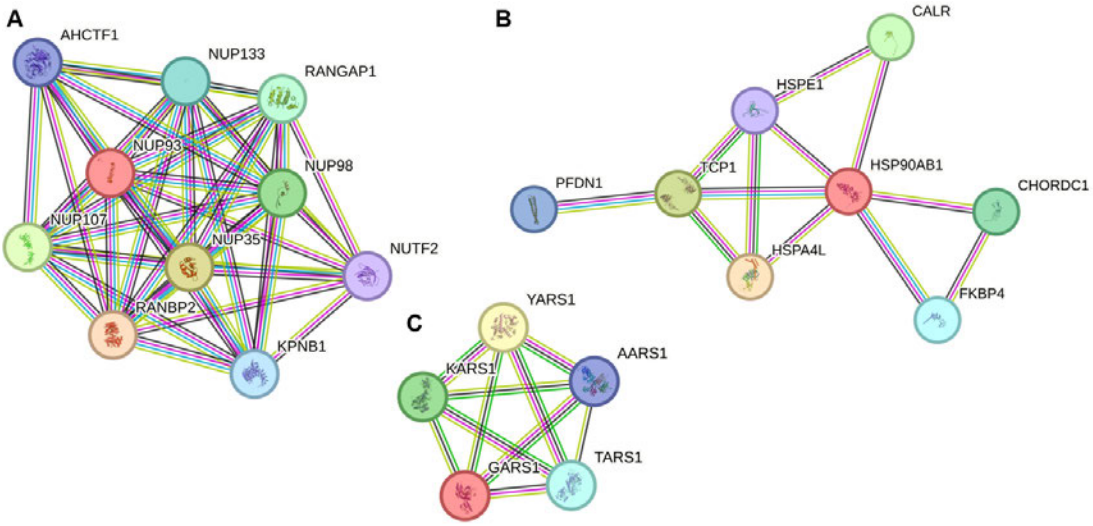

Figure 4.25. Isolated protein networks from **Figure 4.24** identified from STRING analysis. **A)** Nuclear pore-associated proteins, **B)** proteins involved in the UPR and chaperoning and **C)** tRNA ligases.

Gratifyingly, the second group of proteins identified (**Figure 4.25B**) were all directly related to the UPR and ER stress (HSPA4L, HSP90AB1, HSPE1, CALR, TCP1, PFDN1, FKBP4, CHORDC1). The Hsp proteins have previously been discussed as an important class of chaperone proteins indicated in HyT and the UPR. Moreover, HSPA4L is a Hsp70 protein which was shown to affect PARP degradation in **Section 4.3** and HSP90AB1 is a Hsp90 protein, closely related to HSP90B1 which was shown in **Section 4.4** to be genetically upregulated. TCP1 and PFDN1 are both chaperone proteins known to work together in response to misfolding events in the UPR.[213] Finally, an increase in calreticulin (CALR) was observed. Calreticulin is an ER-resident protein known to prevent and rectify misfolding of proteins.[214] Interestingly, a recent study linked calreticulin, ER-stress and autophagy, determining that calreticulin overexpression stimulated the formation of autophagosomes to relieve drug-induced ER stress.[215] More specifically, calreticulin was shown to supress ER stress through complexation (and thus upregulation) of LC3, which was previously identified as an

upregulated gene after **29c** treatment (**Section 4.4**). It is also interesting that these chaperone proteins are generally associated with activity in the cytoplasm, which may complement the suggestion that PARP is undergoing translocation between organelles. The third and final group of proteins identified (**Figure 4.25C**, YARS1, KARS1, AARS1, GARS1, TARS1) consisted of tRNA ligase proteins. There is no clear link of these proteins to HyT-mediated PARP degradation, and further studies would be needed to investigate this further.

Regarding proteins that were found to have decreased in **29c**-treated cells vs olaparib-treated cells, a cluster of transcription-related proteins, including RNA polymerase complex members, were identified (**Figure 4.26**). Whilst this needs further investigation, negative regulation of transcription is a consequence of the UPR (**Figure 4.8**) and may have been induced by **29c** treatment.

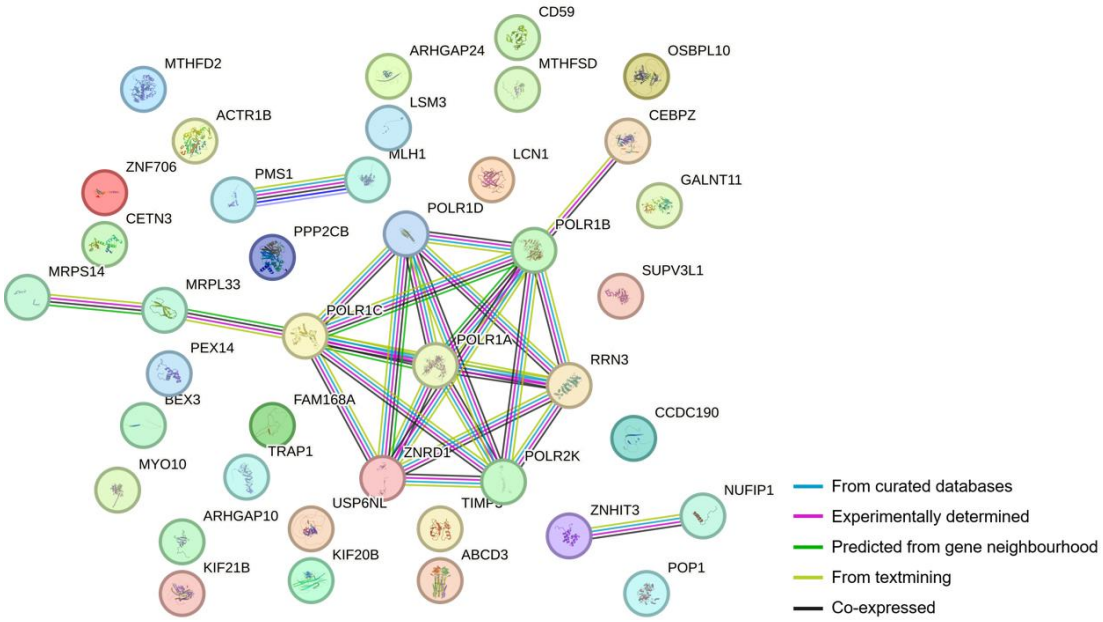

Figure 4.26. Networks of significantly underexpressed proteins from analysis shown in **Figure 4.23** (after **29c** vs olaparib treatment) visualised using STRING with 90% interaction confidence setting.[211]

The IP-MS experiments detailed were useful in understanding the proteins involved in **29c**-mediated PARP degradation by providing further evidence of UPR involvement and new information on possible nuclear export. However, in order to further clarify the broader cellular effects of **29c** treatment, whole cell proteomics experiments were carried out.

4.6.2 Whole cell proteomics

Cell lysates that were submitted for whole cell proteomics analysis by MS were first validated to confirm degradation of PARP. **Figure 4.27 A** and **B** shows the significant decrease in PARP expression with **29c** across the 3 biological repeats. After processing the raw MS data and identifying significantly under- and overexpressed proteins, PARP-1 was not identified. However, a significant reduction in the levels of PARP-1 protein detected in cells treated with **29c** (5 µM) was observed from the raw MS data (**Figure 4.27 C**), thus these samples were used for the proteomics analyses.

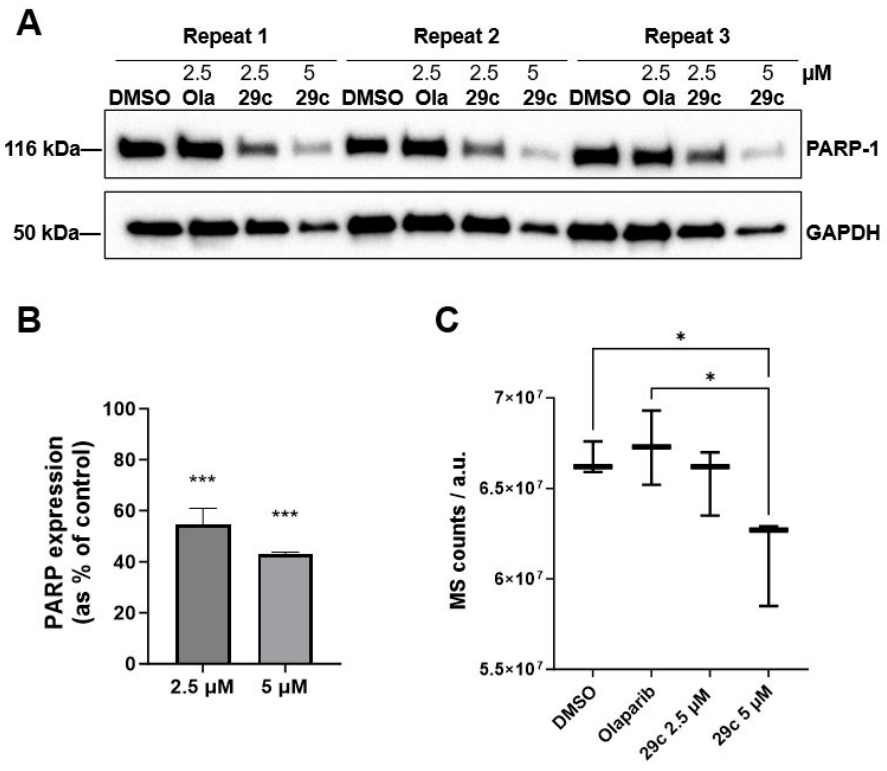

Figure 4.27. Validation of PARP degradation for whole cell proteomics analysis. **A)** Western blot and **B)** corresponding quantification of ES-2 cells treated with the indicated compound for 48 h, PARP expression is expressed as a percentage of olaparib control, (n = 3, unpaired t test vs DMSO, *** $p < 0.001$) **C)** Quantification of PARP protein counts from raw MS data, (n = 3, one-way ANOVA, * $p < 0.05$). For both **B** and **C**, error bars report the standard deviation of the mean from three independent experiments.

A much greater number of significantly differentially expressed proteins was identified for **29c**-treated cells than olaparib-treated cells, even more so than in the IP-MS experiment (**Figure 4.28**).

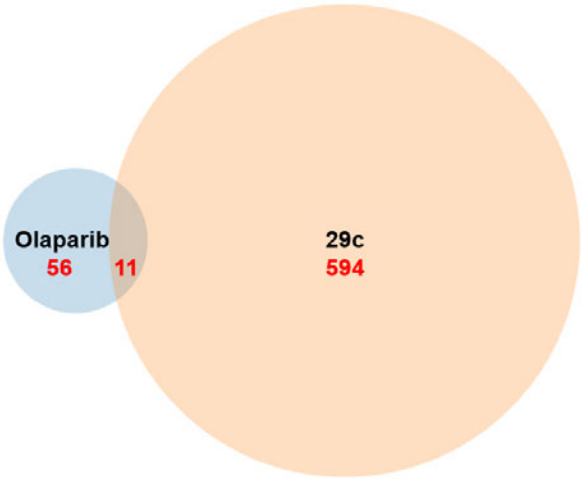

Figure 4.28. Venn diagram of the number of differentially expressed proteins ($p < 0.05$) from whole cell proteomics data of olaparib or **29c**-treated cells. Protein count is indicated in red.

Figure 4.29 illustrates the differentially expressed proteins after **29c** treatment vs olaparib from whole proteome analysis. A large increase in the expression of DDIT3, DNAJC25, SQSTM1 and XBP1 was evident from the volcano plot. ER stress protein DDIT3, also known as CHOP, has been discussed and was identified in Western blot and PCR experiments (**Section 4.3**–**4.4**). Likewise, both SQSTM1 (p62), which is an autophagy protein, and XBP1, a major regulator of the UPR, were identified as highly upregulated by PCR. Finally, although not specifically probed for until now, DNAJC25 is a Hsp40 protein and known ER chaperone.[216] Together, these results further validate the evidence for HyT-mediated activation of the UPR and autophagy. Next, a collection of proteins involved in DNA damage (BRCA2, EXO1, MUTYH, SPIDR, TRIP12, ZRANB3) were identified as underexpressed in **29c**-treated cells. This may suggest that HyT of PARP by **29c** has a significant impact on DNA repair pathways, which is consistent with increased DNA damage foci measured in **Section 4.5**. Interestingly, a loss of TRIP12 was recently shown to sensitise cancer cells to PARPi by increasing PARP-1 trapping.[217]

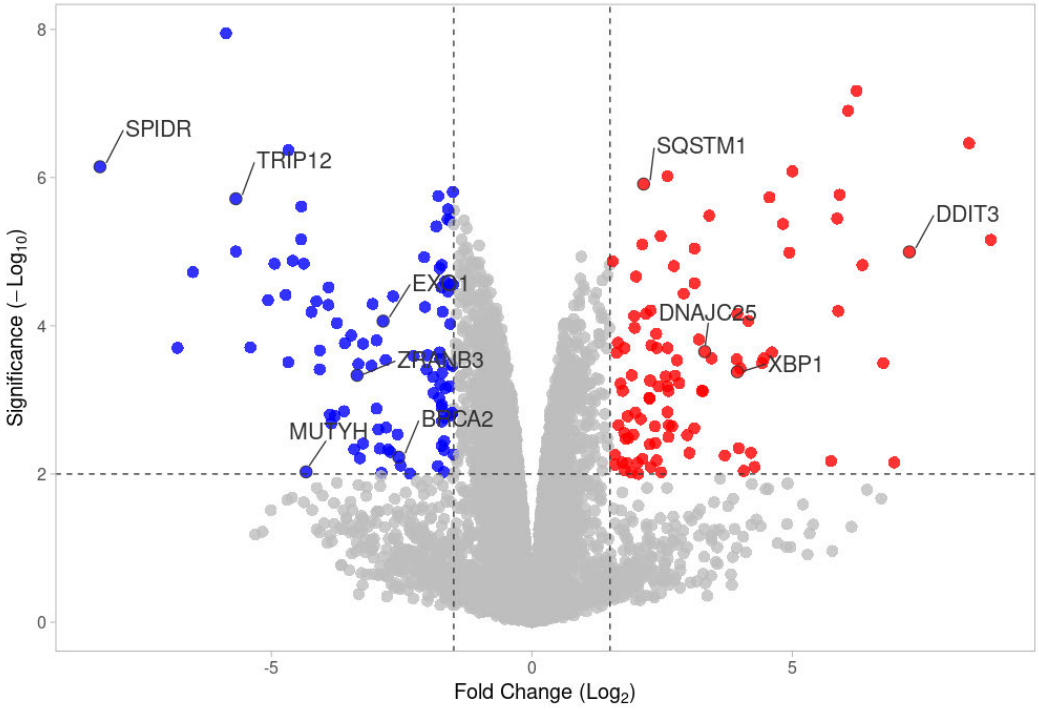

Figure 4.29. Plot of differentially expressed proteins between **29c** and olaparib-treated (5 μM, 48 h) cells as identified by whole cell proteomics analysis (red = increased expression in **29c** treated cells, blue = decreased expression in **29c** treated cells). Horizontal and vertical dashed lines indicate significance (p = 0.01) and fold change (2) cut-off values, respectively. Significantly enriched/depleted proteins of interest are labelled.

4.6.3 Gene set enrichment analysis (GSEA)

In order to associate the under- and over-expressed proteins identified by whole cell proteomics analysis with changes in phenotype, GSEA was performed. As per **Section 4.6.2**, **29c**-treated cells were compared to olaparib-treated cells and Hallmark and Gene Ontology gene sets were used. First, gene sets that were significantly upregulated in **29c**-treated cells were identified (**Figure 4.30**). False discovery rate (FDR) and normalised enrichment scores (NES) were used to rank the results.

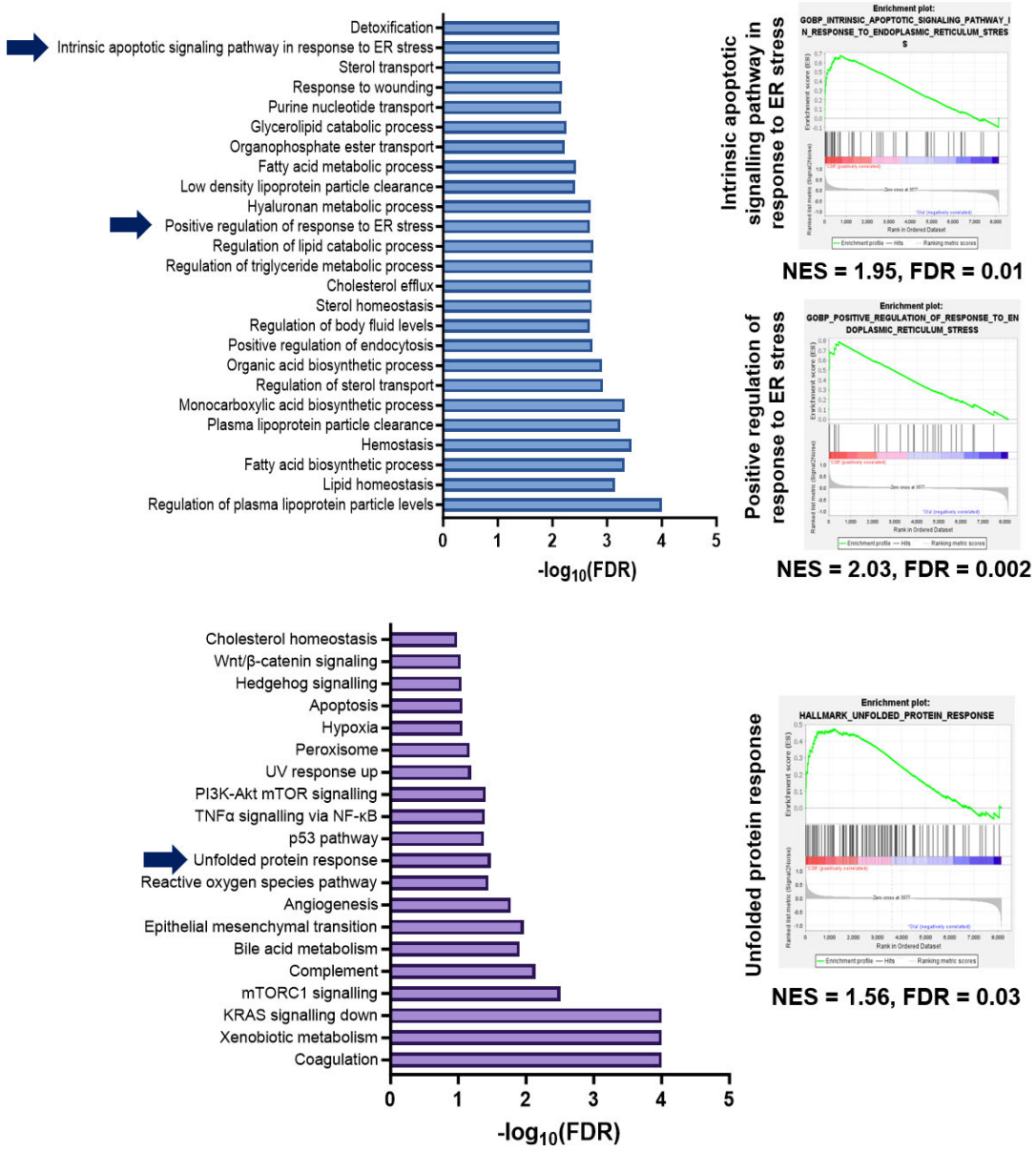

Figure 4.30. GSEA performed on proteomics data from **29c**-treated cells vs olaparib-treated cells (5 µM, 48 h), highlighting gene sets significantly upregulated ($-\log_{10}$(FDR) > 1 and NES > 1). **Left**: upregulated gene sets (**top** = Gene Ontology: Biological Processes set, **bottom** = Hallmark set) and **Right**: corresponding GSEA enrichment plots for gene sets indicated with dark blue arrows.

Examining upregulated genes from the Gene Ontology: Biological Processes gene set, two gene sets related to ER stress were identified and their enrichment plots were generated (**Figure 4.30**, top). Interestingly, apoptotic signalling genes were detected which may link HyT-induced ER stress to the increased cell death caused by **29c** (**Section 4.2**). Several gene sets related to lipids and lipoproteins were identified. Whilst Raman tagging increases the lipophilicity of olaparib, it is not clear if this is

significant enough to induce large changes in overall lipid homeostasis. However, lipid synthesis and metabolism has recently been linked to ER stress,[218] including through the synthesis of lipid droplets to sequester misfolded proteins.[219] For upregulated Hallmark gene sets (**Figure 4.30**, bottom), the UPR was again indicated.

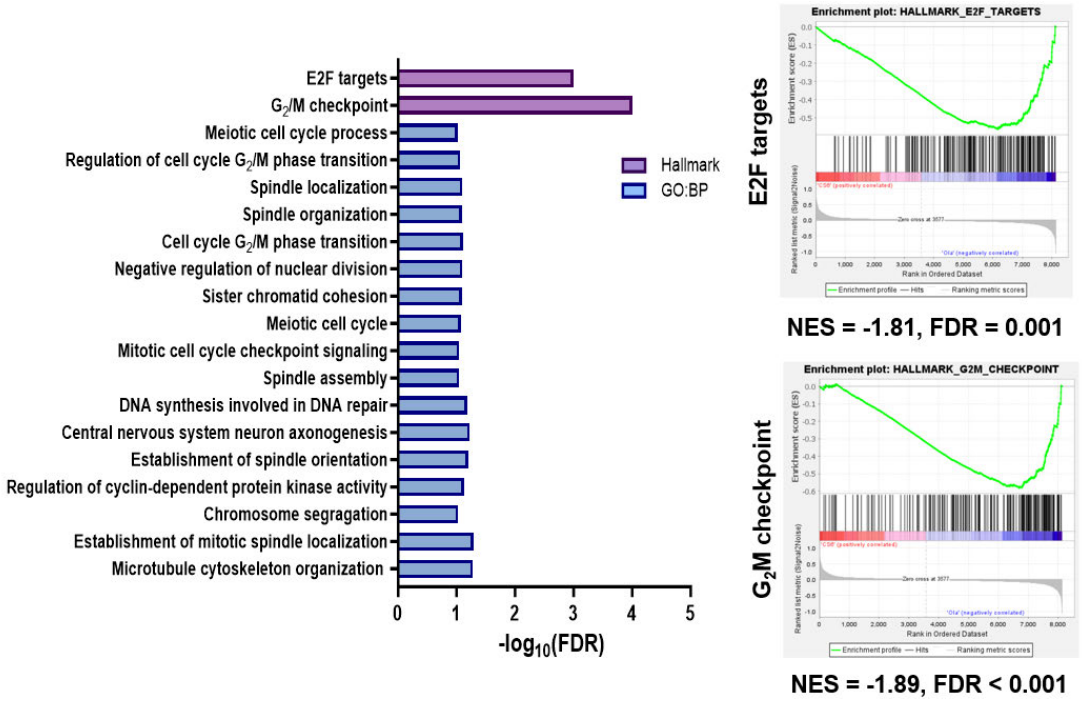

Figure 4.31. GSEA performed on proteomics data from **29c**-treated cells vs olaparib-treated cells (5 µM, 48 h), highlighting gene sets significantly downregulated ($-\log_{10}$(FDR) > 1 and NES < 1). **Left**: downregulated Gene Ontology: Biological Processes and Hallmark gene sets and **Right**: corresponding GSEA enrichment plots for Hallmark gene sets.

Regarding downregulated gene sets, several Hallmark and Gene Ontology: Biological Processes sets were identified (**Figure 4.31**). Hallmark gene sets E2F targets and G_2/M checkpoints were shown to be most significantly downregulated after **29c** treatment. PARP-1 is closely linked to E2F and regulates its activity through transcriptional co-activation.[220, 221] Since E2F transcription factors are master regulators of cell cycle progression, this may indicate that **29c** has had a significant effect on the cell cycle.[222] Both inhibition of PARP-1 activity and knockout of PARP-1 have been shown to significantly reduce E2F(1) transcriptional activity and thus cell proliferation.[223] This is further corroborated by the downregulation of a number of other cell cycle-related gene sets including spindle organisation, mitosis and G_2/M checkpoints. The G_2/M checkpoint is essential to ensure all DNA damage is repaired before cells undergo mitosis and PARPi are known to cause a G_2 phase delay before

mitosis occurs.[224] Connections between PARP-1, E2F and the G_2/M cell cycle transition have also previously been studied,[225] where PARP-1 inhibition was shown to retard E2F-induced cell cycle progression and activate E2F-induced apoptosis. Together, these data suggest that **29c**-mediated degradation of PARP has a greater effect on E2F-dependent transcription than is seen when only its catalytic activity is inhibited following olaparib treatment. This may be responsible for the loss of cell viability observed through disruption of cell cycle progression, in addition to the increased DNA damage illustrated in **Section 4.5**. The apparent additional effects on the cell cycle should be studied in more detail in future work to further link these mechanisms.

4.7 Assessment of drug potency in spheroids

The data presented until now has been acquired using 2D cell culture. Although this is commonplace in cell biology, the use of 3D cell culture is more physiologically relevant. It was thus considered important to assess the activity of **29c** in 3D cell culture. ES-2 spheroids were grown and incubated with olaparib and **29c** at a range of concentrations (**Figure 4.32**). Using the live cell stain calcein-AM (C-AM) and dead cell stain propidium iodide (PI), a quantitative readout of spheroid viability was obtained. **29c** significantly increased the proportion of dead cells upon increasing concentration (**Figure 4.32A** and **C**). At the highest concentration tested, 100 µM, **29c** exhibited ca. 4× greater potency than olaparib and was shown to cause dissociation of cells from the spheroid (**Figure 4.32B**). The change in size of the spheroid was also monitored with increasing concentration (**Figure 4.32D**). **29c** caused a reduction in spheroid area at lower concentrations than olaparib which was sustained until 100 µM. Interestingly, although viability was much lower in **29c**-treated spheroids, olaparib was still capable of reducing spheroid area, with 18% reduction vs 24% for **29c** at 100 µM. This indicates **29c** may be more potent in causing cell death and thus spheroid dissociation, while olaparib may be affecting the proliferation of new cells to inhibit spheroid growth.

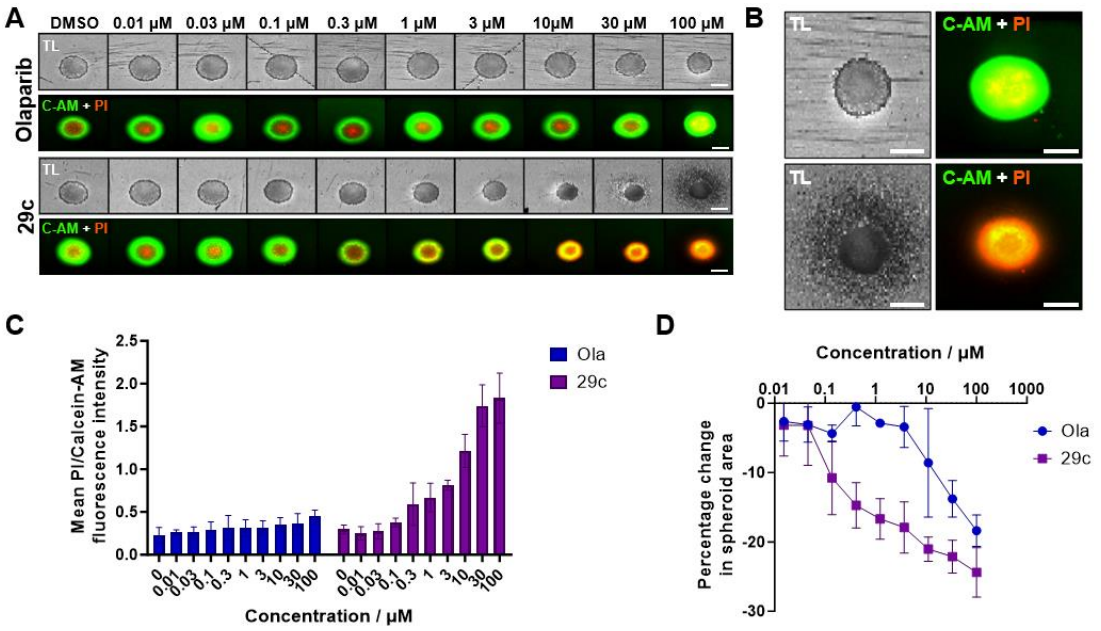

Figure 4.32. Analysis of olaparib and **29c** in ES-2 spheroids. **A)** Representative transmitted light (TL), calcein-AM (C-AM, green) and propidium iodide (PI, red) imaging of spheroids (3D projections) after treatment with olaparib or **29c** at the indicated concentrations. **B)** Representative high magnification images of olaparib-treated (**top**) or **29c**-treated spheroids (**bottom**) at 100 µM. **C)** Quantification of ratio of PI/C-AM signal intensity as a readout of the non-viable cell count. **D)** Quantification of change in spheroid size (determined from TL images) with increasing drug concentration vs DMSO control. Error bars report the standard deviation of the mean from three independent experiments.

4.8 Linking cell studies to SRS imaging

With the knowledge of the new activity of olaparib upon tagging, and demonstration of intracellular tracking in **Chapter 3**, the Raman tags presented can be considered 2-in-1 chemical probes. This work is the first example of a Raman-active protein degrader molecule and one of only a few examples of a protein degrader capable of intracellular imaging. Ideally, SRS microscopy could open up a range of opportunities in this respect, e.g., live cell tracking of compound uptake, monitoring protein degradation in real time, quantification of drug metabolism. However, limitations in the current microscope setup make these ideas extremely challenging. Nevertheless, attempts were made to incorporate SRS imaging in a useful way to showcase these multifunctional molecules. As discussed in **Section 3.6.1**, **26a**–**26c** and **29a**–**29c** were observed in the cytosol and absent from the nucleus. With the new information that these maintain or even enhance the activity of olaparib, it appeared that this biodistribution was worth reconsidering. As discussed extensively, the UPR is activated upon accumulation of unfolded/misfolded protein in the ER. Thus, it was

important to assess whether the cytosolic drug signal that was detected in early SRS imaging was indicative of ER localisation. As determined in **Section 2.5**, the signal intensity of the PhDY tag in **29c** was calculated as ca. 3× lower than the BADY tags. Therefore, for the purposes of imaging, **29a** was used since it contains the BADY motif and was still shown to cause PARP degradation. It was difficult to synchronise the conditions used for SRS imaging to those effective for PARP degradation and other cell studies for a number of reasons. For example, the limit of detection of SRS imaging is relatively high and the low micromolar/nanomolar concentrations effective in initiating PARP degradation would now allow detection of drug Raman signal. Furthermore, longer term imaging at high concentrations (24 h, 100 µM) was shown not to significantly change drug distribution but did start to cause precipitation of the compound into the cell media (**Section 3.6.1**). As such, relatively short incubation times (1–2 h) were used for drug/ER colocalisation studies. ER tracker green was shown to colocalise with the alkyne signal from **29a** (**Figure 4.33E** & **F**). Although there is some overlap with the lipid signal (**Figure 4.33C**), compound signal was not detected within lipid droplets. Moreover, lipid biosynthesis and processing occur within the ER,[226] thus detection of alkyne signal within this region may be indicative of ER localisation rather than lipidic accumulation of the compound. These imaging results suggest drug-bound PARP may reside in the ER.

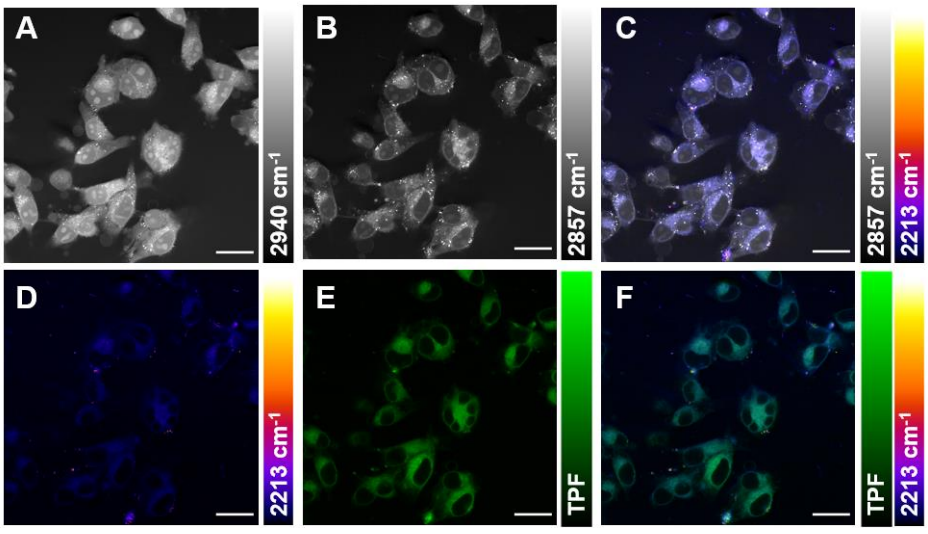

Figure 4.33. SRS imaging of **29a** in ES-2 cells (10 µM, 2 h). Cells were treated with ER tracker green (1 µM, 30 min) and fixed (4% v/v formaldehyde in PBS, 15 min). Contrast achieved by tuning to the indicated wavenumbers for **A)** CH_3 (2940 cm^{-1}, proteins), **B)** CH_2 (2857 cm^{-1}, lipids), **D)** C≡C (2213 cm^{-1}, alkyne). Two-photon fluorescence signal from ER tracker green is shown in image **E**. Images **C** and **F** show overlays of **B** & **D** and **D** & **E**, respectively. False colouring applied to **D** for clarity. Off-resonance frequency image subtracted from the alkyne image to generate **D** to account for background signal. Scale bars 25 µm.

A final imaging experiment was conducted to further link the HyT/degradation studies to SRS imaging. Using the conditions validated to block autophagy and PARP degradation, cells were pre-treated with BafA before imaging with **29a** (**Figure 4.34**). Interestingly, a clear increase in the alkyne signal was observed in cells with BafA treatment. This is consistent with the data presented in **Section 4.3**, indicating the involvement of autophagy in PARP degradation (e.g., BafA-mediated blocking of degradation in **Figure 4.13C**). Although not conclusive, it is possible that by blocking autophagy, **29a** bound to PARP is retained in the cell rather than being degraded by UPR/ER stress machinery. If true, this may also have been hampering SRS imaging throughout the project, i.e., increasing drug incubation times/concentrations may have been futile if the target protein was concurrently being removed from the cell. Although shorter incubation times (such as those used for this imaging study) did not induce PARP-1 degradation, it is possible that there is an initial period during which the cell is able to overcome HyT-induced PARP destabilisation and clear damaged PARP by autophagy, retaining homeostasis. This would not necessarily be observed by Western blot but may explain the differences in drug signal ± BafA even at short drug incubation times. To allow direct comparison to the imaging results, short drug incubations ± BafA should be conducted and analysed by Western blot.

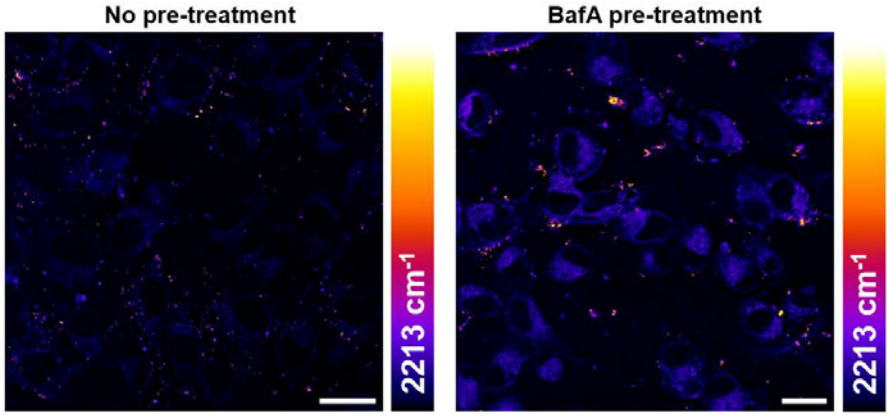

Figure 4.34. SRS imaging of **29a** in live ES-2 cells (10 µM, 2 h) with bafilomycin A pre-treatment (BafA, 5 µM, 18 h, **right** image) or no pre-treatment (**left** image). Off-resonance frequency images subtracted to account for background signal. Scale bars 25 µm.

4.9 Conclusions

In this chapter, the biological effects of Raman-tagged drug treatment on cancer cells were explored and are summarised in **Figure 4.35**. The initial aims of this study were to assess the bioorthogonality of Raman tagging on the PARP inhibitor olaparib by confirming similar cellular activity profiles, namely through viability and DNA damage assays. Interestingly, 2D and 3D cell culture viability assays found that Raman-tagged compounds were much more potent in reducing cell viability compared to olaparib. This effect was more marked in cancer cells than non-cancer cells and was shown to be dependent on PARP, ruling out nonspecific toxicity. Olaparib-tag analogue **29c**, one of the most potent compounds, was found to be much more effective than olaparib in killing an olaparib-resistant cell line and was more effective in *BRCA* -/- cell lines than *BRCA* WT. Furthermore, using a live cell fluorescent reporter, it was discovered that olaparib-tag analogues induce more DNA damage than olaparib. These findings confirmed attachment of Raman tags was not bioorthogonal and warranted further study to confirm the origins of new biological effects. It was revealed that the olaparib-tag analogues caused hydrophobic tag-induced PARP degradation and upregulation of the unfolded protein response (UPR)/ER-stress, confirmed by Western blot, RT-qPCR and proteomics. These analyses suggested an autophagy mechanism of degradation. Proteomics analysis furthermore indicated that **29c** treatment had affected cell cycle progression, which may contribute to the observed reduction in viability. Co-immunoprecipitation of nuclear pore complex proteins with PARP was also observed through the proteomics analysis, which suggested translocation of PARP, consistent with destabilisation and degradation of a protein through the UPR pathway. Multimodal SRS-fluorescence imaging was found to be consistent with translocation of PARP by determining colocalisation of Raman-tagged drug signal with an ER dye. Finally, the autophagic degradation of PARP was again indicated by observing changes in the drug uptake in cells treated with an autophagy inhibitor. Together, this study has investigated extensively the effects of Raman tagging of olaparib and reveals the activation of new pathways which are more effective in killing cancer cells than unmodified olaparib. These results highlight the complexity of using Raman tags for drug imaging and emphasise the need for thorough biological analysis to confirm bioorthogonality. However, if the new reported biological activity can be further tailored and is applicable to new drugs/proteins, it may represent an attractive opportunity for Raman tagging as a theranostic approach.

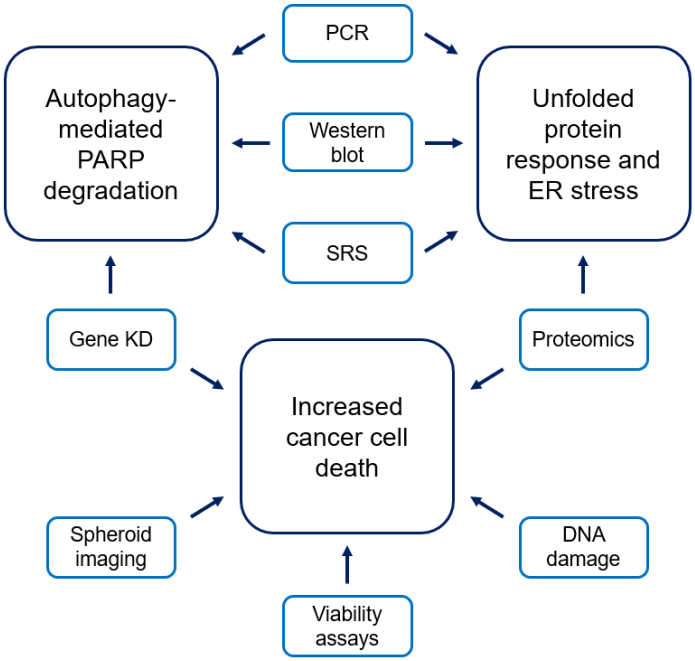

Figure 4.35. Summary of findings detailed in this chapter, highlighting the biological effects of Raman tagging of olaparib. Experimental techniques are shown which allowed these effects to be uncovered and enabled connection of different biological pathways. KD = knockdown.

Chapter 5 Conclusions and Future Work

This thesis has described the development of new Raman-active molecules and their application in intracellular drug imaging. **Chapter 1** contextualises this work within the field of biomedical imaging and highlights the utility of SRS microscopy in gaining a deeper understanding of drug behaviour.

In **Chapter 2**, new Raman-active motifs were developed which were designed to overcome issues with existing tags, primarily poor solubility. Based on parameters relied upon in medicinal chemistry, e.g., partition coefficients (log*D*, log*P)* and fraction of sp^3-hybridised carbons (Fsp^3), structural modifications were made to bisaryl butadiyne (BADY) Raman tags. The relative propensity of the tags to engage in associative intermolecular interactions, which are known to confer poor solubility, was correlated with log*P* by mass spectrometry analysis. X-ray crystallography showed that an increase in Fsp^3 directly affected crystal packing and blocked π-π stacking. Whilst these analyses suggest a combined assessment of both log*P* and Fsp^3 should be carried out in future tag design, ultimately no significant changes in cellular distribution between the tags were observed by SRS imaging.

In **Chapter 3**, the attachment of the newly developed tags to the PARP inhibitor olaparib for intracellular drug tracking was carried out. Extensive *in vitro* studies of these new Raman-active drug analogues were carried out to confirm their suitability for further testing *in cellulo*. Analysis of the physicochemical properties, target protein inhibition and binding, and biological stability of the drug-tag compounds confirmed general suitability for further testing. Drug analogues were generated with log$D_{7.4}$ values close to olaparib (1.8 vs 1.1), which bound to PARP with similar nanomolar affinity (K_D = 2.5 vs 0.7 nM) and inhibited PARP in an enzymatic activity assay (IC_{50} < 5 nM). Study of the drug analogues within the binding site of PARP through SPR and HDX-MS did highlight some differences when compared to olaparib, e.g., slower dissociation of the compounds from the protein, which has previously been linked to increased PARP trapping. Using SRS microscopy, the biodistribution of each compound was determined and correlated with the physicochemical analyses. This revealed that, although within the range of passive permeability, some drug analogues exhibited poor biodistribution. Whilst none of the olaparib analogues could be observed in the nucleus of the cell, i.e., the expected subcellular localisation of a PARP inhibitor, MS allowed detection of the compounds within nuclear fractions at concentrations of pmol/mg. The concentrations of the tagged drug in the nucleus were

comparable to the detected amounts of untagged olaparib. However, absolute concentrations of tagged and untagged olaparib in the whole cell were markedly different, with up to 700-fold lower concentrations of untagged olaparib detected in the cytoplasm of the cell. Together, these MS and imaging results warranted further testing in cells to determine whether apparent differences in uptake and distribution induced changes in drug action.

In **Chapter 4**, the result of Raman tagging olaparib in cancer cell lines was investigated, ultimately confirming bioorthogonality had not been retained. The drug-tag analogues were shown to be up to 250-fold more potent in killing cancer cells and induced degradation of PARP through a proposed hydrophobic tagging (HyT) pathway. Using Western blots, RT-qPCR and proteomics, the compounds were shown to activate the unfolded protein response (UPR), ER stress, and affect cell cycle progression. In addition to these new effects, the drug analogues exhibited enhanced PARP inhibitor activity in cells, determined via a live-cell fluorescent readout of DNA damage. The unexpected cytoplasmic drug distribution identified in **Chapter 3** was proposed to be a result of translocation of PARP to the ER, which is expected of a protein undergoing UPR degradation and was aligned with SRS imaging through colocalisation of tagged olaparib and a fluorescent ER dye. It is unclear whether the increased intracellular concentrations of the olaparib analogues (compared to olaparib) affected their activity in cells. However, irrespective of any possible increased intracellular drug concentrations, the new UPR/ER-stress pathways uncovered do not represent the normal effects of a PARP inhibitor. Likewise, these new pathways and processes do not necessarily indicate increased PARP trapping (as suggested in **Chapter 3**), although this should be investigated further. In summary, assessment of the biological activity of the olaparib analogues indicates that Raman tagging enhanced the activity of olaparib, converting the drug into a dual PARP inhibitor and PARP degrader.

Reflecting on the limitations of this work, the tags developed in **Chapter 2** were shown to be cell permeable but accumulated in lipidic cell regions and were not homogenously distributed throughout the cell (e.g., absent from the nucleus). This highlights an outstanding shortcoming of these Raman tags and future study should focus on further improvement to their physicochemical properties if they are to be used for cellular imaging. Further development of heteroaromatic-based BADY tags offers the best opportunity in this regard, in order to bring tag log*P* further in line with

drug targets and improve solubility. However, careful analysis of tag stability in biological media must be carried out to avoid undesired reactivity of the diyne motif, as has been observed for some of the heteroaromatic tags.[80] Ultimately, it would be practical to develop a universal tag suitable for all drug types. However, this thesis demonstrates the complexity of tagging a single drug target, thus universal drug tagging may require extensive further work. Whilst the choice of drug in **Chapter 3** was made logically based on a number of factors, it may have been prudent to select a drug with a less challenging subcellular localisation, e.g., in the cytoplasm. This would have facilitated SRS imaging and reduced the likelihood of the physicochemical properties of tags negatively affecting resultant drug-tag conjugates. A cytoplasmic drug may also have allowed easier delineation of any effects on biodistribution caused by physiochemical modifications to the tag. Circumventing the limit of detection (LOD) of SRS may also have been possible by choosing a drug that is known to accumulate in punctate organelles, allowing for high local drug concentrations and thus Raman signal.

Although extensive, the investigation of Raman tagging of olaparib with a hydrophobic tag and the consequent effects detailed in **Chapter 4** were not exhaustive, and further work should be conducted. Specifically, it is not clear whether the drug analogues were specific for PARP-1 and consequent biological effects of hydrophobic tagging were solely due to PARP-1 degradation. It is important to further investigate the specificity of the drug analogues, using, for example, tandem mass tag proteomics, as has been performed for a PARP-1 PROTAC.[190] The HyT approach is likely to be less specific than PROTAC-based degradation, considering PROTACs recruit a specific E3 ligase to induce degradation. Throughout all HyT studies, no single mechanism or degradation system has been reported, emphasising the need for further study. Additionally, there remains an opportunity to directly link the increased potency of the tagged compounds in reducing cell viability to PARP degradation. In other words, the autophagy inhibitor shown to block PARP degradation in **Chapter 4** should be used to determine its effect on cell viability with tagged olaparib treatment. If blocking autophagy (and thus PARP degradation) recovers cell viability, the increased potency of the tagged compounds would be further rationalised. It would also be interesting to assess the potency of the compounds in reducing cell viability in a wider variety of cancer cell lines. This would allow a clearer understanding of the therapeutic opportunity for the compounds. Likewise, if specificity and potency was confirmed in 2D cell culture, it would be important to expand to include further work in

3D cell culture models and eventually *in vivo* studies. These studies would help to bolster hydrophobic tagging as a valuable technique within medicinal chemistry. Although unlikely to compete with more specific and well-understood approaches such as PROTACs, the added benefit of 2-in-1 drug imaging and protein degradation does offer unique advantages.

In general, this project has provided some contribution to the field of SRS drug imaging. However, the work presented also highlights the major challenges of chemical tagging methodologies. Future drug imaging by SRS microscopy should be focused on the application and advancement of label-free imaging, ideally using hyperspectral SRS. This obviates many issues associated with a lack of bioorthogonality, however, drugs must still be detectable above the LOD. Targeting drugs that accumulate in the lysosomes, which continues to be demonstrated elegantly by Fu *et al.*,[46, 47, 227] has partially avoided LOD issues but limits applicability, thus it would be interesting to target new types of drugs with hyperspectral imaging.

Raman tags undoubtedly help to combat LOD issues but the development of new tags may be better targeted towards larger biomolecules that are less likely to be affected by structural modification. For example, unmet needs exist within other biomedical imaging fields wherein Raman tagging may be useful. Histopathological techniques are the gold standard in diagnosis of cancer and other diseases but suffer from long turnaround times and are low-throughput. SRS-based histopathology techniques have emerged and would benefit from the ability to simultaneously detect multiple cancer biomarkers.[228] Attachment of Raman tags to antibodies for diagnostic proteins offers relatively facile multiplexing and the fast image acquisition time of SRS would negate arduous fixing and sample preparation protocols associated with traditional methods (**Figure 5.1A**). Analytes such as antibodies would not be as greatly impacted by the attachment of larger Raman tags, such as the highly Raman-active electronic pre-resonance (EPR) tags developed by Min *et al.*, allowing for improvements in detection sensitivity.[75, 76]

EPR tags may also be amenable to structural modification to generate photo-switchable or photo-reactive probes, whose Raman properties could be modulated by switchable fluorescence activity (**Figure 5.1B**). Switchable/blinking probes may also integrate well into the recently reported new field of super resolution SRS microscopy.[112] Development of Raman chemical probes will allow further integration

of SRS microscopy into chemical biology. The recent discovery of covalent diyne tags also opens up opportunities in this regard.[80] It would be interesting to further explore the activity of these tags and make additional structural modifications to fine-tune reactivity to different nucleophiles. For example, with optimisation, it is possible that these tags could be installed within drug structures to generate covalent inhibitors, thus enabling dynamic monitoring of covalent reactivity by SRS (**Figure 5.1C**).

The unexpected effects of Raman tagging in this study should serve as an example of the importance of a thorough analysis of tagged compounds *in cellulo*; it is insufficient to determine suitability through solely protein binding/activity studies. Now that they have been discovered, it would be interesting to determine whether the effects of Raman tagging olaparib could be expanded to other drugs/targets. However, it would first be sensible to optimise the potency of the hydrophobic tags and decipher structure-activity relationships to facilitate future application. It is not clear whether the amenability of olaparib to hydrophobic tagging (i.e., containing a site for tag attachment that protrudes from the PARP active site) is an exclusive example. It may be practical to first target another PARP inhibitor which has previously been modified to generate a PROTAC, e.g., rucaparib (**Figure 5.1D**).[190]

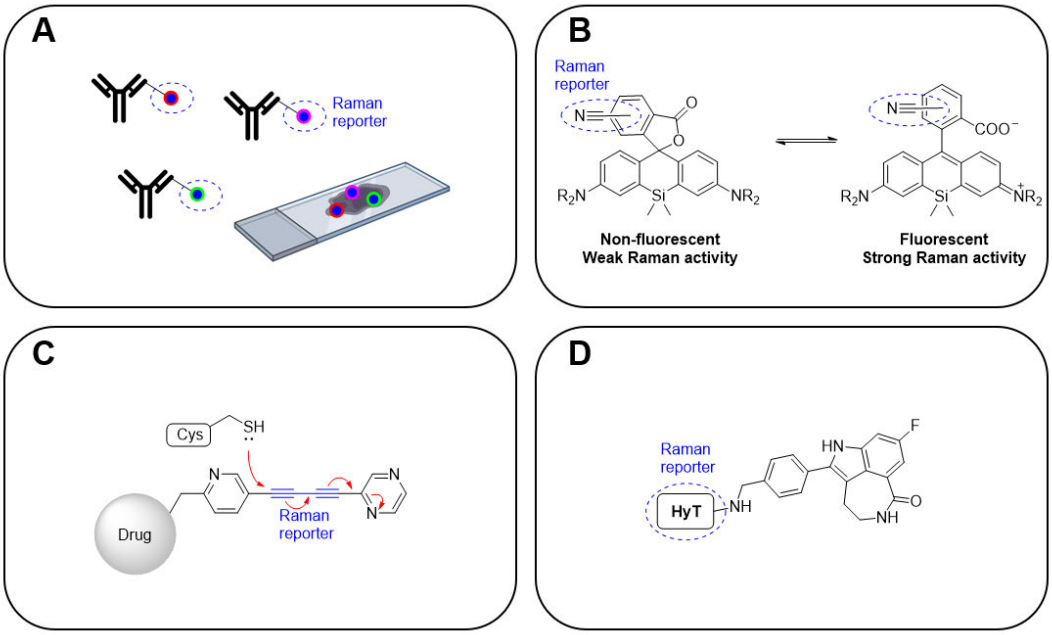

Figure 5.1. Proposed new opportunities for Raman-tagged SRS imaging. **A)** Multiplex Raman tag detection for histopathology. Microscope slide icon from Biorender.com. **B)** Switchable EPR Raman probes. **C)** Covalent reactivity of a Raman-tagged drug within a protein active site. **D)** Raman-active HyT-tagged rucaparib.

As advancements in microscope equipment and software continue to emerge, the possibilities of integrating SRS microscopy further into the drug discovery pipeline will expand. The ability of Raman imaging to draw interest from researchers in a wide range of disciplines – from chemistry, to biology, to engineering to physics – is a testament to its many unique advantages over other techniques and will leave a lasting impact on biomedical imaging.

Chapter 6 Experimental

6.1 Chemical

6.1.1 Computational

ChemDraw Professional, MarvinSketch, or in-house AstraZeneca software was used to obtain calculated physicochemical parameters. The molecular geometry of proposed tag structures was minimised using Gaussian 09 (B3LYP/6-31G (d)), with 'Pulay's direct inversion in the iterative subspace' (DIIS) method applied during self-consistent field (SCF) optimisation. Optimised structure geometries were then extracted using Gabedit 2.5.1 and visualised using Mercury 4.3.1.[229] This Gaussian analysis also provided prediction of Raman intensities and shifts, which were subjected to a scaling factor of 0.96 to account for the anharmonic nature of bonded atoms.[79]

6.1.2 General considerations

Reactions indicated as being carried out under nitrogen were performed using a Schlenk line with flame-dried glassware cycled between a vacuum and the inert gas. All starting materials were used as received from Acros, Fluorochem, Sigma Aldrich/Merck, Fisher Scientific or Combi-Blocks unless otherwise stated. Et_3N was purified by distilling from powdered CaH_2 and stored in an ampoule containing molecular sieves under N_2. Where Schlenk line techniques were employed, solvents were purified using a solvent purification system and transferred under Ar or N_2. Flash chromatography columns were carried out using a CombiFlash® NextGen 100 system with RediSep® pre-packed silica column or manually using ACROS Organics™ Silica gel, (0.035-0.070 mm, 60 Å). Reactions were monitored by thin-layer chromatography (TLC) on normal phase E. Merck silica gel foil-backed plates (Kieselgel 60 F254, 0.2 mm thickness). Compounds were visualised either by exposure of the plate to UV light (254 nm) or by staining with an aqueous solution of potassium permanganate and heating. Melting points (MP) were determined on a Gallenkamp Electrothermal Melting Point apparatus and are uncorrected. Infrared (IR) spectra were recorded by measuring the neat sample on a Shimadzu IRAffinity-1 solid state FT-IR spectrometer. Characteristic bands for absorbances ≥ 1500 cm^{-1} are reported. Fluorescence spectra were acquired using a Shimadzu RF-6000 spectrofluorometer. Nuclear magnetic resonance (NMR) spectra were recorded at ambient temperature using a Bruker AV400, AV500 or AV600 spectrometer operating

at 400, 500 or 600 MHz (^{1}H spectra) and 100, 125 or 150 MHz (^{13}C spectra), respectively. For ^{31}P NMR, a Bruker PRO500 spectrometer was used at 202 MHz. Residual solvent peaks ($CDCl_3$: ^{1}H δ 7.26 ppm, ^{13}C δ 77.16 ppm; DMSO-d_6: ^{1}H δ 2.50 ppm, ^{13}C δ 39.52 ppm.) were used as an internal reference. The abbreviations s = singlet, d = doublet, t = triplet, q = quartet, hept = heptet and br = broad (or combinations thereof) were used to describe the peak multiplicity in ^{1}H NMR spectra. Coupling constants (*J*) are quoted to the nearest 0.1 Hz. ^{13}C NMR signals are assigned as quaternary (C), tertiary (CH), secondary (CH_2) or primary (CH_3) with appropriate coefficients (i.e. 2CH) for symmetrical compounds. For olaparib analogues, 2D NMR experiments were conducted as required to facilitate peak assignment. J_{CF} values are provided only when ^{13}C multiplets were fully resolved. Full spectra for all compounds not previously reported in the literature are provided in **Appendix C**. High-resolution mass spectrometry (HMRS) electrospray ionisation (ESI) measurements were carried out using a Bruker 12 T SolariX, Bruker microTOF II or Kratos MS50TC mass spectrometer. Mass-to-charge ratios are reported for protonated ($[M+H]^+$), sodiated ($[M+Na]^+$) or deprotonated ($[M–H]^-$) molecular ions. Purity of final compounds to be used *in vitro* was determined by RP-HPLC to be ≥ 95% and further validated at AstraZeneca prior to commencing assays.

6.1.3 General procedures

GP 1. Pd-catalysed Cadiot-Chodkiewicz coupling of alkynes

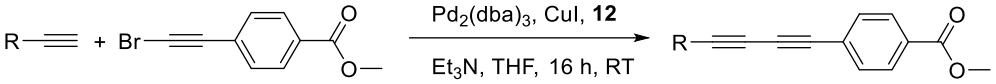

To a solution of $Pd_2(dba)_3$ (0.04 equiv.), CuI (0.02 equiv.), and (*E*)-3-(2-(diphenylphosphaneyl)phenyl)-1-phenylprop-2-en-1-one (**12**, 0.04 equiv.) under N_2 in THF (2 mL : 1 mmol terminal alkyne) was added terminal alkyne (1 equiv.) in THF (1 mL : 1 mmol terminal alkyne) and Et_3N (2 equiv.) and the mixture was stirred for 10 minutes at RT. Methyl 4-(bromoethynyl)benzoate (**8**, 1.2 equiv) in THF (1 mL : 1 mmol terminal alkyne) was added dropwise and the reaction mixture was stirred for 16 h at RT. After the completion of the reaction, as indicated by TLC, the reaction mixture was diluted with EtOAc (5 mL) and washed with NaCl (5 mL, sat. aq.). The aqueous layer was separated and extracted with EtOAc (3 × 10 mL). The combined organic layers were dried over $MgSO_4$ and concentrated *in vacuo*. The crude product was purified by silica gel column chromatography, either manually or using a CombiFlash®

NextGen 100 system with RediSep® pre-packed silica column (using EtOAc in petroleum ether 40-60 as the eluent).

GP 2. Ester hydrolysis

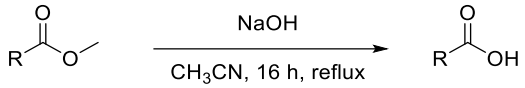

To a solution of methyl ester (1 equiv.) in CH_3CN (25 mL : 1 mmol ester) was added NaOH (5 equiv., 1 M in H_2O). The reaction mixture was heated to reflux and stirred for 16 h. The solvent was removed *in vacuo* and the residue was resuspended in H_2O. The mixture was acidified (ca. pH 2) to form a precipitate, which was collected *via* vacuum filtration and washed with ice-cold H_2O. The desired acid was carried forward without the need for further purification.

GP 3. Amide coupling to olaparib-amine

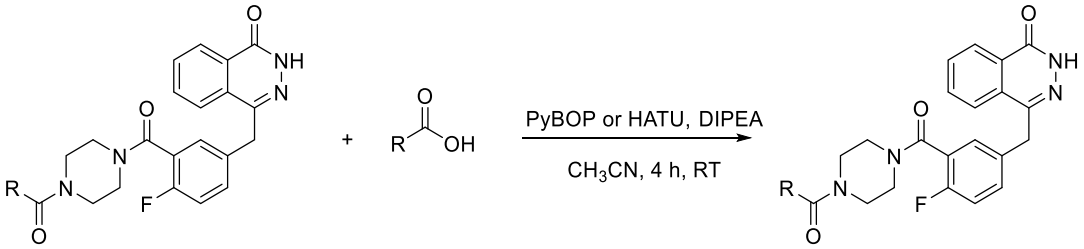

To a solution of carboxylic acid (1 equiv.) and 4-[4''-fluoro-3''-(piperazine-1'''-carbonyl)benzyl]-2*H*-phthalazin-1-one (olaparib-amine **24**, 1 equiv.) in CH_3CN (6 mL : 1 mmol carboxylic acid) was added PyBOP or HATU (1.2 equiv) and DIPEA (4 equiv.). The reaction mixture was stirred for 4 h at RT and the resultant precipitate was collected *via* vacuum filtration and washed with ice-cold H_2O. The crude amide was purified by silica gel column chromatography, either manually or using a CombiFlash® NextGen 100 system with a RediSep® pre-packed silica column (using methanol in DCM as the eluent).

GP 4. Amide coupling to linker compound

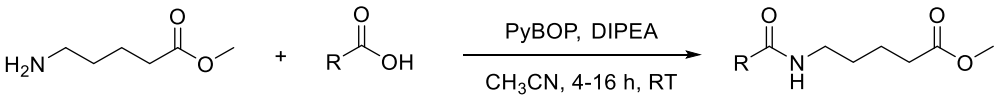

To a solution of carboxylic acid (1 equiv.) and 5-aminopentanoic acid methyl ester hydrochloride **25** (1 equiv.) in CH_3CN (6 mL : 1 mmol carboxylic acid) was added

PyBOP (1.2 equiv) and DIPEA (4 equiv.). The reaction mixture was stirred for 4 – 16 h at RT. After the completion of the reaction, as indicted by TLC, the reaction mixture was poured into ice-cold H_2O. The resultant precipitate was collected *via* vacuum filtration and washed with ice-cold H_2O. The amide-linked tag was carried forward without the need for further purification.

6.1.4 Synthesis and characterisation of reaction products

6-Hydroxymethyl-1,2,3,4-tetrahydronaphthalene (3)

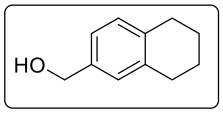

To a suspension of $LiAlH_4$ (418 mg, 11.0 mmol) in THF (25 mL) at 0 °C under N_2 was added dropwise 1,2,3,4-tetrahydro-2-naphthoic acid (500 mg, 2.75 mmol) in THF (25 mL). The reaction mixture was allowed to warm to RT and stirred for 3 h. The reaction was quenched at 0 °C by dropwise addition of H_2O (10 mL) and NaOH (10 mL, 1 M in H_2O). The mixture was stirred for 30 min at RT and filtered over a pad of celite. The organic layers were dried over $MgSO_4$ and concentrated *in vacuo* to afford the title compound **3** as a white solid (418 mg, 2.58 mmol, 94%). $\mathbf{R_f}$ (50% EtOAc in petroleum ether 40-60) = 0.80. **^{1}H NMR** (400 MHz, $CDCl_3$) δ 7.13 – 7.03 (m, 3H, Ar*H*), 4.62 (s, 2H, C*H*$_2$OH), 2.83 – 2.71 (m, 4H, C*H*$_2$), 1.87 – 1.75 (m, 4H, C*H*$_2$). **^{13}C NMR** (126 MHz, $CDCl_3$) δ 138.15 (C), 137.55 (C), 136.88 (C), 129.53 (CH), 128.06 (CH), 124.49 (CH), 65.56 (CH_2), 29.54 (CH_2), 29.31 (CH_2), 23.35 (CH_2), 23.32 (CH_2).

^{1}H and ^{13}C NMR spectroscopic data are in good agreement with the literature.[230]

5,6,7,8-Tetrahydronaphthalene-2-carbaldehyde (4)

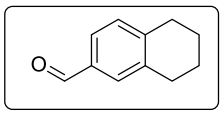

To a solution of **3** (418 mg, 2.58 mmol) in DCM (15 mL) at 0 °C was added dropwise Dess-Martin periodinane (1.20 g, 2.84 mmol) in DCM (10 mL). The reaction mixture was allowed to warm to RT and stirred for 16 h. The reaction mixture was filtered over a pad of celite, and the filtrate was washed with $Na_2S_2O_3$ (20 mL, 5% in H_2O). The aqueous layer was extracted with DCM (2 × 20 mL). The combined organic layers were washed with NaCl (20 mL, sat. aq.), dried over $MgSO_4$, and concentrated *in vacuo*. The crude product was purified by silica gel column chromatography (0 → 20% EtOAc in petroleum ether 40-60) to afford the title compound **4** as a colourless oil (384 mg, 2.40 mmol, 93%). $\mathbf{R_f}$ (20% EtOAc in petroleum ether 40-60) = 0.79. **^{1}H NMR** (601 MHz, $CDCl_3$) δ 9.93 (s, 1H, C*H*O), 7.61 – 7.56 (m, 2H, Ar*H*), 7.21 (d, *J* = 7.8 Hz, 1H, Ar*H*),

2.86 – 2.81 (m, 4H, C*H*$_2$), 1.87 – 1.79 (m, 4H, C*H*$_2$). **^{13}C NMR** (151 MHz, $CDCl_3$) δ 192.50 (CH), 145.04 (C), 138.18 (C), 134.38 (C), 130.96 (CH), 129.96 (CH), 126.77 (CH), 30.02 (CH_2), 29.38 (CH_2), 22.99 (CH_2), 22.86 (CH_2).

^{1}H and ^{13}C NMR spectroscopic data are in good agreement with the literature.[231]

Dimethyl (1-diazo-2-oxopropyl)phosphonate (5)

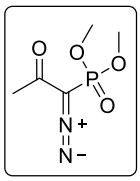

To a suspension of NaH (1.30 g, 54.2 mmol, 60% in mineral oil) in toluene (30 mL) at 0 °C was added dropwise dimethyl 2-oxypropylphosphonate (5.00 g, 30.1 mmol) in THF (10 mL). After gas evolution ceased, 4-acetamidobenzenesulfonyl azide (7.95 g, 33.1 mmol) in THF (20 mL) was added dropwise at RT. The reaction mixture was stirred under N_2 for 16 h. The reaction mixture was diluted with petroleum ether 40-60 (30 mL) and filtered over celite. The filtrate was washed with Et_2O (3 × 50 mL). The combined organic layers were washed with NaCl (50 mL, sat. aq.), dried over $MgSO_4$, and concentrated *in vacuo*. The crude product was purified by silica gel column chromatography (0 → 30% EtOAc in petroleum ether 40-60) to afford the title compound **5** as a yellow oil (3.79 g, 19.7 mmol, 65%). **R_f** (50% EtOAc in petroleum ether 40-60) = 0.12. **IR** (cm^{-1}) 2118 (C=N), 1657 (C=O), 1265 (P=O). **^{1}H NMR** (500 MHz, $CDCl_3$) δ 3.84 (d, $^3J_{PH}$ = 11.9 Hz, 6H, OC*H*$_3$), 2.27 (s, 3H, C*H*$_3$). **^{13}C NMR** (126 MHz, $CDCl_3$) δ 189.85 (d, $^2J_{CP}$ = 13.5 Hz, C), 128.62 (d, $^1J_{CP}$ = 102.4 Hz, C), 53.57 (d, $^2J_{CP}$ = 5.5 Hz, CH_3), 27.14 (CH_3). **^{31}P{^{1}H} NMR** (202 MHz, $CDCl_3$) δ 14.27.

^{1}H and ^{13}C NMR spectroscopic data are in good agreement with the literature.[232]

6-Ethynyl-1,2,3,4-tetrahydro-naphthalene (6)

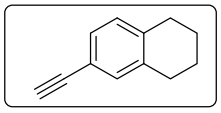

To a solution of 5,6,7,8-tetrahydronaphthalene-2-carbaldehyde **4** (257 mg, 1.61 mmol) in MeOH (4 mL) at 0 °C was added dropwise phosphonate **5** (371 mg, 1.93 mmol) in MeOH (1 mL). The reaction mixture was allowed to warm to RT and stirred for 4 h. The solvent was removed *in vacuo* and the residue was redissolved in Et_2O (10 mL). The mixture was washed with $NaHCO_3$ (10 mL, 5% in H_2O) and the aqueous layer was extracted with Et_2O (3 × 10 mL). The combined organic layers were dried over $MgSO_4$ and concentrated *in vacuo*. The crude product was purified by silica gel column chromatography (petroleum ether 40-60) to afford the title compound **6** as a colourless oil (219 mg, 1.40 mmol, 87%). **R_f** (5% EtOAc in petroleum ether 40-60) = 0.88. **IR** (cm^{-1}) 2103 (C≡C), 1563 (C=C).

^{1}H NMR (601 MHz, $CDCl_3$) δ 7.23 – 7.19 (m, 2H, Ar*H*), 7.01 (d, *J* = 8.6 Hz, 1H, Ar*H*), 2.99 (s, 1H, C*H*), 2.78 – 2.71 (m, 4H, CH_2), 1.83 – 1.75 (m, 4H, CH_2). **^{13}C NMR** (151 MHz, $CDCl_3$) δ 138.51 (C), 137.40 (C), 132.92 (CH), 129.24 (CH), 129.21 (CH), 119.06 (C), 84.22 (C), 76.10 (CH), 29.51 (CH_2), 29.26 (CH_2), 23.11 ($2CH_2$).

^{1}H and ^{13}C NMR spectroscopic data are in good agreement with the literature.[233]

Methyl 4-(bromoethynyl)benzoate (8)

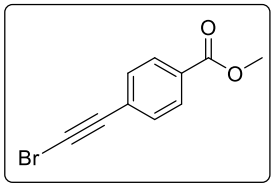

To a solution of methyl 4-ethynylbenzoate (2.00 g, 12.5 mmol) in acetone (75 mL) was added *N*-bromosuccinimide (2.45 g, 13.7 mmol) and $AgNO_3$ (212 mg, 1.25 mmol). The reaction mixture was stirred for 4 h at RT. The solvent was removed *in vacuo* and the residue was redissolved in Et_2O (50 mL). The organic layers were washed with H_2O (3 × 50 mL) and NaCl (50 mL, sat. aq.), dried over $MgSO_4$, and concentrated *in vacuo* to afford the title compound **8** as a beige solid (2.75 g, 11.5 mmol, 92%). **R_f** (20% EtOAc in petroleum ether 40-60) = 0.74. **IR** (cm^{-1}) 2196 (C≡C), 1710 (C=O), 1605 (C=C). **^{1}H NMR** (500 MHz, $CDCl_3$) δ 8.01 – 7.95 (m, 2H, Ar*H*), 7.53 – 7.48 (m, 2H, Ar*H*), 3.92 (s, 3H, CH_3). **^{13}C NMR** (126 MHz, $CDCl_3$) δ 166.55 (C), 132.11 (2CH), 130.17 (C), 129.65 (2CH), 127.48 (C), 79.58 (C), 53.46 (C), 52.41 (CH_3).

^{1}H and ^{13}C NMR spectroscopic data are in good agreement with the literature.[234]

1,4-Diphenylbuta-1,3-diyne (9)

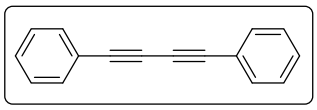

*By-product in the coupling reaction to form **1a**.* **^{1}H NMR** (500 MHz, $CDCl_3$) δ 7.57 – 7.51 (m, 2H, Ar*H*), 7.41 – 7.29 (m, 3H, Ar*H*). **^{13}C NMR** (126 MHz, $CDCl_3$) δ 132.66 (4CH), 129.36 (2CH), 128.59 (4CH), 121.97 (2C), 81.70 (2C), 74.07 (2C).

^{1}H and ^{13}C NMR spectroscopic data are in good agreement with the literature.[235]

Dimethyl 4,4'-(buta-1,3-diyne-1,4-diyl)dibenzoate (10)

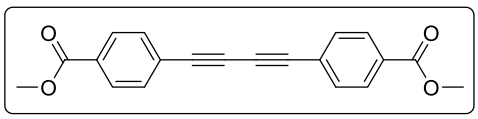

*By-product in the coupling reaction to form **1a** and **1c**.* **^{1}H NMR** (500 MHz, $CDCl_3$) δ 8.02 (d, *J* = 8.7 Hz, 2H, Ar*H*), 7.59 (d, *J* = 8.7 Hz, 2H,

Ar*H*), 3.93 (s, 3H, C*H*$_3$). **^{13}C NMR** (126 MHz, $CDCl_3$) δ 166.42 (2C), 132.62 (4CH), 130.72 (2C), 129.73 (4CH), 126.28 (2C), 82.00 (2C), 76.41 (2C), 52.50 ($2CH_3$).

^{1}H and ^{13}C NMR spectroscopic data are in good agreement with the literature.[236]

1,4-bis(5,6,7,8-tetrahydronaphthalen-2-yl)buta-1,3-diyne (11)

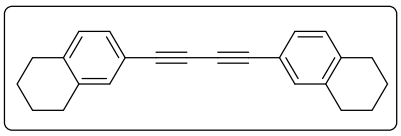

*By-product in the coupling reaction to form **1b**.* **^{1}H NMR** (500 MHz, $CDCl_3$) δ 7.26 – 7.20 (m, 2H, Ar*H*), 7.01 (d, *J* = 8.3 Hz, 1H, Ar*H*), 2.79 – 2.71 (m, 4H, C*H*$_2$), 1.83 – 1.75 (m, 4H, C*H*$_2$). ^{13}C NMR (126 MHz, $CDCl_3$) δ 139.06 (2C), 137.56 (2C), 133.23 (2CH), 129.57 (2CH), 129.36 (2CH), 118.87 (2C), 81.79 (2C), 73.27 (2C), 29.63 ($2CH_2$), 29.27 ($2CH_2$), 23.07 ($4CH_2$).

(***E***)**-3-(2-(Diphenylphosphaneyl)phenyl)-1-phenylprop-2-en-1-one (12)**

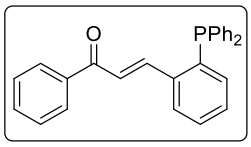

A mixture of 2-phenyl(triphenylphosphoranylidene)ethan-2-one (1.77 g, 4.65 mmol) and 2-(diphenylphosphino)benzaldehyde (750 mg, 2.58 mmol) in toluene (50 mL) was heated to reflux for 25 h under N_2. The solvent was removed *in vacuo* and the residue was purified by silica gel column chromatography (0 → 5% EtOAc in petroleum ether 40-60) to afford a waxy orange solid. The solid was further purified by recrystallisation from hot methanol to yield the title compound **12** as a pale-yellow solid (530 mg, 1.35 mmol, 52%). **R_f** (5% EtOAc in petroleum ether 40-60) = 0.24. **IR** (cm^{-1}) 1659 (C=O), 1606 (C=C). **^{1}H NMR** (601 MHz, $CDCl_3$) δ 8.35 (dd, *J* = 15.8, 4.4 Hz, 1H, C*H*), 7.77 – 7.69 (m, 3H, Ar*H*), 7.53 (ddt, *J* = 8.7, 7.1, 1.1 Hz, 1H, Ar*H*), 7.47 – 7.22 (m, 14H, Ar*H*), 7.17 (dd, *J* = 15.8, 1.1 Hz, 1H, C*H*), 6.94 (ddd, *J* = 8.1, 4.4, 1.1 Hz, 1H, Ar*H*). **^{13}C NMR** (126 MHz, $CDCl_3$) δ 192.04 (C), 143.69 (d, $^3J_{CP}$ = 24.1 Hz, CH), 139.87 (d, $^1J_{CP}$ = 22.2 Hz, C), 138.59 (d, $^2J_{CP}$ = 16.8 Hz, C), 138.10 (C), 136.02 (d, $^1J_{CP}$ = 10.0 Hz, 2C), 134.23 (d, $^2J_{CP}$ = 19.9 Hz, 4CH), 133.86 (CH), 132.56 (CH), 130.08 (CH), 129.26 (CH), 129.13 (2CH), 128.82 (2CH), 128.81 (d, $^3J_{CP}$ = 7.0 Hz, 4CH), 128.69 (2CH), 127.12 (d, $^3J_{CP}$ = 4.0 Hz, CH), 125.79 (d, $^4J_{CP}$ = 3.2 Hz, CH). **^{31}P{^{1}H} NMR** (202 MHz, $CDCl_3$) δ -13.79.

^{1}H, ^{13}C and ^{31}P NMR spectroscopic data are in good agreement with the literature.[237]

Methyl 4-(phenylbuta-1,3-diyn-1-yl)benzoate (1a)

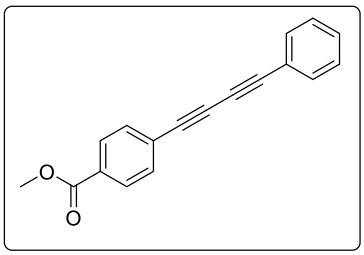

Synthesised according to GP 1 from ethynylbenzene (100 mg, 0.979 mmol) to give the title compound **1a** as a beige solid (187 mg, 0.715 mmol, 73%). $\mathbf{R_f}$ (5% EtOAc in petroleum ether 40-60) = 0.33. **MP** 107–108 °C. **IR** (cm^{-1}) 2212 (C≡C), 1716 (C=O), 1603 (C=C), 1572 (C=C), 1556 (C=C). **^{1}H NMR** (601 MHz, $CDCl_3$) δ 8.01 (d, *J* = 8.7 Hz, 2H, Ar*H*), 7.58 (d, *J* = 8.7 Hz, 2H, Ar*H*), 7.56 – 7.52 (m, 2H Ar*H*), 7.42 – 7.32 (m, 3H, Ar*H*), 3.93 (s, 3H, CH_3). **^{13}C NMR** (151 MHz, $CDCl_3$) δ 166.48 (C), 132.74 (2CH), 132.54 (2CH), 130.46 (C), 129.70 (2CH), 129.65 (CH), 128.65 (2CH), 126.67 (C), 121.64 (C), 83.19 (C), 80.63 (C), 76.87 (C), 73.72 (C), 52.47 (CH_3).

^{1}H and ^{13}C NMR spectroscopic data and melting point are in good agreement with the literature.[238]

Methyl 4-((5,6,7,8-tetrahydronaphthalen-2-yl)buta-1,3-diyn-1-yl)benzoate (1b)

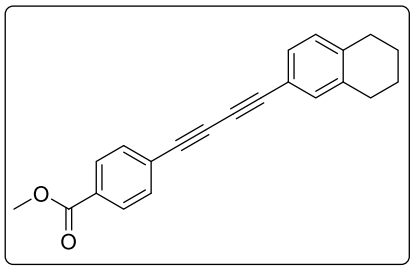

Synthesised according to GP 1 from 6-ethynyl-1,2,3,4-tetrahydronaphthalene **6** (143 mg, 0.916 mmol) to give the title compound **1b** as a white solid (205 mg, 0.650 mmol, 71%). $\mathbf{R_f}$ (20% EtOAc in petroleum ether 40-60) = 0.58. **MP** 204–205 °C. **IR** (cm^{-1}) 2209 (C≡C), 1714 (C=O), 1600 (C=C), 1556 (C=C). **^{1}H NMR** (601 MHz, $CDCl_3$) δ 8.00 (d, *J* = 8.7 Hz, 2H, Ar*H*), 7.57 (d, *J* = 8.7 Hz, 2H, Ar*H*), 7.27 – 7.23 (m, 2H, Ar*H*), 7.05 – 7.01 (m, 1H, Ar*H*), 3.92 (s, 3H, CH_3), 2.79 – 2.72 (m, 4H, CH_2), 1.83 – 1.76 (m, 4H, CH_2). **^{13}C NMR** (151 MHz, $CDCl_3$) δ 166.47 (C), 139.59 (C), 137.67 (C), 133.34 (CH), 132.45 (2CH), 130.26 (C), 129.66 (CH), 129.65 (2CH), 129.44 (CH), 126.87 (C), 118.31 (C), 83.90 (C), 80.13 (C), 77.21 (C), 72.72 (C), 52.41 (CH_3), 29.65 (CH_2), 29.25 (CH_2), 23.02 (CH_2), 23.00 (CH_2). **HRMS-ESI+** (*m/z*) $[M+H]^+$ found 315.1371, $C_{22}H_{18}O_2$ requires 315.1380.

Methyl 4-(cyclohexylbuta-1,3-diyn-1-yl)benzoate (1c)

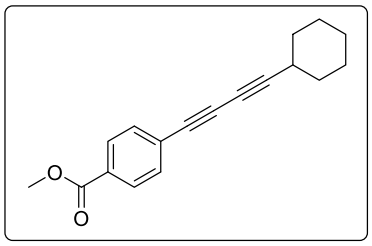

Synthesised according to GP 1 from ethynylcyclohexane (120 mg, 1.11 mmol) to give the title compound **1c** as a yellow solid (204 mg, 0.766 mmol, 69%). $\mathbf{R_f}$ (10% EtOAc in petroleum ether 40-60) = 0.85. **MP** 167–169 °C. **IR** (cm^{-1}) 2236 (C≡C), 1717 (C=O), 1602 (C=C). **^{1}H NMR** (500 MHz, $CDCl_3$) δ 7.97 (d, *J* = 8.7 Hz, 2H, Ar*H*), 7.52 (d, *J* = 8.7 Hz, 2H, Ar*H*), 3.91 (s, 3H, CH_3), 2.56 (hept, *J* = 3.7 Hz, 1H, C*H*), 1.87 – 1.80 (m, 2H, CH_2), 1.73 (ddt, *J* = 10.7, 6.8, 3.7 Hz, 2H, CH_2), 1.53 – 1.39 (m, 3H, CH_2 and CH_ACH_B), 1.39 – 1.27 (m, 3H, CH_2 and CH_ACH_B). **^{13}C NMR** (126 MHz, $CDCl_3$) δ 166.55 (C), 132.50 (2CH), 130.07 (C), 129.61 (2CH), 127.14 (C), 90.43 (C), 77.36 (C), 74.50 (C), 64.96 (C), 52.41 (CH_3), 32.21 ($2CH_2$), 29.96 (CH), 25.85 (CH_2), 24.85 ($2CH_2$). **HRMS-ESI+** (*m/z*) $[M+H]^+$ found 267.1376, $C_{18}H_{18}O_2$ requires 267.1380.

Methyl 4-((4-methylphenyl)lbuta-1,3-diyn-1-yl)benzoate (1d)

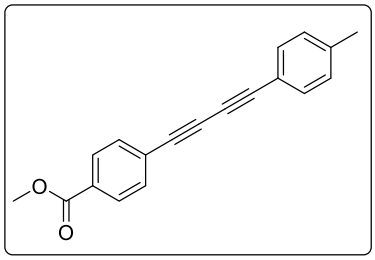

Synthesised according to GP 1 from 1-ethynyl-4-methylbenzene (116 mg, 1.00 mmol) to give the title compound **1d** as a beige solid (209 mg, 0.762 mmol, 76%). $\mathbf{R_f}$ (5% EtOAc in petroleum ether 40-60) = 0.49. **^{1}H NMR** (601 MHz, $CDCl_3$) δ 8.05 – 8.00 (m, 2H, Ar*H*), 7.62 – 7.57 (m, 2H, Ar*H*), 7.48 – 7.43 (m, 2H, Ar*H*), 7.18 (d, J = 7.9 Hz, 2H, Ar*H*), 3.95 (s, 3H, OCH_3), 2.40 (s, 3H, CH_3). **^{13}C NMR** (151 MHz, $CDCl_3$) δ 166.35 (C), 139.98 (C), 132.51 (2CH), 132.35 (2CH), 130.20 (C), 129.53 (2CH), 129.29 (2CH), 126.66 (C), 118.35 (C), 83.41 (C), 80.19 (C), 76.93 (C), 73.00 (C), 52.30 (CH_3), 21.66 (CH_3).

^{1}H and ^{13}C NMR spectroscopic data are in good agreement with the literature.[8]

Methyl 4-((4-(*tert*-butyl)phenyl)buta-1,3-diyn-1-yl)benzoate (1e)

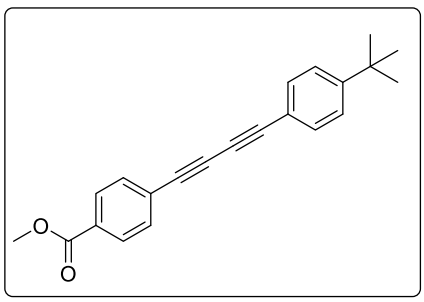

Synthesised according to GP 1 from 1-(*tert*-butyl)-4-ethynylbenzene (158 mg, 1.00 mmol) to give the title compound **1e** as a beige solid (213 mg, 0.674 mmol, 67%). $\mathbf{R_f}$ (5% EtOAc in petroleum ether 40-60) = 0.53. **MP** 151–153 °C. **^{1}H NMR** (500 MHz, $CDCl_3$) δ 8.03 – 7.97 (m, 2H, Ar*H*), 7.61 – 7.55 (m,

2H, Ar*H*), 7.51 – 7.45 (m, 2H, Ar*H*), 7.40 – 7.35 (m, 2H, Ar*H*), 3.93 (s, 3H, C*H*$_3$), 1.32 (s, 9H, C*H*$_3$). **^{13}C NMR** (126 MHz, $CDCl_3$) δ 166.50 (C), 153.22 (C), 132.54 (2CH), 132.50 (2CH), 130.35 (C), 129.69 (2CH), 126.82 (C), 125.71 (2CH), 118.52 (C), 83.58 (C), 80.30 (C), 77.37 (C), 73.12 (C), 52.46 (CH_3), 35.12 (C), 31.24 ($3CH_3$). **HRMS-ESI+** (*m/z*) $[M+H]^+$ found 317.1544, $C_{22}H_{21}O_2$ requires 317.1536.

Methyl 4-((naphthalen-2-yl)buta-1,3-diyn-1-yl)benzoate (1f)

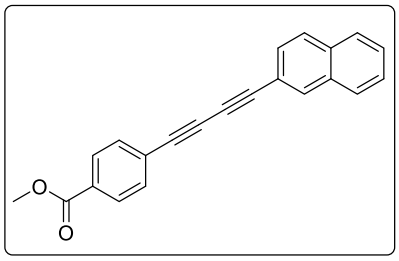

Synthesised according to GP 1 from 2-ethynylnaphthalene (152 mg, 1.00 mmol) to give the title compound **1f** as a yellow solid (205 mg, 0.660 mmol, 66%). **R$_f$** (5% EtOAc in petroleum ether 40-60) = 0.41. **MP** 155–157 °C. **^{1}H NMR** (500 MHz, $CDCl_3$) δ 8.13 – 8.09 (m, 1H, Ar*H*), 8.07 – 8.02 (m, 2H, Ar*H*), 7.88 – 7.81 (m, 3H, Ar*H*), 7.66 – 7.60 (m, 2H, Ar*H*), 7.60 – 7.52 (m, 3H, Ar*H*), 3.96 (s, 3H, C*H*$_3$). **^{13}C NMR** (126 MHz, $CDCl_3$) δ 166.34 (C), 133.33 (C), 133.25 (CH), 132.80 (C), 132.42 (2CH), 130.32 (C), 129.57 (2CH), 128.40 (CH), 128.27 (CH), 127.91 (CH), 127.86 (CH), 127.41 (CH), 126.87 (CH), 126.54 (C), 118.71 (C), 83.52 (C), 80.67 (C), 76.86 (C), 73.88 (C), 52.33 (CH_3). **HRMS-ESI+** (*m/z*) $[M+H]^+$ found 311.1069, $C_{22}H_{15}O_2$ requires 311.1067.

Methyl 4-((2-oxo-1,2,3,4-tetrahydroquinolin-6-yl)buta-1,3-diyn-1-yl)benzoate (1g)

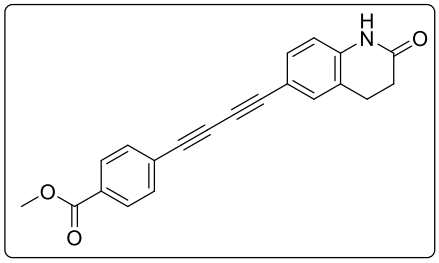

Synthesised according to GP 1 from terminal alkyne **17** (20.0 mg, 0.117 mmol) to give the title compound **1g** as an orange solid (15.2 mg, 44.5 µmol, 38%). **R$_f$** (10% EtOAc in petroleum ether 40-60) = 0.40. **MP** 264–267 °C. **IR** (cm^{-1}) 3165 (N–H), 2211 (C≡C), 1720 (C=O), 1676 (C=O), 1602 (C=C), 1500 (C=C). **^{1}H NMR** (500 MHz, DMSO-d_6) δ 10.35 (s, 1H, N*H*), 7.98 (d, *J* = 8.6 Hz, 2H, Ar*H*), 7.73 (d, *J* = 8.6 Hz, 2H, Ar*H*), 7.48 – 7.40 (m, 2H, Ar*H*), 6.89 (d, *J* = 8.2 Hz, 1H, Ar*H*), 3.87 (s, 3H, C*H*$_3$), 2.89 (t, *J* = 7.6 Hz, 2H, C*H*$_2$), 2.50 – 2.44 (m, 2H, C*H*$_2$). **^{13}C NMR** (126 MHz, DMSO-d_6) δ 170.18 (C), 165.47 (C), 140.20 (C), 132.62 (2CH), 131.98 (CH), 131.93 (CH), 130.10 (C), 129.42 (2CH), 125.43 (C), 124.28 (C), 115.39 (CH), 112.79 (C), 84.02 (C), 80.29 (C), 76.58 (C), 72.14 (C), 52.41 (CH_3),

29.95 (CH_2), 24.35 (CH_2). **HRMS-ESI+** (*m/z*) $[M+H]^+$ found 330.1125, $C_{21}H_{16}NO_3$ requires 330.1125.

Methyl-4-((2,4-dioxo-1,2,3,4-tetrahydroquinazolin-6-yl)buta-1,3-diyn-1-yl)benzoate (1h)

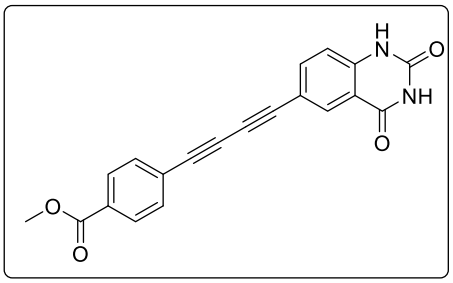

Synthesised according to GP 1 from terminal alkyne **18** (27.9 mg, 0.150 mmol) to give the title compound **1h** as a brown solid (33.1 mg, 96.0 µmol, 64%). $\mathbf{R_f}$ (50% EtOAc + 0.1% AcOH in petroleum ether 40-60) = 0.25. **^{1}H NMR** (601 MHz, DMSO-d_6) δ 11.48 (s, 1H, N*H*), 11.43 (s, 1H, N*H*), 8.05 (d, *J* = 2.0 Hz, 1H, Ar*H*), 7.99 (d, 2H, *J* = 8.5 Hz, Ar*H*), 7.86 (dd, *J* = 8.5, 2.0 Hz, 1H, Ar*H*), 7.76 (d, 2H, *J* = 8.5 Hz, Ar*H*), 7.21 (d, *J* = 8.5 Hz, 1H, Ar*H*), 3.88 (s, 3H, C*H*$_3$). **^{13}C NMR** (151 MHz, DMSO-d_6) δ 165.43 (C), 161.74 (C), 149.98 (C), 141.89 (C), 138.40 (CH), 132.71 (2CH), 131.40 (CH), 130.27 (C), 129.42 (2CH), 125.13 (C), 116.27 (CH), 114.80 (C), 113.59 (C), 82.39 (C), 80.69 (C), 76.18 (C), 72.88 (C), 52.41 (CH_3). **HRMS-ESI+** (*m/z*) $[M+Na]^+$ found 367.0694, $C_{20}H_{12}N_2O_4Na$ requires 367.0689.

6-((Trimethylsilyl)ethynyl)-3,4-dihydroquinolin-2(1*H*)-one (15)

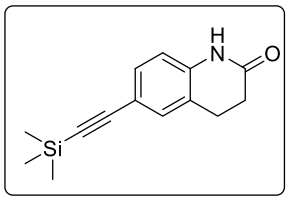

To a mixture of $PdCl_2(PPh_3)_2$ (14.0 mg, 0.02 mmol) and CuI (1.90 mg, 0.01 mmol) in pyridine (0.30 mL) and DMF (0.30 mL) under N_2 was added 6-bromo-3,4-dihydro-1*H*-quinolin-2-one **13** (226 mg, 1.00 mmol) in Et_3N (0.20 mL, 2.00 mmol). To the reaction mixture was added dropwise ethynyltri(methyl)silane (0.28 mL, 2.00 mmol). The reaction mixture was heated to 90 °C and subjected to microwave irradiation for 4 h. The volatile components were removed *in vacuo* and the residue was redissolved in DCM (5 mL) and H_2O (5 mL). The aqueous layer was extracted with (3 × 10 mL). The combined organic layers were washed with H_2O (3 × 10 mL) and NaCl (10 mL, sat. aq.), dried over $MgSO_4$, and concentrated *in vacuo*. The crude product was purified by silica gel column chromatography (0 → 40% EtOAc in petroleum ether 40-60) to afford the title compound **15** as a brown solid (134 mg, 0.55 mmol, 55%). $\mathbf{R_f}$ (40% EtOAc in petroleum ether 40-60) = 0.69. **IR** (cm^{-1}) 3203 (N–H), 2153 (C≡C), 1680 (C=O), 1613 (C=C), 1503 (C=C). **^{1}H NMR** (601 MHz, DMSO-d_6) δ 10.24 (s, 1H, N*H*), 7.28 (d, *J* = 1.8 Hz, 1H, Ar*H*), 7.23 (dd, *J* = 8.2, 1.8 Hz, 1H, Ar*H*),

6.81 (d, *J* = 8.2 Hz, 1H, Ar*H*), 2.85 (t, *J* = 7.6 Hz, 2H, CH_2), 2.47 – 2.41 (m, 2H, CH_2), 0.21 (s, 9H, CH_3). **^{13}C NMR** (151 MHz, DMSO-d_6) δ 170.13 (C), 138.95 (C), 131.09 (CH), 130.67 (CH), 123.90 (C), 115.24 (C), 115.07 (CH), 105.60 (C), 92.45 (C), 30.06 (CH_2), 24.30 (CH_2), -0.01 ($3CH_3$).

^{1}H and ^{13}C NMR spectroscopic data are in good agreement with the literature.[239]

6-((trimethylsilyl)ethynyl)quinazoline-2,4(1*H*,3*H*)-dione (16)

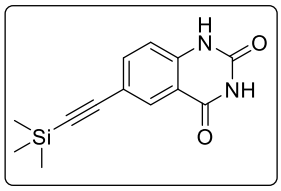

To a mixture of $PdCl_2(PPh_3)_2$ (21.0 mg, 0.03 mmol) and CuI (2.85 mg, 0.02 mmol) in pyridine (0.50 mL) and DMF (0.50 mL) under N_2 was added 6-(bromoethynyl)quinazoline-2,4(1*H*,3*H*)-dione **14** (362 mg, 1.50 mmol) in Et_3N (0.30 mL, 3.00 mmol). To the reaction mixture was added dropwise ethynyltri(methyl)silane (0.42 mL, 3.00 mmol). The reaction mixture was heated to 100 °C and subjected to microwave irradiation for 6 h. The volatile components were removed *in vacuo* and the crude product was purified by silica gel column chromatography (0 → 70% EtOAc in petroleum ether 40-60) to afford the title compound **16** as a yellow solid (284 mg, 1.10 mmol, 73%). **R_f** (50% EtOAc in petroleum ether 40-60) = 0.32. **^{1}H NMR** (500 MHz, DMSO-d_6) δ 11.41 (s, 1H, N*H*), 11.33 (s, 1H, N*H*), 7.86 (d, *J* = 1.9 Hz, 1H, Ar*H*), 7.68 (dd, *J* = 8.4, 1.9 Hz, 1H, Ar*H*), 7.14 (dd, *J* = 8.5, 0.5 Hz, 1H, Ar*H*), 0.23 (s, 9H, CH_3). **^{13}C NMR** (126 MHz, DMSO-d_6) δ 161.94 (C), 150.05 (C), 140.94 (C), 137.52 (CH), 130.24 (CH), 115.95 (C), 115.87 (CH), 114.53 (C), 104.00 (C), 93.97 (C), -0.15 ($3CH_3$). **HRMS-ESI+** (*m/z*) $[M+H]^+$ found 259.0973, $C_{13}H_{15}N_2O_2Si$ requires 259.0897.

6-Ethynyl-3,4-dihydroquinolin-2(1*H*)-one (17)

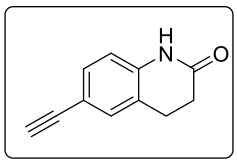

To a solution of **15** (131 mg, 0.535 mmol) in MeOH (2 mL) was added K_2CO_3 (7.4 mg, 0.05 mmol). The reaction mixture was stirred for 24 h at RT. The solvent was removed *in vacuo* and the residue was redissolved in a mixture of DCM (5 mL) and H_2O (5 mL). The aqueous layer was extracted with DCM (2 × 5 mL). The combined organic layers were washed with NaCl (5 mL, sat. aq.), dried over $MgSO_4$, and concentrated *in vacuo* to afford the title compound **17** as an orange solid (87.8 mg, 0.513 mmol, 96%). The desired compound was carried forward without the need for further purification. **R_f** (40% EtOAc in petroleum ether 40-60) = 0.35. **IR** (cm^{-1}) 3250 (N–H), 2103 (C≡C), 1663 (C=O), 1613 (C=C), 1497 (C=C). **^{1}H NMR** (500 MHz, DMSO-d_6) δ 10.22 (s, 1H, N*H*), 7.29 (d, *J* = 1.8 Hz, 1H, Ar*H*), 7.25 (dd, *J* = 8.2, 1.8 Hz, 1H, Ar*H*),

6.83 (d, *J* = 8.2 Hz, 1H, Ar*H*), 4.01 (s, 1H, C*H*), 2.86 (t, *J* = 7.3 Hz, 2H, CH_2), 2.48 – 2.41 (m, 2H, CH_2). **^{13}C NMR** (126 MHz, DMSO-d_6) δ 170.13 (C), 138.91 (C), 131.07 (CH), 130.77 (CH), 123.93 (C), 115.10 (CH), 114.79 (C), 83.67 (C), 79.25 (CH), 30.07 (CH_2), 24.38 (CH_2).

^{1}H and ^{13}C NMR spectroscopic data are in good agreement with the literature.[239]

6-ethynylquinazoline-2,4(1*H*,3*H*)-dione (18)

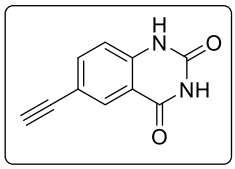

To a solution of **16** (129 mg, 0.500 mmol) in MeOH (2 mL) was added K_2CO_3 (7.4 mg, 0.05 mmol). The reaction mixture was stirred for 24 h at RT. The solvent was removed *in vacuo* and the residue was resuspended in H_2O (5 mL). The resultant precipitate was filtered and washed consecutively with H_2O (2 × 5 mL) and petroleum ether 40-60 (2 × 5 mL) to afford the title compound **18** as a beige solid (93.1 mg, 0.500 mmol, quant.). The desired compound was carried forward without the need for further purification. **R_f** (50% EtOAc in petroleum ether 40-60) = 0.25. **^{1}H NMR** (500 MHz, DMSO-d_6) δ 11.40 (s, 1H, N*H*), 11.31 (s, 1H, N*H*), 7.89 (d, *J* = 1.9 Hz, 1H, Ar*H*), 7.71 (dd, *J* = 8.4, 1.9 Hz, 1H, Ar*H*), 7.16 (d, *J* = 8.4 Hz, 1H, Ar*H*), 4.19 (s, 1H, CH). **^{13}C NMR** (126 MHz, DMSO-d_6) δ 161.97 (C), 150.05 (C), 140.97 (C), 137.75 (CH), 130.18 (CH), 115.98 (C), 115.41 (CH), 114.54 (C), 82.35 (C), 80.52 (CH). **HRMS-ESI+** (*m/z*) $[M+H]^+$ found 187.0518, $C_{10}H_7N_2O_2$ requires 187.0502.

4-(Phenylbuta-1,3-diyn-1-yl)benzoic acid (23a)

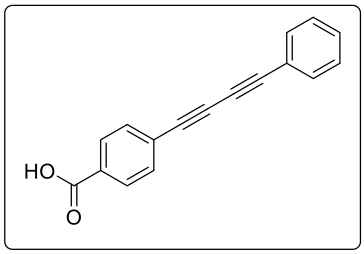

Synthesised according to GP 2 from ester **1a** (64.8 mg, 0.249 mmol) to give the title compound **23a** as a yellow solid (57.4 mg, 0.234 mmol, 94%). **R_f** (5% MeOH in DCM) = 0.30. **IR** (cm^{-1}) 3203 (O–H), 2214 (C≡C), 2175 (C≡C), 1640 (C=O). **^{1}H NMR** (500 MHz, DMSO-d_6) δ 13.25 (br s, 1H, CO_2H) 7.98 (d, *J* = 8.5 Hz, 2H, Ar*H*), 7.73 (d, *J* = 8.5 Hz, 2H, Ar*H*), 7.67 – 7.62 (m, 2H, Ar*H*), 7.56 – 7.43 (m, 3H, Ar*H*). **^{13}C NMR** (126 MHz, DMSO-d_6) δ 166.47 (C), 132.57 (2CH), 132.49 (2CH), 131.69 (C) 130.26 (CH), 129.56 (2CH), 128.96 (2CH), 124.62 (C), 120.11 (C), 83.07 (C), 80.88 (C), 75.76 (C), 73.17 (C).

^{1}H and ^{13}C NMR spectroscopic data are in good agreement with the literature.[240]

4-((5,6,7,8-Tetrahydronaphthalen-2-yl)buta-1,3-diyn-1-yl)benzoic acid (23b)

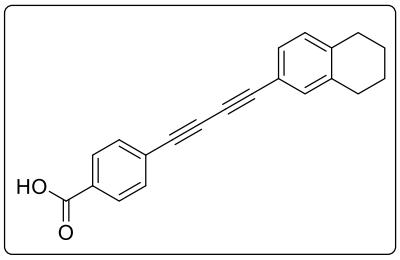

Synthesised according to GP 2 from ester **1b** (153 mg, 0.487 mmol) to give the title compound **23b** as a white solid (120 mg, 0.398 mmol, 82%). $\mathbf{R_f}$ (5% MeOH in DCM) = 0.33. **MP** 305–307 °C. **IR** (cm^{-1}) 2212 (C≡C), 1682 (C=O), 1603 (C=C). **^{1}H NMR** (500 MHz, DMSO-d_6) δ 7.86 (d, *J* = 8.1 Hz, 2H, Ar*H*), 7.52 (d, *J* = 8.1 Hz, 2H, Ar*H*), 7.33 – 7.27 (m, 2H, Ar*H*), 7.11 (d, *J* = 8.4 Hz, 1H, Ar*H*), 2.76 – 2.69 (m, 4H, CH_2), 1.77 – 1.69 (m, 4H, CH_2). **^{13}C NMR** (126 MHz, DMSO-d_6) δ 165.95 (C), 140.29 (C), 138.07 (C), 133.38 (CH), 133.16 (2CH), 132.95 (C), 130.67 (CH), 130.03 (CH), 129.91 (2CH), 125.83 (C), 117.37 (C), 84.38 (C), 80.74 (C), 76.88 (C), 72.77 (C), 29.33 (CH_2), 28.88 (CH_2), 22.78 ($2CH_2$). **HRMS-ESI-** (*m/z*) $[M-H]^-$ found 299.1061, $C_{21}H_{15}O_2$ requires 299.1078.

4-(Cyclohexylbuta-1,3-diyn-1-yl)benzoic acid (23c)

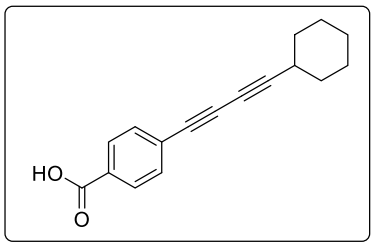

Synthesised according to GP 2 from ester **1c** (131 mg, 0.491 mmol) to give the title compound **23c** as a beige solid (107 mg, 0.422 mmol, 86%). $\mathbf{R_f}$ (5% MeOH in DCM) = 0.42. **MP** 255–259 °C. **IR** (cm^{-1}) 3280 (O–H), 2235 (C≡C), 1686 (C=O), 1603 (C=C), 1583 (C=C), 1539 (C=C). **^{1}H NMR** (500 MHz, DMSO-d_6) δ 13.21 (br s, 1H, CO_2H), 7.92 (d, *J* = 8.6 Hz, 2H, Ar*H*), 7.64 (d, *J* = 8.6 Hz, 2H, Ar*H*), 2.71 – 2.62 (m, 1H, C*H*), 1.84 – 1.75 (m, 2H, CH_2), 1.69 – 1.59 (m, 2H, CH_2), 1.52 –1.38 (m, 3H, CH_2 and CH_ACH_B), 1.37 –1.28 (m, 3H, CH_2 and CH_ACH_B). **^{13}C NMR** (126 MHz, DMSO-d_6) δ 166.54 (C), 132.67 (C), 132.44 (2CH), 129.46 (2CH), 128.73 (C), 90.54 (C), 76.45 (C) 74.62 (C), 64.65 (C), 31.44 ($2CH_2$), 28.77 (CH), 25.08 (CH_2), 24.09 ($2CH_2$). **HRMS-ESI+** (*m/z*) $[M+H]^+$ found 253.1242, $C_{17}H_{17}O_2$ requires 253.1223.

4-((2-Oxo-1,2,3,4-tetrahydroquinolin-6-yl)buta-1,3-diyn-1-yl)benzoic acid (23g)

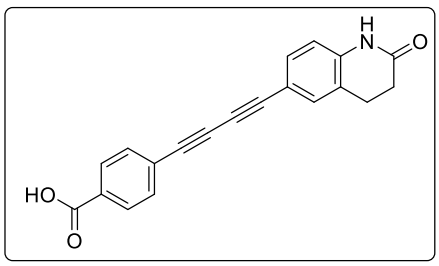

Synthesised according to GP 2 from ester **1g** (101 mg, 0.307 mmol) to give the title compound **23g** as a white solid (68.2 mg, 0.215 mmol, 70%). $\mathbf{R_f}$ (20% MeOH in DCM) = 0.82. **MP** 299–302 °C. **IR** (cm^{-1}) 3191 (N–H), 2209 (C≡C), 1681 (C=O), 1603 (C=C), 1500 (C=C). **^{1}H NMR** (500 MHz,

DMSO-d_6) δ 13.22 (br s, 1H, CO_2H), 10.35 (s, 1H, N*H*), 7.96 (d, *J* = 8.7 Hz, 2H, Ar*H*), 7.70 (d, *J* = 8.7 Hz, 2H, Ar*H*), 7.46 (d, *J* = 1.8 Hz, 1H, Ar*H*), 7.42 (dd, *J* = 8.2, 1.8 Hz, 1H, Ar*H*), 6.89 (d, *J* = 8.2 Hz, 1H, Ar*H*), 2.89 (t, *J* = 7.6 Hz, 2H, CH_2), 2.50 – 2.44 (m, 2H, CH_2). **^{13}C NMR** (126 MHz, DMSO-d_6) δ 170.17 (C), 166.49 (C), 140.16 (C), 132.46 (2CH), 131.96 (CH), 131.91 (CH), 131.39 (C), 129.54 (2CH), 124.95 (C), 124.27 (C), 115.38 (CH), 112.84 (C), 83.82 (C), 80.48 (C), 76.26 (C), 72.18 (C), 29.95 (CH_2), 24.35 (CH_2). **HRMS-ESI+** (*m/z*) $[M+H]^+$ found 316.0964, $C_{20}H_{14}NO_3$ requires 316.0968.

4-((2,4-dioxo-1,2,3,4-tetrahydroquinazolin-6-yl)buta-1,3-diyn-1-yl)benzoic acid (23h)

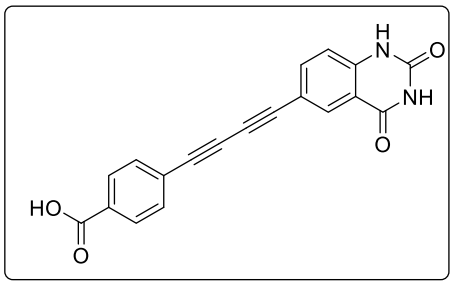

Synthesised according to GP 2 ester **1h** (30.0 mg, 87.1 µmol) to give the title compound **23h** as a beige solid (20.7 mg, 62.7 µmol, 72%). **R_f** (20% MeOH in DCM) = 0.51. **^{1}H NMR** (601 MHz, DMSO-d_6) δ 13.24, (s, 1H, O*H*), 11.48 (s, 1H, N*H*), 11.43 (s, 1H, N*H*), 8.04 (d, *J* = 2.0 Hz, 1H, Ar*H*), 7.99 – 7.95 (m, 2H, Ar*H*), 7.86 (dd, *J* = 8.5, 2.0 Hz, 1H, Ar*H*), 7.75 – 7.71 (m, 2H, Ar*H*), 7.21 (d, *J* = 8.5 Hz, 1H, Ar*H*). **^{13}C NMR** (151 MHz, DMSO-d_6) δ 166.47 (C), 161.76 (C), 149.99 (C), 141.88 (C), 138.41 (CH), 132.58 (2CH), 131.55 (CH), 131.38 (C), 129.56 (2CH), 124.68 (C), 116.28 (CH), 114.81 (C), 113.65 (C), 82.22 (C), 80.90 (C), 75.88 (C), 72.94 (C).

4-(4-Fluoro-3-(4-(4-(phenylbuta-1,3-diyn-1-yl)benzoyl)piperazine-1-carbonyl)benzyl)-phthalazin-1(2*H*)-one (26a)

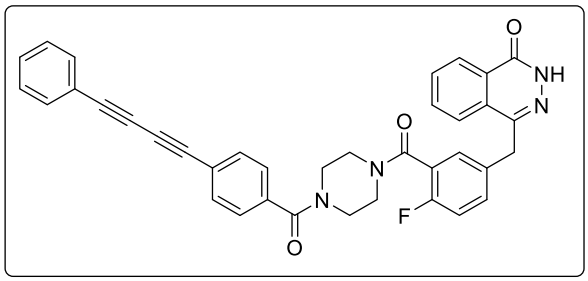

Synthesised according to GP 3 from carboxylic acid **23a** (43.0 mg, 0.175 mmol) to give the title compound **26a** as a yellow solid (76.1 mg, 0.128 mmol, 73%). **R_f** (5% MeOH in DCM) = 0.36. **MP** 237–238 °C. **IR** (cm^{-1}) 3169 (N–H), 2212 (C≡C), 1670 (C=O), 1627 (C=O), 1000 (C–F). **^{1}H NMR** (500 MHz, DMSO-d_6) δ 12.58 (s, 1H, N*H*), 8.26 (d, *J* = 7.9 Hz, 1H, Ar*H*), 7.95 –7.83 (m, 3H, Ar*H*), 7.69 (d, *J* = 7.8 Hz, 2H, Ar*H*), 7.66 – 7.60 (m, 2H, Ar*H*), 7.54 – 7.42 (m, 6H, Ar*H*), 7.37 – 7.34 (m, 1H, Ar*H*), 7.25 – 7.20 (m, 1H, Ar*H*), 4.33 (s, 2H, CH_2^{mb}), 3.67 – 3.11 (m,

8H, CH_2^{pip}). **^{13}C NMR** (126 MHz, DMSO-d_6) δ 168.22 (C), 164.05 (C), 159.36 (C), 156.36 (d, $^1J_{CF}$ = 244.4 Hz, C), 144.79 (C), 136.67 (C), 134.83 (d, $^3J_{CF}$ = 6.1 Hz, CH), 133.46 (CH), 132.47 (2CH), 132.45 (2CH), 131.77 (d, $^3J_{CF}$ = 7.8 Hz, CH), 131.52 (CH), 130.17 (CH), 129.07 (C), 128.95 (2CH), 127.89 (C), 127.57 (2CH), 126.06 (CH), 125.44 (CH), 123.47 (d, $^2J_{CF}$ = 18.3 Hz, C), 121.64 (C), 120.22 (C), 118.04 (C), 115.93 (d, $^2J_{CF}$ = 21.3 Hz, CH), 82.46 (C), 81.08 (C), 74.54 (C), 73.32 (C), 46.02 (2CH_2), 40.93 (2CH_2), 36.41 (CH_2). **HRMS-ESI+** (*m/z*) $[M+H]^+$ found 595.2138, $C_{37}H_{27}N_4O_3F$ requires 595.2140. *(mb = methylene bridge, pip = piperazine)*

4-(4-Fluoro-3-(4-(4-((5,6,7,8-tetrahydronaphthalen-2-yl)buta-1,3-diyn-1-yl)benzoyl)-piperazine-1-carbonyl)benzyl)phthalazin-1(2*H*)-one (26b)

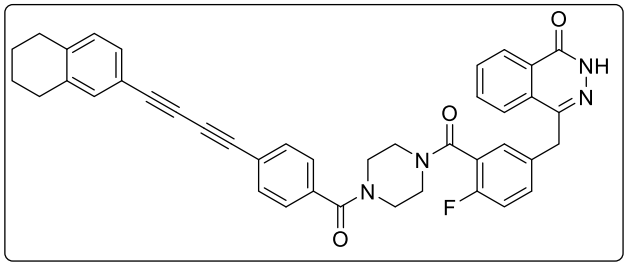

Synthesised according to GP 3 from carboxylic acid **23b** (58.9 mg, 0.196 mmol) to give the title compound **26b** as a yellow solid (167 mg, 0.476 mmol, 87%). **R_f** (5% MeOH in DCM) = 0.37. **MP** 179–183 °C. **IR** (cm^{-1}) 3165 (N–H), 2214 (C≡C), 1659 (C=O), 1630 (C=O), 1000 (C–F). **^{1}H NMR** (500 MHz, DMSO-d_6) δ 12.58 (s, 1H, N*H*), 8.26 (d, *J* = 7.8 Hz, 1H, Ar*H*), 8.01 – 7.77 (m, 3H, Ar*H*), 7.67 (d, *J* = 7.9 Hz, 2H, Ar*H*), 7.54 – 7.40 (m, 3H, Ar*H*), 7.37 – 7.34 (m, 1H, Ar*H*), 7.34 – 7.28 (m, 2H, Ar*H*), 7.25 – 7.22 (m, 1H, Ar*H*), 7.12 (d, *J* = 8.4 Hz, 1H, Ar*H*), 4.33 (s, 2H, CH_2^{mb}), 3.69 – 3.14 (m, 8H, CH_2^{pip}), 2.76 – 2.70 (m, 4H, CH_2^{tet}), 1.76 – 1.70 (m, 4H, CH_2^{tet}). **^{13}C NMR** (126 MHz, DMSO-d_6) δ 168.24 (C), 164.05 (C), 159.35 (C), 156.36 (d, $^1J_{CF}$ = 244.4 Hz, C), 144.79 (C), 139.63 (C), 137.54 (C), 136.53 (C), 134.82 (d, $^3J_{CF}$ = 5.2 Hz, CH), 133.45 (CH), 132.82 (CH), 132.43 (2CH), 131.78 (d, $^3J_{CF}$ = 6.6 Hz, CH), 131.52 (CH), 129.52 (CH), 129.39 (CH), 129.07 (C), 128.91 (C), 127.88 (C), 127.56 (2CH), 126.05 (CH), 125.44 (CH), 123.42 (d, $^2J_{CF}$ = 18.0 Hz, C), 121.82 (C), 118.04 (C), 117.03 (C), 115.93 (d, $^2J_{CF}$ = 18.0 Hz, CH) , 83.05 (C), 80.63 (C), 74.81 (C), 72.46 (C), 46.02 (2CH_2), 40.93 (2CH_2), 36.41 (CH_2), 28.82 (CH_2), 28.39 (CH_2), 22.29 (2CH_2). **HRMS-ESI+** (*m/z*) $[M+H]^+$ found 649.2590, $C_{41}H_{34}N_4O_2F$ requires 649.2609. *(mb = methylene bridge, pip = piperazine, tet = tetralin)*

4-(3-(4-(4-(Cyclohexylbuta-1,3-diyn-1-yl)benzoyl)piperazine-1-carbonyl)-4-fluoro-benzyl)phthalazin-1(2*H*)-one (26c)

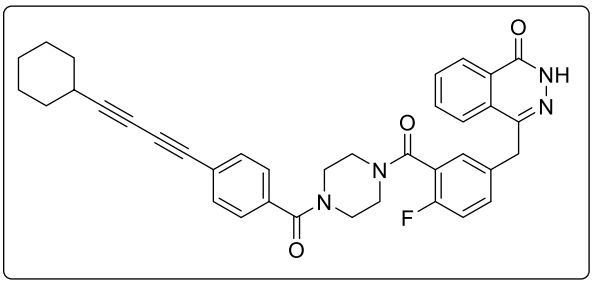

Synthesised according to GP 3 from carboxylic acid **23c** (97.8 mg, 0.388 mmol) to give the title compound **26c** as a beige solid (172 mg, 0.287 mmol, 74%). $\mathbf{R_f}$ (5% MeOH in DCM) = 0.34. **MP** 168–173 °C. **IR** (cm^{-1}) 3172 (N–H), 2238 (C≡C), 1637 (C=O), 1617 (C=O), 1001 (C–F). **^{1}H NMR** (500 MHz, DMSO-d_6) δ 12.58 (s, 1H, N*H*), 8.25 (d, *J* = 7.8 Hz, 1H, Ar*H*), 7.99 – 7.76 (m, 3H, Ar*H*), 7.61 (d, *J* = 7.7 Hz, 2H, Ar*H*), 7.43 (d, *J* = 7.7 Hz, 2H, Ar*H*), 7.38 – 7.27 (m, 2H, Ar*H*), 7.27 – 7.18 (m, 1H, Ar*H*), 4.33 (s, 2H, CH_2^{mb}), 3.82 – 3.07 (m, 8H, CH_2^{pip}), 2.72 – 2.62 (m, 1H, CH^{cy}), 1.84 – 1.76 (m, 2H, CH_2^{cy}), 1.69 – 1.58 (m, 2H, CH_2^{cy}), 1.50 – 1.36 (m, 3H, CH_2^{cy} and $CH_ACH_B^{cy}$), 1.34 – 1.28 (m, 3H, CH_2^{cy} and $CH_ACH_B^{cy}$). **^{13}C NMR** (126 MHz, DMSO-d_6) δ 168.28 (C), 164.04 (C), 159.35 (C), 157.35 (d, $^1J_{CF}$ = 244.7 Hz, C), 144.79 (C), 136.20 (C), 134.80 (d, $^3J_{CF}$ = 3.0 Hz, CH), 133.45 (CH), 132.38 (2CH), 131.74 (d, $^3J_{CF}$ = 7.6 Hz, CH), 131.51 (CH), 129.06 (C), 128.90 (C), 127.88 (C), 127.48 (2CH), 126.05 (CH), 125.44 (CH), 123.47 (d, $^2J_{CF}$ = 18.0 Hz, C), 122.13 (C), 115.92 (d, $^2J_{CF}$ = 22.1 Hz, CH), 89.86 (C), 75.24 (C), 74.72 (C), 64.73 (C), 46.20 ($2CH_2$), 41.10 ($2CH_2$), 36.41 (CH_2), 31.47 ($2CH_2$), 28.76 (CH), 25.08 (CH_2), 24.10 ($2CH_2$). **HRMS-ESI+** (*m/z*) $[M+H]^+$ found 601.2619, $C_{37}H_{33}N_4O_3F$ requires 601.2609. *(mb = methylene bridge, pip = piperazine, cy = cyclohexane)*

4-(4-Fluoro-3-(4-(4-((2-oxo-1,2,3,4-tetrahydroquinolin-6-yl)buta-1,3-diyn-1-yl)benzoyl)piperazine-1-carbonyl)benzyl)phthalazin-1(2*H*)-one (26g)

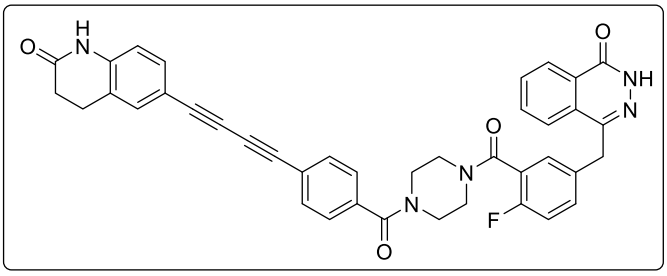

Synthesised according to GP 3 from carboxylic acid **23g** (20.9 mg, 66.0 µmol) to give the title compound **26g** as a yellow solid (21.4 mg, 32.3 µmol, 49%). $\mathbf{R_f}$ (5% MeOH in DCM) = 0.35. **MP** 248–249 °C. **IR** (cm^{-1}) 3196 (N–H), 2212 (C≡C), 1656 (C=O), 1639 (C=O), 1609 (C=O), 1004 (C–F).**^{1}H NMR** (500 MHz, DMSO-d_6) δ 12.59 (s, 1H, N*H*), 10.35 (s, 1H, N*H*), 8.26 (d, *J* = 7.9 Hz, 1H, Ar*H*), 8.02 – 7.77 (m, 3H, Ar*H*), 7.67 (d, *J* = 7.9 Hz, 2H, Ar*H*), 7.53 – 7.41 (m, 5H, Ar*H*), 7.41 – 7.34 (m, 1H, Ar*H*), 7.33 – 7.21 (m, 1H,

Ar*H*), 6.89 (d, *J* = 8.2 Hz, 1H, Ar*H*), 4.34 (s, 2H, CH_2^{mb}), 3.77 – 3.11 (m, 8H, CH_2^{pip}), 2.90 (t, *J* = 7.6 Hz, 2H, CH_2^{lac}), 2.49 – 2.46 (m, 2H, CH_2^{lac}). **^{13}C NMR** (151 MHz, DMSO-d_6) δ 170.17 (C), 164.05 (C), 159.36 (C), 156.36 (d, $^1J_{CF}$ = 243.2 Hz, C), 144.79 (C), 140.07 (C), 136.44 (C), 134.81 (CH), 133.46 (CH), 132.38 (2CH), 131.90 (CH), 131.86 (CH), 131.77 (d, $^3J_{CF}$ = 7.5 Hz, CH), 131.51 (CH), 129.07 (C), 128.9 (d, $^4J_{CF}$ = 12.6 Hz, C), 127.88 (C), 127.55 (2CH), 126.05 (CH), 125.44 (CH), 124.26 (C), 123.47 (d, $^2J_{CF}$ = 18.2 Hz, C), 121.91 (C), 115.91 (d, $^2J_{CF}$ = 21.7 Hz, CH), 115.37 (CH), 112.97 (C), 83.15 (C), 80.67 (C), 74.98 (C), 72.31 (C), 46.03 ($2CH_2$), 41.10 ($2CH_2$), 36.41 (CH_2), 29.96 (CH_2), 24.36 (CH_2). **HRMS-ESI+** (*m/z*) $[M+H]^+$ found 664.2355, $C_{40}H_{31}N_5O_4F$ requires 664.2357. *(mb = methylene bridge, pip = piperazine, lac = lactam)*

6-((4-(4-(2-fluoro-5-((4-oxo-3,4-dihydrophthalazin-1 yl)methyl)benzoyl)piperazine-1-carbonyl)phenyl)buta-1,3-diyn-1-yl)quinazoline-2,4(1*H*,3*H*)-dione (26h)

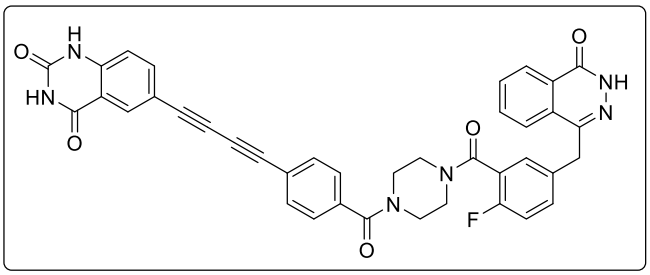

Synthesised according to GP 3 from carboxylic acid **23h** (15.5 mg, 46.9 µmol) to give the title compound **26h** as a yellow solid (19.4 mg, 28.6 µmol, 61%). **R_f** (10% MeOH in DCM) = 0.31. **^{1}H NMR** (500 MHz, DMSO-d_6) δ 12.58 (s, 1H, N*H*), 11.47 (s, 1H, N*H*), 11.41 (s, 1H, N*H*), 8.26 (d, *J* = 7.9 Hz, 1H, Ar*H*), 8.05 – 8.01 (d, *J* = 2.0 Hz, 1H, Ar*H*), 8.00 – 7.75 (m, 3H, Ar*H*), 7.85 (dd, *J* = 8.5, 2.0 Hz, 1H, Ar*H*), 7.69 (d, *J* = 7.8 Hz, 2H, Ar*H*), 7.53 – 7.41 (m, 3H, Ar*H*), 7.39 – 7.30 (m, 1H, Ar*H*), 7.28 – 7.22 (m, 1H, Ar*H*), 7.20 (d, *J* = 8.5 Hz, 1H, Ar*H*), 4.33 (s, 2H, CH_2^{mb}), 3.82 – 3.10 (m, 8H, CH_2^{pip}).**^{13}C NMR** (126 MHz, DMSO) δ 169.03 (C), 168.22 (C), 164.05 (C), 161.77 (C), 159.35 (C), 156.42 (d, $^1J_{CF}$ = 202.4 Hz, C), 155.38 (C), 149.99 (C), 144.79 (C), 141.81 (C), 138.38 (CH), 136.66 (CH), 134.82 (d, $^3J_{CF}$ = 2.5 Hz, CH), 133.45 (CH), 132.51 (2CH), 131.77 (d, $^3J_{CF}$ = 7.9 Hz, CH), 131.52 (CH), 131.30 (CH), 129.06 (C), 128.93 (d, $^4J_{CF}$ = 8.4 Hz, C), 127.88 (C), 127.57 (2CH), 126.05 (CH), 125.44 (CH), 123.49 (d, $^2J_{CF}$ = 17.6 Hz, C), 121.63 (C), 116.27 (C), 115.91 (d, $^2J_{CF}$ = 20.7 Hz, CH), 114.80 (C), 113.77 (C), 81.58 (C), 81.11 (C), 74.62 (C), 73.09 (C), 46.31 ($2CH_2$), 41.82 ($2CH_2$), 36.41 (CH_2). **HRMS-ESI+** (*m/z*) $[M+H]^+$ found 679.2196, $C_{39}H_{28}N_6O_5F$ requires 679.2100.

Methyl 5-(4-(phenylbuta-1,3-diyn-1-yl)benzamido)pentanoate (27a)

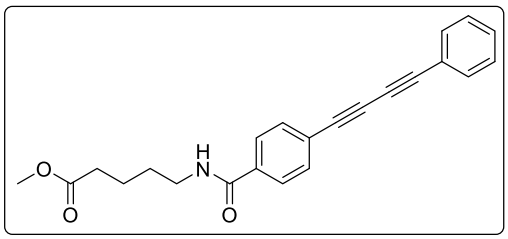

Synthesised according to GP 4 from carboxylic acid **23a** (47.4 mg, 0.192 mmol) to give the title compound **27a** as a white solid (56.4 mg, 0.157 mmol, 82%). $\mathbf{R_f}$ (50% EtOAc in petroleum ether 40-60) = 0.57. **MP** 129–130 °C. **IR** (cm^{-1}) 3306 (N–H), 2215 (C≡C), 1730 (C=O), 1633 (C=O), 1535 (C=C). **^{1}H NMR** (500 MHz, DMSO-d_6) δ 8.58 (t, *J* = 5.7 Hz, 1H, N*H*), 7.87 (d, *J* = 8.5 Hz, 2H, Ar*H*), 7.70 (d, *J* = 8.5 Hz, 2H, Ar*H*), 7.66 – 7.60 (m, 2H, Ar*H*), 7.53 – 7.42 (m, 3H, Ar*H*), 3.58 (s, 3H, CH_3) 3.30 – 3.22 (m, 2H, CH_2NH), 2.34 (t, *J* = 7.1 Hz, 2H, CH_2CO$_2$CH$_3$), 1.62 – 1.48 (m, 4H, CH_2CH_2). **^{13}C NMR** (126 MHz, DMSO-d_6) δ 173.25 (C), 165.11 (C), 135.42 (C), 132.46 (2CH), 132.32 (2CH), 130.18 (CH), 128.95 (2CH), 127.55 (2CH), 122.89 (C), 120.21 (C), 82.67 (C), 81.13 (C), 75.07 (C), 73.26 (C), 51.17 (CH_3), 38.46 (CH_2),* 32.89 (CH_2), 28.41 (CH_2), 21.92 (CH_2 **HRMS-ESI+** (*m/z*) $[M+H]^+$ found 360.1599, $C_{23}H_{22}NO_3$ requires 360.1594. **obscured by DMSO-d_6 signal.*

Methyl 5-(4-((5,6,7,8-tetrahydronaphthalen-2-yl)buta-1,3-diyn-1-yl)benzamido)-pentanoate (27b)

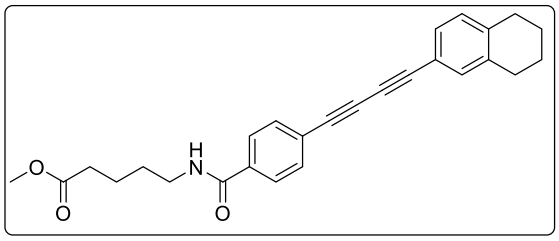

Synthesised according to GP 4 from carboxylic acid **23b** (120 mg, 0.398 mmol) to give the title compound **27b** as a beige solid (125 mg, 0.302 mmol, 76%). $\mathbf{R_f}$ (5% MeOH in DCM) = 0.87. **MP** 121–122 °C. **IR** (cm^{-1}) 2216 (C≡C), 1701 (C=O), 1640 (C=O), 1546 (C=C). **^{1}H NMR** (500 MHz, DMSO-d_6) δ 8.58 (t, *J* = 5.8 Hz, 1H, N*H*), 7.87 (d, *J* = 8.7 Hz, 2H, Ar*H*), 7.68 (d, *J* = 8.7 Hz, 2H, Ar*H*), 7.34 – 7.30 (m, 2H, Ar*H*), 7.12 (d, *J* = 8.5 Hz, 1H, Ar*H*), 3.58 (s, 3H, CH_3), 3.26 (dt ≡ q, *J* = 6.4 Hz, 2H, CH_2NH), 2.78 – 2.70 (m, 4H, CH_2^{tet}), 2.34 (t, *J* = 7.1 Hz, 2H, CH_2CO$_2$CH$_3$), 1.78 – 1.69 (m, 4H, CH_2^{tet}), 1.61 – 1.48 (m, 4H, CH_2CH_2). **^{13}C NMR** (126 MHz, DMSO) δ 173.25 (C), 165.12 (C), 139.65 (C), 137.55 (C), 135.29 (C), 132.82 (CH), 132.26 (2CH), 129.52 (CH), 129.40 (CH), 127.54 (2CH), 123.07 (C), 117.02 (C), 83.27 (C), 80.69 (C), 75.35 (C), 72.41 (C), 51.17 (CH_3), 38.80 (CH_2), 32.89 (CH_2), 28.83 (CH_2), 28.41 (CH_2), 28.39 (CH_2), 22.29 ($2CH_2$), 21.91 (CH_2). **HRMS-ESI+** (*m/z*) $[M+H]^+$ found 414.2059, $C_{27}H_{28}NO_3$ requires 414.2064. *(tet = tetralin)*

Methyl 5-(4-(cyclohexylbuta-1,3-diyn-1-yl)benzamido)pentanoate (27c)

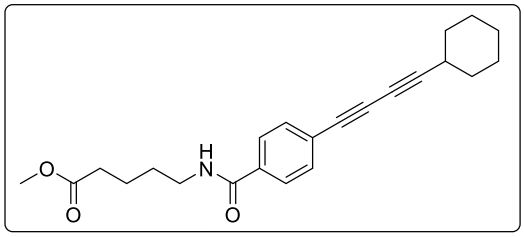

Synthesised according to GP 4 from carboxylic acid **23c** (175 mg, 0.695 mmol) to give the title compound **27c** as a white solid (239 mg, 0.653 mmol, 94%). $\mathbf{R_f}$ (50% EtOAc in petroleum ether 40-60) = 0.63. **MP** 129–130 °C. **IR** (cm^{-1}) 3332 (N–H), 2236 (C≡C), 1730 (C=O), 1630 (C=O), 1530 (C=C). **^{1}H NMR** (500 MHz, DMSO-d_6) δ 8.54 (t, *J* = 5.7 Hz, 1H, N*H*), 7.83 (d, *J* = 8.5 Hz, 2H, Ar*H*), 7.62 (d, *J* = 8.5 Hz, 2H, Ar*H*), 3.58 (s, 3H, CH_3) 3.25 (dt ≡ q, *J* = 6.3 Hz, 2H, CH_2NH), 2.71 – 2.61 (m, 1H, CH^{cy}), 2.34 (t, *J* = 7.1 Hz, 2H, CH_2CO$_2$CH$_3$), 1.82 – 1.76 (m, 2H, CH_2^{cy}), 1.69 – 1.60 (m, 2H, CH_2^{cy}), 1.60 – 1.50 (m, 4H, CH_2CH_2), 1.50 – 1.36 (m, 3H, CH_2^{cy} and CH_ACH$_B^{cy}$), 1.34 – 1.28 (m, 3H, CH_2^{cy} and CH$_A$CH_B^{cy}). **^{13}C NMR** (126 MHz, DMSO-d_6) δ 173.24 (C), 165.16 (C), 135.00 (C), 132.21 (2CH), 127.45 (2CH), 123.39 (C), 90.10 (C), 75.80 (C), 74.79 (C), 64.71 (C), 51.16 (CH_3), 38.64 (CH_2),* 32.89 (CH_2), 31.47 ($2CH_2$), 28.75 (CH), 28.41 (CH_2), 25.08 (CH_2), 24.08 ($2CH_2$), 21.91 (CH_2). **HRMS-ESI+** (*m/z*) $[M+H]^+$ found 366.2071, $C_{23}H_{28}NO_3$ requires 366.2064. *(cy = cyclohexane) *obscured by DMSO-d_6 signal.*

5-(4-(Phenylbuta-1,3-diyn-1-yl)benzamido)pentanoic acid (28a)

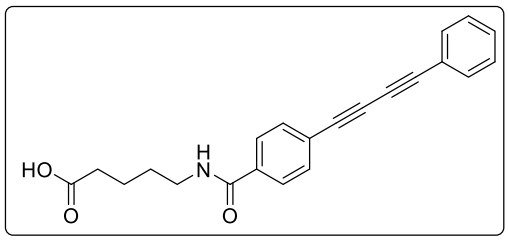

Synthesised according to GP 2 from ester **27a** (125 mg, 0.348 mmol) to give the title compound **28a** as a yellow solid (108 mg, 0.313 mmol, 90%). $\mathbf{R_f}$ (2.5% MeOH in DCM) = 0.49. **MP** 143–145 °C **IR** (cm^{-1}) 3303 (N–H), 2214 (C≡C), 1690 (C=O), 1622 (C=O), 1533 (C=C). **^{1}H NMR** (500 MHz, DMSO-d_6) δ 8.58 (t, *J* = 5.7 Hz, 1H, N*H*), 7.87 (d, *J* = 8.2 Hz, 2H, Ar*H*), 7.69 (d, *J* = 8.2 Hz, 2H, Ar*H*), 7.65 – 7.60 (m, 2H, Ar*H*), 7.54 – 7.42 (m, 3H, Ar*H*), 3.29 – 3.22 (m, 2H, CH_2NH), 2.27 – 2.21 (m, 2H, CO$_2$CH_2), 1.57 – 1.50 (m, 4H, CH_2CH_2). **^{13}C NMR** (126 MHz, DMSO-d_6) δ 174.42 (C), 165.16 (C), 135.47 (C), 132.48 (2CH), 132.35 (2CH), 130.20 (CH), 128.97 (2CH), 127.59 (2CH), 122.92 (C), 120.24 (C), 82.69 (C), 81.17 (C), 75.11 (C), 73.30 (C), 39.17 (CH_2),* 33.34 (CH_2), 28.54 (CH_2), 22.02 (CH_2). **HRMS** (ESI) $[M+H]^+$ found 346.1432, $C_{22}H_{20}NO_3$ requires 346.1438. **obscured by DMSO-d_6 signal.*

5-(4-((5,6,7,8-Tetrahydronaphthalen-2-yl)buta-1,3-diyn-1-yl)benzamido)-pentanoic acid (28b)

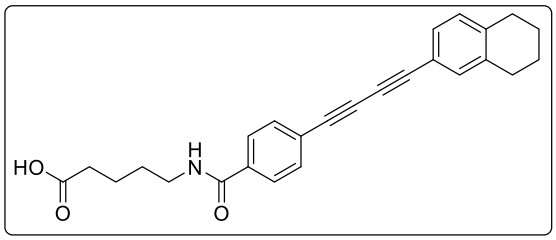

Synthesised according to GP 2 from ester **27b** (125 mg, 0.303 mmol) to give the title compound **28b** as a yellow solid (108 mg, 0.271 mmol, 90%). $\mathbf{R_f}$ (5% MeOH in DCM) = 0.11. **MP** 181–18 °C. **IR** (cm^{-1}) 3303 (N–H), 2215 (C≡C), 1694 (C=O), 1626 (C=O), 1530 (C=C). **^{1}H NMR** (500 MHz, DMSO-d_6) δ 8.59 (t, *J* = 5.7 Hz, 1H, N*H*), 7.87 (d, *J* = 8.5 Hz, 2H, Ar*H*), 7.68 (d, *J* = 8.5 Hz, 2H, Ar*H*), 7.35 – 7.27 (m, 2H, Ar*H*), 7.12 (d, *J* = 8.5 Hz, 1H, Ar*H*), 3.29 – 3.23 (m, 2H, CH_2NH), 2.77 – 2.68 (m, 4H, CH_2^{tet}), 2.26 – 2.20 (m, 2H, CO_2CH_2), 1.76 – 1.70 (m, 4H, CH_2^{tet}), 1.56 – 1.50 (m, 4H, CH_2CH_2). **^{13}C NMR** (126 MHz, DMSO-d_6) δ 174.53 (C), 165.06 (C), 139.68 (C), 137.58 (C), 135.34 (C), 132.85 (CH), 132.28 (2CH), 129.55 (CH), 129.43 (CH), 127.57 (2CH), 123.09 (C), 117.04 (C), 83.25 (C), 80.72 (C), 75.32 (C), 72.43 (C), 38.83 (CH_2),* 33.89 (CH_2), 28.83 (CH_2), 28.50 (CH_2), 28.39 (CH_2), 22.29 ($2CH_2$), 22.19 (CH_2). **HRMS-ESI+** (*m/z*) $[M+H]^+$ found 400.1894, $C_{26}H_{26}NO_3$ requires 400.1907. *(tet = tetralin). *obscured by DMSO-d_6 signal.*

5-(4-(Cyclohexylbuta-1,3-diyn-1-yl)benzamido)pentanoic acid (28c)

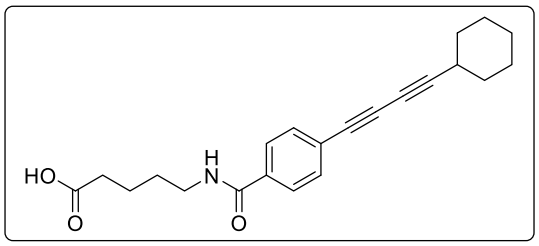

Synthesised according to GP 2 from ester **27c** (200 mg, 0.547 mmol) to give the title compound **28c** as a yellow solid (167 mg, 0.476 mmol, 87%). $\mathbf{R_f}$ (5% MeOH in DCM) = 0.67. **MP** 200–201 °C. **IR** (cm^{-1}) 3336 (N–H), 2238 (C≡C), 1676 (C=O), 1625 (C=O), 1536 (C=C). **^{1}H NMR** (500 MHz, DMSO-d_6) δ 8.58 (t, *J* = 5.7 Hz, 1H, N*H*), 7.84 (d, *J* = 8.7 Hz, 2H, Ar*H*), 7.62 (d, *J* = 8.7 Hz, 2H, Ar*H*), 3.29 – 3.22 (m, 2H, CH_2NH), 2.71 – 2.63 (m, 1H, CH^{cy}), 2.26 – 2.20 (m, 2H, CO_2CH_2), 1.84 – 1.76 (m, 2H, CH_2^{cy}), 1.69 – 1.60 (m, 2H, CH_2^{cy}), 1.57 – 1.50 (m, 4H, CH_2CH_2), 1.50 – 1.36 (m, 3H, CH_2^{cy} and $CH_ACH_B^{cy}$), 1.34 – 1.28 (m, 3H, CH_2^{cy} and $CH_ACH_B^{cy}$). **^{13}C NMR** (126 MHz, DMSO-d_6) δ 174.46 (C), 165.15 (C), 135.05 (C), 132.21 (2CH), 127.47 (2CH), 123.38 (C), 90.10 (C), 75.80 (C), 74.81 (C), 64.73 (C), 38.82 (CH_2),* 33.51 (CH_2), 31.48 ($2CH_2$), 28.77 (CH), 28.53 (CH_2), 25.10 (CH_2), 24.09 ($2CH_2$), 22.07 (CH_2). **HRMS-ESI+** (*m/z*) $[M+Na]^+$ found 374.1736, $C_{22}H_{25}NO_3Na$ requires 374.1732. *(cy = cyclohexane). *obscured by DMSO-d_6 signal.*

_N_-(5-(4-(2-Fluoro-5-((4-oxo-3,4-dihydrophthalazin-1-yl)methyl)benzoyl)piperazin-1-yl)-5-oxopentyl)-4-(phenylbuta-1,3-diyn-1-yl)benzamide (29a)[1]

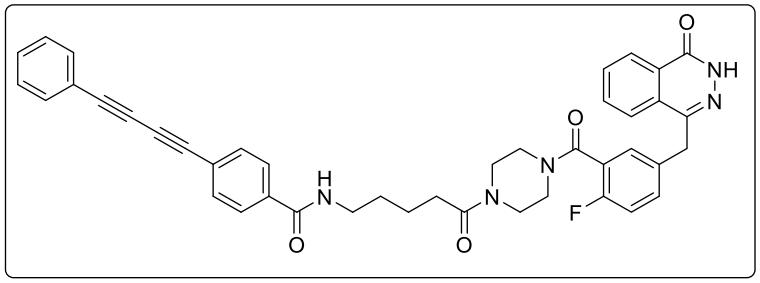

Synthesised according to GP 3 from carboxylic acid **28a** (54.2 mg, 0.157 mmol) to give the title compound **29a** as a grey solid (92.2 mg, 0.133 mmol, 85%). **R_f** (5% MeOH in DCM) = 0.40. **MP** 154–157 °C. **IR** (cm^{-1}) 2212 (C≡C), 1669 (C=O), 1647 (C=O), 1633 (C=O), 1536 (C=O), 1008 (C–F). **^{1}H NMR** (500 MHz, DMSO-d_6) δ 12.59 (s, 1H N*H*), 8.67 – 8.53 (m, 1H, N*H*), 8.27 (d, *J* = 7.8 Hz, 1H, Ar*H*), 7.98 – 7.94 (m, 1H, Ar*H*), 7.93 – 7.81 (m, 4H, Ar*H*), 7.70 (t, *J* = 8.3 Hz, 2H, Ar*H*), 7.63 (d, *J* = 8.6 Hz, 2H, Ar*H*), 7.54 – 7.41 (m, 4H, Ar*H*), 7.40 – 7.34 (m, 1H, Ar*H*), 7.24 (t, *J* = 8.7 Hz, 1H, Ar*H*), 4.34 (s, 2H, CH_2^{mb}), 3.69 – 3.48 (m, 6H, CH_2^{pip}), 3.30 – 3.25 (m, 2H, CH_2^{pip}), 3.21 – 3.11 (m, 2H, C*H*$_2$NH), 2.43 – 2.29 (m, 2H, C*H*$_2$CO), 1.60 – 1.51 (m, 4H, C*H*$_2$C*H*$_2$). **^{13}C NMR** (151 MHz, DMSO-d_6) δ 170.78 (C), 165.09 (C), 164.00 ($^3J_{CF}$ = 10.4 Hz, C), 159.36 (C), 156.35 (d, $^1J_{CF}$ = 245.7 Hz, C), 144.80 (C), 135.45 (C), 134.82 (d, $^3J_{CF}$ = 3.4 Hz, CH), 133.47 (CH), 132.45 (2CH), 132.32 (2CH), 131.75 (d, $^3J_{CF}$ = 7.8 Hz, C), 131.54 (CH), 130.17 (2CH), 129.07 (C), 128.94 (C), 127.89 (C), 127.54 (2CH), 126.06 (CH), 125.42 (CH), 122.89 (d, $^2J_{CF}$ = 25.4 Hz, C), 120.20 (C), 115.91 (d, $^2J_{CF}$ = 20.5 Hz, CH), 82.67 (C), 81.14 (C), 75.09 (C), 73.26 (C), 46.46 (CH_2), 44.71 (CH_2), 41.69 (CH_2), 40.91 (CH_2), 38.82 (CH_2),* 36.41 (CH_2), 31.89 (CH2), 28.66 (CH2), 22.15 (CH2). **HRMS-ESI+** (*m/z*) $[M+H]^+$ found 694.2837, $C_{42}H_{37}N_5O_4F$ requires 694.2824. *(mb = methylene bridge, pip = piperazine) *obscured by DMSO-d_6 signal.*

[1] This compound, and some subsequent olaparib compounds, showed doubling of piperazine CH_2 peaks in ^{13}C NMR. This is may be caused by amide bond rotation/piperazine ring inversion, a phenomenon previously studied by NMR.[241]

_N_-(5-(4-(2-Fluoro-5-((4-oxo-3,4-dihydrophthalazin-1-yl)methyl)benzoyl)piperazin-1-yl)-5-oxopentyl)-4-((5,6,7,8-tetrahydronaphthalen-2-yl)buta-1,3-diyn-1-yl)benzamide (29b)

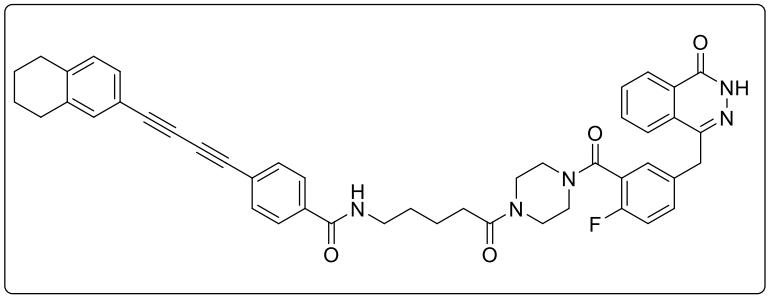

Synthesised according to GP 3 from carboxylic acid **28b** (108 mg, 0.271 mmol) to give the title compound **29b** as a pale green solid (181 mg, 0.242 mmol, 89%). **R_f** (5% MeOH in DCM) = 0.32. **MP** 152–155 °C. **IR** (cm^{-1}) 2214 (C≡C), 1626 (C=O),* 1550 (C=O), 1013 (C–F). **^{1}H NMR** (500 MHz, DMSO-d_6) δ 12.59 (s, 1H, N*H*), 8.61 – 8.55 (m, 1H, N*H*), 8.27 (d, *J* = 7.7 Hz, 1H, Ar*H*), 7.97 (d, *J* = 8.1 Hz, 1H, Ar*H*), 7.94 – 7.81 (m, 4H, Ar*H*), 7.68 (t, *J* = 8.3 Hz, 2H, Ar*H*), 7.48 – 7.42 (m, 1H, Ar*H*), 7.39 – 7.34 (m, 1H, Ar*H*), 7.34 – 7.29 (m, 2H, Ar*H*), 7.24 (t, *J* = 9.0 Hz, 1H, Ar*H*), 7.13 (d, *J* = 8.4 Hz, 1H, Ar*H*), 4.34 (s, 2H, CH_2^{mb}), 3.67 – 3.24 (m, 8H, CH_2^{pip}), 3.22 – 3.10 (m, 2H, C*H*$_2$NH), 2.79 – 2.68 (m, 4H, CH_2^{tet}), 2.40 – 2.30 (m, 2H, C*H*$_2$CO), 1.77 – 1.70 (m, 4H, CH_2^{tet}), 1.59 – 1.51 (m, 4H, C*H*$_2$C*H*$_2$). **^{13}C NMR** (151 MHz, DMSO-d_6) δ 170.78 (C), 165.10 (C), 164.01 ($^3J_{CF}$ = 10.5 Hz, C), 162.28 (C), 159.37 (C), 156.34 (d, $^1J_{CF}$ = 244.8 Hz, C), 144.80 (C), 139.63 (C), 137.53 (C), 135.31 (C), 134.81 (CH), 133.46 (CH), 132.81 (CH), 132.24 (2CH), 131.73 (d, $^3J_{CF}$ = 7.7 Hz, CH), 131.53 (CH), 129.50 (CH), 129.39 (CH), 129.07 (C), 128.92 (d, $^4J_{CF}$ = 3.6 Hz, C), 127.89 (C), 127.52 (2CH), 126.06 (CH), 125.41(CH), 123.58 (d, $^2J_{CF}$ = 18.2 Hz, C), 123.08 (C), 117.03 (C), 115.90 (d, $^2J_{CF}$ = 21.4 Hz, CH), 83.28 (C), 80.69 (C), 75.38 (C), 72.42 (C), 46.46 (CH_2), 44.71 (CH_2), 41.38 (CH_2), 40.91 (CH_2), 39.29 (CH_2) 36.42 (CH_2), 31.90 (CH_2), 28.82 (CH_2), 28.66 (CH_2), 28.39 (CH_2), 22.29 ($2CH_2$), 22.16 (CH_2). **HRMS-ESI+** (*m/z*) $[M+H]^+$ found 748.3295, $C_{46}H_{43}N_5O_4F$ requires 748.3294. *(mb = methylene bridge, pip = piperazine, tet = tetralin; * broad band obscuring individual C=O peaks.)*

4-(Cyclohexylbuta-1,3-diyn-1-yl)-*N*-(5-(4-(2-fluoro-5-((4-oxo-3,4-dihydrophthalazin-1-yl)methyl)benzoyl)piperazin-1-yl)-5-oxopentyl)benzamide (29c)

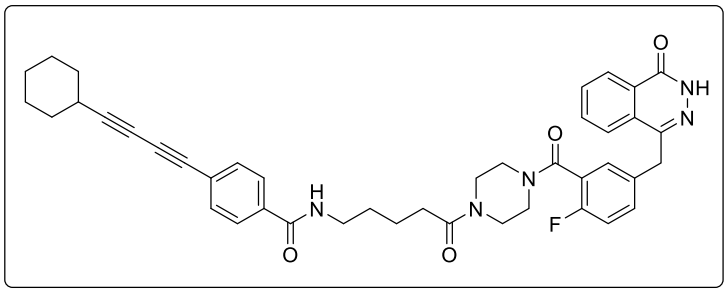

Synthesised according to GP 3 from carboxylic acid **28c** (244 mg, 0.695 mmol) to give the title compound **29c** as a yellow solid (285 mg, 0.407 mmol, 56%). $\mathbf{R_f}$ (5% MeOH in DCM) = 0.37. **MP** 160–165 °C. **IR** (cm^{-1}) 2236 (C≡C), 1629 (C=O), 1550 (C=O), 1013 (C–F). **^{1}H NMR** (500 MHz, DMSO-d_6) δ 12.58 (s, 1H, N*H*), 8.60 – 8.48 (m, 1H, N*H*), 8.26 (d, *J* = 7.8 Hz, 1H, Ar*H*), 7.96 (d, *J* = 8.0 Hz, 1H, Ar*H*), 7.89 (t, *J* = 7.8 Hz, 1H, Ar*H*), 7.86 – 7.79 (m, 3H, Ar*H*), 7.61 (t, *J* = 8.2 Hz, 2H, Ar*H*), 7.48 – 7.40 (m, 1H, Ar*H*), 7.38 – 7.32 (m, 1H, Ar*H*), 7.23 (t, *J* = 9.0 Hz, 1H, Ar*H*), 4.33 (s, 2H, CH_2^{mb}), 3.66 – 3.47 (m, 4H, CH_2^{pip}), 3.42 – 3.34 (m, 2H, CH_2^{pip}), 3.28 – 3.23 (m, 2H, CH_2^{pip}), 3.20 – 3.09 (m, 2H, CH_2NH), 2.69 – 2.60 (m, 1H, CH^{cy}), 2.41 – 2.28 (m, 2H, CH_2CO), 1.83 – 1.75 (m, 2H, CH_2^{cy}), 1.69 – 1.58 (m, 2H, CH_2^{cy}), 1.58 – 1.50 (m, 4H, CH_2^{cy}), 1.50 – 1.39 (m, 2H, CH_2^{cy}), 1.37 – 1.21 (m, 4H, CH_2CH_2). **^{13}C NMR** (126 MHz, DMSO-d_6) δ 170.75 (C), 165.13 (C), 164.03 ($^3J_{CF}$ = 8.6 Hz, C), 159.36 (C), 156.31 (d, $^1J_{CF}$ = 244.6 Hz, C), 144.80 (C), 135.02 (C), 134.81 (CH), 133.47 (CH), 132.20 (2CH), 131.72 (d, $^3J_{CF}$ = 7.8 Hz, CH), 131.53 (CH), 129.07 (C), 128.91 (d, $^4J_{CF}$ = 3.4 Hz, C), 127.89 (C), 127.44 (2CH), 126.06 (CH), 125.42 (CH), 123.57 (d, $^2J_{CF}$ = 18.1 Hz, C), 123.39 (C), 118.03 (C), 115.89 (d, $^2J_{CF}$ = 21.7 Hz, CH), 90.10 (C), 75.82 (C), 74.79 (C), 64.71 (C), 46.46 (CH_2), 44.70 (CH_2), 41.37 (CH_2), 40.83 (CH_2), 38.83 (CH_2),* 36.42 (CH_2), 31.89 (CH_2), 31.47 ($2CH_2$), 28.76 (CH), 28.66 (CH_2), 25.08 (CH_2), 24.08 ($2CH_2$), 22.15 (CH_2). **HRMS-ESI+** (*m/z*) $[M+H]^+$ found 700.3314, $C_{42}H_{43}N_5O_4F$ requires 700.3294. *(mb = methylene bridge, pip = piperazine, cy = cyclohexane) *obscured by DMSO-d_6 signal.*

6.1.5 Characterisation of compounds **26i**–**26k** and **29i**

4-(4-Fluoro-3-(4-(4-(pyridin-3-ylbuta-1,3-diyn-1-yl)benzoyl)piperazine-1-carbonyl)benzyl)phthalazin-1(2*H*)-one (26i)

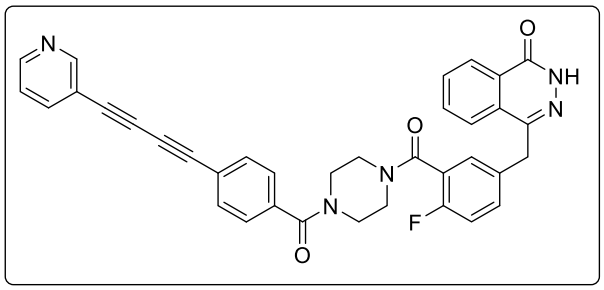

R_f (20:1 DCM:MeOH) = 0.52. **MP** 127 °C. **^{1}H NMR** (500 MHz, DMSO-d_6) δ 12.59 (s, 1H, N*H*), 8.86 – 8.80 (m, 1H, Ar*H*), 8.66 (dd, *J* = 4.9, 1.7 Hz, 1H, Ar*H*), 8.26 (d, *J* = 7.9 Hz, 1H, Ar*H*), 8.07 (dt, *J* = 8.0, 1.9 Hz, 1H, Ar*H*), 8.01 – 7.76 (m, 3H, Ar*H*), 7.72 (d, *J* = 7.8 Hz, 2H, Ar*H*), 7.55 – 7.21 (m, 6H, Ar*H*), 4.34 (s, 2H, CH_2^{mb}), 3.89 – 3.30 (m, 8H, CH_2^{pip}). **^{13}C NMR** (126 MHz, DMSO) δ 168.18 (C), 164.06 (C), 159.37 (C), 156.36 (d, $^1J_{CF}$ = 244.7 Hz, C), 152.69 (CH), 149.97 (CH), 144.80 (C), 139.75 (CH), 136.92 (C), 134.81 (d, $^3J_{CF}$ = 3.2 Hz, CH), 133.46 (CH), 132.61 (2CH), 131.79 (d, $^3J_{CF}$ = 7.9 Hz, CH), 131.53 (CH), 129.07 (C), 128.91 (C), 127.89 (C), 127.60 (2CH), 126.06 (CH), 125.44 (CH), 123.68 (CH), 123.47 (d, $^2J_{CF}$ = 18.5 Hz, C), 121.29 (C), 117.70 (C), 115.93 (d, $^2J_{CF}$ = 22.3 Hz, CH), 82.04 (C), 79.34 (C), 76.16 (C), 74.10 (C), 46.43 ($2CH_2$), 41.24 ($2CH_2$), 36.41 (CH_2). **HRMS-ESI+** (*m/z*) $[M+H]^+$ found 596.2097, $C_{36}H_{27}N_5O_3F$ requires 596.2092. *(mb = methylene bridge, pip = piperazine)*

***N*-(5-(4-(2-fluoro-5-((4-oxo-3,4-dihydrophthalazin-1-yl)methyl)benzoyl)piperazin-1-yl)-5-oxopentyl)-4-(pyridin-3-ylbuta-1,3-diyn-1-yl)benzamide (29i)**

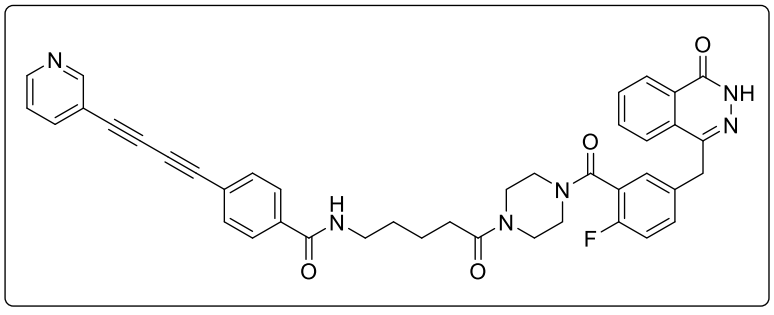

R_f (20:1 DCM:MeOH) = 0.48. **MP** 136–138 °C. **^{1}H NMR** (500 MHz, DMSO-d_6) δ 12.60 (s, 1H, N*H*), 8.83 (dd, *J* = 2.2, 0.9 Hz, 1H, Ar-*H*), 8.66 (dd, *J* = 4.9, 1.7 Hz, 1H, Ar*H*), 8.62 – 8.57 (d, *J* = 5.1 Hz, 1H, N*H*), 8.27 (dd, *J* = 7.9, 1.5 Hz, 1H, Ar*H*), 8.07 (dt, *J* = 8.0, 1.9 Hz, 1H, Ar*H*), 7.99 – 7.95 (m, 1H, Ar*H*), 7.93 – 7.85 (m, 3H, Ar*H*), 7.84 (td, *J* = 7.5, 1.2 Hz, 1H, Ar*H*), 7.72 (t, *J* = 8.5 Hz, 2H, Ar*H*), 7.50 (ddd, *J* = 7.9, 4.9, 1.0 Hz, 1H, Ar*H*), 7.48 – 7.42 (m, 1H, Ar*H*), 7.38 – 7.34 (m, 1H, Ar*H*), 7.24 (t, *J* = 9.0 Hz, 1H, Ar*H*), 4.34 (s, 2H, CH_2^{mb}), 3.66 – 3.49 (m, 4H, CH_2^{pip}), 3.41 – 3.35 (m, 2H,

C*H*$_2^{pip}$), 3.29 – 3.27 (m, 2H, C*H*$_2^{pip}$), 3.21 – 3.11 (m, 2H, C*H*$_2$NH), 2.41 – 2.29 (2H, m, C*H*$_2$CO), 1.66 – 1.47 (m, 4H, C*H*$_2$). **^{13}C NMR** (126 MHz, DMSO) δ 170.78 (C), 166.91 (C), 165.05 (C), 164.03 (C), 159.36 (C), 156.04 (d, $^1J_{CF}$ = 242.5 Hz, C), 152.69 (CH), 149.99 (CH), 144.81, 139.75 (CH), 135.67 (C), 134.82 (d, $^3J_{CF}$ = 5.0 Hz, CH), 133.48 (CH), 132.43 (2CH), 131.76 (d, $^3J_{CF}$ = 7.0 Hz, CH), 131.54 (CH), 129.07 (C), 128.92 (C), 127.89 (C), 127.57 (2CH), 126.06 (CH), 125.43 (CH), 123.67 (CH), 123.48 (d, $^2J_{CF}$ = 18.1 Hz, C), 122.54 (C), 117.68 (C), 115.90 (d, $^2J_{CF}$ = 23.3 Hz, CH), 82.08 (C), 79.54 (C), 76.10 (C), 74.63 (C), 46.32 (2CH$_2$), 41.23 (2CH$_2$), 36.42 (CH$_2$), 31.89 (CH$_2$), 28.65 (CH$_2$), 22.15 (CH$_2$).**1 CH$_2$ signal obscured by DMSO-d$_6$ signal.* **HRMS-ESI+** (*m/z*) [M+H]$^+$ found 695.2779, $C_{41}H_{36}N_6O_4F$ requires 695.2777. *(mb = methylene bridge, pip = piperazine)*

4-(4-Fluoro-3-(4-(5-(pyridin-3-ylbuta-1,3-diyn-1-yl)pyrazine-2-carbonyl)piperazine-1-carbonyl)benzyl)phthalazin-1(2*H*)-one (26j)

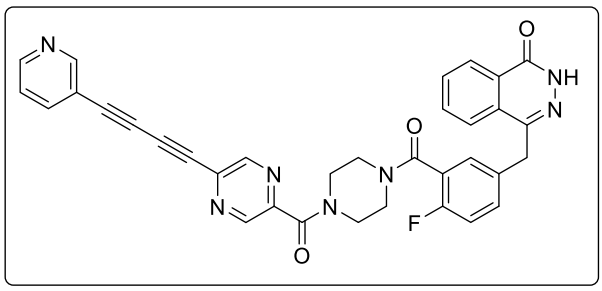

R$_f$ (20:1 DCM:MeOH) = 0.30. **MP** 208–209 °C (decomp). **^{1}H NMR** (500 MHz, DMSO-*d*$_6$) δ 12.62 – 12.54 (m, 1H, N*H*), 9.02 – 8.95 (m, 1H, Ar*H*), 8.96 – 8.91 (m, 1H, Ar*H*), 8.91 – 8.87 (m, 1H, Ar*H*), 8.70 (dd, *J* = 4.9, 1.6 Hz, 1H, Ar*H*), 8.27 (t, *J* = 8.7 Hz, 1H, Ar*H*), 8.17 – 8.11 (m, 1H, Ar*H*), 8.01 – 7.78 (m, 3H, Ar*H*), 7.53 (dd, *J* = 8.0, 4.9 Hz, 1H, Ar*H*), 7.50 – 7.42 (m, 1H, Ar*H*), 7.42 – 7.36 (m, 1H, Ar*H*), 7.25 (dt, *J* = 18.7, 9.0 Hz, 1H, Ar*H*), 4.35 (s, 1H, C*H*$_A^{mb}$), 4.33 (s, 1H, C*H*$_B^{mb}$), 3.80 – 3.72 (m, 2H, C*H*$_2^{pip}$), 3.69 – 3.52 (m, 4H, C*H*$_2^{pip}$), 3.45 – 3.38 (m, 1H, C*H*$_A^{pip}$), 3.25 – 3.18 (m, 1H, C*H*$_B^{pip}$). **^{13}C NMR** (126 MHz, DMSO) δ 164.26 (C), 164.10 (C), 159.37 (C), 156.50 (d, $^1J_{CF}$ = 238.6 Hz, C), 153.00 (CH), 150.50 (CH), 147.71 (C), 147.64 (C), 146.88 (CH), 144.87 (C), 144.80 (CH), 140.12 (CH), 137.76 (C), 134.81 (d, $^3J_{CF}$ = 6.5 Hz, CH), 133.47(CH), 131.84 (CH), 131.55 (d, $^3J_{CF}$ = 8.3 Hz, CH), 129.04 (d, $^4J_{CF}$ = 14.2 Hz, C), 127.89 (C), 126.06 (CH), 125.43 (CH), 123.73 (CH), 123.41 (d, $^2J_{CF}$ = 18.1 Hz, C), 116.97 (C), 115.92 (d, $^2J_{CF}$ = 21.6 Hz, CH), 81.42 (C), 78.76 (C), 76.47 (C), 75.25 (C), 46.10 (2CH$_2$), 41.63 (2CH$_2$), 36.42 (CH$_2$). **HRMS-ESI+** (*m/z*) [M+H]$^+$ found 598.1996, $C_{34}H_{25}N_7O_3F$ requires 598.1997. *(mb = methylene bridge, pip = piperazine)*

4-(4-Fluoro-3-(4-(5-((1-methyl-1*H*-imidazol-5-yl)buta-1,3-diyn-1-yl)pyrazine-2-carbonyl)piperazine-1-carbonyl)benzyl)phthalazin-1(2*H*)-one (26k)

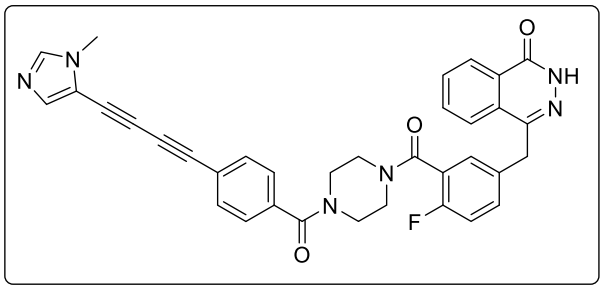

R_f (20:1 DCM:MeOH) = 0.38. **MP** 210–212 °C. **^{1}H NMR** (601 MHz, DMSO-d_6) δ 12.58 (s, 1H, N*H*), 8.26 (d, *J* = 7.9 Hz, 1H, Ar*H*), 7.99 – 7.78 (m, 4H, Ar*H*), 7.69 (d, *J* = 7.8 Hz, 2H, Ar*H*), 7.55 – 7.32 (m, 5H, Ar*H*), 7.27 – 7.20 (m, 1H, Ar*H*), 4.33 (s, 2H, CH_2^{mb}), 3.69 (s, 3H, CH_3), 3.79 – 3.40 (m, 8H, CH_2^{pip}). **^{13}C NMR** (126 MHz, DMSO) δ 168.18 (C), 164.04 (C), 159.35 (C), 156.35 (d, $^1J_{CF}$ = 241.6 Hz, C), 144.78 (C), 140.45 (CH), 137.70 (C), 134.80 (d, $^3J_{CF}$ = 6.7 Hz, CH), 133.45 (CH), 132.40 (2CH), 131.75 (d, $^3J_{CF}$ = 9.0 Hz, CH), 131.51 (CH), 129.06 (C), 128.88 (C), 127.88 (C), 127.58 (2CH), 126.04 (CH), 125.43 (CH), 123.46 (d, $^2J_{CF}$ = 17.7 Hz, C), 121.48 (CH), 117.63 (C), 115.91 (d, $^2J_{CF}$ = 20.6 Hz, CH), 113.75 (C), 83.68 (C), 80.42 (C), 74.23 (C), 70.83 (C), 46.35n ($2CH_2$), 41.63 ($2CH_2$), 36.40 (CH_2), 31.93 (CH_3). **HRMS-ESI+** (*m/z*) $[M+H]^+$ found 599.2211, $C_{35}H_{28}N_6O_3F$ requires 599.2201. *(mb = methylene bridge, pip = piperazine)*

6.1.6 X-ray crystallography

A single crystal of **1a** and **1b** (produced as described in the main text) was selected and subjected to X-ray diffraction using a D8 VENTURE diffractometer (Bruker). Crystal structures were solved and refined using ShelXT, Olex2 and ShelXL by Dr Gary Nichol. All further structure manipulations and analyses were carried out using Mercury 4.3.1 (Cambridge Crystallographic Data Centre) NB: **1b** underwent a crystallographic phase-change during cooling to 100K, details of which can be found in **Appendix A**.

6.1.7 Mass spectrometry

All experiments were carried out on a 12 T SolariX FT-ICR spectrometer (Bruker Daltonics) using the following parameters: flow rate, 120 µL/h; capillary voltage, 4500 V; nebulizer pressure, 1.0 bar; dry temp, 200 °C; average scans, 1; accumulation time, 0.5 s, skimmer 1 voltage. 10.0 V. For evaluation of aggregation/stacking, compounds were dissolved in THF and diluted 10-fold with methanol to achieve a final concentration of 10 µM. For compounds **1a**–**1f**, monomers $[M+Na]^+$ (*m/z* = 283.07, 311.11, 337.09, 339.10, 297.06, 289.12, respectively) and dimers $[2M+Na]^+$ (*m/z* = 543.15, 643.19, 651.22, 655.25, 571.16, 555.25, respectively). were identified. Dimers were isolated and fragmented over a period of 25.5 minutes, increasing the

collision voltage by 0.1 V from 0 to 5 V every 30 s. Compass DataAnalysis 5.0 (Bruker Daltonik GmbH) was used to process MS data. Extracted ion chromatograms (EIC) for each dimer and corresponding monomers were normalised by dividing by the total ion chromatogram for each sample run. Normalised EIC data was expressed as the dimer fraction [dimer /(monomer+dimer)] and half-wave collision values were obtained by fitting a dose-response curve on Origin 9.6.0.172 (OriginLab Corporation).

6.1.8 Spontaneous Raman scattering spectroscopy

Solutions of each tag in DMSO (10 mM) were prepared and mixed 1:1 by volume with a solution of EdU in DMSO (100 mM). Spontaneous Raman spectra of a droplet of liquid sample were acquired using an inVia™ confocal Raman spectrometer (Renishaw). A 297 mW 785 nm diode laser was used to excite the sample through a 10× objective at 100% laser power. For extended scans the recorded spectral range for grating 1200 g mm^{-1} was 400–3000 cm^{-1} and the total data acquisition was 40 s. For static scans, data was acquired from 2000–2400 cm^{-1} with 10 × 15 s acquisitions. Data was acquired using WiRE 3.4 (Renishaw). The raw spectral data was first baseline corrected using a method previously reported; computational scripts can be found https://github.com/StatguyUser/BaselineRemoval.[242] All further processing was performed using Origin 9.6.0.172 (OriginLab Corporation). Line smoothing was performed automatically by the adjacent averaging method with 10 points.

6.2 Biochemical and biophysical

The methods detailed in **Sections 6.2.2**–**6.2.6** were carried out at, or in collaboration with, AstraZeneca.

6.2.1 Protein modelling

Protein structures were visualised and manipulated using Pymol 3.0.2. For docking of ligands in the PARP-1 protein active site, Flare 4.0.2 was used. The PDB structure of olaparib co-crystallised with PARP-1 was obtained (PBD: 7KK4), prepared and minimised. The lowest LF rank-scoring pose for each ligand was selected.

6.2.2 Determination of physicochemical parameters

According to published methods,[161, 243] ePSA and log$D_{7.4}$ values for olaparib and olaparib analogues were determined using chromatographic methods. For ePSA, a supercritical fluid chromatography system (SFC) was performed on a Waters Acquity UPC2 system, using 20 mM ammonium formate in MeOH as the co-solvent. A

Phenomenex Chirex 3014 4.6 × 50 mm column was used, maintained at a temperature of 40 °C, with a flow rate of 4.0 mL min^{-1}. Comparing to a series of known calibration standards previously analysed by AstraZeneca, retention times (UV detection, λ = 254 nm) were determined and used as an estimate of ePSA. Chromatographic method details are provided in **Table 6.1**.

For logD, reverse phase chromatography was performed on a Waters Acquity UPC2 system, using 5% acetonitrile in water with 10 mM ammonium acetate (mobile phase A) and 5% water in acetonitrile with 10 mM ammonium acetate (mobile phase B). An Acquity BEH C18, 1.7µm, 50 × 2.1 mm column was used, maintained at a temperature of 40 °C, with a flow rate of 1.0 mL min^{-1}. Comparing to a series of known calibration standards previously analysed by AstraZeneca, retention times (UV detection, λ = 254 nm) were determined and used as an estimate of log*D*. Chromatographic method details are provided in **Table 6.2**.

Table 6.1. SFC gradient method for ePSA determination.

Time / min	% co-solvent
	5
2	60
3.5	60
3.6	5
4	5

Table 6.2. RP-UPLC gradient method for log$D_{7.4}$ determination.

Time / min	%A	%B	Curve
	99.9	0.1	
0.17	99.9	0.1	6
1.50	0.1	99.9	6
1.80	0.1	99.9	6
1.81	99.9	0.1	11
2.20	99.9	0.1	6

6.2.3 Compound stability

Compounds were dissolved in DMSO and diluted to give a final concentration of 100 µM (1% DMSO) in RPMI-1640 cell media or DMSO. Clozapine was used as an internal standard. RP-UPLC with MS detection (ESI+) was performed on a Thermo Scientific Vanquish system, using 5% acetonitrile in water with 0.1% formic acid (mobile phase A) and 5% water in acetonitrile with 0.1% formic acid (mobile phase

B). An Acquity UPLC CSH C18, 2.1mm × 50mm, 1.7µm column was used, maintained at a temperature of 40 °C, with a flow rate of 0.7 mL min^{-1}. Chromatographic method details are provided in **Table 6.3**.

Table 6.3. RP-UPLC gradient method for stability assay.

Time / min	%A	%B
	95	5
4.00	5	95
4.50	5	95
4.51	95	5
5.00	95	5

6.2.4 PARP activity assay

Adapted based on a protocol provided by Dr Derek Barratt. PARP-1 recombinant protein (2.4 nM, Reaction Biology cat. no. PAR-21-346) and core histones (0.01 mg/mL, Reaction Biology cat. no. HMT-35-435) were added to reaction buffer (Tris·HCl (20 mM, pH 8.0), NaCl (50 mM), $MgCl_2$ (10 mM), DTT (1 mM), 0.01% Brij35, 1% DMSO, DNA (10 µg/mL, Sigma Aldrich)) in a multi-well plate. Compounds were added by acoustic technology using an Echo550 liquid handler (Labcyte) and the mixtures were incubated at RT for 20 min. NAD (Sigma Aldrich) was added to each well at a final concentration of 0.5 µM. The plate was centrifugated briefly to mix, sealed and incubated at RT for 2 h. Concentration of NAD^+ was determined using the NAD/NADH-Glo™ luminescence assay (Promega), according to the manufacturer's instructions.

6.2.5 Surface plasmon resonance (SPR)

Adapted based on protocol provided by Dr Christopher Stubbs. Using a Biacore 8K+ SPR system (Cytiva), full length PARP-1-TEV-6His-6Lys recombinant protein (prepared in house, 50 µg/mL final concentration) was a immobilised onto a Series S NTA sensor chip (Cytiva) in immobilisation buffer (10 mM 4-(2-hydroxyethyl)-1-piperazineethanesulfonic acid (HEPES) pH 7.5, 150 mM NaCl, 0.1 mM tris(2-carboxyethyl)phosphine (TCEP), 0.05% (w/v) Tween-20, 1% (v/v) DMSO). Based on the relative molecular weights of the protein/ligands, immobilisation levels of 3000 – 5000 RU were aimed for. The protein was further crosslinked to the chip with 1:1 (v/v) 0.4 M 1-Ethyl-3-(3-dimethylaminopropyl)-carbodiimide (EDC) and 0.2 M *N*-hydroxysuccinimide (NHS). Compounds were diluted to working concentrations of

100 µM in DMSO and diluted in serial dilutions (total 8 concentrations, 2-fold dilutions, highest concentration 2000 nM), normalising the DMSO concentration. The samples were injected into the system in sample running buffer (10 mM *N*,*N*-bis(2-hydroxyethyl)glycine (BICINE) pH 7.5, 150 mM NaCl, 0.1 mM TCEP, 0.05% (w/v) Tween-20, 1% (v/v) DMSO) using a single cycle kinetics analysis method (contact time 120s, dissociation time 3600 s, flow rate 30 µL/min). Between each compound injection, the system was washed with 50% (v/v) DMSO in running buffer.

6.2.6 Hydrogen-deuterium exchange mass spectrometry (HDX-MS)

Adapted based on protocol provided by Dr Christopher Stubbs. Full length PARP-1-TEV-6His-6Lys recombinant protein (prepared in house, 5 µM final concentration) was mixed with compounds (20 µM final concentration). A LEAP HDX-2 automated system was used to carry out the HDX experiments with labelling buffer (10 mM HEPES pH 7.5, 150 mM NaCl, 0.1 mM TCEP, 1% (v/v) DMSO in D_2O). The reactions were carried out in triplicate. Exchange reactions were carried out at timepoints of 30, 300 and 3000 s, after which the reactions were quenched with quench solution (3 M urea, 1.6% (v/v) formic acid) at 1 °C. The samples were then immediately loaded onto the sample loop in the HDX system and subjected to LC-MS analysis. Samples were digested by a Enzymate Pepsin Column (300 Å, 5 µm, 2.1 mm x 30 mm) for 3 min at 20 °C (80 µL/min, 5% CH_3CN in H_2O (+0.1% formic acid)) and peptides were separated on a ACQUITY UPLC BEH C18 Column (130 Å, 1.7 µm, 1 x 50 mm) for 14 min (80 µL/min, 5% CH_3CN in H_2O → 95% CH_3CN in H_2O (+0.1% formic acid)). Mass spectrometry was performed using a Synapt G2-Si system (*m/z* = 50–2000, positive ion mode) using a method based on a published protocol.[244] MS data was processed ProteinLynx Global Server 3.0.3 (PLGS) and imported into DynamX analysis software. Peptides were inspected for overlapping ions and excluded from analysis as appropriate. The time course data were imported and manually inspected for correct assignment. Where problems arose in identifying unique isotope distributions, other charge states were first inspected to attempt to rescue the peptides. Problematic peptides were excluded from the analysis. 220 peptides were used in the analysis with 71% overall coverage. The curated DynamX data were exported and further analysed using a custom MATLAB script to calculate fractional deuterium uptake (%) based upon the peptide sequences assuming the first two residues rapidly back-exchange. A pooled standard deviation was calculated across all peptides/conditions. For peptides with errors ≤ the pooled standard deviation, the pooled standard

deviation was used for significance testing; for peptides with larger errors, the measured errors for those peptides were used to reduce false positives. Statistical significance was determined using a Benjamini-Hochberg FDR-adjusted t-test with a threshold of $p < 0.01$.

6.3 Cell biology

6.3.1 General considerations

All experimental steps were carried out at RT unless otherwise stated. For the preparation of buffers, water used was distilled and purified using a Milli-Q purification system. Buffers, reagents and plasticware for cell culture were either provided and maintained sterile or autoclaved prior to use. Protocol steps described as being carried out at 37 °C indicate incubation in a humidified incubator with 5% CO_2.

6.3.2 Cell culture

Cell lines were cultured in the appropriate media, as indicated in **Table 6.4**. Cultured cells were maintained in a humidified incubator at 37 °C and 5% CO_2. For cell harvesting, adherent cells in T75 flasks at 70–80% confluence were rinsed with PBS and incubated with 0.05% trypsin-EDTA (Gibco) at 37 °C for 2 min. The trypsin was quenched by the addition of media (10× original volume) to give a single cell suspension, which was aliquoted into new cell culture flasks with fresh media as required. Cell lines were routinely tested for mycoplasma contamination and authenticated by short tandem repeat (STR) profiling. Cells were pelleted by centrifugation (300 *g*, 4 min). For cell counting, an aliquot of cell solution in media was mixed with Trypan Blue dye (Gibco) in a 1:1 ratio and the mixture was added to both chambers of a NanoEnTek C-slide (2 x 10 µL). The slide was imaged using a Countess II cytometer (Applied Biosystems) with automatic focusing. The quantity of live cells was recorded and the mean value of the two slide chambers was used for cell dilution. Cells were regularly transferred to liquid nitrogen storage to maintain low passage numbers. To do so, cell pellets were resuspended in freezing media (10% (v/v) DMSO in FBS (Gibco)) and transferred to cryovials for short-term storage at -80 °C or long-term storage under liquid nitrogen at -196 °C. Cells were recovered from liquid nitrogen storage by quickly warming and transferring to pre-warmed cell media. Residual DMSO was removed by replacing the media after ca. 18 h.

Table 6.4. Cell lines

Cell line	Description	Origin	Culture media*
DLD-1 *BRCA2* -/-	DLD-1 cells with CRISPR-Cas9 knockout of the *BRCA2* gene	AstraZeneca	RPMI 1640 phenol red-free (Sigma)
DLD-1 WT	Human colorectal adenocarcinoma.	ATCC (AstraZeneca)	RPMI 1640 phenol red-free (Sigma)
ES-2	Human ovarian clear cell adenocarcinoma. *BRCA* WT	ATCC	DMEM high glucose (Sigma)
ES-2 53BP1 mApple†	ES-2 cell line with 53BP1 fluorescent reporter for DNA damage[206]	Brunton group, ECRC	DMEM high glucose (Sigma)
ES-2 Ola 50:1	ES-2 cell line resistant to 50 μM olaparib[245]	Gourley group, ECRC	DMEM high glucose (Sigma)
HEK-293	Human embryonic kidney cells	ATCC	1:1 DMEM:F12 (Gibco) Glutamine (Gibco, 2 mM)
HeLa	Human cervical adenocarcinoma	ATCC	DMEM high glucose (Sigma)
RTIF	Red fluorescent protein telomerase reverse transcriptase (TERT) immortalised fibroblasts (RTIF) generated from skin punch biopsies[187]	Gourley group, ECRC	1:1 DMEM:F12 (Gibco)
SKLMS-1	Human vulvar leiomyosarcoma *BRCA1* -/-	ATCC	MEM (Sigma)
SKUT-1	Human uterine leiomyosarcoma *BRCA2* -/-	ATCC	MEM (Sigma)

** Each with the addition of 10% (v/v) FBS (Gibco) and 1% (v/v) penicillin/streptomycin (10,000 U/mL), with the exception of DLD-1 cell lines, which were supplemented with 10% (v/v) FBS (Gibco) and 1% (v/v) GlutaMAX (Gibco). †Transfected to stably express fluorescent reporter by Dr Amy Davies prior to the start of this project.*

6.3.3 Reagents

Table 6.5. Buffers

Buffer	Components
Block (immunofluorescence)	2% (v/v) BSA in wash buffer
Block (Western blot)	5% (v/v) BSA in wash buffer
Crystal violet staining solution	0.5% (w/v) crystal violet 25% (v/v) methanol in H_2O
Fixation	3.7% (v/v) Formaldehyde 0.2% (v/v) Triton X-100 PIPES (100 mM) EGTA (10 mM) $MgCl_2$ (1 mM) H_2O
Fractionation A*	Tris·HCl (20 mM, pH 7.4) EGTA (1 mM) $MgCl_2$ (1 mM)
Fractionation B*	0.1% (v/v) Triton X-100 0.1% (w/v) sodium deoxycholate Tris·HCl (10 mM, pH 7.4) $MgCl_2$ (2.5 mM) KCl (1.5 mM) LiCl (0.2 M)
Glycine	Glycine in TBS (0.1 M)
Lysis (immunoprecipitation)*	1% (v/v) NP-40 NaCl (0.15 M) Tris·HCl (5 mM, pH 7.4) EDTA (2 mM)
PBS (phosphate-buffered saline)	1 PBS tablet (2 g, Sigma) 200 mL H_2O
RIPA (radioimmunoprecipitation assay) Lysis*	1% (v/v) Triton X-100 0.5% (w/v) sodium deoxycholate 0.1% (w/v) SDS Trizma HCl (50 mM) NaCl (0.15 M) H_2O
Sample (protein denaturing)	NuPAGE™ LDS Sample Buffer (4X, Invitrogen) 5% (v/v) β-mercaptoethanol
Tris buffered saline (TBS, 10X)	Tris·HCl (0.2 M) NaCl (1.5 M) adjusted to pH 7.6 with NaOH
Tris glycine SDS (TGS) running	TGS buffer (10X, Bio-Rad) H_2O
Wash (immunofluorescence)	0.1% (v/v) Triton X-100 in TBS
Wash (Western blot)	0.1% (v/v) TWEEN 20 in TBS

** With the addition of 2% (v/v) protease inhibitor (Sigma Aldrich) and 0.4% (v/v) phosphatase inhibitor (Sigma Aldrich) directly before use.*

Table 6.6. Antibodies

Target	Supplier	Cat. no.	Dilution	
			WB	IF
PARP-1	CST	2729	1:3000	1:2000
GAPDH	CST	5174	1:1000	-
α-Tubulin	CST	3873	1:1000	-
RCAS-1	CST	12290	1:1000	-
Histone H4	CST	2935	1:1000	-
pH2A.X (Ser139)	CST	9718	-	1:2000
LC3	MBL	PM036	1:1000	-
p62	CST	39749	1:1000	
CHOP	CST	5554	1:1000	
HSP70	CST	4872	1:1000	-
Normal rabbit IgG	CST	3900	1:2500	-
HRP-conjugated anti-rabbit IgG	CST	7074	1:3000	-
HRP-conjugated anti-mouse IgG	CST	7076	1:3000	-
Alexa Fluor™ 594 goat anti-rabbit	Invitrogen	R37117	-	1:250
Alexa Fluor™ 405 goat anti-rabbit	Invitrogen	A48255	-	1:250

Table 6.7. Primers

Target	Sequence
ATF4	F: 5'-GGG ACA GAT TGG ATG TTG GAG A R: 5'-ACC CAA CAG GGC ATC CAA GT
DDIT3	F: 5'-CAG AAC CAG CAG AGG TCA CA R: 5'-AGC TGT GCC ACT TTC CTT TC
DNAJB9	F: 5'-GCC ATG AAG TAC CAC CCT GAC A R: 5'-TCG TCT ATT AGC ATC TGA GAG TGT
EDEM1	F: 5'-ACG AGC AGT GAA AGC CCT TTG G R: 5'-CCA CTC TGC TTT CCA ACC CAG T
GAPDH	F: 5'-GTC TCC TCT GAC TTC AAC AGC G R: 5'-ACC ACC CTG TTG CTG TAG CCA A
HSP90B1	F: 5'-GGA GAG TCG TGA AGC AGT TGA G R: 5'-CCA CCA AAG CAC ACG GAG ATT C
HSPA5	F: 5'-CTG TCC AGG CTG GTG TGC TCT R: 5'-CTT GGT AGG CAC CAC TGT GTT C
LC3A	F: 5'-CGT CCT GGA CAA GAC CAA GT R: 5'-CTC GTC TTT CTC CTG CTC GT
LC3B	F: 5'-GAT GTC CGA CTT ATT CGA GAG C R: 5'-TTG AGC TGT AAG CGC CTT CTA
PARP1	F: 5'-CCA AGC CAG TTC AGG ACC TCA T R: 5'-GGA TCT GCC TTT TGC TCA GCT TC
SQSTM1	F: 5'-TGT GTA GCG TCT GCG AGG GAA A R: 5'-AGT GTC CGT GTT TCA CCT TCC G
XBP1s	F: 5'-TGC TGA GTC CGC AGC AGG TG R: 5'-GCT GGC AGG CTC TGG GGA AG

6.3.4 Cell viability

6.3.4.1 Viability assays carried out at University of Edinburgh

Cells were plated (4000 cells/well) in 96-well plates. After ca. 24 h, cell growth media was replaced with drug-containing media and the cells were incubated for 72 h. Alamar Blue cell viability reagent (Invitrogen) was added at a concentration of 10% (v/v) and the cells were incubated at 37 °C for 2 h. The fluorescence signal of each well was measured (λ_{ex} = 540 – 570 nm, λ_{em} = 580 – 610 nm) using a Spark 20M multimode microplate reader (Tecan). For calculation of the IC_{50} values for each compound, the fluorescence reading from control wells containing no cells was subtracted from the drug-treated wells and the resultant values were expressed as a percentage of fluorescence reading of the cell-containing DMSO-treated wells. Non-linear regression (log(inhibitor) vs normalised response – variable slope) analysis was performed and IC_{50} values were calculated using GraphPad Prism 9. For PARP-1 knockdown experiments, the above protocol was carried out with the following

modifications: a) as per **Section 6.3.6**, cells were trypsinised and replated in 24-well plates (20,000 cells/well) and allowed to adhere for 24 h, b) drugs were added at the indicated concentrations and the cells were incubated for a further 48 h, c) cell viability was expressed as a percentage of DMSO control with background subtraction and displayed in bar charts.

6.3.4.2 Viability assays carried out at AstraZeneca

Adapted based on a protocol provided by Dr Pamela Lochhead. This protocol was carried out using DLD-1 WT and DLD-1 *BRCA2* -/- cell lines. On day 0, using a Multidrop™ liquid dispenser (Thermo Scientific), cells were plated (WT: 150 cells/well, *BRCA2* -/-: 300 cells/well) into 96-well plates containing compounds and incubated at 37 °C. On day 6, the cell media was aspirated and replaced with fresh compound-containing media using an i7 automated workstation (Beckman Coulter). The cells were then incubated for a further 24 h at 37 °C. Using a Multidrop™ liquid handling system (Thermo Scientific), CellTitre-Glo® Luminescent cell viability reagent (Promega) was added, according to the manufacturer's instructions. Luminescence intensity was determined using an EnVision plate reader (PerkinElmer). Percentage cell viability was calculated based on DMSO-treated wells and processed to obtain IC_{50} curves using in-house AstraZeneca software.

6.3.5 Crystal violet assay

Cells were plated in 6-well plates to achieve ca. 80% confluency in DMSO-treated wells at the assay endpoint. Cells were treated with compound at the indicated concentrations for 48 h. Growth media was removed and the cells were washed with PBS. Cells were fixed (3.7% formaldehyde in PBS) for 10 minutes and washed twice with PBS. Crystal violet staining solution (300 µL/well) was added and the cells were incubated for 15 minutes with gentle agitation. The staining solution was removed and the cells were washed three times with H_2O.

6.3.6 Small-interfering RNA transfection

Cells were plated in 10 cm^2 dishes to achieve ca. 80% confluency at the point of transfection. Lipofectamine® RNAiMAX reagent was used according to the manufacturer's instructions, incubating cells with the appropriate siRNA (10 µM final concentration) for 24 h. During the transfection protocol, antibiotic-free media was used. Transfection efficiency was measured qualitatively using a GFP-containing DNA sequence (pAAV-GFP Control Vector, part no. AAV-400, Cell Biolabs). A dicer-

substrate short interfering RNA sequence (DsiRNA) was purchased from Integrated DNA Technologies as a pre-annealed duplex to target PARP1 (5'-rGrArArGrUrCrArUrCrGrArUrArUrCrUrUrUrArArGrArUA-3', 5'-rCrUrArUrCrUrUrArArArGrArUrArUrCrGrArUrGrArCrUrUrCrCrA-3'). A scrambled control sequence (5'-rGrArArGrGrUrGrArUrArArArGrUrCrGrUrArUrGrA-3') was used.

6.3.7 RNA extraction

Cells were plated in 10 cm^2 cell culture dishes to achieve ca. 80% confluency at the point of cell lysis, with/without prior drug treatment, as indicated. Cells were pelleted by centrifugation (300 *g*, 4 min) and RNA was isolated using the RNeasy® Mini kit (QIAGEN), according to the manufacturer's instructions. RNA concentrations were measured using a NanoDrop™ 1000 spectrophotometer (Thermo Fisher Scientific) and samples were stored short-term at -20 °C or long-term at -80 °C.

6.3.8 Reverse transcription quantitative PCR (RT-qPCR)

Using 0.5-1 µg of total RNA for each sample, complimentary DNA (cDNA) was synthesised using the RevertAid First Strand cDNA Synthesis Kit (Thermo Scientific) according to the manufacturer's instructions. Quantitative PCR (qPCR) sample mixtures were prepared using 1.5 µL of cDNA, primers (1 µM, **Table 6.7**) and SYBR® Select Master Mix (Applied Biosystems) according to the manufacturer's instructions with a reaction volume of 15 µL. PCR was performed using a StepOnePlus™ qPCR system (Applied Biosystems) and data was collected and processed using the in-built software. Data was analysed using the $\Delta\Delta C_t$ method and the fold change in gene expression ($2^{-\Delta\Delta Ct}$) vs DMSO control was used to express results.

6.3.9 Western blot

6.3.9.1 Cell lysis and protein extraction

Cells were plated in 6-well cell culture plates to achieve ca. 80% confluency at the point of cell lysis. Growth media was aspirated, and the cells were washed with PBS at 4 °C. Cells were incubated with RIPA lysis buffer (50 µL/well) for 5 min at 4 °C with gentle agitation. Cells were scraped, transferred into Eppendorf tubes and centrifuged (13,300 *g*, 10 min, 4 °C). Supernatants were transferred to clean Eppendorf tubes and stored short-term at -20 °C or long-term at -80 °C.

6.3.9.2 Protein quantification

Lysate protein concentration was determined using the Pierce™ bicinchoninic acid (BCA) assay, according to the manufacturer's instructions. Samples were assessed against known concentrations of bovine serum albumin (Thermo Scientific).

6.3.9.3 SDS-PAGE and transfer

Protein samples were added to sample buffer diluted in RIPA buffer to achieve a total loaded protein content of 20 µg. Proteins were denatured at 95 °C for 5 min and loaded onto 3-15% Mini-PROTEAN® TGX™ precast protein gels (Bio-Rad) with at least one Precision Plus Protein Dual Color Standard molecular weight ladder (Bio-Rad). Proteins were separated by gel electrophoresis using TGS running buffer for ca. 40 min at 170 V.

Proteins were transferred to a PVDF membrane (Trans-Blot Midi 0.2 µM, Bio-Rad) using a Trans-Blot Turbo transfer machine (7 min, 25 V, 1.3 A). Membranes were blocked in block buffer for 1 h and washed with wash buffer (3 × 7 min). The membrane was immunoblotted with primary antibodies at 4 °C overnight, washed with wash buffer (3 × 7 min) and incubated with secondary antibodies for 1 h. The membrane was washed with wash buffer (3 × 7 min), incubated in Clarity™ Western ECL chemiluminescent substrate (Bio-Rad) and visualised immediately using a ChemiDoc XRS+ system (Bio-Rad). Membranes were stripped for re-blotting as required using ReBlot Plus Strong Antibody Stripping Solution (Millipore).

6.3.10 Cell fractionation

Cells were grown in 10 cm^2 cell culture dishes to achieve ca. 80% confluency at the point of cell lysis. Growth media was aspirated and the cells were washed with PBS at 4 °C. Cells were and incubated in fractionation buffer A (100 µL per 10 cm^2 plate) at 4 °C for 5 min with gentle agitation. Cells were scraped, transferred to Eppendorf tubes and rotated at 4 °C for 5 min. The mixtures were centrifugated (800 *g*, 5 min, 4 °C), sonicated (30 s on + 30 s off, 5 cycles, 4 °C) and supernatants were removed and retained as the cytoplasmic fractions. The cell pellets were washed with fractionation buffer A and re-centrifugated (800 *g*, 5 min, 4 °C) twice. The pellet was resuspended in buffer B and rotated at 4 °C for 15 min. The mixtures were centrifugated (2000 *g*, 5 min, 4 °C), sonicated (30 s on + 30 s off, 5 cycles, 4 °C) and the supernatants were retained as the perinuclear fractions. The cell pellets were washed with fractionation buffer B and re-centrifugated as above. The cell pellet was

resuspended in RIPA buffer, sonicated (30 s on + 30 s off, 5 cycles, 4 °C), centrifugated (17,000 *g*, 15 min, 4 °C) and the supernatants were retained as the nuclear fractions. Protein concentrations were quantified using the method outlined in **Section 6.3.9.2**. For further analysis by MS, a XEVO TQ-XS LC-MS system (Waters) was used at AstraZeneca. 5% acetonitrile in water with 0.1% formic acid was used as mobile phase A and 5% water in acetonitrile with 0.1% formic acid as mobile phase B. A gradient of 95% to 5% A over 3.5 minutes was used with a C18 CSH column 2.1 x 50 mm, 1.7 µm (Waters) set to 40 °C. Lysate samples were diluted 10-fold in DMSO and mixed with clozapine as an internal standard before injection.

6.3.11 Immunoprecipitation

6.3.11.1 With SDS-PAGE analysis

Cells were plated in 15 cm^2 cell culture dishes to achieve ca. 80% confluency at the point of cell lysis. Growth media was aspirated and the cells were washed with PBS at 4 °C. Cells were incubated in immunoprecipitation lysis buffer (250 µL per plate) for 5 minutes at 0 °C. Cells were scraped, transferred to Eppendorf tubes and sonicated (30 s on + 30 s off, 5 cycles, 4 °C). Cell suspensions were centrifugated (13,300 *g*, 10 min, 4 °C) and the supernatants were retained. Protein concentrations were quantified using the method outlined in **Section 6.3.9.2**. Supernatants (1 mg/mL protein) were added separately to IP or IgG control antibodies (1 µg/mL). Dynabeads (20 µL/sample) were added according to the manufacturer's instructions and the mixtures were rotated at 4 °C overnight. Supernatants were discarded and the remaining beads were washed twice with immunoprecipitation lysis buffer and three times with PBS. Samples were analysed by SDS-PAGE, as per **Section 6.3.9.3**.

6.3.11.2 With mass spectrometry analysis (IP-MS)

Carried out by Dr Agata Makar. Samples were subjected to overnight on-bead digestion at 4 °C in digest buffer with 2 µg/mL trypsin (100 µL/sample, Thermo Scientific) in proteolysis buffer (2 M urea, 50 mM Tris-HCl pH 7.5, 1 mM DTT), alkylation with iodoacetamide (10 mM) and desalting using C18 stage-tips. Peptides were resuspended in a solution of 0.1% TFA in H_2O (12 µL). 5 µL of the resultant mixture was then injected and separated by an Ultimate 3000 Nano liquid chromatography system, using a C18 packed column (Aurora, IonOptiks, Australia). Mixtures were eluted with an increasing gradient of CH_3CN (4% → 29%) in H_2O supplemented with 0.5% acetic acid over a period of 40 minutes. Peptides were analysed in data-dependent mode on a Thermo Scientific Orbitrap Fusion Lumos

Tribrid Mass Spectrometer with MS1 resolution 120k scanning 350-1400 and rapid ion trap MS2 scan. FragPipe was used for data analysis using the pre-set “LFQ-MBR” workflow and searching against the Uniprot *Homo Sapiens* database. Data obtained from the MS was analysed using R LIMMA package/Perseus software.

6.3.12 Whole cell proteomics

Carried out by Dr Agata Makar. Cell pellets were resuspended in guanidine hydrochloride (6 M) containing tris(2-carboxyethyl) phosphine hydrochloride (TCEP, 1.5 mg/mL, Sigma) and chloroacetamide (1 mg/mL, Sigma) and digested with Lysyl (FUJIFILM Wako Pure Chemicals U.S.A. Corporation) for 4 h at 37 °C. Subsequently, samples were digested overnight using trypsin (Thermo Scientific). To stop the digestion reaction, trifluoroacetic acid (TFA) (Thermo Scientific) was added to the sample and the mixture was vortexed. For desalting, C18 columns were activated with MeOH, followed by 0.1% TFA wash. Samples were added to the C18 columns and centrifugated (500 *g*, 5 min), washed with 0.1% TFA (2 × 50µL) and eluted with 20 µL of elution buffer (50% acetonitrile, 0.05% TFA). The eluents were evaporated in a vacuum concentrator for 20 min and resuspended in 0.1% TFA (15 µL). The samples were subjected to LC-MS analysis as per **Section 6.3.11.2**. Data obtained was analysed using DIA-NN and Perseus software.

6.3.13 Gene set enrichment analysis

Gene set enrichment analysis (GSEA) was carried out using the GSEA 4.3.2 software with unmodified standard parameters. Hallmarks and Gene Ontology: Biological Processes gene sets were examined and differential expression with FDR < 0.05 was considered significant.

6.3.14 Spheroid imaging

ES-2 cells were plated (2,000 cells/well) in ultra-low attachment U-bottom 96-well plates (Corning) and allowed to settle for 48 h. Drug compounds were added at the indicated concentrations and incubated for 48 h. Hoescht 33342 (2 µM final concentration), calcein-AM (2 µM final concentration) and propidium iodide (1 µg/mL final concentration) were added to each well 1 h prior to imaging. Spheroids were imaged live using an ImageXpress Micro Confocal imaging system (Molecular Devices) fitted with a 10X objective, acquiring 1 Z-stack image for each well. Analysis was performed using the MetaXpress software and further manipulated using GraphPad Prism 9.

6.3.15 Immunofluorescence

Cells were grown on sterilised coverslips to achieve ca. 80% confluency at the point of cell fixation. Growth media was aspirated and simultaneously replaced with fixation buffer (pre-warmed to 37 °C). Cells were incubated at 37 °C for 10 min, washed with wash buffer and incubated in glycine for 10 min. The cells were washed twice with wash buffer and incubated in block buffer for 30 min. Coverslips were inverted onto primary antibodies diluted in block buffer (50 µL per coverslip) and incubated in a humidified container at 4 °C overnight. Cells were washed with wash buffer (3 × 5 min) with gentle agitation. Coverslips were inverted onto secondary antibodies diluted in block buffer (50 µL per coverslip) and incubated for 45 min in darkness. Cells were washed with wash buffer (3 × 5 min) with gentle agitation and rinsed in H_2O. The coverslips were mounted with Fluoroshield™ with/without DAPI (Sigma Aldrich) onto microscope slides and allowed to set at 4 °C overnight. Imaging was performed using an Olympus FV3000 laser scanning confocal microscope. Image processing and analysis was performed using ImageJ.

6.3.16 High-throughput imaging

ES-2 53BP1 mApple cells were plated at the indicated cell density in black 96-well thin-bottomed microplates (Corning) and allowed to adhere for 24 h. Cells were then incubated with compounds for 48 h and imaged live using an ImageXpress Micro Confocal imaging system (Molecular Devices) fitted with a 20X water immersion objective. 9 fields of view per well were collected. Hoescht 33342 (Thermo Scientific, 1 µM final concentration) was added to the cells 1 h prior to imaging. Data was collected using the MetaXpress software (Molecular Devices) and analysed using IN Carta software (Molecular Devices). To quantitatively assess DNA damage, nuclei were first segmented using SINAP, an AI-based segmentation protocol with the ‘nuclei.a.h5’ setting applied. Foci within segmented nuclei were counted using the ‘fast puncta’ method.

6.3.17 Stimulated Raman scattering (SRS) microscopy

Cells were imaged at ca. 80% confluency in FluoroDish Cell Culture Dishes (35 mm, World Precision Instruments), treated with compound for the indicated time and imaged live or after fixing in 4% (v/v) formaldehyde in PBS. As required, ER-tracker Green (Invitrogen, 1 µM final concentration) or Hoescht 33342 (Thermo Scientific, 1 µM final concentration) were added according to the manufacturer’s instructions.

Hyperspectral images (obtained from a drop of concentrated sample in DMSO) were recorded using the inbuilt 'sweep' function of the picoEmerald S software that adjusted the pump laser ~0.3 nm for each new image recorded. Hyperspectral images were analysed using the ‘Measure Stack’ feature on ImageJ 1.53c to quantify the change in signal intensity. Images were acquired using a custom-built multi-modal microscope setup, as previously described in Hulme Group publications. A picoEmerald S (APE, Berlin, Germany) laser provided both a tunable pump laser (700–990 nm, 2 ps, 80 MHz repetition rate) and a spatially and temporally overlapped Stokes laser (1032nm, 2 ps, 80 MHz repetition rate). The output beams were inserted into the scanning unit of an Olympus FV1000MPE microscope using a series of dielectric mirrors and a 3× lens-based beam expanding module. The resulting 3.6 mm beams were expanded by a further 3.6× lens within the microscope and directed into an Olympus XLPL25XWMP N.A. 1.05 objective lens using a short-pass 690 nm dichroic mirror (Olympus). For SRS measurements the Stokes beam was intensity modulated with a 20 MHz EoM built into the picoEmerald S. Forward scattered light was collected by a further 25× Olympus XLPL25XWMP N.A. 1.05 objective lens and Stokes light was removed by filtering with an ET890/220m filter (Chroma). Blue two-photon fluorescence signals were filtered using the following series of filters: FF552-Di02, FF483/639-Di01 and FF01-400/40. Green two-photon fluorescence signals were filtered using the following series of filters: FF552-Di02, FF483/639-Di01 and FF510/84. Red two-photon fluorescence signals were filtered using the following series of filters: FF552-Di02, and FF440/520-Di01 and HQ610/75m (Chroma). All other filters from Semrock. A telescope focused the light onto an APE silicon photodiode connected to an APE lock in amplifier with the time constant set to 20 µs. The lock in amplifier signal was fed into an Olympus FV10-Analog unit. Laser powers after the objective were measured up to 20–50 mW for the pump laser and up to 70 mW for the Stokes laser. All images were recorded at 512 × 512 (for hyperspectral scans) or 1024 × 1024 pixels (for normal imaging) with a pixel dwell time between 2 and 20 µs, using FluoView FV10-ASW scanning software (Olympus). Off-resonance images were acquired by tuning to a wavelength ca. ± 2 nm and were used to subtract background from alkyne on-resonance images. Image analysis and processing was performed using ImageJ 1.53c.

References

1. S. Gupta, A. Prakash and B. Medhi, *Indian J. Pharmacol.*, 2022, **54**, 309-313.
2. I. Vermeulen, E. M. Isin, P. Barton, B. Cillero-Pastor and R. M. A. Heeren, *Drug Discov. Today*, 2022, **27**, 2086-2099.
3. J. K. Willmann, N. van Bruggen, L. M. Dinkelborg and S. S. Gambhir, *Nat. Rev. Drug Discov.*, 2008, **7**, 591-607.
4. H. Son, K. Jang, H. Lee, S. E. Kim, K. W. Kang and H. Lee, *Nucl. Med. Mol. Imaging*, 2019, **53**, 208-215.
5. Y. Shen, F. Hu and W. Min, *Annu. Rev. Biophys.*, 2019, **48**, 347-369.
6. S. M. Ametamey, M. Honer and P. A. Schubiger, *Chem. Rev.*, 2008, **108**, 1501-1516.
7. A. McEwen and C. Henson, *Bioanalysis*, 2015, **7**, 557-568.
8. E. G. Solon, *Chem. Res. Toxicol.*, 2012, **25**, 543-555.
9. J. D. Kaggie, M. V. Haase, S. P. Campbell, C. M. Wright, M. J. Graves and K. K. Changani, in *Modern Magnetic Resonance*, ed. G. A. Webb, Springer International Publishing, 2017, pp. 1-20.
10. A. Nilsson, R. J. A. Goodwin, M. Shariatgorji, T. Vallianatou, P. J. H. Webborn and P. E. Andrén, *Anal. Chem.*, 2015, **87**, 1437-1455.
11. M. A. Miller and R. Weissleder, *Nat. Rev. Cancer*, 2017, **17**, 399-414.
12. C. F. Steven, E. Chiarparin, A. N. Hulme and V. G. Brunton, in *Stimulated Raman Scattering Microscopy: Techniques and Applications*, eds. J.-X. Cheng, W. Min, Y. Ozeki and D. Polli, Elsevier, 2022, pp. 403-419.
13. M. Fernández-Suárez and A. Y. Ting, *Nat. Rev. Mol. Cell Biol.*, 2008, **9**, 929-943.
14. H. Fang, Y. Chen, Z. Jiang, W. He and Z. Guo, *Acc. Chem. Res.*, 2023, **56**, 258-269.
15. S. Jeong, D. A. Greenfield, M. Hermsmeier, A. Yamamoto, X. Chen, K. F. Chan and C. L. Evans, *Sci. Rep.*, 2020, **10**, 1-12.
16. S. Michlewska, M. Kubczak, M. Maroto-Díaz, N. Sanz del Olmo, P. Ortega, D. Shcharbin, R. Gomez Ramirez, F. Javier de la Mata, M. Ionov and M. Bryszewska, *Biomolecules*, 2019, **9**, 411-411.
17. M. B. Schierling, E. Doblhofer and T. Scheibel, *Biomater. Sci.*, 2016, **4**, 1515-1523.

18. G. Normand, M. Maker, J. Penraat, K. Kovach, J. G. Ghosh, C. Grosskreutz and S. Chandra, *Commun, Biol.*, 2020, **3**, 1-11.
19. A. M. Laughney, E. Kim, M. M. Sprachman, M. A. Miller, R. H. Kohler, K. S. Yang, J. D. Orth, T. J. Mitchison and R. Weissleder, *Sci. Transl. Med.*, 2014, **6**, 261ra152-261ra152.
20. H. Wang, D. Lee and L. Wei, *Chem. Biomed. Imaging*, 2023, **1**, 3-17.
21. S. Dochow, H. Fatakdawala, J. E. Phipps, D. Ma, T. Bocklitz, M. Schmitt, J. W. Bishop, K. B. Margulies, L. Marcu and J. Popp, *J. Biophotonics*, 2016, **9**, 958-966.
22. W. J. Tipping, M. Lee, A. Serrels, V. G. Brunton and A. N. Hulme, *Chem. Soc. Rev.*, 2016, **45**, 2075-2089.
23. S. Tian, Z. Zhang, F. Meng, Z. Wang and L. Luo, *Chem. Biomed. Imaging*, 2023, **1**, 575-589.
24. D. Polli and G. Cerullo, in *Stimulated Raman Scattering Microscopy: Techniques and Applications*, eds. J.-X. Cheng, W. Min, Y. Ozeki and D. Polli, Elsevier, 2022, pp. 81-90.
25. C. W. Freudiger, W. Min, B. G. Saar, S. Lu, G. R. Holtom, C. He, J. C. Tsai, J. X. Kang and X. S. Xie, *Science*, 2008, **322**, 1857-1861.
26. C. H. C. Jr and M. T. Cicerone, *Nat. Photon.*, 2015, **9**, 295-305.
27. A. Adamczyk, S. Orzechowska, A. M. Nowakowska, K. Brzozowski, K. Majzner and M. Baranska, *TrAC, Trends Anal. Chem.*, 2023, **169**, 117366.
28. C. Zhang, D. Zhang and J.-X. Cheng, *Annu. Rev. Biomed. Eng.*, 2015, **17**, 415-445.
29. E. Ploetz, S. Laimgruber, S. Berner, W. Zinth and P. Gilch, *Appl. Phys. B*, 2007, **87**, 389-393.
30. Y. Li, B. Shen, S. Li, Y. Zhao, J. Qu and L. Liu, *Adv. Biol.*, 2021, **5**, 2000184.
31. K. Brzozowski, E. Matuszyk, A. Pieczara, J. Firlej, A. M. Nowakowska and M. Baranska, *Biotechnol. Adv.*, 2022, **60**, 108003.
32. C.-S. Liao, P. Wang, C. Y. Huang, P. Lin, G. Eakins, R. T. Bentley, R. Liang and J.-X. Cheng, *ACS Photonics*, 2018, **5**, 947-954.
33. M. Lee and W. J. Tipping, in *Neurophotonics and Biomedical Spectroscopy*, eds. R. R. Alfano and L. Shi, Elsevier, 2019, pp. 401-425.
34. H. J. Lee and J.-X. Cheng, *Methods*, 2017, **128**, 119-128.
35. Y. Yuan and F. Lu, *J. Vis. Exp.*, 2022, **186**, e64449.

36. B. G. Saar, C. W. Freudiger, J. Reichman, C. M. Stanley, G. R. Holtom and X. S. Xie, *Science*, 2010, **330**, 1368-1370.
37. B. Manifold and D. Fu, *Annu. Rev. Anal. Chem.*, 2022, **15**, 269-289.
38. C. Tentellino, W. J. Tipping, L. M. C. McGee, L. M. Bain, C. Wetherill, S. Laing, I. Tyson-Hirst, C. J. Suckling, R. Beveridge, F. J. Scott, K. Faulds and D. Graham, *RSC Chem. Biol.*, 2022, **3**, 1403-1415.
39. C. Zeng, F. Hu, R. Long and W. Min, *Analyst*, 2018, **143**, 4844-4848.
40. B. Figueroa, F. X. Xu, R. Hu, S. Men and D. Fu, *J. Phys. Chem. B*, 2022, **126**, 7595-7603.
41. A. Feizpour, T. Marstrand, L. Bastholm, S. Eirefelt and C. L. Evans, *J. Invest. Dermatol.*, 2020, **141**, 1-9.
42. M. J. B. Moester, L. Zada, B. Fokker, F. Ariese and J. F. De Boer, *J. Raman Spectrosc.*, 2019, **50**, 1321-1328.
43. W. J. Tipping, M. Lee, A. Serrels, V. G. Brunton and A. N. Hulme, *Chem. Sci.*, 2017, **8**, 5606-5615.
44. B. Figueroa, W. Fu, T. Nguyen, K. Shin, B. Manifold, F. Wise and D. Fu, *Biomed. Opt. Express*, 2018, **9**, 6116.
45. T. Iino, K. Hashimoto, T. Asai, K. Kuchitsu and Y. Ozeki, *Analyst*, 2021, **146**, 1234-1238.
46. D. Fu, J. Zhou, W. S. Zhu, P. W. Manley, Y. K. Wang, T. Hood, A. Wylie and X. S. Xie, *Nat. Chem.*, 2014, **6**, 614-622.
47. B. S. Wong, E. L. Dunnington, R. Wu, J. I. Kim, K. Hu, T. H. Ro and D. Fu, *Anal. Chem.*, 2024, **96**, 1547-1555.
48. B. Manifold, B. Figueroa and D. Fu, in *Stimulated Raman Scattering Microscopy: Techniques and Applications*, eds. J.-X. Cheng, W. Min, Y. Ozeki and D. Polli, Elsevier, 2022, pp. 69-79.
49. M. Z. Vardaki, V. G. Gregoriou and C. L. Chochos, *RSC Chem. Biol.*, 2024, **5**, 273-292.
50. S. L. Harbeson and R. D. Tung, in *Annu. Rep. Med. Chem.*, Academic Press Inc., 2011, vol. 46, pp. 403-417.
51. L. Shao and M. C. Hewitt, *Drug News Perspect.*, 2010, **23**, 398-398.
52. H. Yamakoshi, K. Dodo, A. Palonpon, J. Ando, K. Fujita, S. Kawata and M. Sodeoka, *J. Am. Chem. Soc.*, 2012, **134**, 20681-20689.
53. E. Buchy, B. Vukosavljevic, M. Windbergs, D. Sobot, C. Dejean, S. Mura, P. Couvreur and D. Desmaële, *Beilstein J. Org. Chem.*, 2016, **12**, 1127-1135.

54. S. You, Y. Liu, Z. Arp, Y. Zhao, E. J. Chaney, M. Marjanovic and S. A. Boppart, *J. Biomed. Opt.*, 2017, **22**, 70502.
55. S. Vanden-Hehir, S. A. Cairns, M. Lee, L. Zoupi, M. P. Shaver, V. G. Brunton, A. Williams and A. N. Hulme, *Biomacromolecules*, 2019, **20**, 4008-4014.
56. H. Yamakoshi, A. F. Palonpon, K. Dodo, J. Ando, S. Kawata, K. Fujita and M. Sodeoka, *Chem. Commun.*, 2014, **50**, 1341-1343.
57. C.-C. Wang, S. Moorhouse, C. Stain, M. Seymour, E. Green, S. Penfield and J. Moger, *J. Biophotonics*, 2018, **11**, e201800108-e201800108.
58. K. Aljakouch, T. Lechtonen, H. K. Yosef, M. K. Hammoud, W. Alsaidi, C. Kötting, C. Mügge, R. Kourist, S. F. El-Mashtoly and K. Gerwert, *Angew. Chem. Int. Ed.*, 2018, **57**, 7250-7254.
59. K. Meister, J. Niesel, U. Schatzschneider, N. Metzler-Nolte, D. A. Schmidt and M. Havenith, *Angew. Chem. Int. Ed.*, 2010, **49**, 3310-3312.
60. J. M. Crawford, C. Portmann, X. Zhang, M. B. J. Roeffaers and J. Clardy, *Proc. Natl. Acad. Sci. U. S. A.*, 2012, **109**, 10821-10826.
61. D. Lin-Vien, N. B. Colthup, W. G. Fateley and J. G. Grasselli, in *The Handbook of Infrared and Raman Characteristic Frequencies of Organic Molecules*, Elsevier, 1991, pp. 95-104.
62. H. Yamakoshi, K. Dodo, M. Okada, J. Ando, A. Palonpon, K. Fujita, S. Kawata and M. Sodeoka, *J. Am. Chem. Soc.*, 2011, **133**, 6102-6105.
63. C. Le Droumaguet, C. Wang and Q. Wang, *Chem. Soc. Rev.*, 2010, **39**, 1233-1239.
64. M. M. Gaschler, F. Hu, H. Feng, A. Linkermann, W. Min and B. R. Stockwell, *ACS Chem. Biol.*, 2018, **13**, 1013-1020.
65. S. M. E. Simpkins, M. D. Weller and L. R. Cox, *Chem. Commun.*, 2007, 4035-4035.
66. E. Bomal, V. Croué, R. Yeo, R. Scopelliti and H. Frauenrath, *Chem. Eur. J.*, 2020, **26**, 8907-8915.
67. J. Du, H. Wang and L. Wei, *ACS Chem. Biol.*, 2022, **17**, 1621-1637.
68. J. Du and L. Wei, *J. Am. Chem. Soc.*, 2022, **144**, 777-786.
69. J. Ao, X. Fang, X. Miao, J. Ling, H. Kang, S. Park, C. Wu and M. Ji, *Nat. Commun.*, 2021, **12**, 3089
70. Y. Yang, X. Bai and F. Hu, *Nat. Commun.*, 2024, **15**, 2578

71. F. Hu, C. Zeng, R. Long, Y. Miao, L. Wei, Q. Xu and W. Min, *Nat. Methods*, 2018, **15**, 194-200.
72. C. Chen, Z. Zhao, N. Qian, S. Wei, F. Hu and W. Min, *Nat. Commun.*, 2021, **12**, 3405
73. S. Buckhout-White, C. M. Spillmann, W. R. Algar, A. Khachatrian, J. S. Melinger, E. R. Goldman, M. G. Ancona and I. L. Medintz, *Nat. Commun.*, 2014, **5**, 5615.
74. L. Wei and W. Min, *J. Phys. Chem. Lett.*, 2018, **9**, 4294-4301.
75. Y. Miao, N. Qian, L. Shi, F. Hu and W. Min, *Nat. Commun.*, 2021, **12**, 4518.
76. L. Wei, Z. Chen, L. Shi, R. Long, A. V. Anzalone, L. Zhang, F. Hu, R. Yuste, V. W. Cornish and W. Min, *Nature*, 2017, **544**, 465-470.
77. H. Fujioka, J. Shou, R. Kojima, Y. Urano, Y. Ozeki and M. Kamiya, *J. Am. Chem. Soc.*, 2020, **142**, 20701-20707.
78. J. Du, X. Tao, T. Begušić and L. Wei, *J. Phys. Chem. B*, 2023, **127**, 4979-4988.
79. K. Sepp, M. Lee, M. T. J. Bluntzer, G. V. Helgason, A. N. Hulme and V. G. Brunton, *J. Med. Chem.*, 2020, **63**, 2028-2034.
80. M. P. Ravindra, M. Lee, S. Dimova, C. F. Steven, M. T. J. Bluntzer, V. G. Brunton and A. N. Hulme, *Chem. Eur. J.*, 2023, **29**, e202300953.
81. N. Das, Y. Dai, P. Liu, C. Hu, L. Tong, X. Chen and Z. Smith, *Sensors*, 2017, **17**, 1592.
82. B. Isherwood, P. Timpson, E. J. McGhee, K. I. Anderson, M. Canel, A. Serrels, V. G. Brunton and N. O. Carragher, *Pharmaceutics*, 2011, **3**, 141-170.
83. A. Pieczara, R. A. Arellano Reyes, T. E. Keyes, P. Dawiec and M. Baranska, *ACS Sensors*, 2024, **9**, 995-1003.
84. X. Li, M. Jiang, J. W. Y. Lam, B. Z. Tang and J. Y. Qu, *J. Am. Chem. Soc.*, 2017, **139**, 17022-17030.
85. J. Lin, M. E. Graziotto, P. A. Lay and E. J. New, *Cells*, 2021, **10**, 1699.
86. E. C. Randall, K. B. Emdal, J. K. Laramy, M. Kim, A. Roos, D. Calligaris, M. S. Regan, S. K. Gupta, A. C. Mladek, B. L. Carlson, A. J. Johnson, F. K. Lu, X. S. Xie, B. A. Joughin, R. J. Reddy, S. Peng, W. M. Abdelmoula, P. R. Jackson, A. Kolluri, K. A. Kellersberger, J. N. Agar, D. A. Lauffenburger, K. R. Swanson, N. L. Tran, W. F. Elmquist, F. M. White, J. N. Sarkaria and N. Y. R. Agar, *Nat. Commun.*, 2018, **9**, 1-13.

87. S. F. El-Mashtoly, D. Petersen, H. K. Yosef, A. Mosig, A. Reinacher-Schick, C. Kötting and K. Gerwert, *Analyst*, 2014, **139**, 1155-1161.
88. Z. An, O. Aksoy, T. Zheng, Q.-W. Fan and W. A. Weiss, *Oncogene*, 2018, **37**, 1561-1575.
89. M. Tuck, F. Grélard, L. Blanc and N. Desbenoit, *Front. Chem.*, 2022, **10**, 904688.
90. E. Yang, J. H. Kim, C. M. Tressler, X. E. Shen, D. R. Brown, C. C. Johnson, T.-H. Hahm, I. Barman and K. Glunde, *Biosens. Bioelectron.*, 2023, **239**, 115597.
91. A. Walter, P. Paul-Gilloteaux, B. Plochberger, L. Sefc, P. Verkade, J. G. Mannheim, P. Slezak, A. Unterhuber, M. Marchetti-Deschmann, M. Ogris, K. Bühler, D. Fixler, S. H. Geyer, W. J. Weninger, M. Glösmann, S. Handschuh and T. Wanek, *Front. Phys.*, 2020, **8**, 47-47.
92. E. L. Dunnington, B. S. Wong and D. Fu, *Anal. Chem.*, 2024, DOI: 10.1021/acs.analchem.4c01413.
93. C. Bellodi, M. R. Lidonnici, A. Hamilton, G. V. Helgason, A. R. Soliera, M. Ronchetti, S. Galavotti, K. W. Young, T. Selmi, R. Yacobi, R. A. Van Etten, N. Donato, A. Hunter, D. Dinsdale, E. Tirrò, P. Vigneri, P. Nicotera, M. J. Dyer, T. Holyoake, P. Salomoni and B. Calabretta, *J. Clin. Invest.*, 2009, **119**, 1109-1123.
94. G. A. Horne, J. Stobo, C. Kelly, A. Mukhopadhyay, A. L. Latif, J. Dixon-Hughes, L. McMahon, P. Cony-Makhoul, J. Byrne, G. Smith, S. Koschmieder, T. H. Brümmendorf, P. Schafhausen, P. Gallipoli, F. Thomson, W. Cong, R. E. Clark, D. Milojkovic, G. V. Helgason, L. Foroni, F. E. Nicolini, T. L. Holyoake and M. Copland, *Leukemia*, 2020, **34**, 1775-1786.
95. R. Mitchell, L. E. M. Hopcroft, P. Baquero, E. K. Allan, K. Hewit, D. James, G. Hamilton, A. Mukhopadhyay, J. O'Prey, A. Hair, J. V. Melo, E. Chan, K. M. Ryan, V. Maguer-Satta, B. J. Druker, R. E. Clark, S. Mitra, P. Herzyk, F. E. Nicolini, P. Salomoni, E. Shanks, B. Calabretta, T. L. Holyoake and G. V. Helgason, *J. Natl. Cancer. Inst.*, 2018, **110**, 467-478.
96. B. G. Saar, L. R. Contreras-Rojas, X. S. Xie and R. H. Guy, *Mol. Pharm.*, 2011, **8**, 969-975.
97. A. R. Pries, M. Höpfner, F. Le Noble, M. W. Dewhirst and T. W. Secomb, *Nat. Rev. Cancer*, 2010, **10**, 587-593.

98. M. Macias-Silva, G. Vazquez-Victorio and J. Hernandez-Damian, *Curr. Chem. Biol.*, 2010, **4**, 124-132.
99. D. Monaghan, E. O'Connell, F. L. Cruickshank, B. O'Sullivan, F. J. Giles, A. N. Hulme and H. O. Fearnhead, *Biochem. Biophys. Res. Commun.*, 2014, **443**, 761-767.
100. I. A. Inverarity and A. N. Hulme, *Org. Biomol. Chem.*, 2007, **5**, 636-636.
101. J. Seidel, Y. Miao, W. Porterfield, W. Cai, X. Zhu, S.-J. Kim, F. Hu, S. Bhattarai-Kline, W. Min and W. Zhang, *Chem. Commun.*, 2019, **55**, 9379-9382.
102. S. Vanden-Hehir, W. J. Tipping, M. Lee, V. G. Brunton, A. Williams and A. N. Hulme, *Nanomaterials*, 2019, **9**, 1-19.
103. B. Priem, C. Tian, J. Tang, Y. Zhao and W. J. M. Mulder, *Expert Opin. Drug Deliv.*, 2015, **12**, 1881-1894.
104. M. Masserini, *ISRN Biochem.*, 2013, **2013**, 1-18.
105. M. Li, R. Wang and Q. Bao, *J. Control. Release*, 2024, **367**, 676-686.
106. B. Manifold, E. Thomas, A. T. Francis, A. H. Hill and D. Fu, *Biomed. Opt. Express*, 2019, **10**, 3860-3874.
107. I. J. Pence, B. A. Kuzma, M. Brinkmann, T. Hellwig and C. L. Evans, *Biomed. Opt. Express*, 2021, **12**, 6095.
108. C. Zong, R. Premasiri, H. Lin, Y. Huang, C. Zhang, C. Yang, B. Ren, L. D. Ziegler and J.-X. Cheng, *Nat. Commun.*, 2019, **10**, 5318.
109. A. J. X. Choorakuttil, A. Pruccoli, M. J. Winterhalder, P. Zirak, D. Gudavičius, G. Martynaitis, D. Petrulionis, D. Samsonas, L. Kontenis and A. Zumbusch, *Appl. Phys. Lett.*, 2023, **123**, 163701.
110. L. Gong, W. Zheng, Y. Ma and Z. Huang, *Phys. Rev. Appl.*, 2019, **11**, 034041.
111. L. Gong, S. Lin and Z. Huang, *Opt. Lett.*, 2023, **48**, 6516.
112. H. Jang, Y. Li, A. A. Fung, P. Bagheri, K. Hoang, D. Skowronska-Krawczyk, X. Chen, J. Y. Wu, B. Bintu and L. Shi, *Nat. Methods*, 2023, **20**, 448-458.
113. H. Kawagoe, J. Ando, M. Asanuma, K. Dodo, T. Miyano, H. Ueda, M. Sodeoka and K. Fujita, *Sci. Rep.*, 2021, **11**, 15742.
114. Y. Suzuki, K. Kobayashi, Y. Wakisaka, D. Deng, S. Tanaka, C.-J. Huang, C. Lei, C.-W. Sun, H. Liu, Y. Fujiwaki, S. Lee, A. Isozaki, Y. Kasai, T. Hayakawa, S. Sakuma, F. Arai, K. Koizumi, H. Tezuka, M. Inaba, K. Hiraki, T. Ito, M. Hase, S. Matsusaka, K. Shiba, K. Suga, M. Nishikawa, M. Jona, Y.

Yatomi, Y. Yalikun, Y. Tanaka, T. Sugimura, N. Nitta, K. Goda and Y. Ozeki, *Proc. Natl. Acad. Sci. U. S. A.*, 2019, **116**, 15842-15848.

115. K. S. Shin, S. Men, A. Wong, C. Cobb-Bruno, E. Y. Chen and D. Fu, *Anal. Chem.*, 2022, **94**, 3791-3799.
116. D. Tsikritsis, E. J. Legge and N. A. Belsey, *Analyst*, 2022, **147**, 4642-4656.
117. K. West, C. Wang, A. S. Batsanov and M. R. Bryce, *J. Org. Chem.*, 2006, **71**, 8541-8544.
118. A. S. Shetty, J. Zhang and J. S. Moore, *J. Am. Chem. Soc.*, 1996, **118**, 1019-1027.
119. M. San Angelo, D. Khago, B. Choi, F. R. Fronczek and R. Isovitsch, *J. Mol. Struct.*, 2019, **1177**, 9-15.
120. W. Wei, S. Cherukupalli, L. Jing, X. Liu and P. Zhan, *Drug Discov. Today*, 2020, **25**, 1839-1845.
121. F. Lovering, J. Bikker and C. Humblet, *J. Med. Chem.*, 2009, **52**, 6752-6756.
122. J. J. Li and M. Yang, in *Drug Discovery with Privileged Building Blocks*, CRC Press, Boca Raton, 2021, pp. 57-66.
123. M. Ishikawa and Y. Hashimoto, *J. Med. Chem.*, 2011, **54**, 1539-1554.
124. A. M. Cook and C. Wolf, *Tetrahedron Lett.*, 2015, **56**, 2377-2392.
125. N.-E. Choi, J.-Y. Lee, E.-C. Park, J.-H. Lee and J. Lee, *Molecules*, 2021, **26**, 217.
126. J. Lin, K. Yang and E. J. New, *Org. Biomol. Chem.*, 2021, **19**, 9339-9357.
127. N. J. Silva, F. B. C. Machado, H. Lischka and A. J. A. Aquino, *Phys. Chem. Chem. Phys.*, 2016, **18**, 22300-22310.
128. K. Carter-Fenk and J. M. Herbert, *Phys. Chem. Chem. Phys.*, 2020, **22**, 24870-24886.
129. W. Shen and S. A. Thomas, *Org. Lett.*, 2000, **2**, 2857-2860.
130. C. A. Fleckenstein and H. Plenio, *Chem. Soc. Rev,*, 2010, **39**, 694-711.
131. M. Schilz and H. Plenio, *J. Org. Chem.*, 2012, **77**, 2798-2807.
132. W. Shi, Y. Luo, X. Luo, L. Chao, H. Zhang, J. Wang and A. Lei, *J. Am. Chem. Soc.*, 2008, **130**, 14713-14720.
133. R. Frański and B. Gierczyk, *J. Am. Soc. Mass Spectrom.*, 2010, **21**, 545-549.
134. S. N. Jackson, D. C. Barbacci, A. Bonci and A. S. Woods, *J. Am. Soc. Mass Spectrom.*, 2019, **30**, 1199-1203.
135. H. J. Cho, S. W. Kim, S. Kim, S. Lee, J. Lee, Y. Cho, Y. Lee, T. W. Lee, H. J. Shin and C. Song, *J. Mater. Chem.*, 2020, **8**, 17289-17296.

136. S. Bera, X. Dong, B. Krishnarjuna, S. A. Raab, D. A. Hales, W. Ji, Y. Tang, L. J. W. Shimon, A. Ramamoorthy, D. E. Clemmer, G. Wei and E. Gazit, *Cell Rep. Phys. Sci*, 2021, **2**, 100391-100391.
137. J. K. D. Surette, M. A. Macdonald, M. J. Zaworotko and R. D. Singer, *J. Chem. Crystallogr.*, 1994, **24**.
138. C. Janiak, *J. Chem. Soc., Dalton Trans.*, 2000, 3885-3896.
139. D. Gheidari, M. Mehrdad and S. Maleki, *Sustain. Chem. Pharm.*, 2022, **27**.
140. L. Wei and S. V. Malhotra, *Curr. Med. Chem.*, 2010, **17**, 234-253.
141. A. S. El-Azab, N. Y. Khalil, A. A. M. Abdel-Aziz and X. Liu, *J. Chem.*, 2021, **2021**, 1-8.
142. N. M. Riad, D. P. Zlotos and U. Holzgrabe, *IUCrData*, 2017, **2**.
143. H. Kakuta, Y. Koiso, K. Nagasawa and Y. Hashimoto, *Bioorg. Med. Chem. Lett.*, 2003, **13**, 83-86.
144. A. Karimi, R. Borner, G. Mata and N. W. Luedtke, *J. Am. Chem. Soc.*, 2020, **142**, 14422-14426.
145. H. Yamakoshi, D. Shibata, K. Bando, S. Kajimoto, A. Kohyama, S. Egoshi, K. Dodo, Y. Iwabuchi, M. Sodeoka, K. Fujita and T. Nakabayashi, *Chem. Commun.*, 2023, **59**, 14563-14566.
146. S. Bochum, S. Berger and U. M. Martens, in *Small Molecules in Oncology*, ed. U. M. Martens, Springer International Publishing, 2018, pp. 217-233.
147. C. Z. Gao, W. Dong, Z. W. Cui, Q. Yuan, X. M. Hu, Q. M. Wu, X. Han, Y. Xu and Z. L. Min, *J. Enzyme Inhib. Med. Chem.*, 2019, **34**, 150-162.
148. R. Ambur Sankaranarayanan, S. Kossatz, W. Weber, M. Beheshti, A. Morgenroth and F. M. Mottaghy, *J. Clin. Med.*, 2020, **9**, 2130.
149. Q. Wang and J. Zhang, *Eur. J. Med. Chem.*, 2022, **242**, 114690.
150. G. M. Thurber, T. Reiner, K. S. Yang, R. H. Kohler and R. Weissleder, *Mol. Cancer Ther.*, 2014, **13**, 986-995.
151. E. Kim, K. S. Yang, R. J. Giedt and R. Weissleder, *Chem. Commun.*, 2014, **50**, 4504.
152. A. Rutkowska, D. W. Thomson, J. Vappiani, T. Werner, K. M. Mueller, L. Dittus, J. Krause, M. Muelbaier, G. Bergamini and M. Bantscheff, *ACS Chem. Biol.*, 2016, **11**, 2541-2550.
153. R. Huang and P.-K. Zhou, *Signal Transduct. Target. Ther.*, 2021, **6**, 254
154. E. E. Alemasova and O. I. Lavrik, *Nucleic Acids Res.*, 2019, **47**, 3811-3827.

155. L. Van Beek, É. McClay, S. Patel, M. Schimpl, L. Spagnolo and T. Maia De Oliveira, *Int. J. Mol. Sci.*, 2021, **22**, 5112.
156. M. J. Suskiewicz, D. Munnur, Ø. Strømland, J.-C. Yang, Laura, C. Chatrin, K. Zhu, D. Baretić, S. Goffinont, M. Schuller, W.-F. Wu, Jonathan, D. Ahel, S. Sanyal, D. Neuhaus and I. Ahel, *Nucleic Acids Res.*, 2023, **51**, 8217-8236.
157. G. Papeo, N. Avanzi, S. Bettoni, A. Leone, M. Paolucci, R. Perego, F. Quartieri, F. Riccardi-Sirtori, S. Thieffine, A. Montagnoli and R. Lupi, *SLAS Discov.*, 2014, **19**, 1212-1219.
158. T. Helleday, *Mol. Oncol.*, 2011, **5**, 387-393.
159. S. Chen, R. Cao, L. Xiang, Z. Li, H. Chen, J. Zhang and X. Feng, *Biomater. Sci.*, 2023, **11**, 6436-6456.
160. G. H. Goetz, L. Philippe and M. J. Shapiro, *ACS Med. Chem. Lett.*, 2014, **5**, 1167-1172.
161. G. H. Goetz, W. Farrell, M. Shalaeva, S. Sciabola, D. Anderson, J. Yan, L. Philippe and M. J. Shapiro, *J. Med. Chem.*, 2014, **57**, 2920-2929.
162. P. Ertl, in *Molecular Drug Properties: Measurement and Prediction*, ed. R. Mannhold, Wiley, 2007, pp. 111-126.
163. S. Das, S. Singh, V. Chawla, P. A. Chawla and R. Bhatia, *Trends Anal. Chem.*, 2024, **171**, 117501.
164. P. Stojanovic, K. Luger and J. Rudolph, *Biochemistry*, 2023, **62**, 2382-2390.
165. T. A. Hopkins, Y. Shi, L. E. Rodriguez, L. R. Solomon, C. K. Donawho, E. L. DiGiammarino, S. C. Panchal, J. L. Wilsbacher, W. Gao, A. M. Olson, D. F. Stolarik, D. J. Osterling, E. F. Johnson and D. Maag, *Mol. Cancer. Res.*, 2015, **13**, 1465-1477.
166. K. S. Yang, G. Budin, C. Tassa, O. Kister and R. Weissleder, *Angew. Chem. Int. Ed.*, 2013, **52**, 10593-10597.
167. X. Wang, W. Liu, K. Li, K. Chen, S. He, J. Zhang, B. Gu, X. Xu and S. Song, *Eur. J. Nucl. Med. Mol. Imag.*, 2023, **50**, 2606-2620.
168. A. A. Gopal, B. Fernandez, J. Delano, R. Weissleder and J. M. Dubach, *Cell Chemical Biology*, 2024, DOI: 10.1016/j.chembiol.2023.12.019.
169. D. Narang, C. Lento and D. J. Wilson, *Biomedicines*, 2020, **8**, 224.
170. K. Ryan, B. Bolaňos, M. Smith, P. B. Palde, P. D. Cuenca, T. L. Vanarsdale, S. Niessen, L. Zhang, D. Behenna, M. A. Ornelas, K. T. Tran, S. Kaiser, L. Lum, A. Stewart and K. S. Gajiwala, *J. Biol. Chem.*, 2021, **296**, 100251.
171. J. Rudolph, K. Jung and K. Luger, *Proc. Natl. Acad. Sci. U. S. A.*, 2022, **119**.

172. H. Xue, A. Bhardwaj, Y. Yin, C. Fijen, A. Ephstein, L. Zhang, X. Ding, J. M. Pascal, T. L. Vanarsdale and E. Rothenberg, *Sci. Adv.*, 2022, **8**.
173. Jennine, M.-F. Langelier, Jamie, Amanda, Connie, Kelly, M. McCauley, Jamin, Ben and John, *Mol. Cell*, 2015, **60**, 755-768.
174. L. Zandarashvili, M.-F. Langelier, U. K. Velagapudi, M. A. Hancock, J. D. Steffen, R. Billur, Z. M. Hannan, A. J. Wicks, D. B. Krastev, S. J. Pettitt, C. J. Lord, T. T. Talele, J. M. Pascal and B. E. Black, *Science*, 2020, **368**, eaax6367.
175. T. E. H. Ogden, J.-C. Yang, M. Schimpl, L. E. Easton, E. Underwood, Philip, Michael, M.-F. Langelier, John, Kevin and D. Neuhaus, *Nucleic Acids Res.*, 2021, **49**, 2266-2288.
176. M. Borgini and P. Wipf, *ACS Med. Chem. Lett.*, 2023, **14**, 652-657.
177. L. M. Colletti, Y. Liu, G. Koev, P. L. Richardson, C. M. Chen and W. Kati, *Anal. Biochem.*, 2008, **383**, 186-193.
178. L. J. Gordon, M. Allen, P. Artursson, M. M. Hann, B. J. Leavens, A. Mateus, S. Readshaw, K. Valko, G. J. Wayne and A. West, *SLAS Discov.*, 2016, **21**, 156-164.
179. M. Groessl, O. Zava and P. J. Dyson, *Metallomics*, 2011, **3**, 591.
180. M. A. C. Bruin, G. S. Sonke, J. H. Beijnen and A. D. R. Huitema, *Clin. Pharmacokinet.*, 2022, **61**, 1649-1675.
181. L. Henneman, M. H. Van Miltenburg, E. M. Michalak, T. M. Braumuller, J. E. Jaspers, A. P. Drenth, R. De Korte-Grimmerink, E. Gogola, K. Szuhai, A. Schlicker, R. Bin Ali, C. Pritchard, I. J. Huijbers, A. Berns, S. Rottenberg and J. Jonkers, *Proc. Natl. Acad. Sci. U. S. A.*, 2015, **112**, 8409-8414.
182. L. Oplustil O'Connor, S. L. Rulten, A. N. Cranston, R. Odedra, H. Brown, J. E. Jaspers, L. Jones, C. Knights, B. Evers, A. Ting, R. H. Bradbury, M. Pajic, S. Rottenberg, J. Jonkers, D. Rudge, N. M. B. Martin, K. W. Caldecott, A. Lau and M. J. O'Connor, *Cancer Res.*, 2016, **76**, 6084-6094.
183. P. Fang, J. A. Madden, L. Neums, R. K. Moulder, M. L. Forrest and J. Chien, *Mol. Cancer Res.*, 2018, **16**, 961-973.
184. C. P. Irwin, Y. Portorreal, C. Brand, Y. Zhang, P. Desai, B. Salinas, W. A. Weber and T. Reiner, *Neoplasia* 2014, **16**, 432-440.
185. C. Cao, J. Yang, Y. Chen, P. Zhou, Y. Wang, W. Du, L. Zhao and Y. Chen, *J. Med. Chem.*, 2020, **63**, 11012-11033.

186. H.-J. Shin, H.-K. Kwon, J.-H. Lee, X. Gui, A. Achek, J.-H. Kim and S. Choi, *Sci. Rep.*, 2015, **5**, 15798.
187. A. Hallas-Potts, J. C. Dawson and C. S. Herrington, *Sci. Rep.*, 2019, **9**.
188. M. K. Gomez, G. Illuzzi, C. Colomer, M. Churchman, R. L. Hollis, M. J. O'Connor, C. Gourley, E. Leo and D. W. Melton, *Cancers*, 2020, **12**, 1503-1503.
189. A. Go, J. W. Jang, W. Lee, J. D. Ha, H. J. Kim and H. J. Nam, *Eur. J. Med. Chem.*, 2020, **204**, 112635.
190. S. Wang, L. Han, J. Han, P. Li, Q. Ding, Q.-J. Zhang, Z.-P. Liu, C. Chen and Y. Yu, *Nat. Chem. Biol.*, 2019, **15**, 1223-1231.
191. B. Schwanhäusser, D. Busse, N. Li, G. Dittmar, J. Schuchhardt, J. Wolf, W. Chen and M. Selbach, *Nature*, 2011, **473**, 337-342.
192. S. R. Choi, H. M. Wang, M. H. Shin and H.-S. Lim, *Int. J. Mol. Sci.*, 2021, **22**, 6407.
193. Y. Wang, J. Zhang, J. Deng, C. Wang, L. Fang, Y. Zhang and J. Li, *CCS Chem.*, 2023, **5**, 2207-2214.
194. S. Xie, J. Zhu, J. Li, F. Zhan, H. Yao, J. Xu and S. Xu, *J. Med. Chem.*, 2023, **66**, 10917-10933.
195. A. Ma, E. Stratikopoulos, K.-S. Park, J. Wei, T. C. Martin, X. Yang, M. Schwarz, V. Leshchenko, A. Rialdi, B. Dale, A. Lagana, E. Guccione, S. Parekh, R. Parsons and J. Jin, *Nat. Chem. Biol.*, 2020, **16**, 214-222.
196. S. Xie, F. Zhan, J. Zhu, Y. Sun, H. Zhu, J. Liu, J. Chen, Z. Zhu, D. H. Yang, Z. S. Chen, H. Yao, J. Xu and S. Xu, *Angew. Chem.*, 2023, **135**.
197. Q. He, X. Zhao, D. Wu, S. Jia, C. Liu, Z. Cheng, F. Huang, Y. Chen, T. Lu and S. Lu, *Eur. J. Med. Chem.*, 2023, **260**, 115741.
198. Z. Qi and L. Chen, in *Autophagy: Biology and Diseases*, ed. Q. Zheng-Hong, Springer Singapore, 2019, pp. 167-177.
199. N. M. Kocaturk and D. Gozuacik, *Front. Cell Dev. Biol.*, 2018, **6**, 128.
200. Y. Wang and W.-D. Le, in *Autophagy: Biology and Diseases*, ed. Q. Zheng-Hong, Springer Singapore, 2019, pp. 527-550.
201. Y. Li, S. Li and H. Wu, *Cells*, 2022, **11**, 851.
202. R. E. Lackie, A. Maciejewski, V. G. Ostapchenko, J. Marques-Lopes, W.-Y. Choy, M. L. Duennwald, V. F. Prado and M. A. M. Prado, *Front. Neurosci.*, 2017, **11**.
203. T. E. Rusten and H. Stenmark, *Nat. Cell Biol.*, 2010, **12**, 207-209.

204. S. Olivari, T. Cali, K. E. H. Salo, P. Paganetti, L. W. Ruddock and M. Molinari, *Biochem. Biophys. Res. Commun.*, 2006, **349**, 1278-1284.
205. S. Panier and S. J. Boulton, *Nat. Rev. Mol. Cell Biol.*, 2014, **15**, 7-18.
206. K. S. Yang, R. H. Kohler, M. Landon, R. Giedt and R. Weissleder, *Sci. Rep.*, 2015, **5**, 10129.
207. F. Yang, C. Baumann and R. De La Fuente, *Dev. Biol.*, 2009, **331**, 326-338.
208. K. Schork, K. Podwojski, M. Turewicz, C. Stephan and M. Eisenacher, in *Quantitative Methods in Proteomics*, eds. K. Marcus, M. Eisenacher and B. Sitek, Springer US, 2021, pp. 1-20.
209. T. Mosler, H. I. Baymaz, J. F. Gräf, I. Mikicic, G. Blattner, E. Bartlett, M. Ostermaier, R. Piccinno, J. Yang, A. Voigt, M. Gatti, S. Pellegrino, M. Altmeyer, K. Luck, I. Ahel, V. Roukos and P. Beli, *Nucleic Acids Res.*, 2022, **50**, 11600-11618.
210. D. Huang and W. L. Kraus, *Mol. Cell*, 2022, **82**, 2315-2334.
211. D. Szklarczyk, R. Kirsch, M. Koutrouli, K. Nastou, F. Mehryary, R. Hachilif, A. L. Gable, T. Fang, Nadezhda, S. Pyysalo, P. Bork, Lars and Christian, *Nucleic Acids Res.*, 2023, **51**, D638-D646.
212. E. M. Sontag, F. Morales-Polanco, J.-H. Chen, G. McDermott, P. T. Dolan, D. Gestaut, M. A. Le Gros, C. Larabell and J. Frydman, *Nat. Cell Biol.*, 2023, **25**, 699-713.
213. H. Sun, M. Wu, M. Wang, X. Zhang and J. Zhu, *Front. Neurosci.*, 2022, **16**.
214. S. Bansal, M. Vachher and A. Burman, *J. Proteins Proteomics*, 2023, **14**, 187-200.
215. Y. Yang, F. Ma, Z. Liu, Q. Su, Y. Liu, Z. Liu and Y. Li, *J. Biol. Chem.*, 2019, **294**, 772-782.
216. K. F. R. Pobre, G. J. Poet and L. M. Hendershot, *J. Biol. Chem.*, 2019, **294**, 2098-2108.
217. M. Gatti, R. Imhof, Q. Huang, M. Baudis and M. Altmeyer, *Cell Rep.*, 2020, **32**, 107985.
218. G. Garcia, H. Zhang, S. Moreno, C. K. Tsui, B. M. Webster, R. Higuchi-Sanabria and A. Dillin, *eLife*, 2023, **12**, e83884.
219. I. Hapala, E. Marza and T. Ferreira, *Biol Cell*, 2011, **103**, 271-285.
220. C. M. Simbulan-Rosenthal, D. S. Rosenthal, R. Luo, R. Samara, L. A. Espinoza, P. O. Hassa, M. O. Hottiger and M. E. Smulson, *Oncogene*, 2003, **22**, 8460-8471.

221. P. Iglesias, M. Seoane, I. Golán, I. Castro-Piedras, M. Fraga, V. M. Arce and J. A. Costoya, *Cancers*, 2020, **12**, 2907.
222. D. G. Johnson, *Front. Biosci.*, 1998, **3**, 447-458.
223. P. Iglesias, M. Seoane, I. Golán-Cancela, M. Fraga, V. M. Arce and J. A. Costoya, *Int. J. Mol. Sci.*, 2023, **24**, 8849.
224. I. Dale Rein, K. Solberg Landsverk, F. Micci, S. Patzke and T. Stokke, *Cell Cycle*, 2015, **14**, 3248-3260.
225. A. Kumari, T. Iwasaki, S. Pyndiah, E. K. Cassimere, C. D. Palani and D. Sakamuro, *Cell Death Differ.*, 2015, **22**, 311-322.
226. J. Jacquemyn, A. Cascalho and R. E. Goodchild, *EMBO Rep.*, 2017, **18**, 1905-1921.
227. F. X. Xu, E. G. Rathbone and D. Fu, *J. Phys. Chem. B*, 2023, **127**, 2187-2197.
228. M. Lee, C. S. Herrington, M. Ravindra, K. Sepp, A. Davies, A. N. Hulme and V. G. Brunton, *Analyst*, 2021, **146**, 789-802.
229. A. R. Allouche, *J. Comput. Chem.*, 2011, **32**, 174-182.
230. A. Nuzzi, A. Fiasella, J. A. Ortega, C. Pagliuca, S. Ponzano, D. Pizzirani, S. M. Bertozzi, G. Ottonello, G. Tarozzo, A. Reggiani, T. Bandiera, F. Bertozzi and D. Piomelli, *Eur. J. Med. Chem.*, 2016, **111**, 138-159.
231. B. C. Hong, H. C. Tseng and S. H. Chen, *Tetrahedron*, 2007, **63**, 2840-2850.
232. J. A. Nieman, S. K. Nair, S. E. Heasley, B. L. Schultz, H. M. Zerth, R. A. Nugent, K. Chen, K. J. Stephanski, T. A. Hopkins, M. L. Knechtel, N. L. Oien, J. L. Wieber and M. W. Wathen, *Bioorg. Med. Chem. Lett.*, 2010, **20**, 3039-3042.
233. H. Xu, B. Ma, Z. Fu, H. Y. Li, X. Wang, Z. Y. Wang, L. J. Li, T. J. Cheng, M. Zheng and H. X. Dai, *ACS Catal.*, 2021, **11**, 1758-1764.
234. W. Shi, Z. Guan, P. Cai and H. Chen, *J. Catal.*, 2017, **353**, 199-204.
235. L. Van Gelderen, G. Rothenberg, V. Roberto Calderone, K. Wilson and N. Raveendran Shiju, *Appl. Organomet. Chem.*, 2013, **27**, 23-27.
236. M. Mokhtar, G. Alzhrani, E. S. Aazam, T. S. Saleh, S. Al-Faifi, S. Panja and D. Maiti, *Chem. Eur. J.*, 2021, **27**, 8875-8885.
237. A. G. Jarvis, P. E. Sehnal, S. E. Bajwa, A. C. Whitwood, X. Zhang, M. S. Cheung, Z. Lin and I. J. S. Fairlamb, *Chem. Eur. J.*, 2013, **19**, 6034-6043.
238. A. Sagadevan, P.-C. Lyu and K. C. Hwang, *Green Chem.*, 2016, **18**, 4526-4530.

239. G. R. Martinez, K. A. M. Walker, D. R. Hirschfeld, J. Bruno, D. S. Yang and P. J. Malone, *J. Med. Chem.*, 1992, **35**, 620-628.
240. C. Ding, Y. Chen, H. Li, B. Wang, Q. Wei, H. Tang, S. Jia, Z. He, P. Wang and X. Zhou, *Chin. Chem. Lett.*, 2019, **30**, 1393-1396.
241. R. Wodtke, J. Steinberg, M. Köckerling, R. Löser and C. Mamat, *RSC Adv,*, 2018, **8**, 40921-40933.
242. Z. M. Zhang, S. Chen and Y. Z. Liang, *Analyst*, 2010, **135**, 1138-1146.
243. J. D. Krass, B. Jastorff and H.-G. Genieser, *Anal. Chem.*, 1997, **69**, 2575-2581.
244. M. Guttman, T. E. Wales, D. Whittington, J. R. Engen, J. M. Brown and K. K. Lee, *J. Am. Soc. Mass Spectrom.*, 2016, **27**, 662-668.
245. M. K. Gomez, G. Illuzzi, C. Colomer, M. Churchman, R. L. Hollis, M. J. O'Connor, C. Gourley, E. Leo and D. W. Melton, *Cancers*, 2020, **12**.

Appendices

Appendix A. Supplementary figures and tables

Table A1. Crystal structure and refinement data for compounds **1a** and **1b**.

Compound	1a	1b	1b
Formula	$C_{18}H_{12}O_2$	$C_{22}H_{18}O_2$	$C_{22}H_{18}O_2$
$D_{calc.}$/ g cm^{-3}	1.338	1.276	1.243
μ/mm^{-1}	0.087	0.080	0.078
Formula Weight	260.28	314.36	314.36
Colour	colourless	colourless	colourless
Shape	lath-shaped	block-shaped	block-shaped
Size/mm^3	0.28×0.07×0.01	0.54×0.18×0.16	0.54×0.18×0.16
T/K	100.00	100.0	260.00
Crystal System	triclinic	triclinic	monoclinic
Space Group	P-1	P-1	$P2_1/n$
a/Å	5.9569(6)	6.9580(5)	18.7900(7)
b/Å	7.5952(8)	18.6935(13)	6.9992(2)
c/Å	14.4775(16)	26.3250(19)	26.5475(9)
α/°	90.906(5)	106.881(2)	90
β/°	98.988(4)	91.463(3)	105.8602(11)
γ/°	92.955(4)	91.315(3)	90
V/Å^3	645.93(12)	3273.8(4)	3358.5(2)
Z	2	8	8
Z'	1	4	2
Wavelength/Å	0.71073	0.71073	0.71073
Radiation type	MoK_α	MoK_α	MoK_α
Θ_{min}/°	2.686	2.184	2.254
Θ_{max}/°	26.398	26.561	25.372
Measured Refl's.	39741	54446	83811
Indep't Refl's	2648	17153	6154
Refl's I≥2 σ(I)	1557	12538	4683
R_{int}	0.0979	0.0607	0.0426
Parameters	231	889	473
Restraints	0	5	10
Largest Peak	0.326	0.352	0.196
Deepest Hole	-0.277	-0.242	-0.171
GooF	1.053	1.046	1.038
wR_2 (all data)	0.1866	0.2060	0.1298
wR_2	0.1525	0.1801	0.1146
R_1 (all data)	0.1323	0.0912	0.0607
R_1	0.0703	0.0620	0.0441

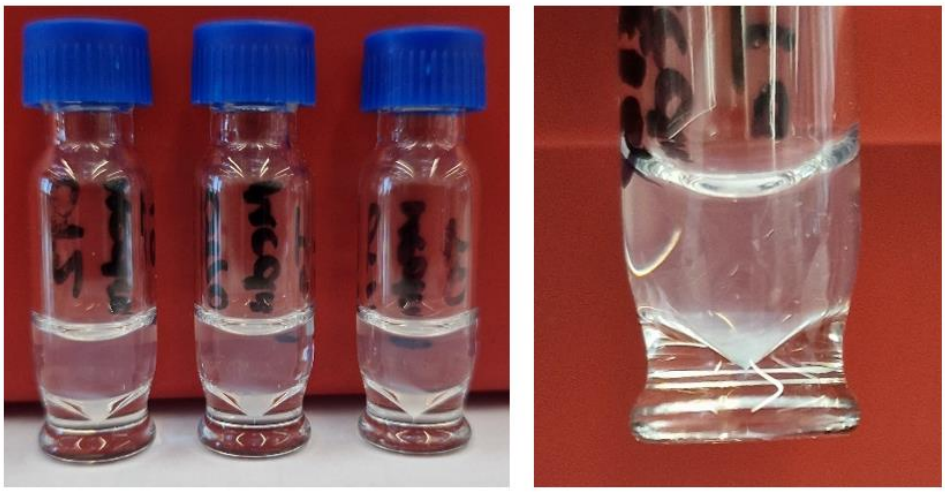

Figure A1. Left: Image showing precipitation of **26a**, **29a** and **29c** (L to R) from media during the LC-MS stability assay. **Right**: Magnification of vial containing **29a**.

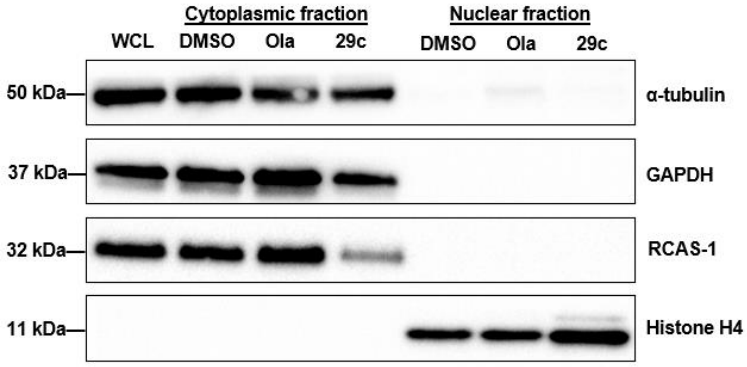

Figure A2. Representative Western blot after treatment with the indicated compound (2.5 µM, 48 h) and subsequent subcellular fractionation. WCL = whole cell lysate (non-fractionated).

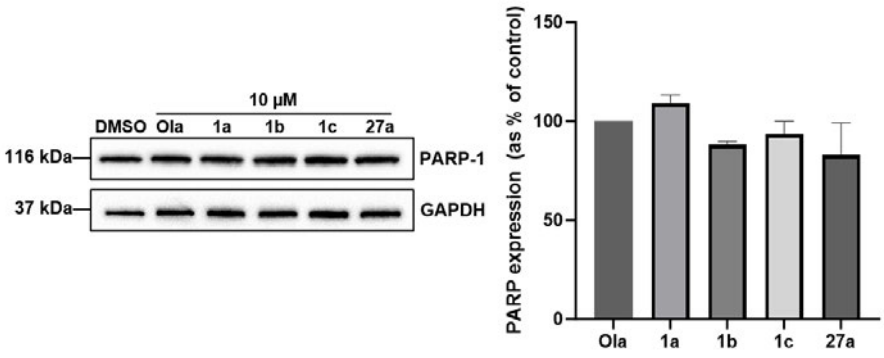

Figure A3. Representative Western blot and corresponding quantification of PARP-1 expression after treatment with **1a**–**1c** and **27a** (10 µM, 48 h). PARP expression is expressed as a percentage of olaparib control. Error bars report the standard deviation of the mean from three independent experiments.

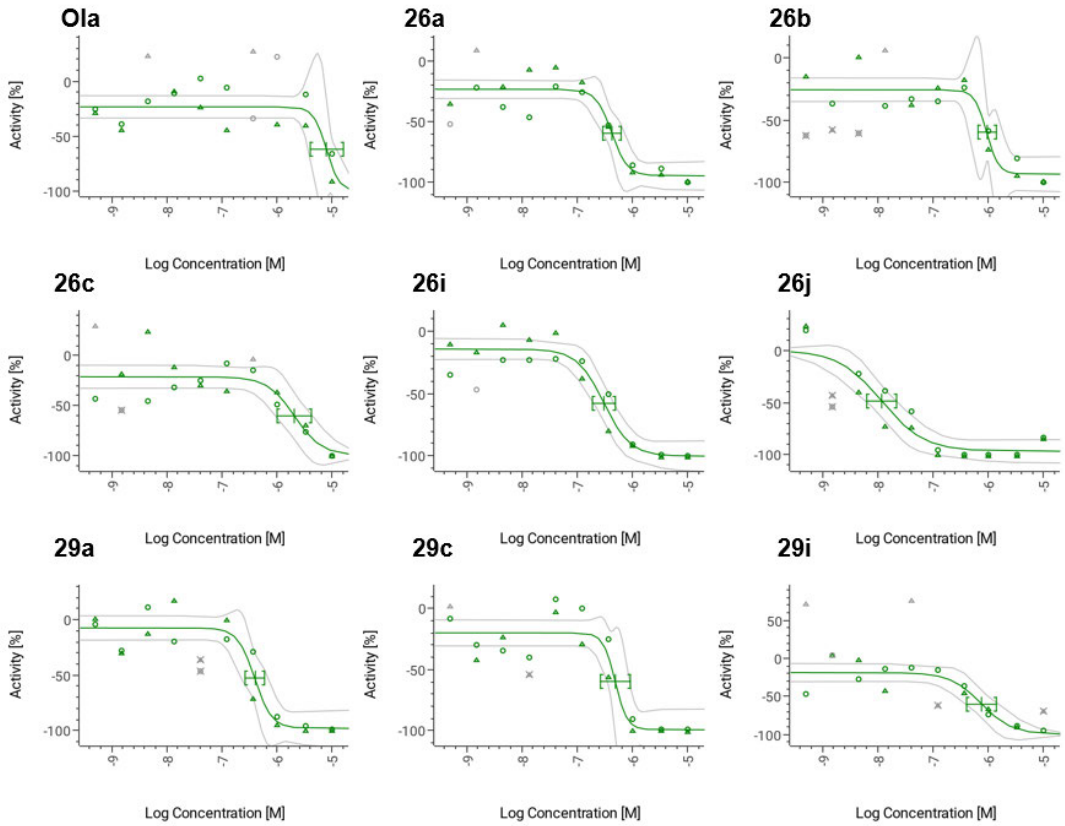

Figure A4. Dose-response curves from DLD-1 WT viability assays carried out at AstraZeneca.

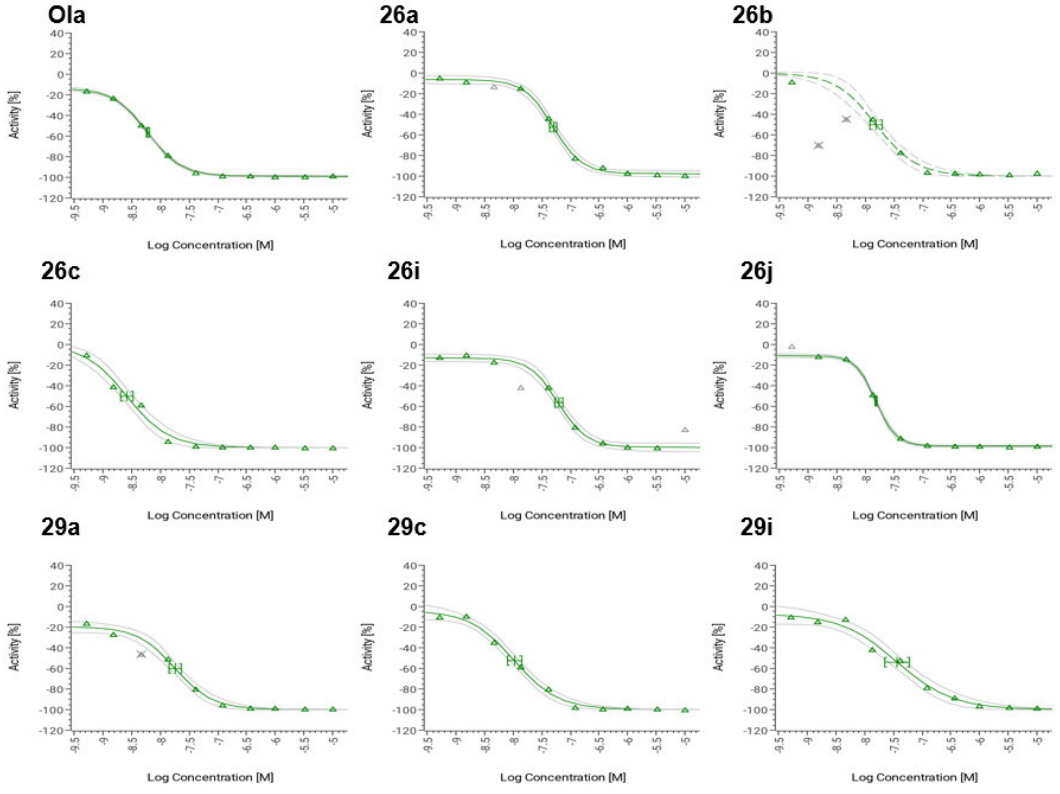

Figure A5. Dose-response curves from DLD-1 *BRCA2* -/- viability assays carried out at AstraZeneca.

Appendix B. HDX-MS data

HDX-MS deuterium uptake graphs after treatment of PARP-1 with the indicated compounds. Individual peptides and their residue numbers representative of digested portions of the protein are indicated above each graph. AZ14349334 and AZ14349342 are **26a** and **29a**, respectively.

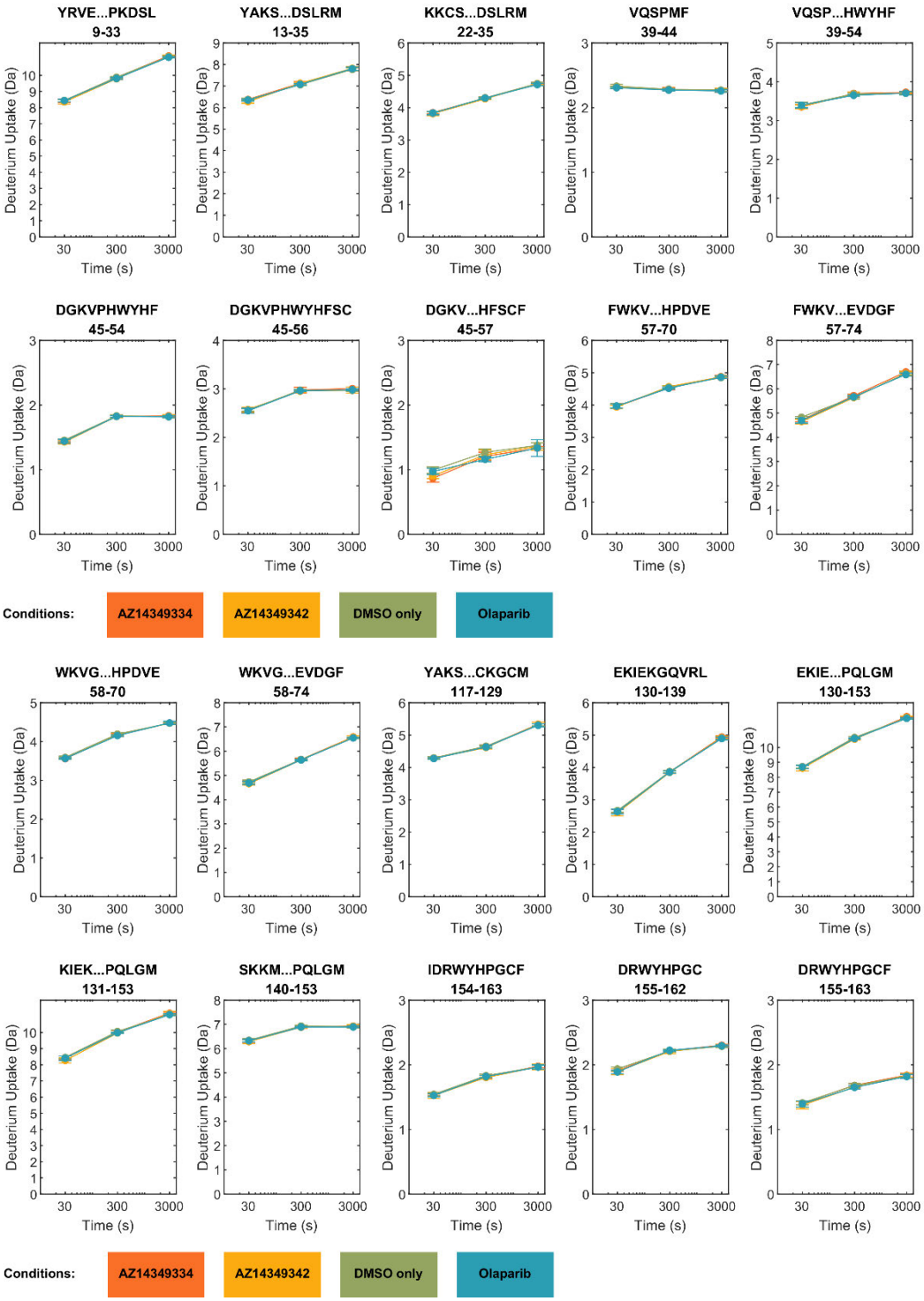

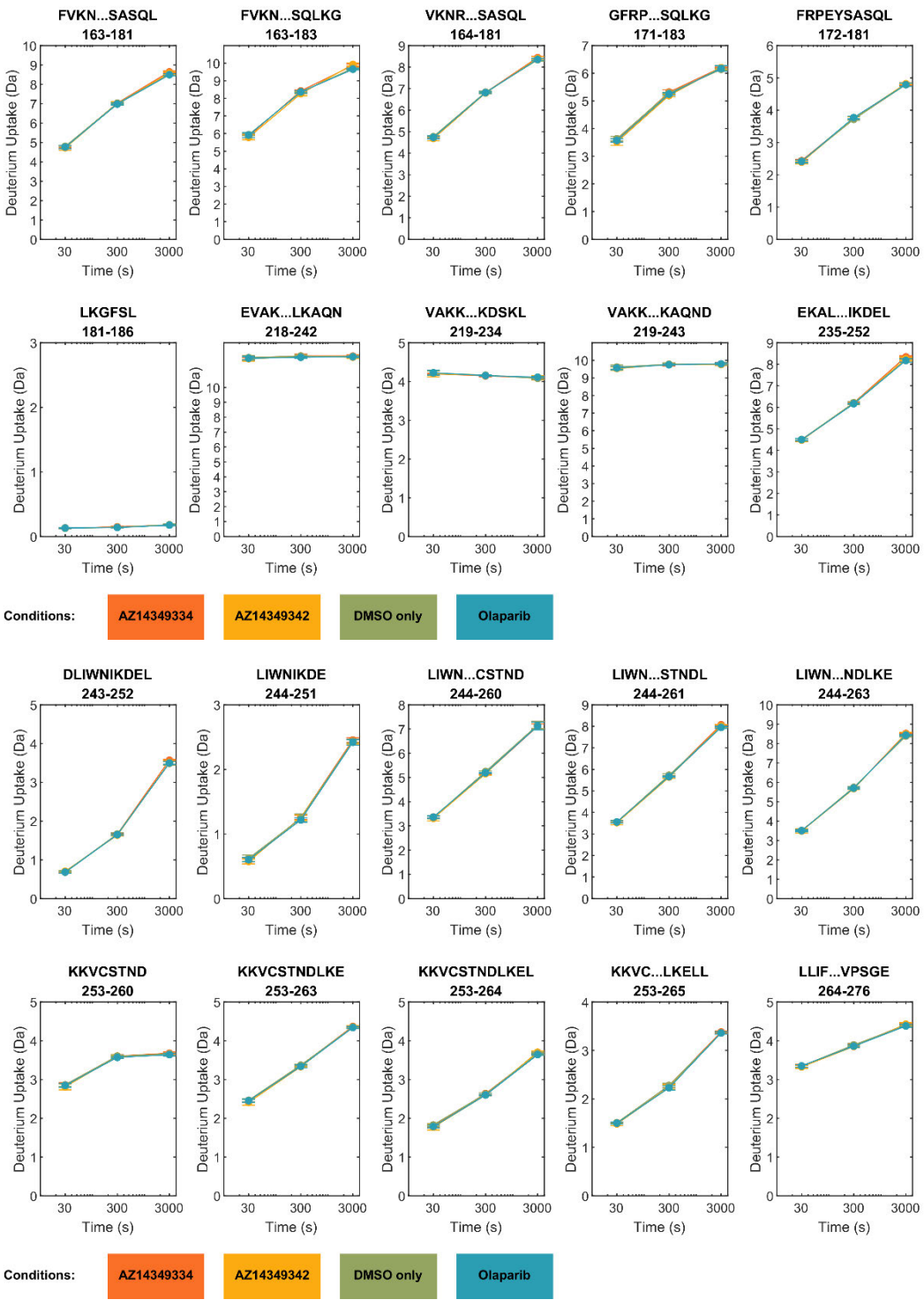
FVKN...SASQL
163-181
FVKN...SQLKG
163-183
VKNR...SASQL
164-181
GFRP...SQLKG
171-183
FRPEYSASQL
172-181
LKGFSL
181-186
EVAK...LKAQN
218-242
VAKK...KDSKL
219-234
VAKK...KAQND
219-243
EKAL...IKDEL
235-252
Deuterium Uptake (Da)
Time (s)
30
300
3000
Conditions:
AZ14349334
AZ14349342
DMSO only
Olaparib
DLIWNIKDEL
243-252
LIWNIKDE
244-251
LIWN...CSTND
244-260
LIWN...STNDL
244-261
LIWN...NDLKE
244-263
KKVCSTND
253-260
KKVCSTNDLKE
253-263
KKVCSTNDLKEL
253-264
KKVC...LKELL
253-265
LLIF...VPSGE
264-276
Deuterium Uptake (Da)
Time (s)
30
300
3000
Conditions:
AZ14349334
AZ14349342
DMSO only
Olaparib

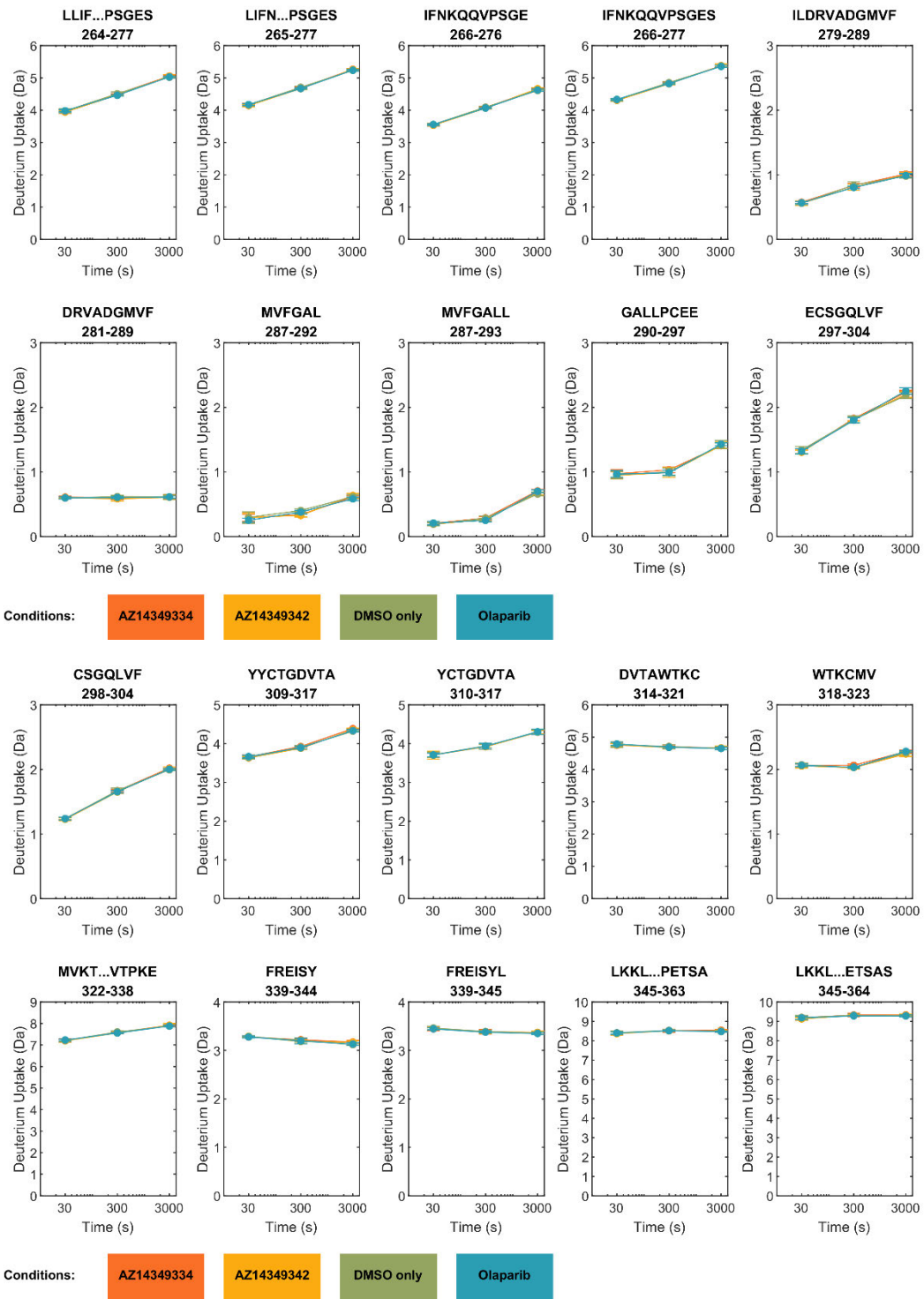
LLIF...PSGES
264-277
LIFN...PSGES
265-277
IFNKQQVPSGE
266-276
IFNKQQVPSGES
266-277
ILDRVADGMVF
279-289
DRVADGMVF
281-289
MVFGAL
287-292
MVFGALL
287-293
GALLPCEE
290-297
ECSGQLVF
297-304
Deuterium Uptake (Da)
Time (s)
Conditions:
AZ14349334
AZ14349342
DMSO only
Olaparib
CSGQLVF
298-304
YYCTGDVTA
309-317
YCTGDVTA
310-317
DVTAWTKC
314-321
WTKCMV
318-323
MVKT...VTPKE
322-338
FREISY
339-344
FREISYL
339-345
LKKL...PETSA
345-363
LKKL...ETSAS
345-364
Deuterium Uptake (Da)
Time (s)
Conditions:
AZ14349334
AZ14349342
DMSO only
Olaparib

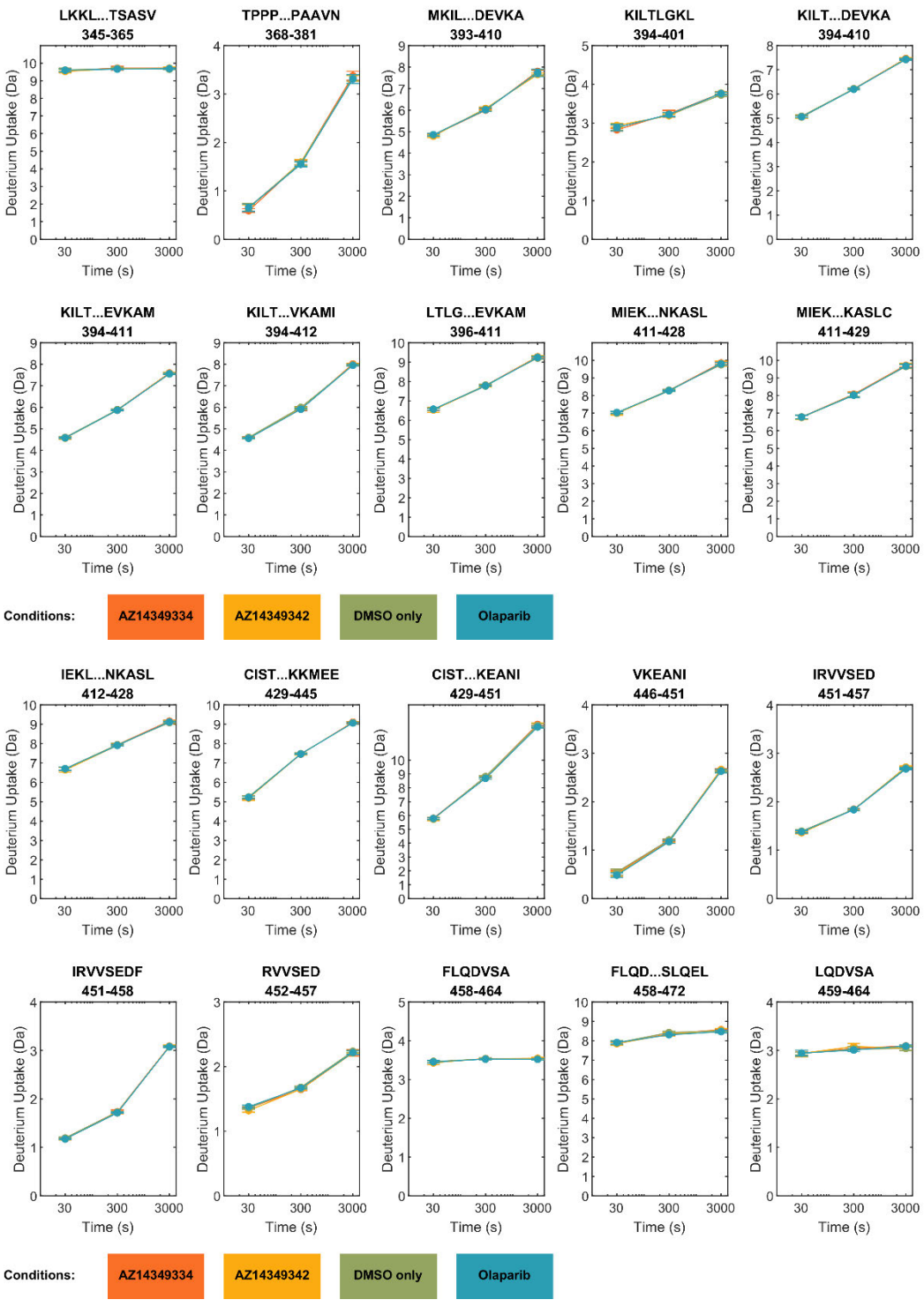
LKKL...TSASV
345-365
TPPP...PAAVN
368-381
MKIL...DEVKA
393-410
KILTLGKL
394-401
KILT...DEVKA
394-410
KILT...EVKAM
394-411
KILT...VKAMI
394-412
LTLG...EVKAM
396-411
MIEK...NKASL
411-428
MIEK...KASLC
411-429
IEKL...NKASL
412-428
CIST...KKMEE
429-445
CIST...KEANI
429-451
VKEANI
446-451
IRVVSED
451-457
IRVVSEDF
451-458
RVVSED
452-457
FLQDVSA
458-464
FLQD...SLQEL
458-472
LQDVSA
459-464
Deuterium Uptake (Da)
Time (s)
30
300
3000
Conditions:
AZ14349334
AZ14349342
DMSO only
Olaparib

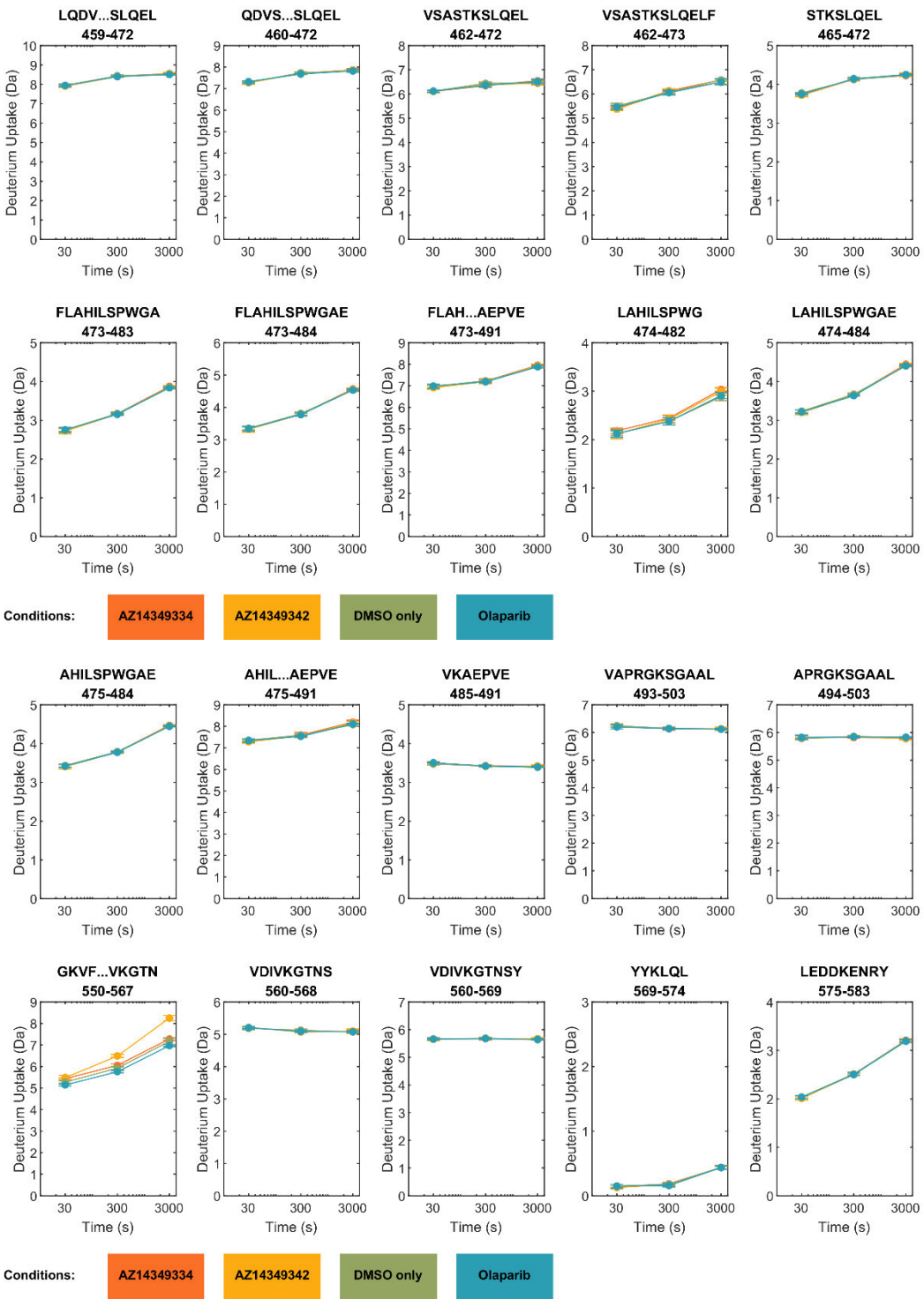
LQDV...SLQEL
459-472
QDVS...SLQEL
460-472
VSASTKSLQEL
462-472
VSASTKSLQELF
462-473
STKSLQEL
465-472
FLAHILSPWGA
473-483
FLAHILSPWGAE
473-484
FLAH...AEPVE
473-491
LAHILSPWG
474-482
LAHILSPWGAE
474-484
Deuterium Uptake (Da)
Time (s)
30
300
3000
Conditions:
AZ14349334
AZ14349342
DMSO only
Olaparib
AHILSPWGAE
475-484
AHIL...AEPVE
475-491
VKAEPVE
485-491
VAPRGKSGAAL
493-503
APRGKSGAAL
494-503
GKVF...VKGTN
550-567
VDIVKGTNS
560-568
VDIVKGTNSY
560-569
YYKLQL
569-574
LEDDKENRY
575-583
Conditions:
AZ14349334
AZ14349342
DMSO only
Olaparib

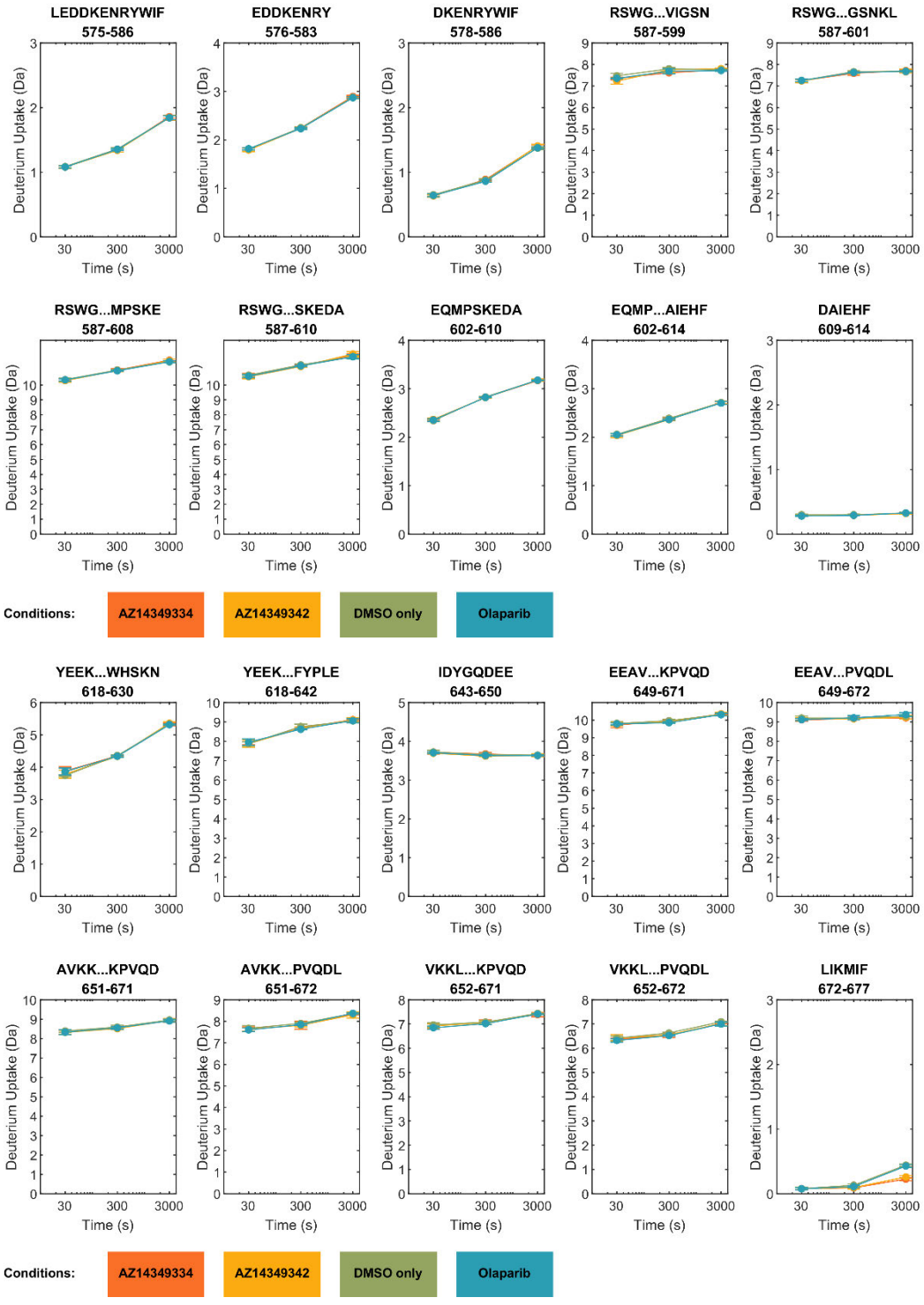
LEDDKENRYWIF
575-586
EDDKENRY
576-583
DKENRYWIF
578-586
RSWG...VIGSN
587-599
RSWG...GSNKL
587-601
RSWG...MPSKE
587-608
RSWG...SKEDA
587-610
EQMPSKEDA
602-610
EQMP...AIEHF
602-614
DAIEHF
609-614
Deuterium Uptake (Da)
Time (s)
30
300
3000
Conditions:
AZ14349334
AZ14349342
DMSO only
Olaparib
YEEK...WHSKN
618-630
YEEK...FYPLE
618-642
IDYGQDEE
643-650
EEAV...KPVQD
649-671
EEAV...PVQDL
649-672
AVKK...KPVQD
651-671
AVKK...PVQDL
651-672
VKKL...KPVQD
652-671
VKKL...PVQDL
652-672
LIKMIF
672-677

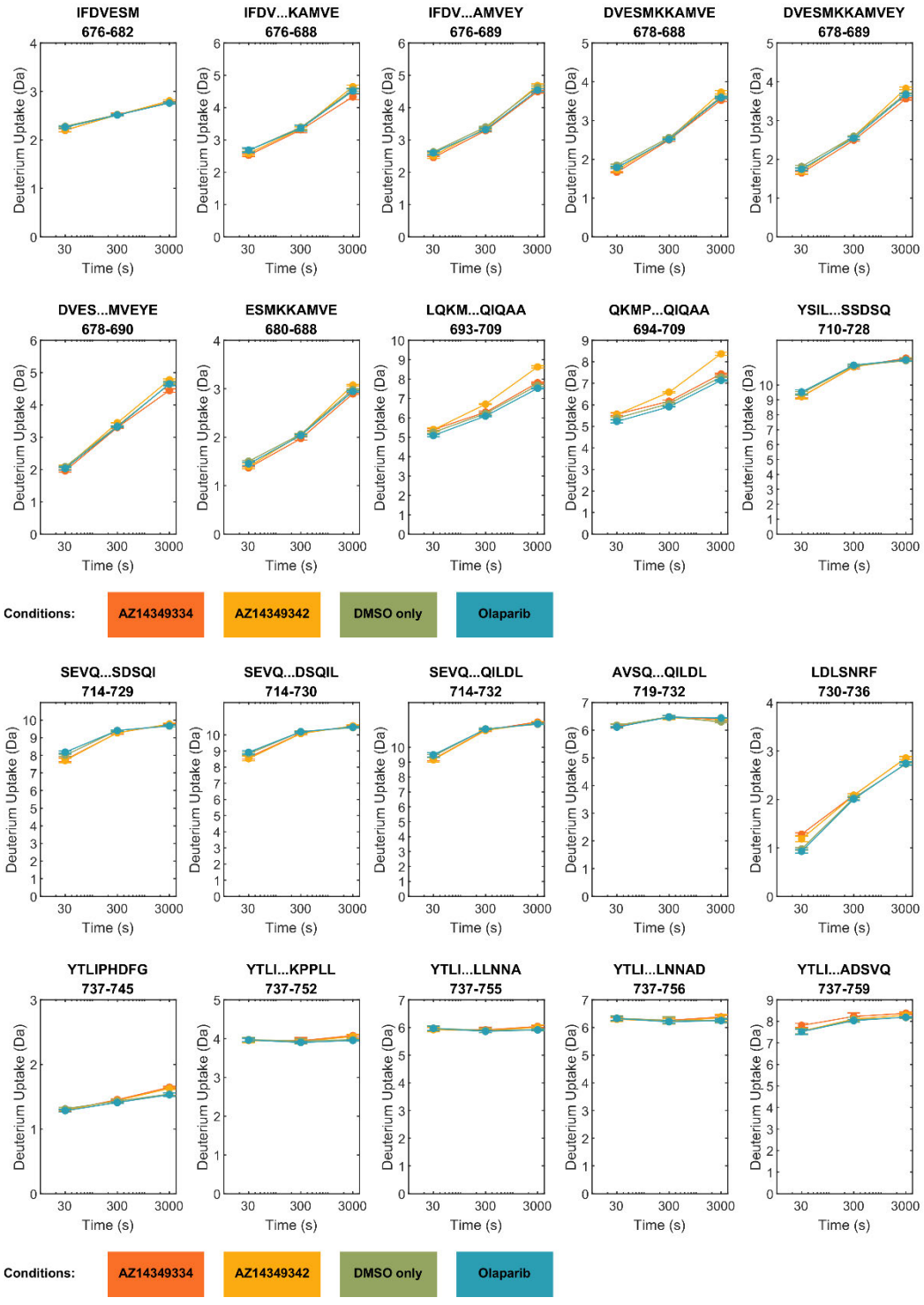
IFDVESM
676-682
IFDV...KAMVE
676-688
IFDV...AMVEY
676-689
DVESMKKAMVE
678-688
DVESMKKAMVEY
678-689
DVES...MVEYE
678-690
ESMKKAMVE
680-688
LQKM...QIQAA
693-709
QKMP...QIQAA
694-709
YSIL...SSDSQ
710-728
Deuterium Uptake (Da)
Time (s)
30
300
3000
Conditions:
AZ14349334
AZ14349342
DMSO only
Olaparib
SEVQ...SDSQI
714-729
SEVQ...DSQIL
714-730
SEVQ...QILDL
714-732
AVSQ...QILDL
719-732
LDLSNRF
730-736
YTLIPHDFG
737-745
YTLI...KPPLL
737-752
YTLI...LLNNA
737-755
YTLI...LNNAD
737-756
YTLI...ADSVQ
737-759
Deuterium Uptake (Da)
Time (s)
30
300
3000
Conditions:
AZ14349334
AZ14349342
DMSO only
Olaparib

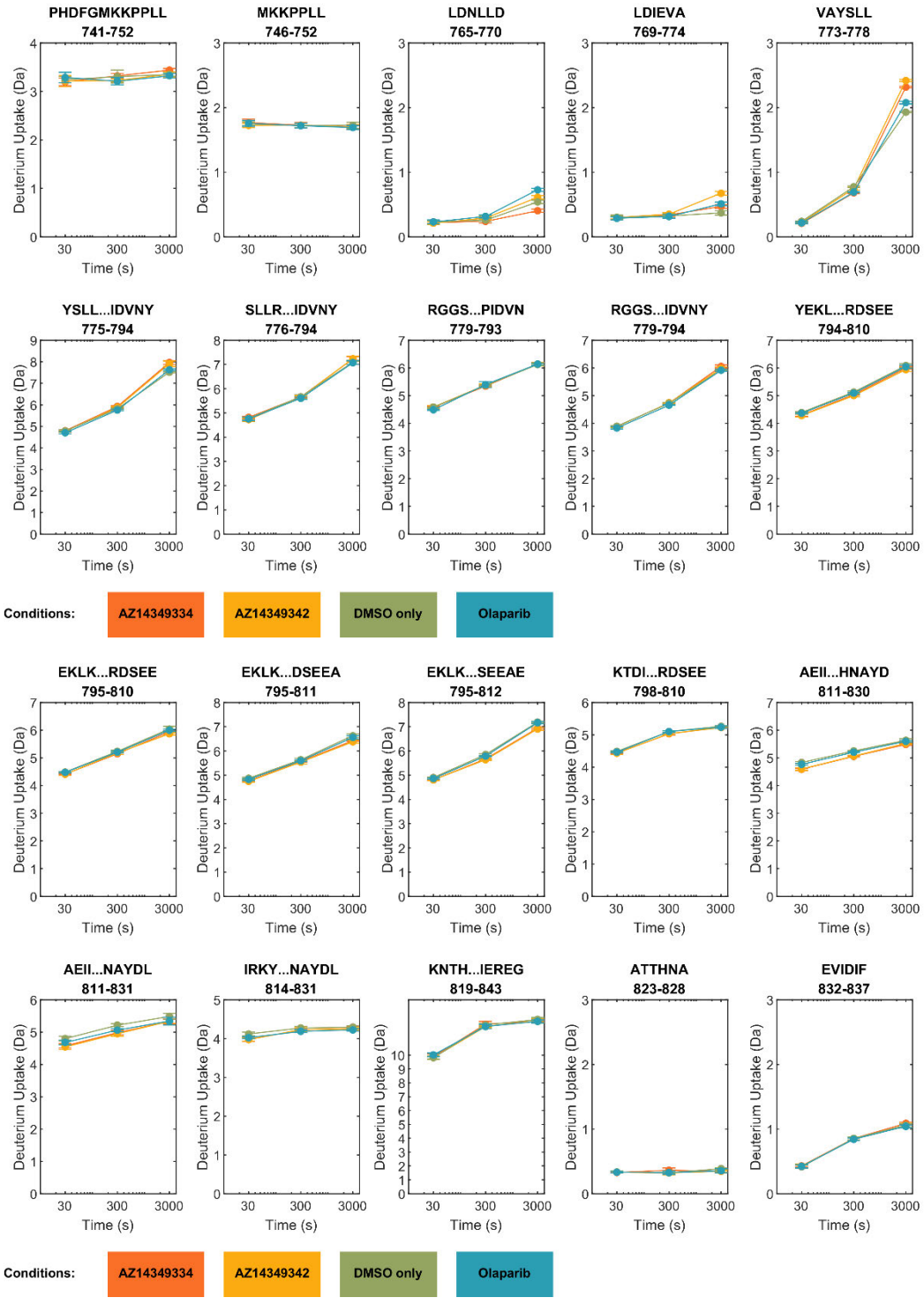
PHDFGMKKPPLL
741-752
MKKPPLL
746-752
LDNLLD
765-770
LDIEVA
769-774
VAYSLL
773-778
YSLL...IDVNY
775-794
SLLR...IDVNY
776-794
RGGS...PIDVN
779-793
RGGS...IDVNY
779-794
YEKL...RDSEE
794-810
Deuterium Uptake (Da)
Time (s)
30
300
3000
Conditions:
AZ14349334
AZ14349342
DMSO only
Olaparib
EKLK...RDSEE
795-810
EKLK...DSEEA
795-811
EKLK...SEEAE
795-812
KTDI...RDSEE
798-810
AEII...HNAYD
811-830
AEII...NAYDL
811-831
IRKY...NAYDL
814-831
KNTH...IEREG
819-843
ATTHNA
823-828
EVIDIF
832-837
Deuterium Uptake (Da)
Time (s)
30
300
3000
Conditions:
AZ14349334
AZ14349342
DMSO only
Olaparib

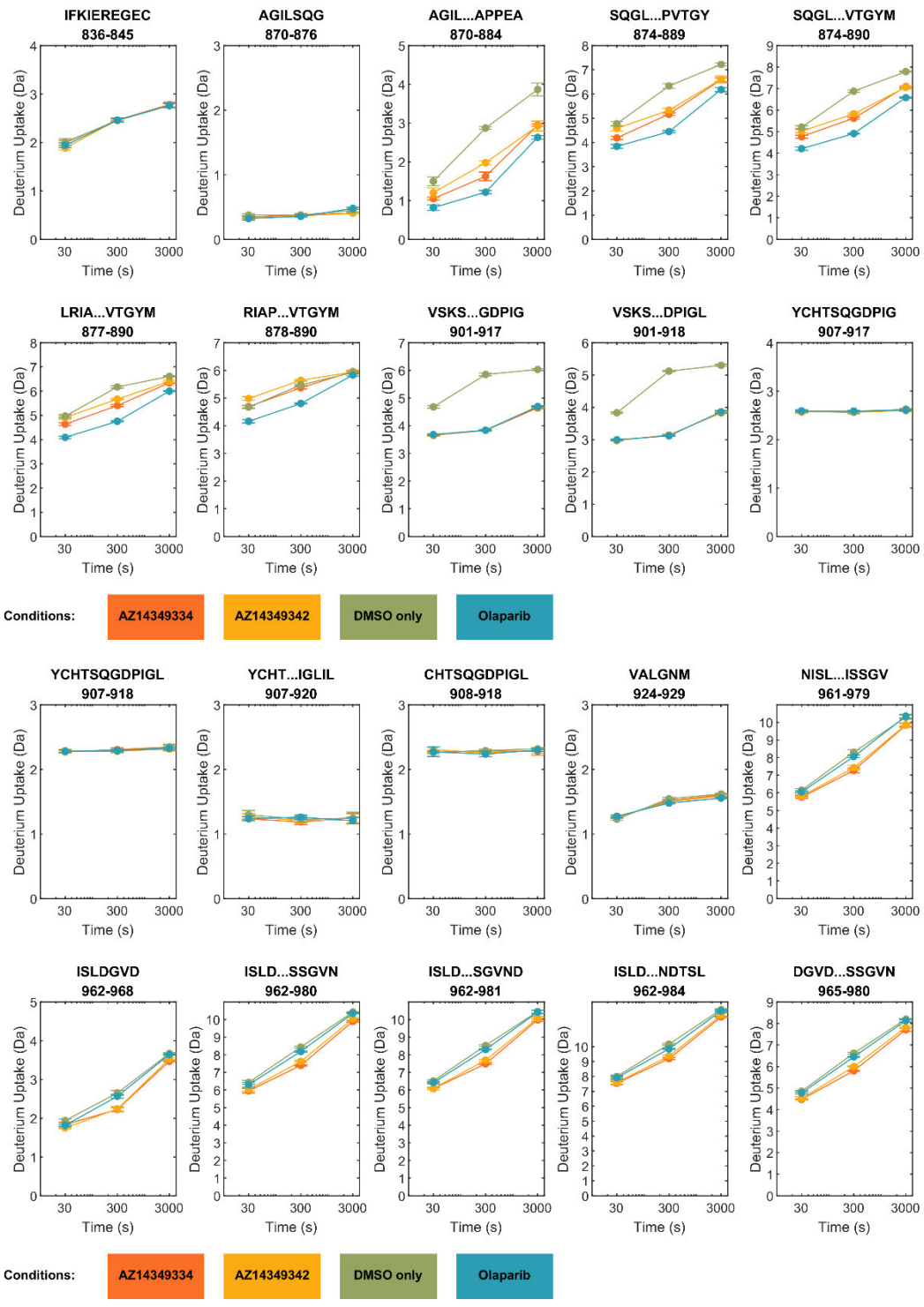
IFKIEREGEC
836-845
AGILSQG
870-876
AGIL...APPEA
870-884
SQGL...PVTGY
874-889
SQGL...VTGYM
874-890
LRIA...VTGYM
877-890
RIAP...VTGYM
878-890
VSKS...GDPIG
901-917
VSKS...DPIGL
901-918
YCHTSQGDPIG
907-917
YCHTSQGDPIGL
907-918
YCHT...IGLIL
907-920
CHTSQGDPIGL
908-918
VALGNM
924-929
NISL...ISSGV
961-979
ISLDGVD
962-968
ISLD...SSGVN
962-980
ISLD...SGVND
962-981
ISLD...NDTSL
962-984
DGVD...SSGVN
965-980
Deuterium Uptake (Da)
Time (s)
30
300
3000
Conditions:
AZ14349334
AZ14349342
DMSO only
Olaparib

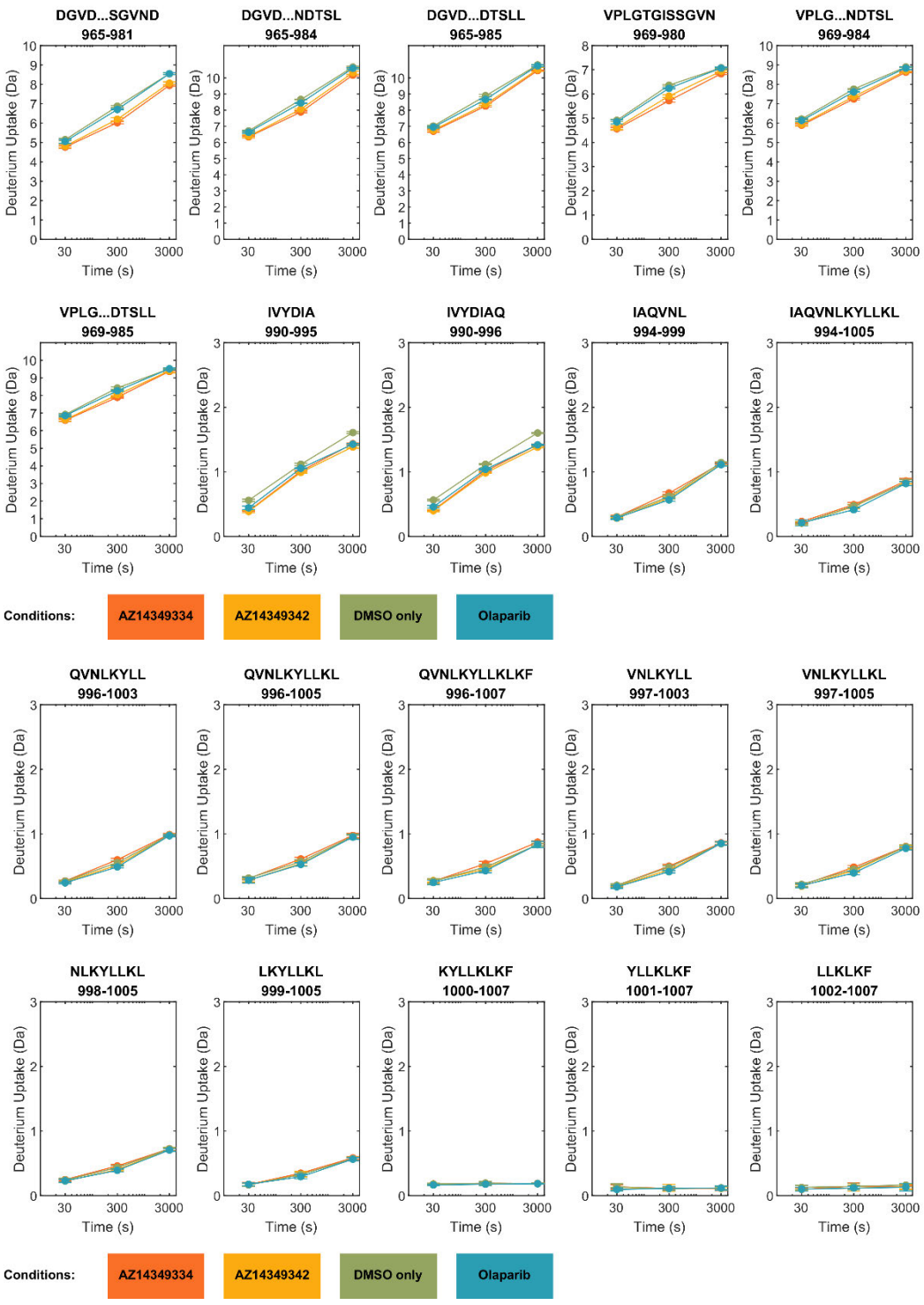
DGVD...SGVND
965-981
DGVD...NDTSL
965-984
DGVD...DTSLL
965-985
VPLGTGISSGVN
969-980
VPLG...NDTSL
969-984
VPLG...DTSLL
969-985
IVYDIA
990-995
IVYDIAQ
990-996
IAQVNL
994-999
IAQVNLKYLLKL
994-1005
Deuterium Uptake (Da)
Time (s)
30
300
3000
Conditions:
AZ14349334
AZ14349342
DMSO only
Olaparib
QVNLKYLL
996-1003
QVNLKYLLKL
996-1005
QVNLKYLLKLKF
996-1007
VNLKYLL
997-1003
VNLKYLLKL
997-1005
NLKYLLKL
998-1005
LKYLLKL
999-1005
KYLLKLKF
1000-1007
YLLKLKF
1001-1007
LLKLKF
1002-1007

Appendix C. NMR spectra

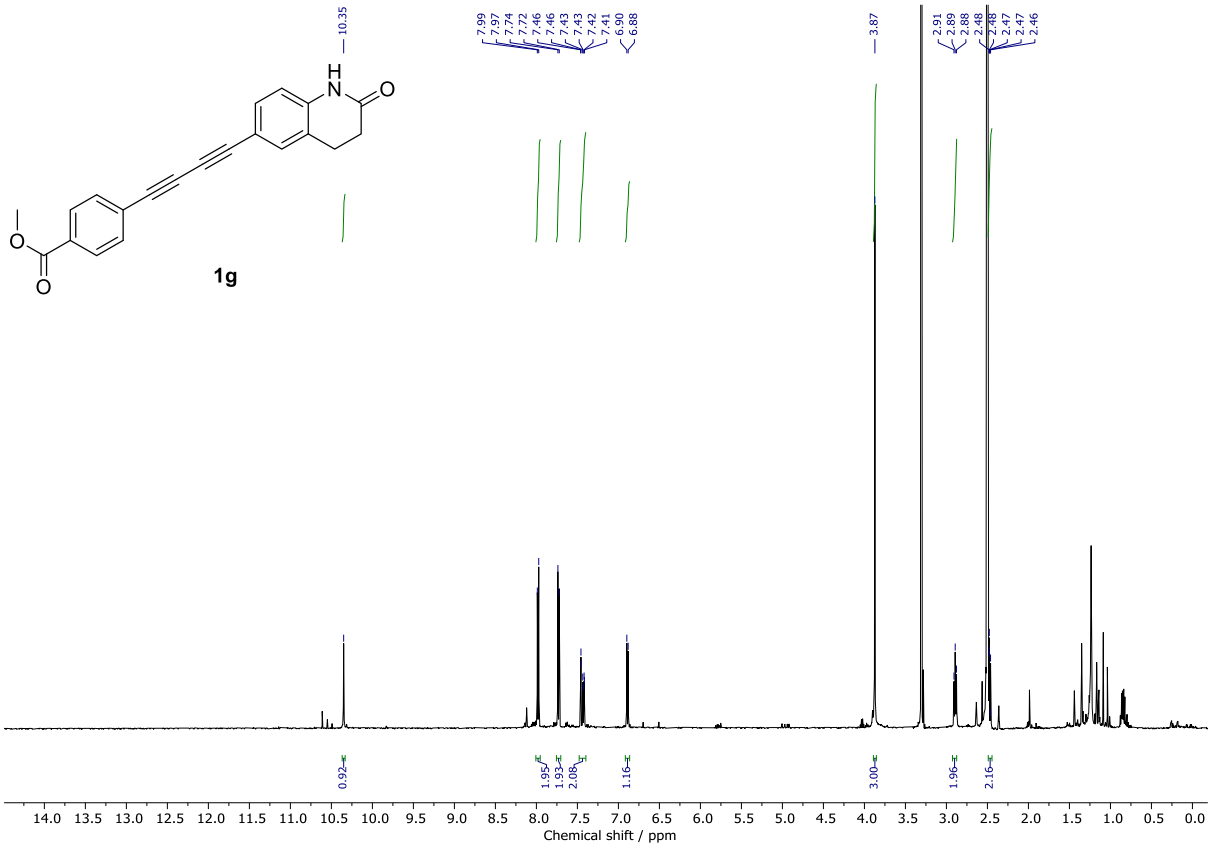

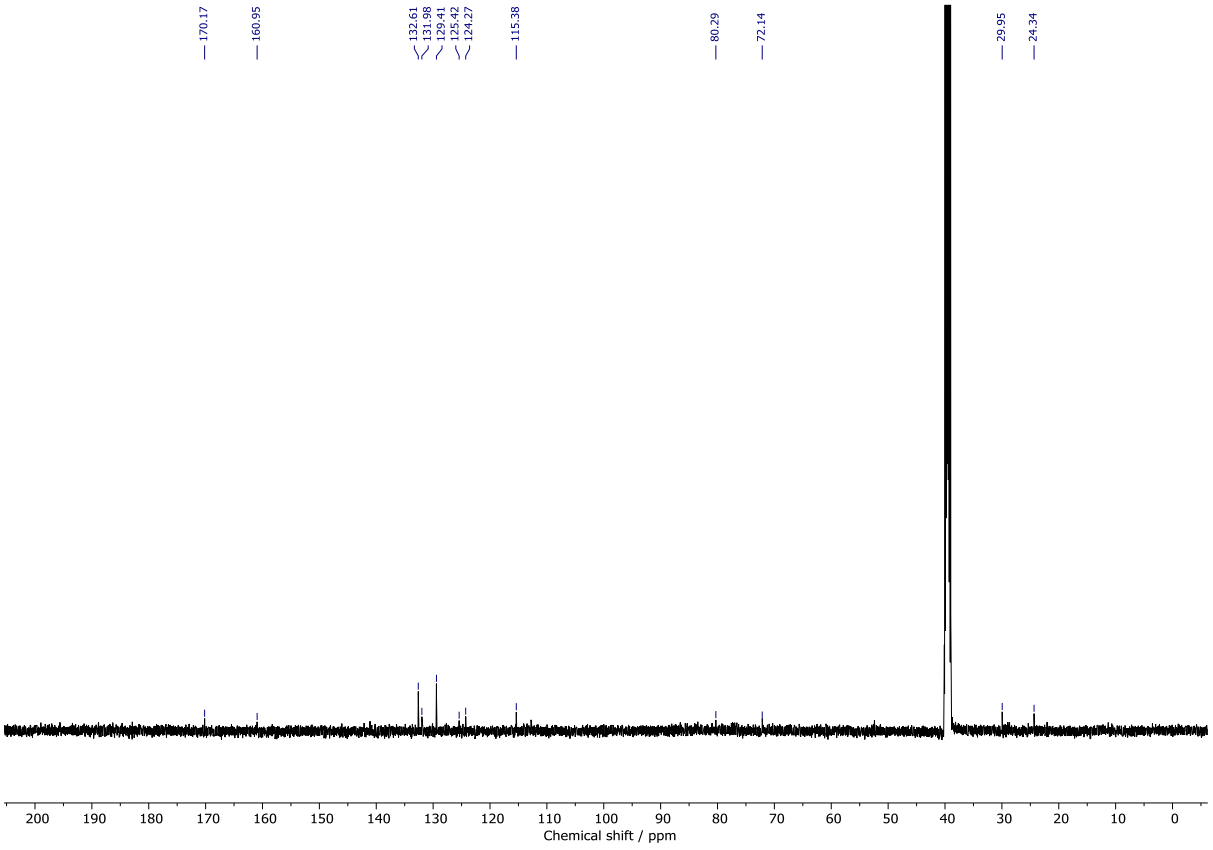

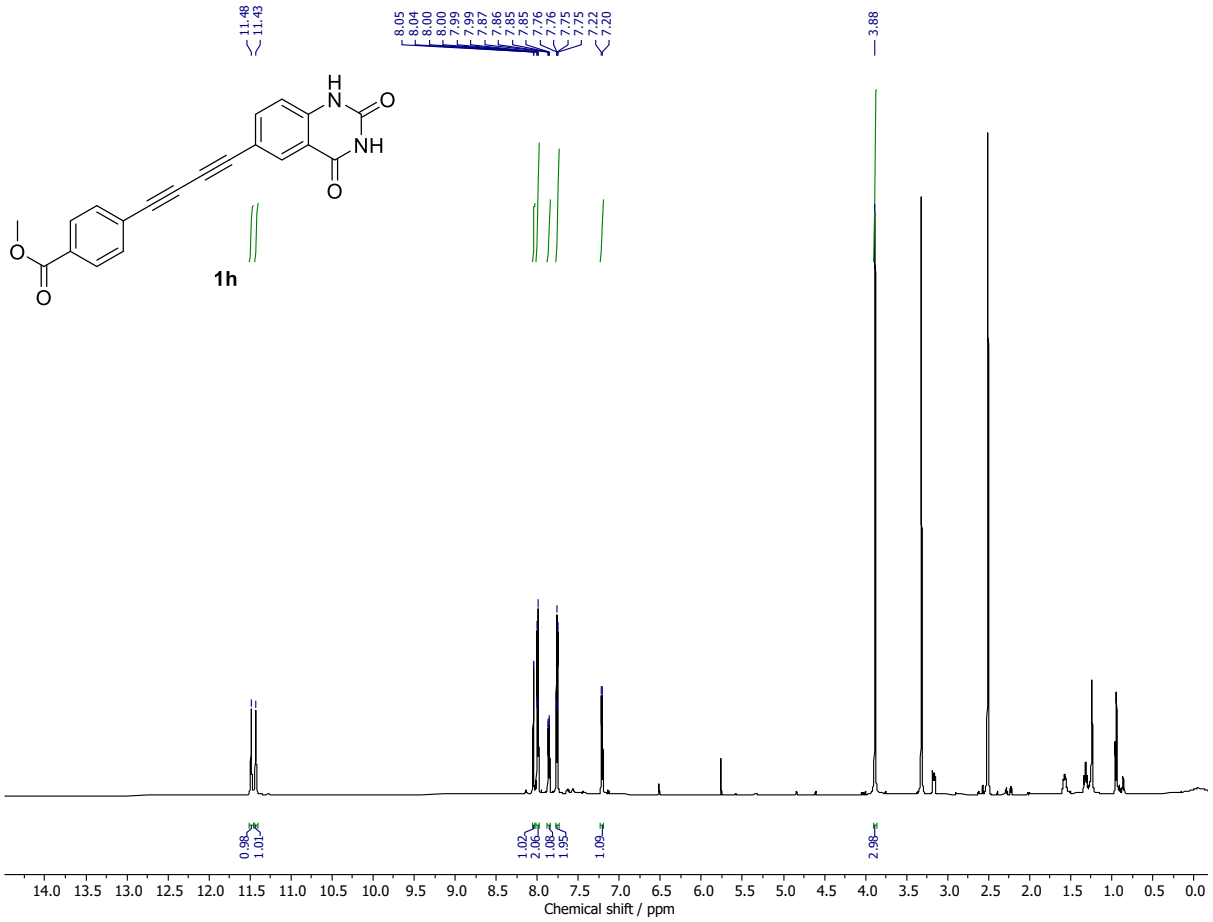
11.48
11.43
8.05
8.04
8.04
8.00
8.00
7.99
7.99
7.87
7.86
7.85
7.85
7.76
7.76
7.75
7.75
7.22
7.20
3.88
H
N
O
NH
O
O
O
1h
0.98
1.01
1.02
2.06
1.08
1.95
1.09
2.98
14.0 13.5 13.0 12.5 12.0 11.5 11.0 10.5 10.0 9.5 9.0 8.5 8.0 7.5 7.0 6.5 6.0 5.5 5.0 4.5 4.0 3.5 3.0 2.5 2.0 1.5 1.0 0.5 0.0
Chemical shift / ppm

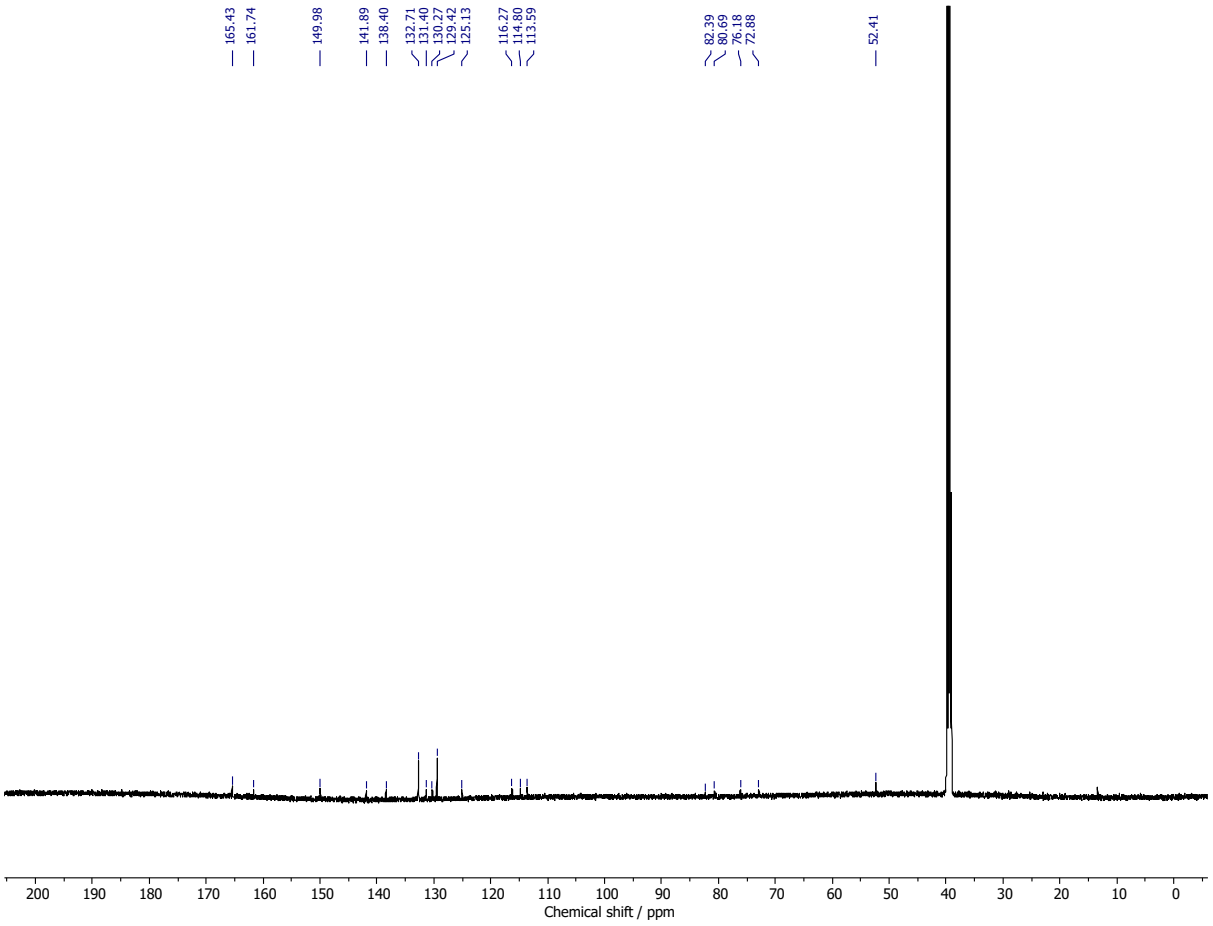
165.43
161.74
149.98
141.89
138.40
132.71
131.40
130.27
129.42
125.13
116.27
114.80
113.59
82.39
80.69
76.18
72.88
52.41
200 190 180 170 160 150 140 130 120 110 100 90 80 70 60 50 40 30 20 10 0
Chemical shift / ppm

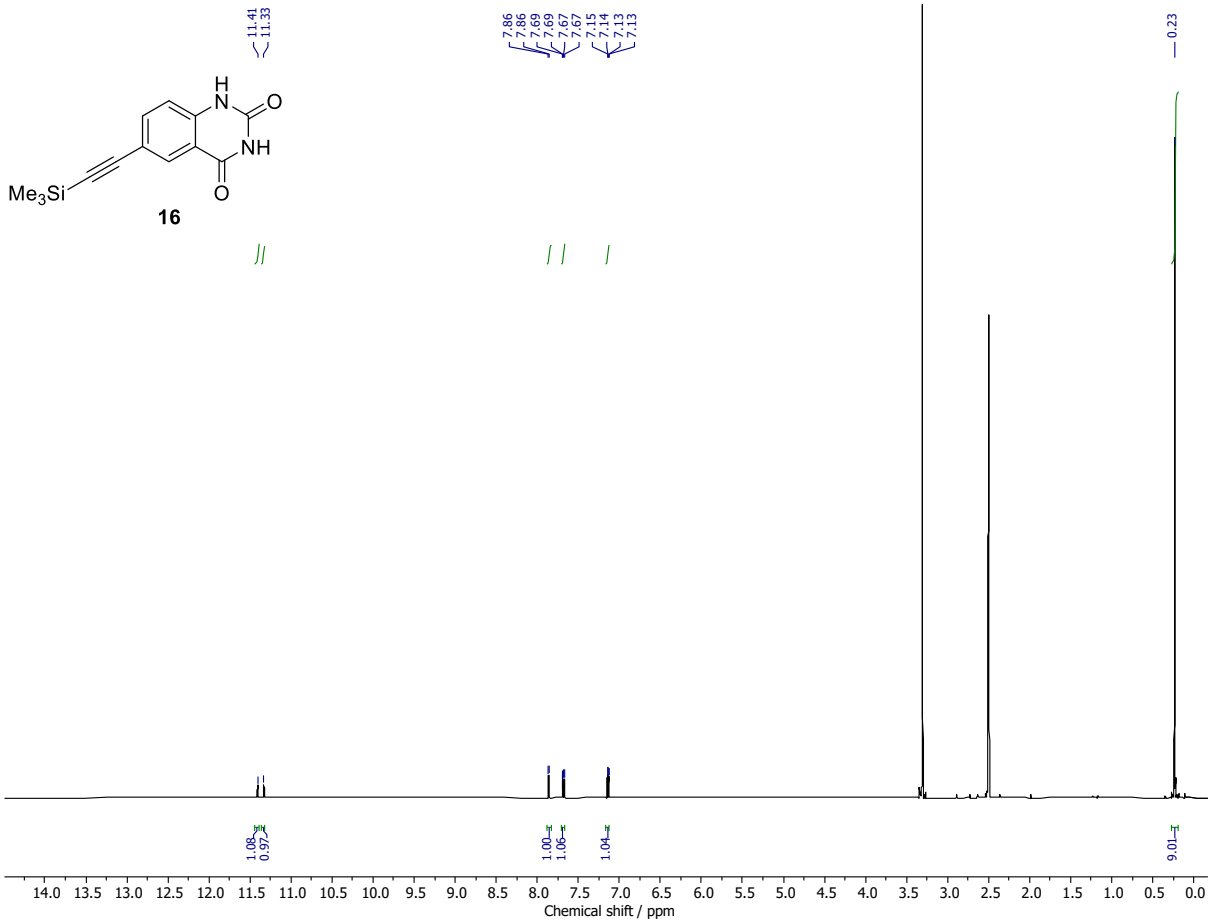
11.41
11.33
7.86
7.86
7.69
7.69
7.67
7.67
7.15
7.14
7.13
7.13
0.23
H
N
O
NH
O
Me3Si
16
1.08
0.97
1.00
1.06
1.04
9.01
14.0 13.5 13.0 12.5 12.0 11.5 11.0 10.5 10.0 9.5 9.0 8.5 8.0 7.5 7.0 6.5 6.0 5.5 5.0 4.5 4.0 3.5 3.0 2.5 2.0 1.5 1.0 0.5 0.0
Chemical shift / ppm

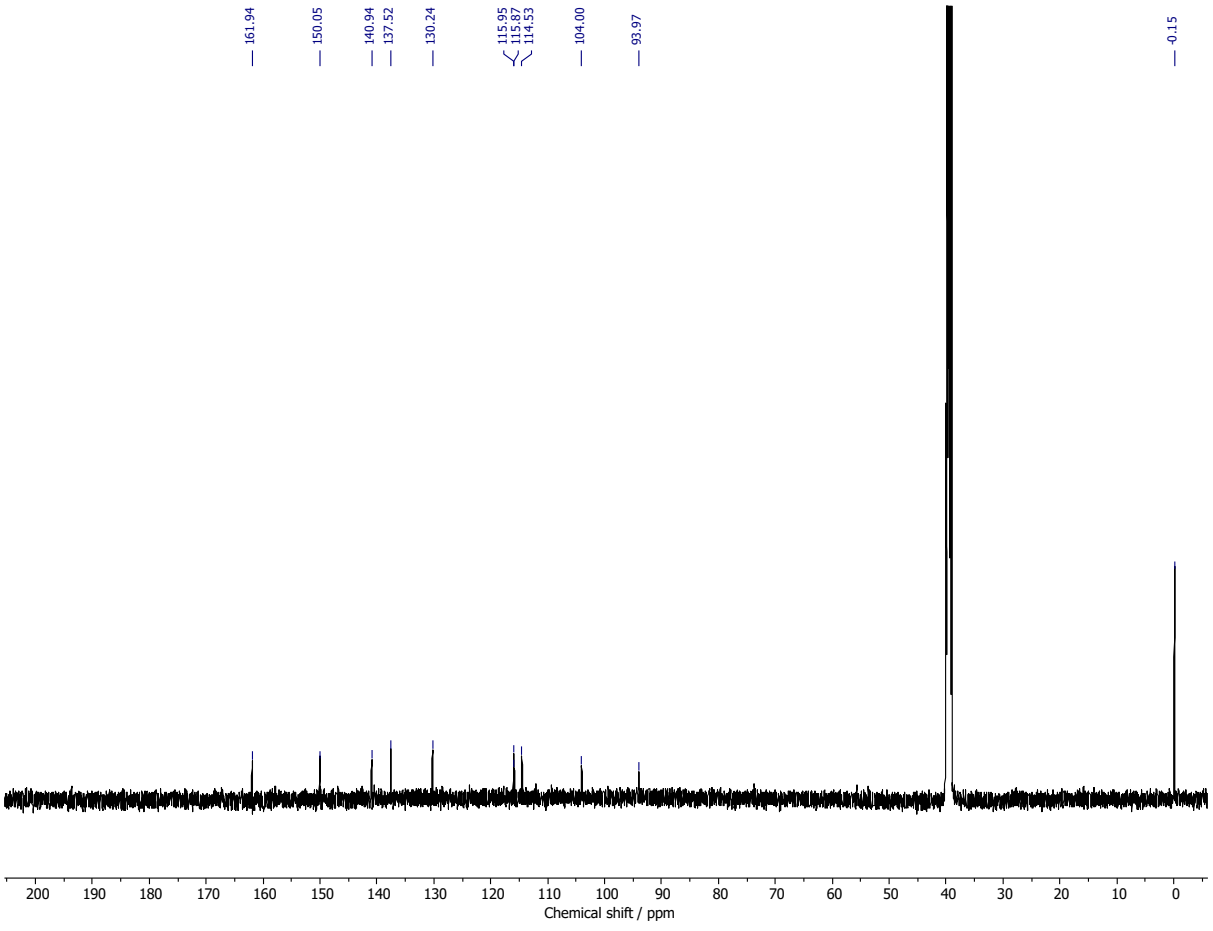
161.94
150.05
140.94
137.52
130.24
115.95
115.87
114.53
104.00
93.97
-0.15
200 190 180 170 160 150 140 130 120 110 100 90 80 70 60 50 40 30 20 10 0
Chemical shift / ppm

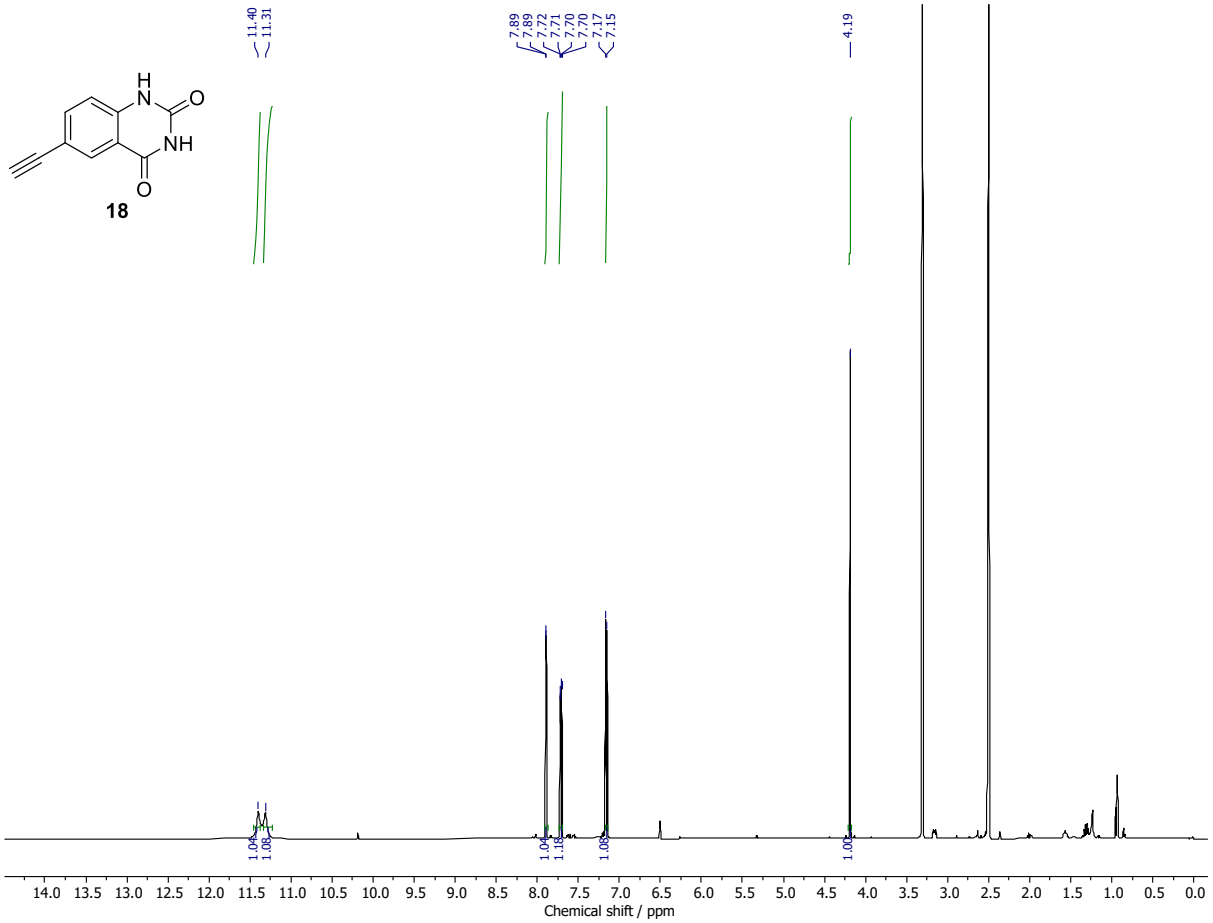
11.40
11.31
7.89
7.89
7.72
7.71
7.70
7.70
7.17
7.15
4.19
1.04
1.08
1.04
1.18
1.00
1.00
14.0 13.5 13.0 12.5 12.0 11.5 11.0 10.5 10.0 9.5 9.0 8.5 8.0 7.5 7.0 6.5 6.0 5.5 5.0 4.5 4.0 3.5 3.0 2.5 2.0 1.5 1.0 0.5 0.0
Chemical shift / ppm

18

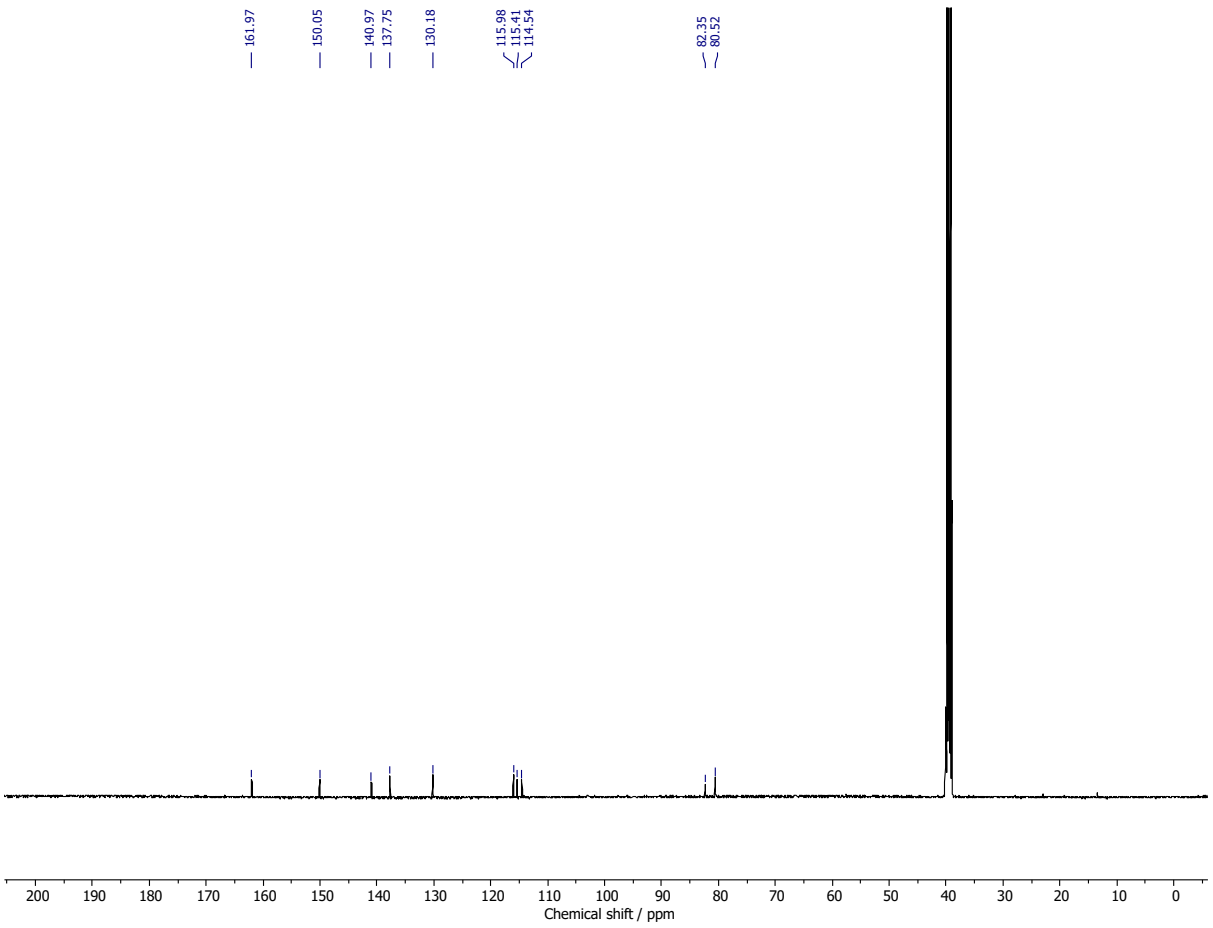
161.97
150.05
140.97
137.75
130.18
115.98
115.41
114.54
82.35
80.52
200 190 180 170 160 150 140 130 120 110 100 90 80 70 60 50 40 30 20 10 0
Chemical shift / ppm

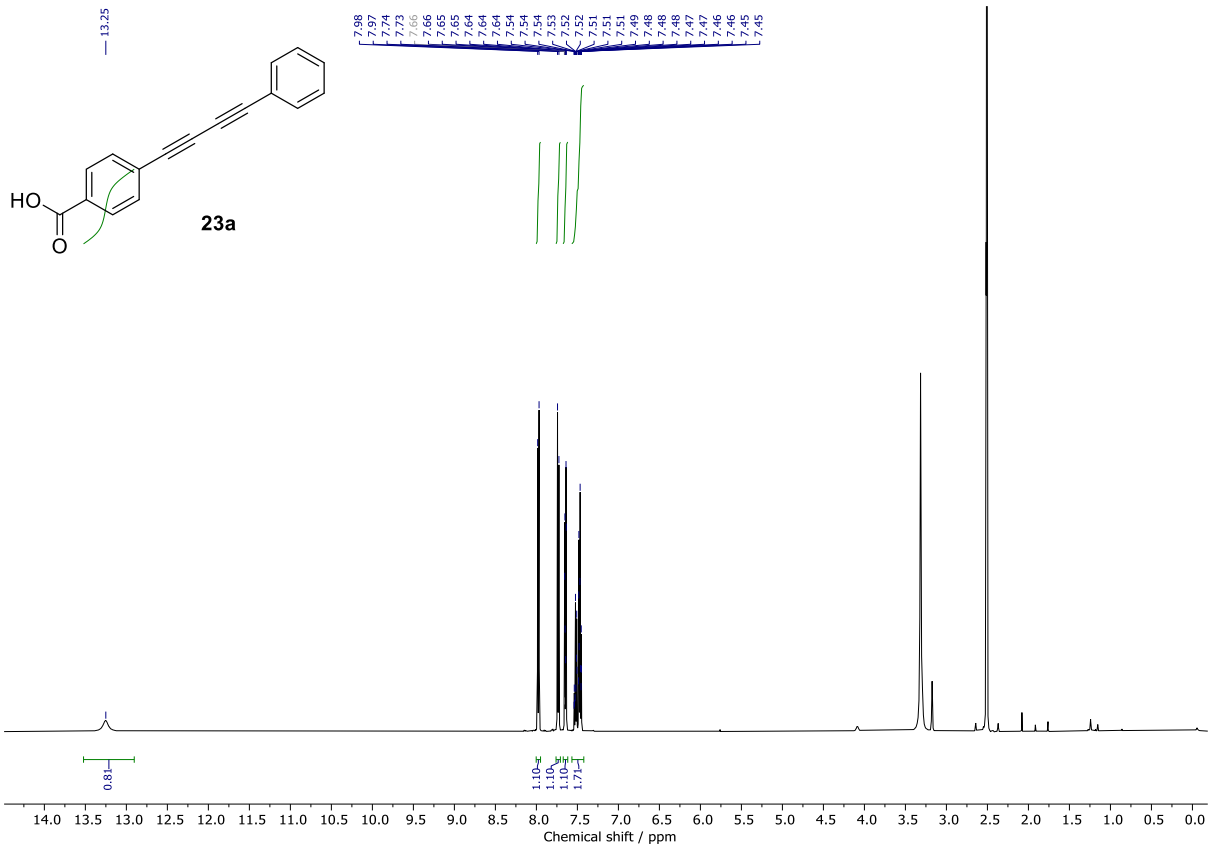
13.25
7.98
7.97
7.74
7.73
7.66
7.65
7.65
7.64
7.64
7.64
7.54
7.54
7.54
7.53
7.52
7.52
7.51
7.51
7.51
7.49
7.48
7.48
7.48
7.47
7.47
7.46
7.46
7.45
7.45
HO
O
23a
0.81
1.10
1.10
1.10
1.71
14.0 13.5 13.0 12.5 12.0 11.5 11.0 10.5 10.0 9.5 9.0 8.5 8.0 7.5 7.0 6.5 6.0 5.5 5.0 4.5 4.0 3.5 3.0 2.5 2.0 1.5 1.0 0.5 0.0
Chemical shift / ppm

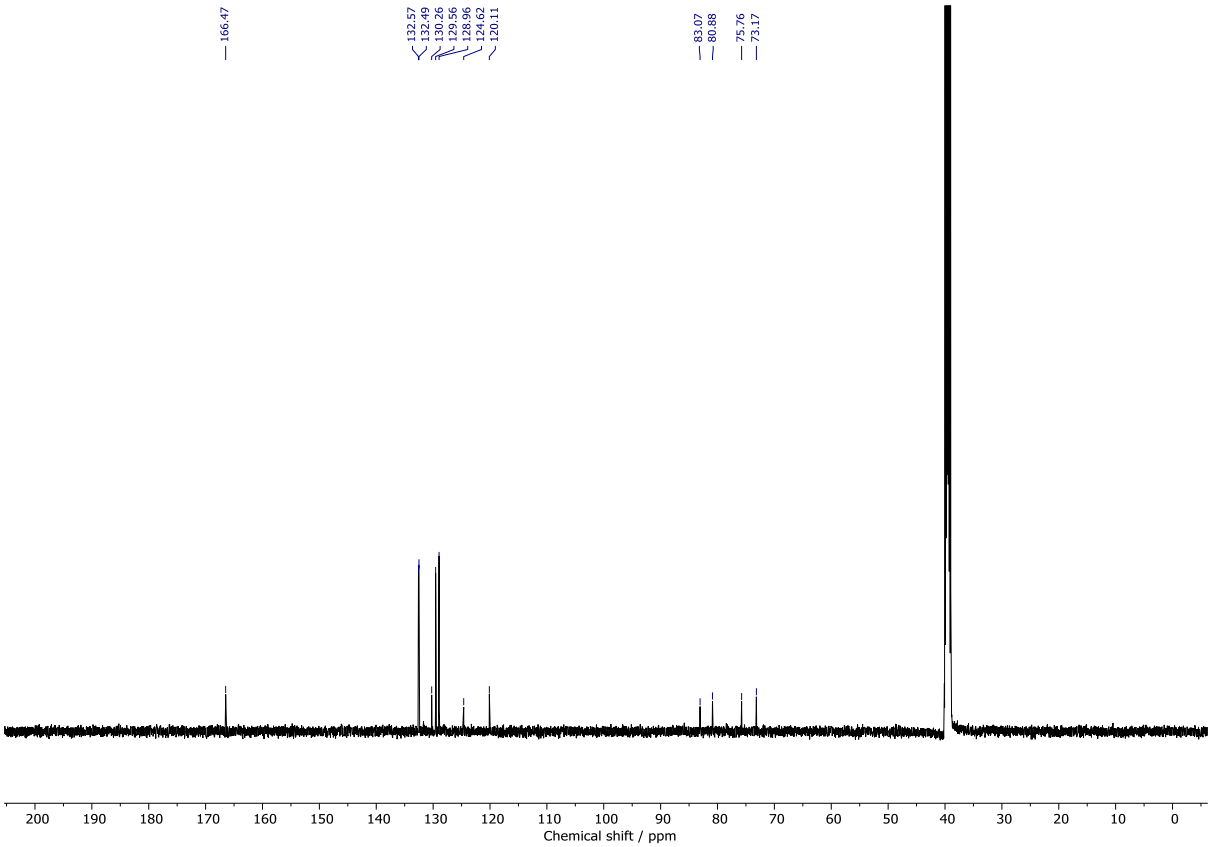
166.47
132.57
132.49
130.26
129.56
128.96
124.62
120.11
83.07
80.88
75.76
73.17
200 190 180 170 160 150 140 130 120 110 100 90 80 70 60 50 40 30 20 10 0
Chemical shift / ppm

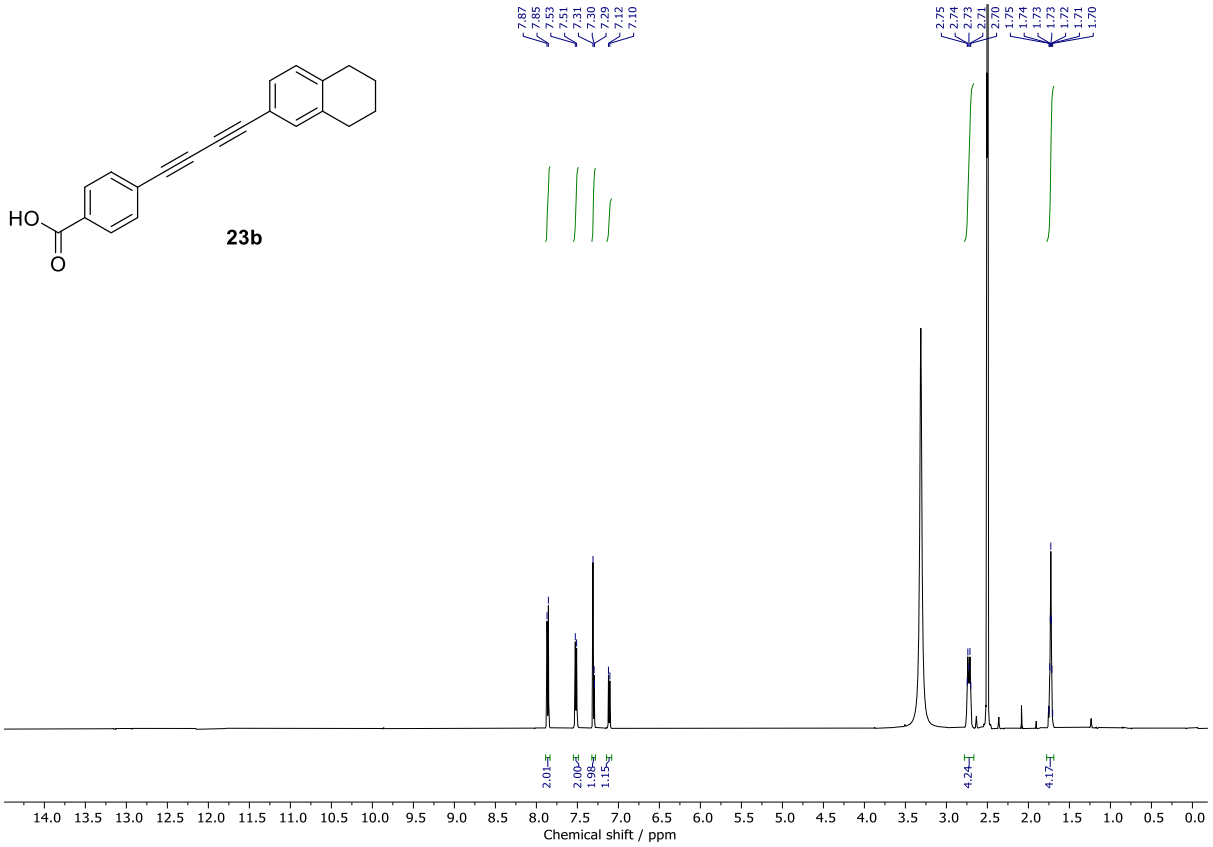
HO
O
23b
7.87
7.85
7.53
7.51
7.31
7.30
7.29
7.12
7.10
2.75
2.74
2.73
2.71
2.70
1.75
1.74
1.73
1.73
1.72
1.71
1.70
2.01
2.00
1.98
1.15
4.24
4.17
Chemical shift / ppm

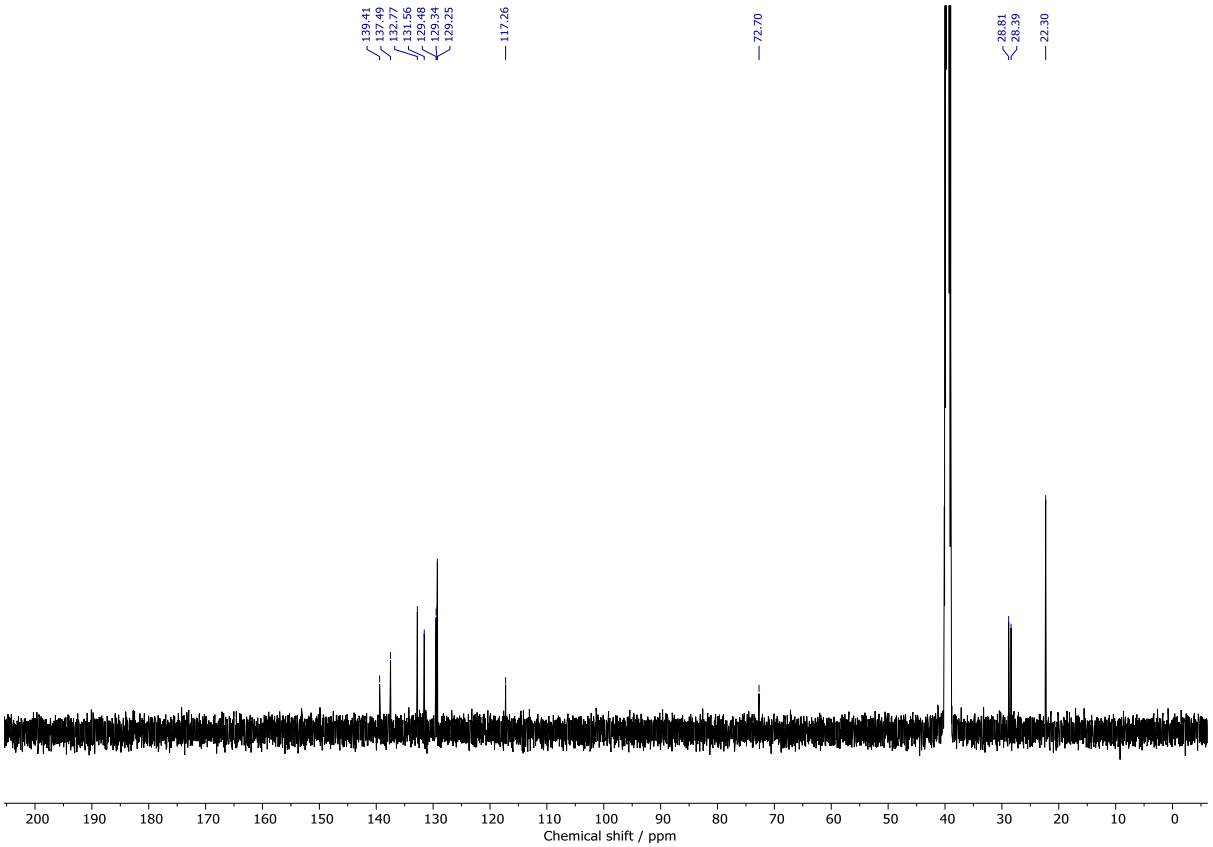
139.41
137.49
132.77
131.56
129.48
129.34
129.25
117.26
72.70
28.81
28.39
22.30
Chemical shift / ppm

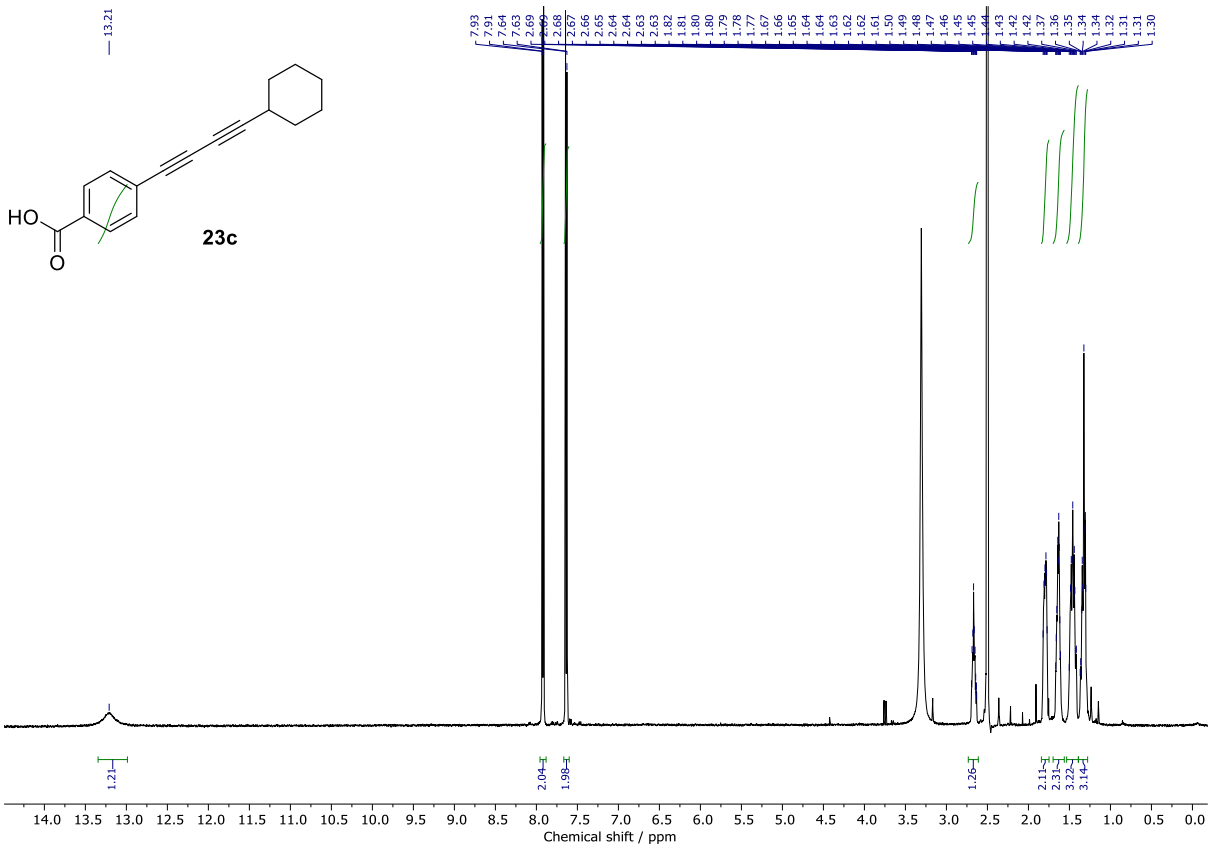
HO
O
23c
Chemical shift / ppm

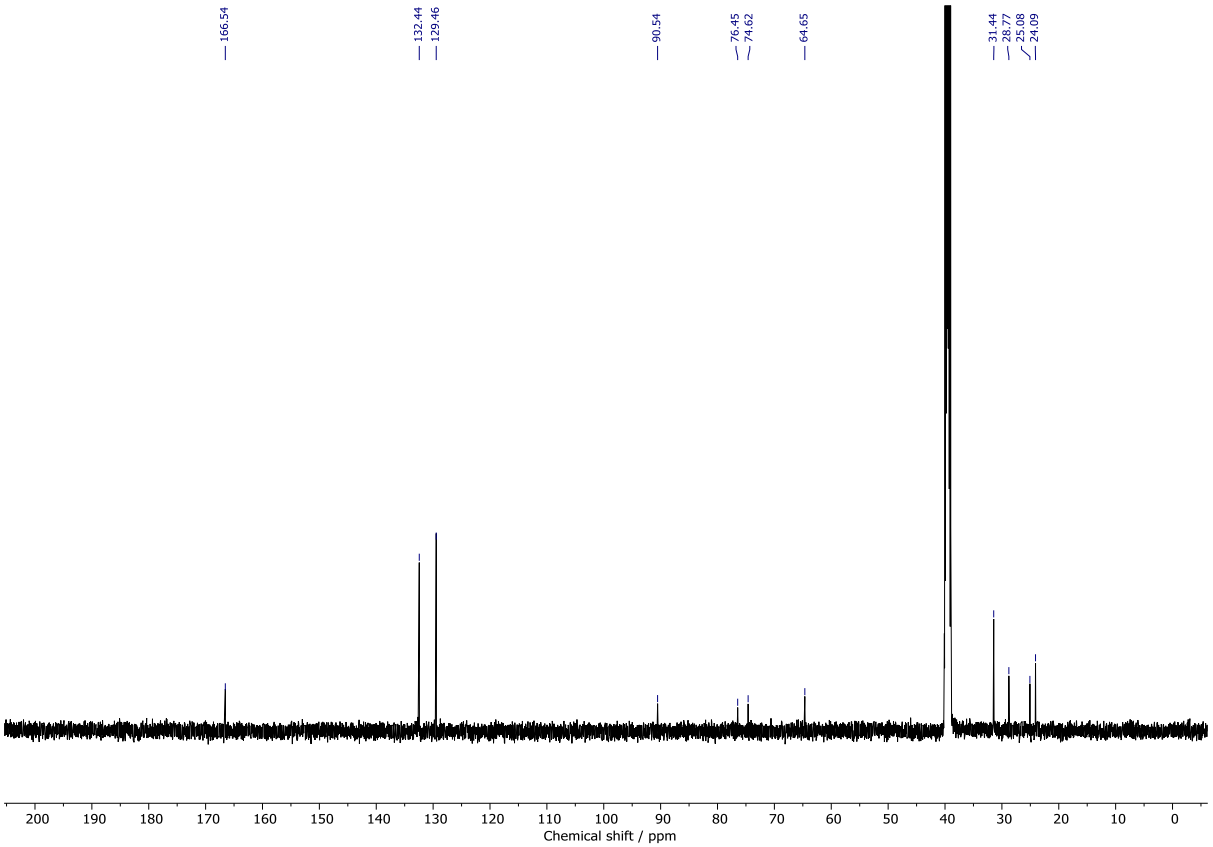
Chemical shift / ppm

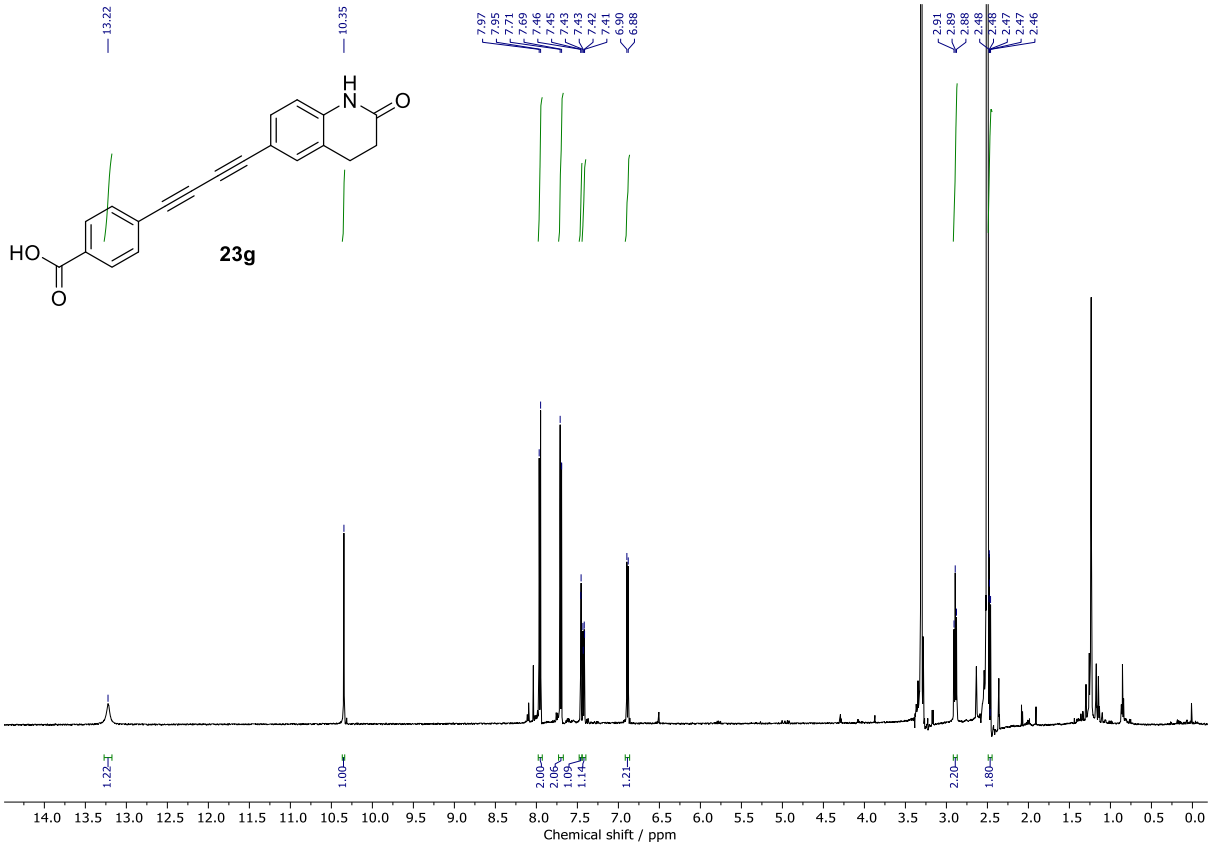
13.22
10.35
7.97
7.95
7.71
7.69
7.46
7.45
7.43
7.42
7.41
6.90
6.88
2.91
2.89
2.88
2.48
2.47
2.47
2.46
HO
O
H
N
O
23g
1.22
1.00
2.00
2.06
1.09
1.14
1.21
2.20
1.80
Chemical shift / ppm

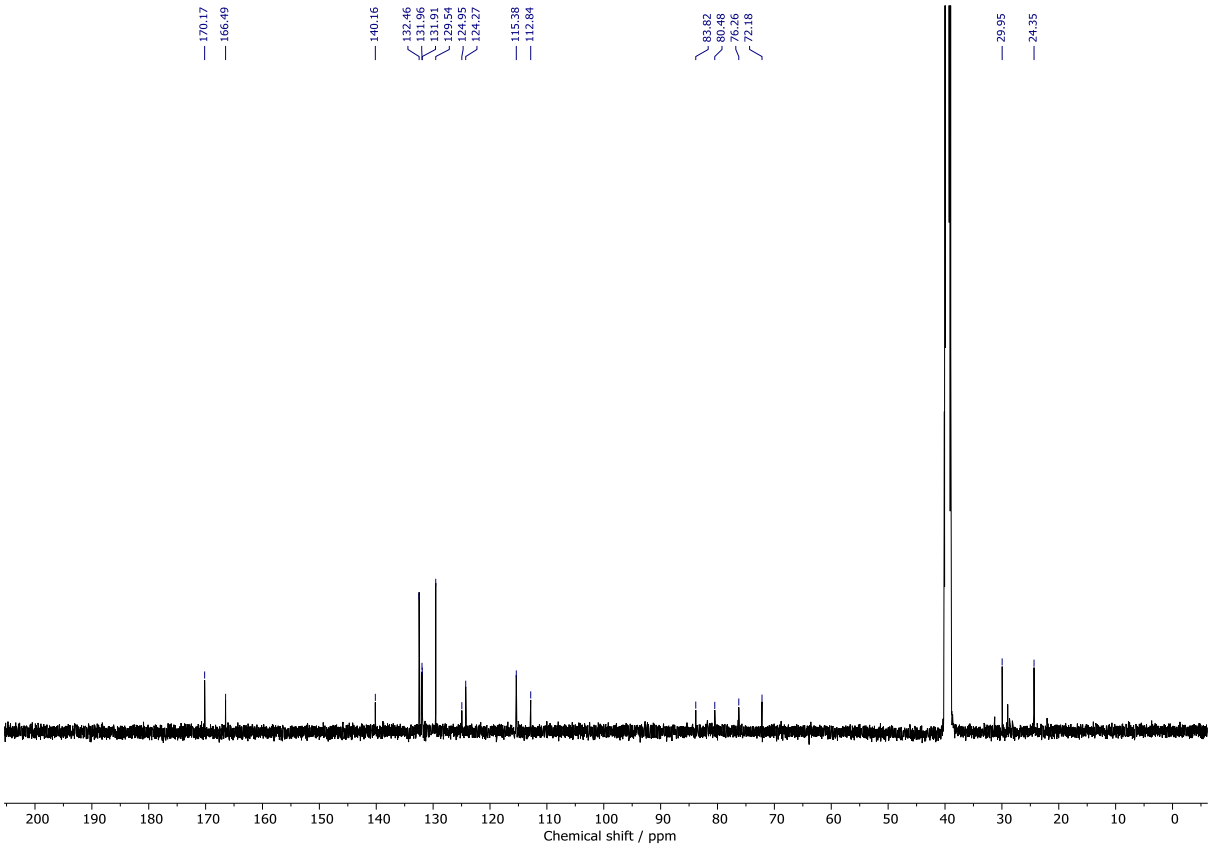
170.17
166.49
140.16
132.46
131.96
131.91
129.54
124.95
124.27
115.38
112.84
83.82
80.48
76.26
72.18
29.95
24.35
Chemical shift / ppm

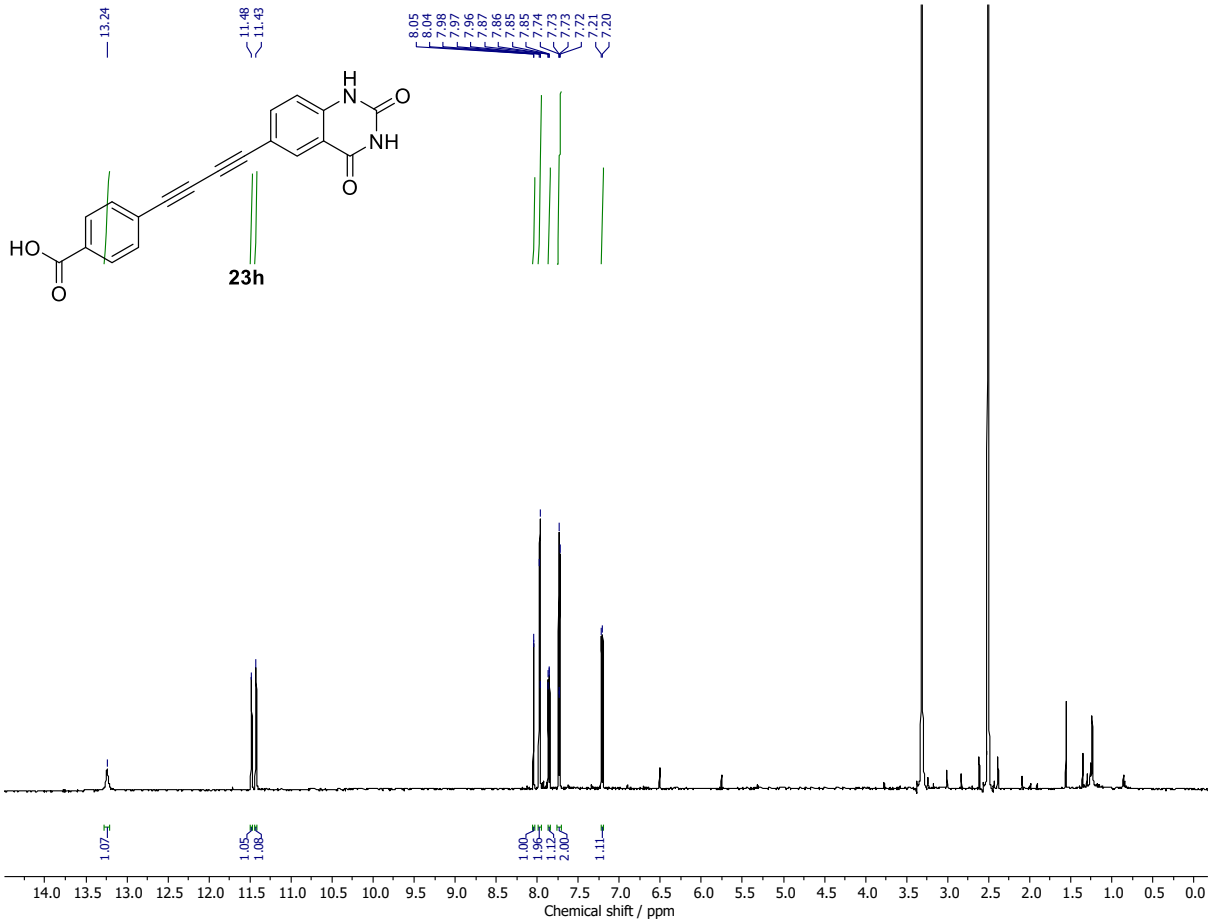
13.24
11.48
11.43
8.05
8.04
7.98
7.97
7.96
7.87
7.86
7.85
7.74
7.73
7.73
7.72
7.21
7.20
HO
O
H
N
O
NH
O
23h
1.07
1.05
1.08
1.00
1.96
1.12
2.00
1.11
14.0 13.5 13.0 12.5 12.0 11.5 11.0 10.5 10.0 9.5 9.0 8.5 8.0 7.5 7.0 6.5 6.0 5.5 5.0 4.5 4.0 3.5 3.0 2.5 2.0 1.5 1.0 0.5 0.0
Chemical shift / ppm

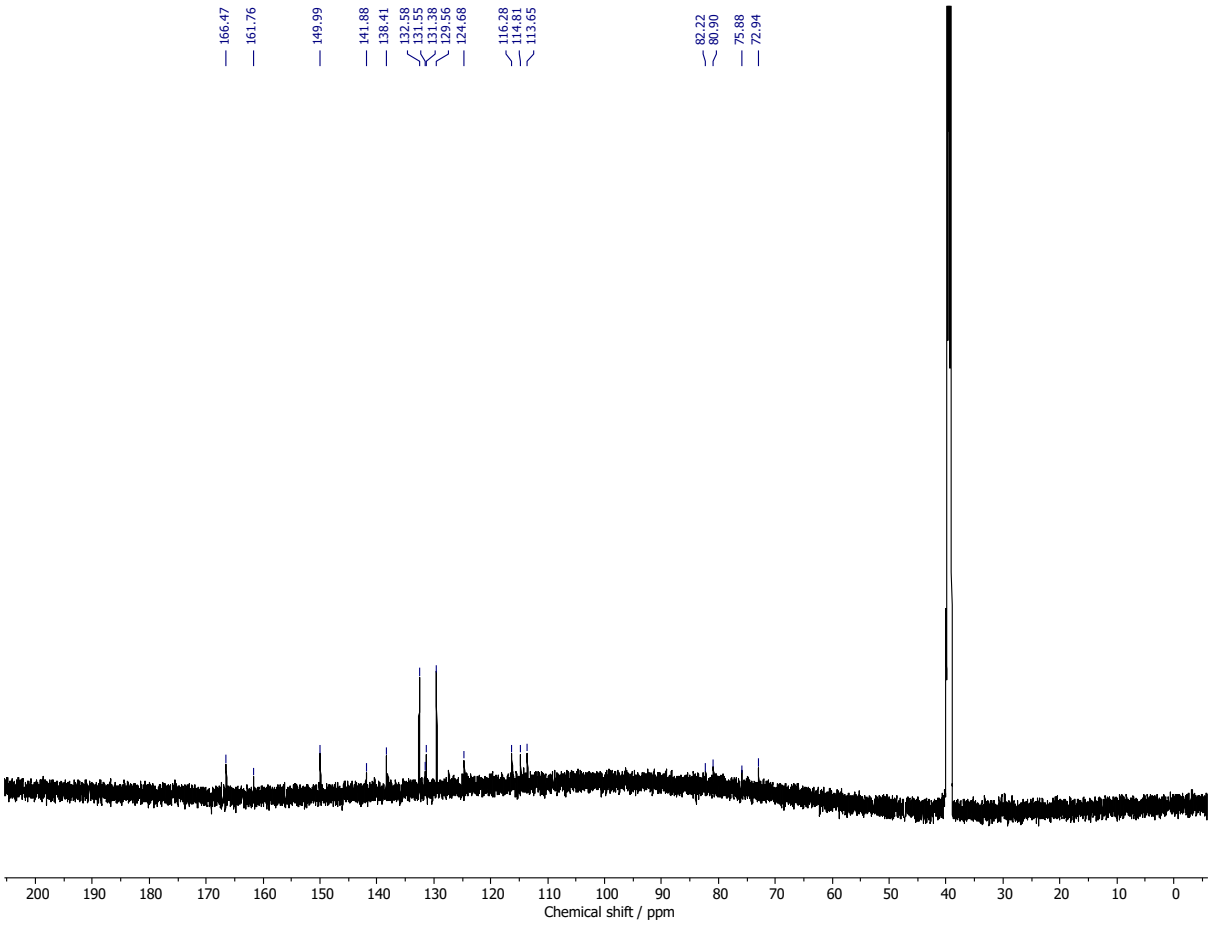
166.47
161.76
149.99
141.88
138.41
132.58
131.55
131.38
129.56
124.68
116.28
114.81
113.65
82.22
80.90
75.88
72.94
200 190 180 170 160 150 140 130 120 110 100 90 80 70 60 50 40 30 20 10 0
Chemical shift / ppm

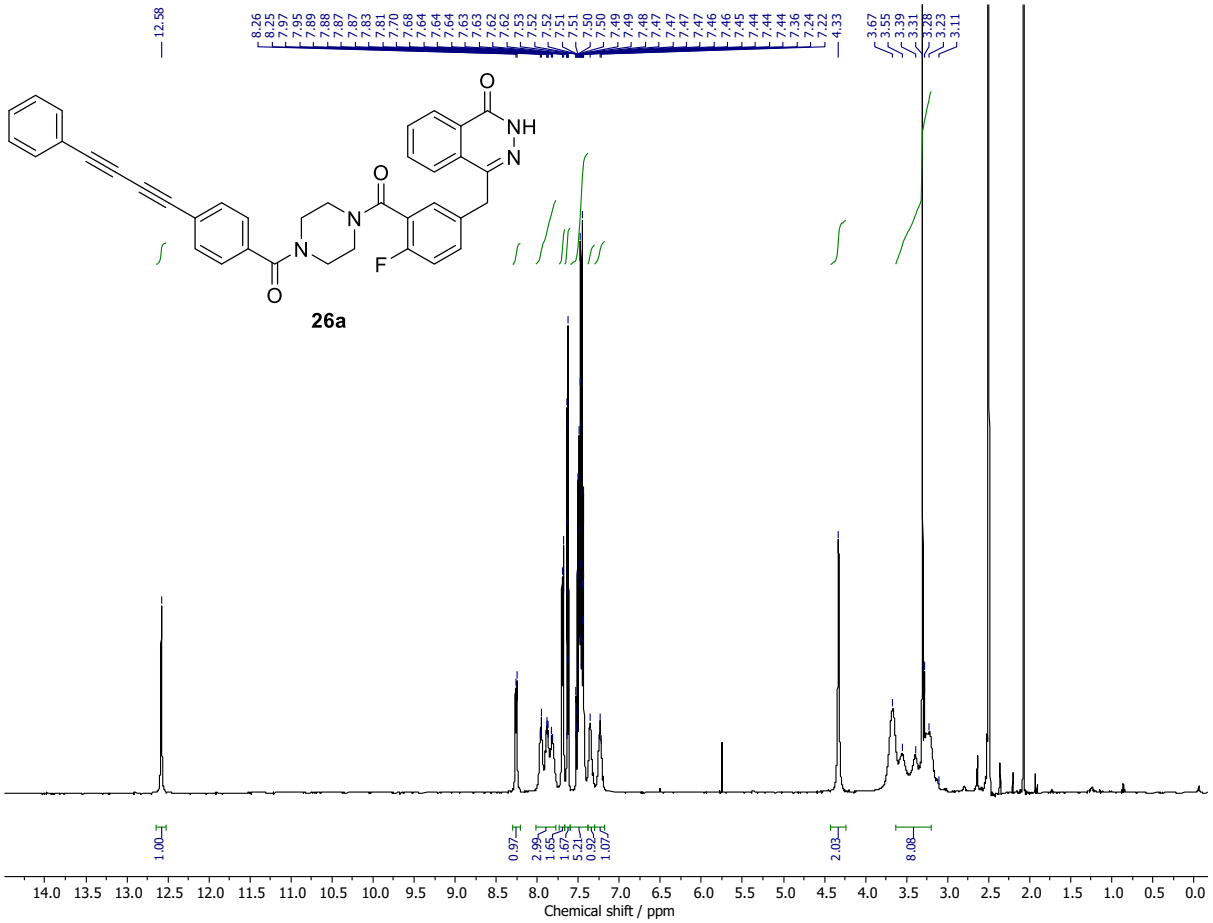
12.58
8.26
8.25
7.97
7.95
7.89
7.88
7.87
7.87
7.83
7.81
7.70
7.68
7.64
7.64
7.64
7.63
7.63
7.62
7.62
7.62
7.53
7.52
7.52
7.51
7.51
7.50
7.50
7.49
7.49
7.48
7.47
7.47
7.47
7.47
7.46
7.46
7.45
7.44
7.44
7.44
7.36
7.24
7.22
4.33
3.67
3.55
3.39
3.31
3.28
3.23
3.11
O
NH
N
O
N
N
O
F
26a
1.00
0.97
2.99
1.65
1.67
5.21
0.92
1.07
2.03
8.08
14.0 13.5 13.0 12.5 12.0 11.5 11.0 10.5 10.0 9.5 9.0 8.5 8.0 7.5 7.0 6.5 6.0 5.5 5.0 4.5 4.0 3.5 3.0 2.5 2.0 1.5 1.0 0.5 0.0
Chemical shift / ppm

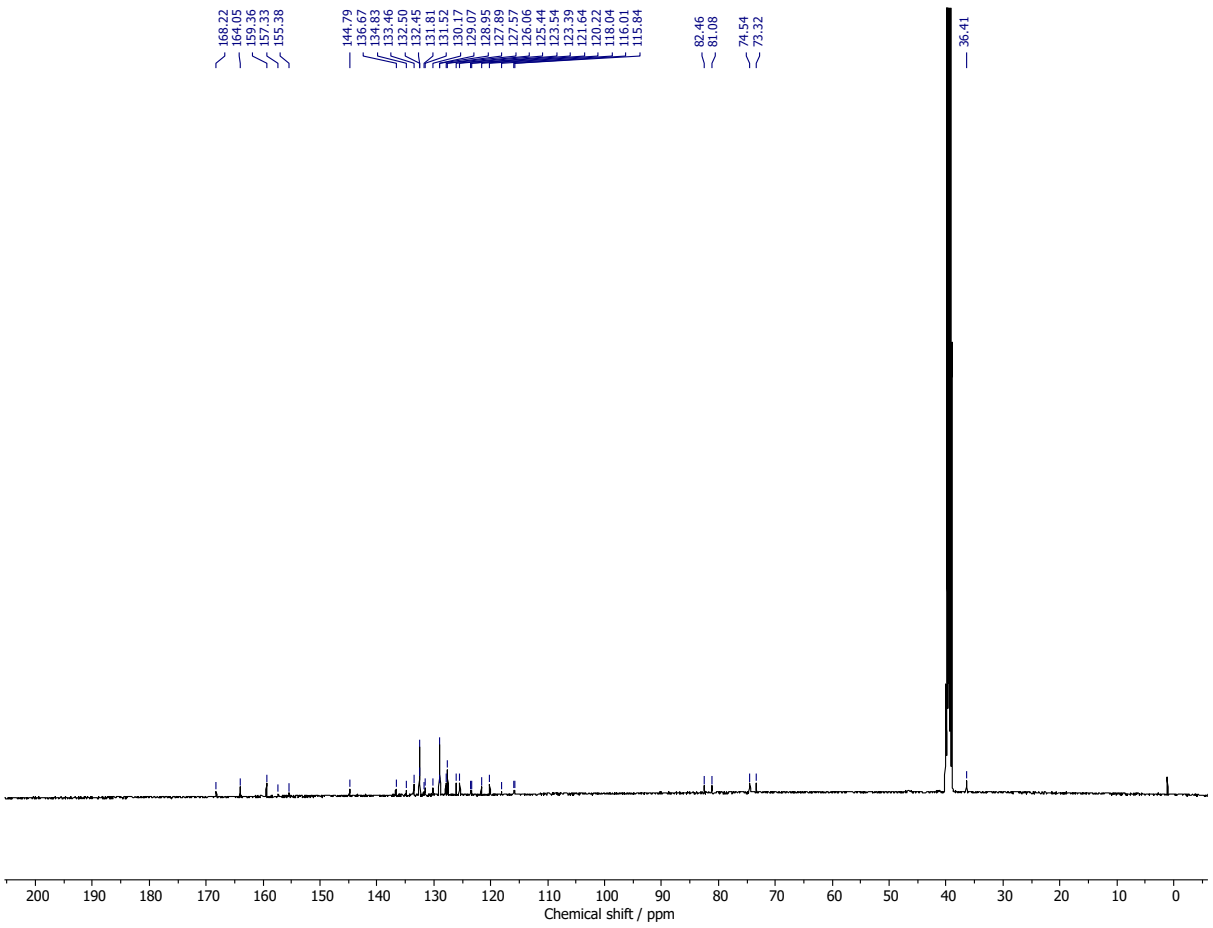
168.22
164.05
159.36
157.33
155.38
144.79
136.67
134.83
133.46
132.50
132.45
131.81
131.52
130.17
129.07
128.95
127.89
127.57
126.06
125.44
123.54
123.39
121.64
120.22
118.04
116.01
115.84
82.46
81.08
74.54
73.32
36.41
200 190 180 170 160 150 140 130 120 110 100 90 80 70 60 50 40 30 20 10 0
Chemical shift / ppm

12.58
8.26
8.25
7.95
7.88
7.83
7.81
7.68
7.66
7.48
7.46
7.36
7.32
7.31
7.30
7.23
7.13
7.11
4.33
3.67
3.54
3.39
3.23
2.74
2.73
2.71
1.74
1.73
1.73
1.72
1.71
O
NH
N
O
N
N
F
O

26b

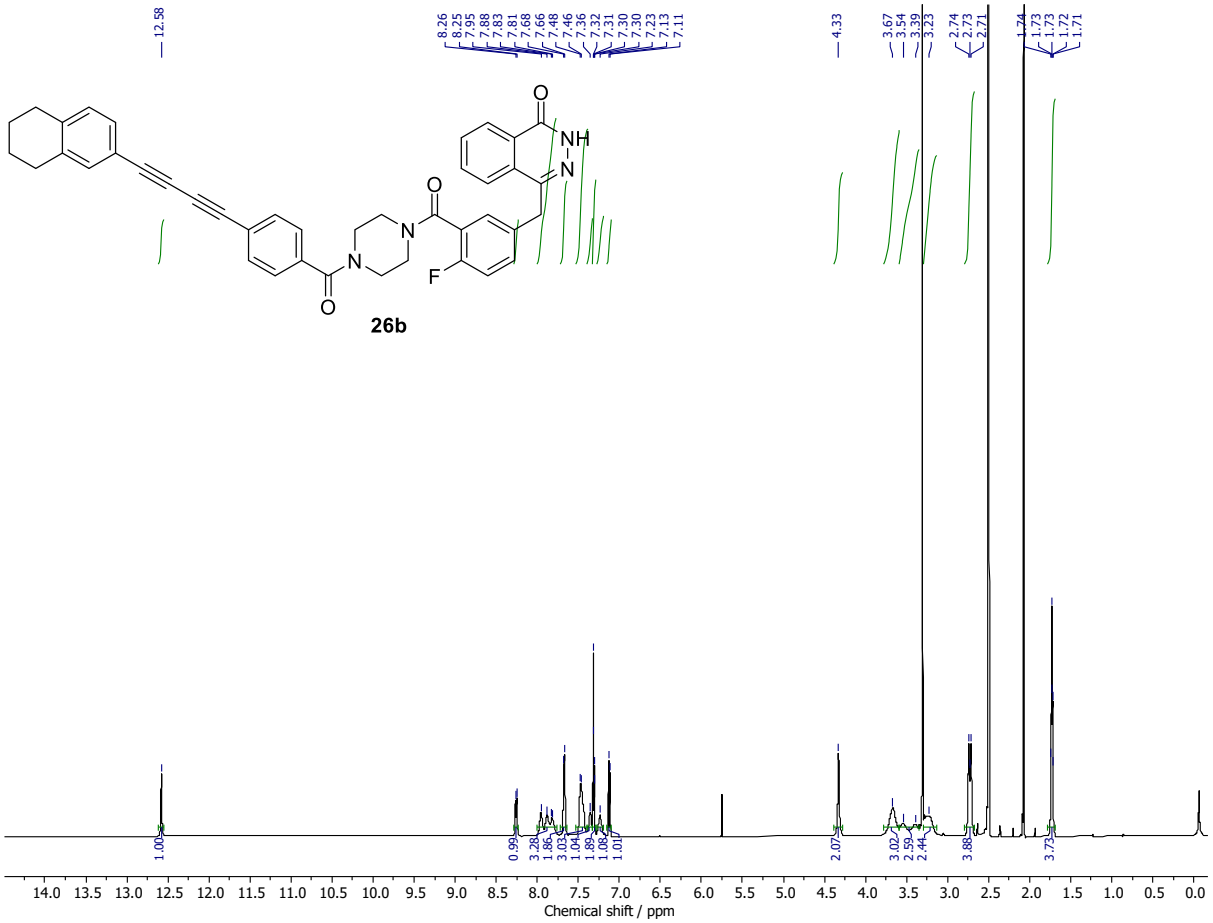
1.00
0.99
3.28
1.86
3.03
1.04
1.89
1.08
1.01
2.07
3.02
2.59
2.44
3.88
3.73
14.0 13.5 13.0 12.5 12.0 11.5 11.0 10.5 10.0 9.5 9.0 8.5 8.0 7.5 7.0 6.5 6.0 5.5 5.0 4.5 4.0 3.5 3.0 2.5 2.0 1.5 1.0 0.5 0.0
Chemical shift / ppm

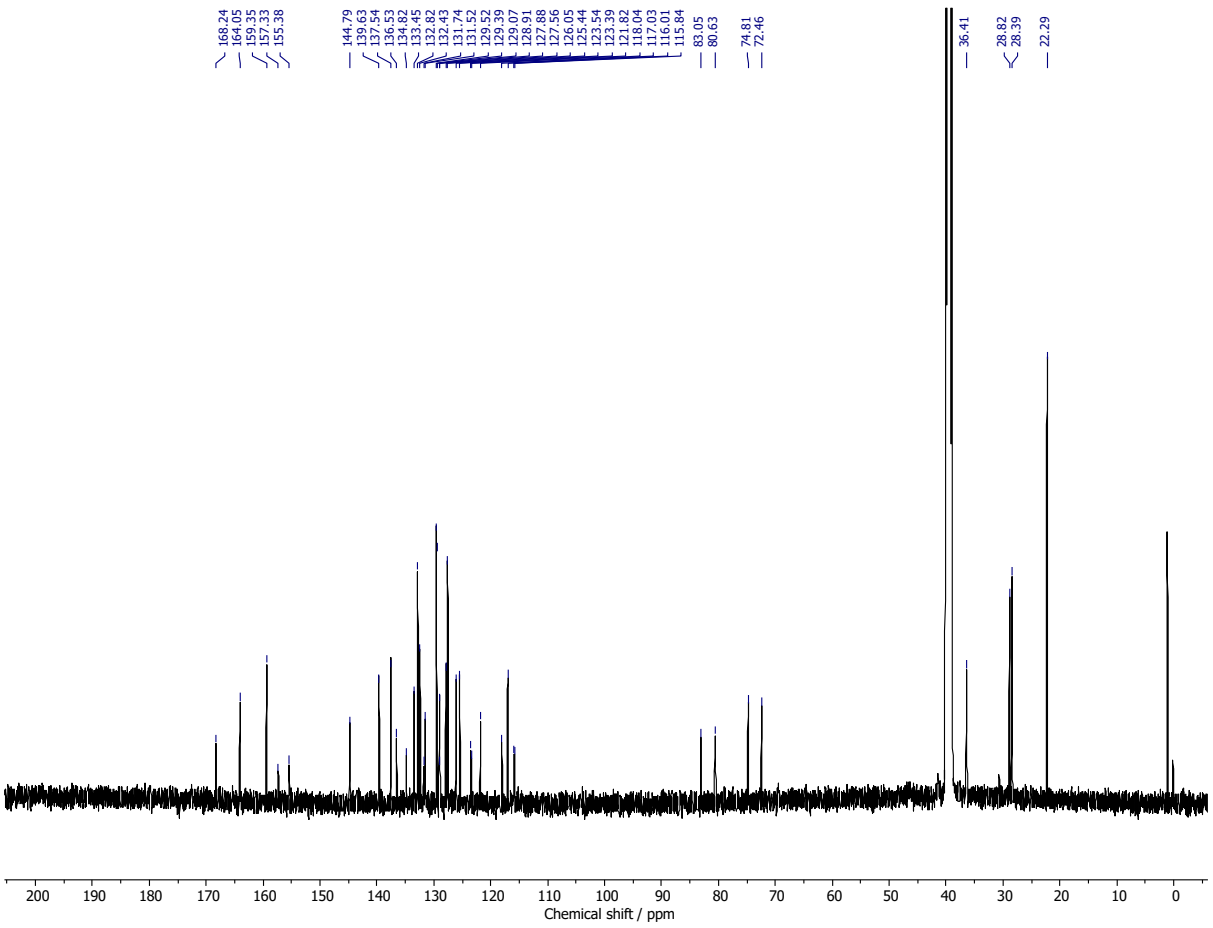
168.24
164.05
159.35
157.33
155.38
144.79
139.63
137.54
136.53
134.82
133.45
132.82
132.43
131.74
131.52
129.52
129.39
129.07
128.91
127.88
127.56
126.05
125.44
123.54
121.39
121.82
119.04
117.03
116.01
115.84
83.05
80.63
74.81
72.46
36.41
28.82
28.39
22.29
200 190 180 170 160 150 140 130 120 110 100 90 80 70 60 50 40 30 20 10 0
Chemical shift / ppm

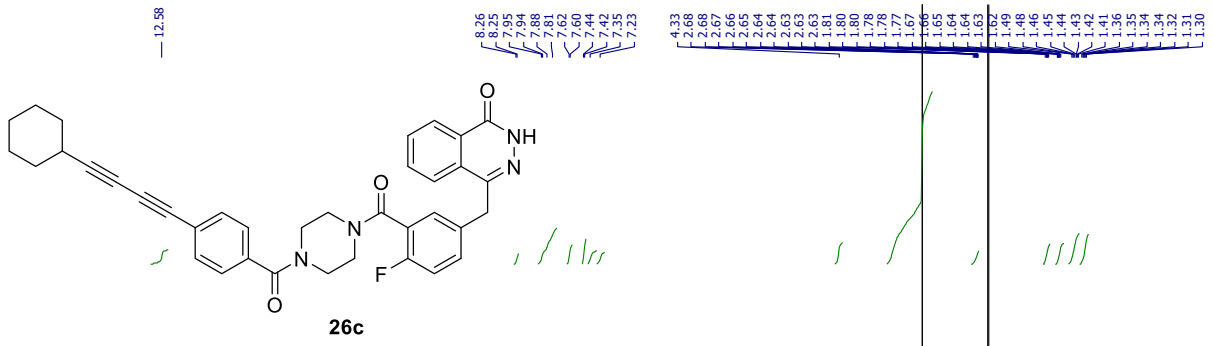
12.58
8.26
8.25
7.95
7.94
7.88
7.81
7.62
7.60
7.44
7.42
7.35
7.23
4.33
2.68
2.68
2.67
2.66
2.65
2.64
2.64
2.63
2.63
2.63
1.81
1.80
1.80
1.78
1.78
1.77
1.67
1.66
1.65
1.64
1.64
1.63
1.62
1.49
1.48
1.46
1.45
1.44
1.43
1.42
1.41
1.36
1.35
1.34
1.34
1.32
1.31
1.30
O
NH
N
O
N
N
F
O

26c

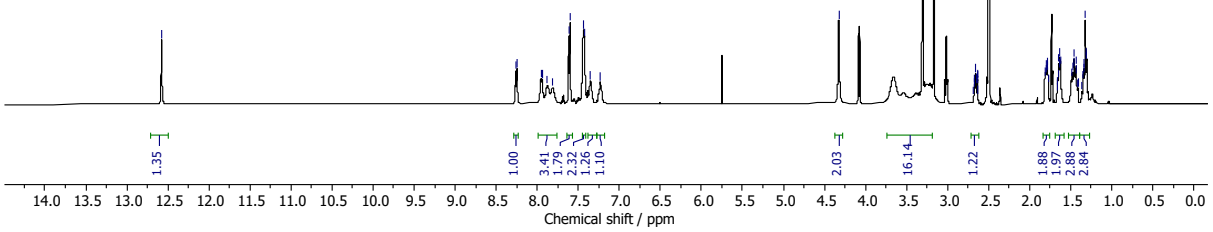
1.35
1.00
3.41
1.79
2.32
1.26
1.10
2.03
16.14
1.22
1.88
1.97
2.88
2.84
14.0 13.5 13.0 12.5 12.0 11.5 11.0 10.5 10.0 9.5 9.0 8.5 8.0 7.5 7.0 6.5 6.0 5.5 5.0 4.5 4.0 3.5 3.0 2.5 2.0 1.5 1.0 0.5 0.0
Chemical shift / ppm

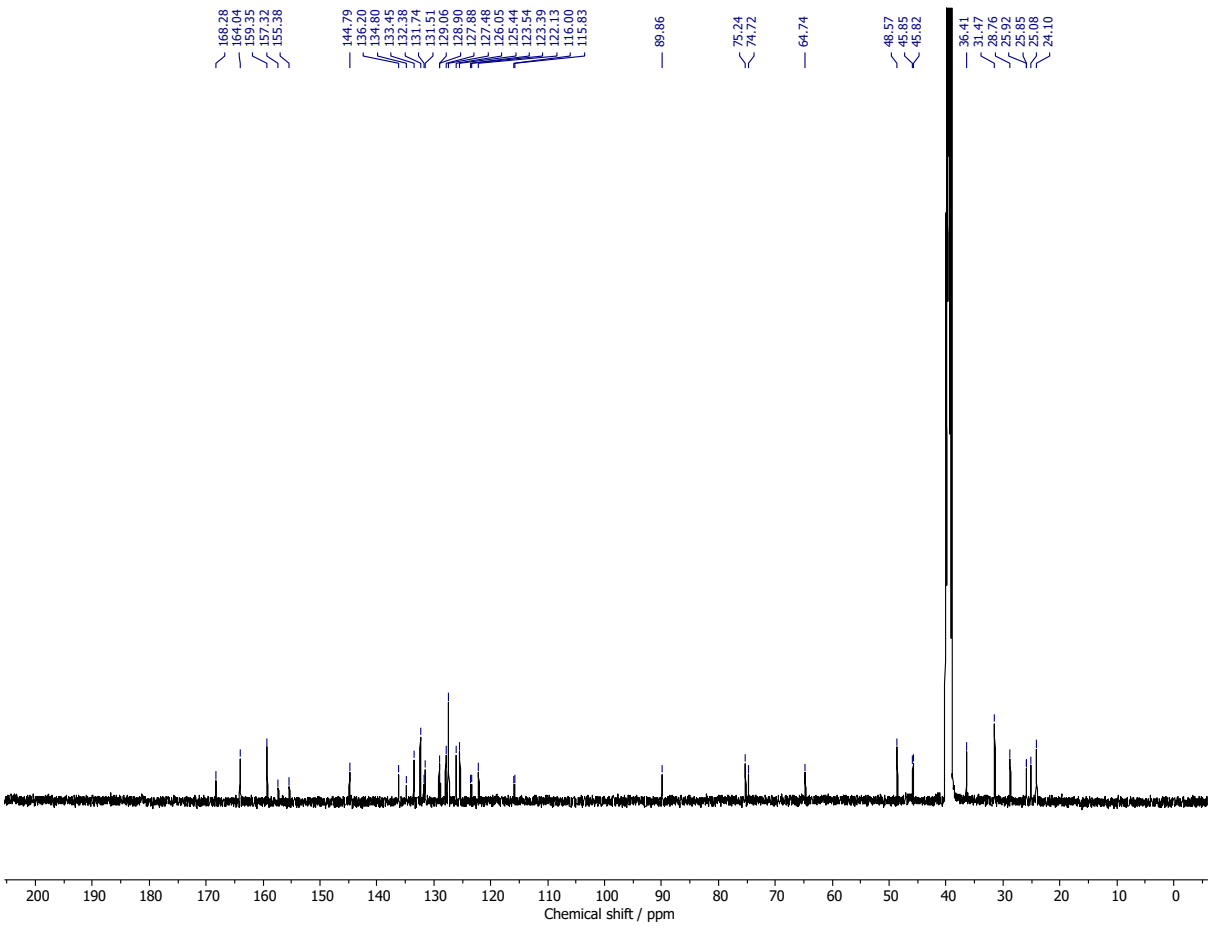
168.28
164.04
159.35
157.32
155.38
144.79
136.20
134.80
133.45
132.38
131.74
131.51
129.06
128.90
127.88
127.48
126.05
125.44
123.54
123.39
122.13
116.00
115.83
89.86
75.24
74.72
64.74
48.57
45.85
45.82
36.41
31.47
28.76
25.92
25.85
25.08
24.10
200 190 180 170 160 150 140 130 120 110 100 90 80 70 60 50 40 30 20 10 0
Chemical shift / ppm

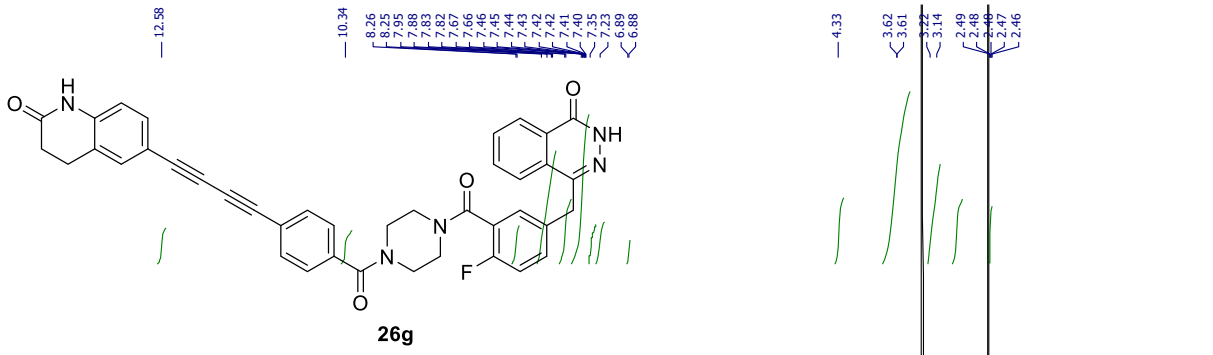
12.58
10.34
8.26
8.25
7.95
7.88
7.83
7.82
7.67
7.66
7.46
7.45
7.44
7.43
7.42
7.42
7.41
7.40
7.35
7.23
6.89
6.88
4.33
3.62
3.61
3.22
3.14
2.49
2.48
2.48
2.47
2.46
O
H
N
O
NH
N
O
N
N
F
O

26g

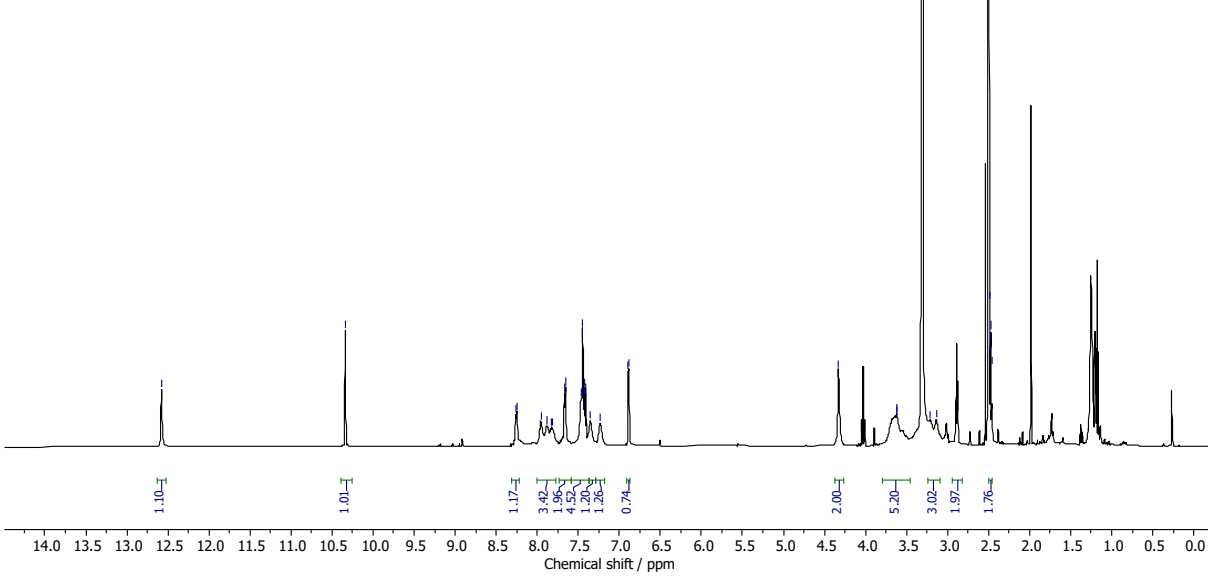
1.10
1.01
1.17
3.42
1.95
4.52
1.20
1.26
0.74
2.00
5.20
3.02
1.97
1.76
14.0 13.5 13.0 12.5 12.0 11.5 11.0 10.5 10.0 9.5 9.0 8.5 8.0 7.5 7.0 6.5 6.0 5.5 5.0 4.5 4.0 3.5 3.0 2.5 2.0 1.5 1.0 0.5 0.0
Chemical shift / ppm

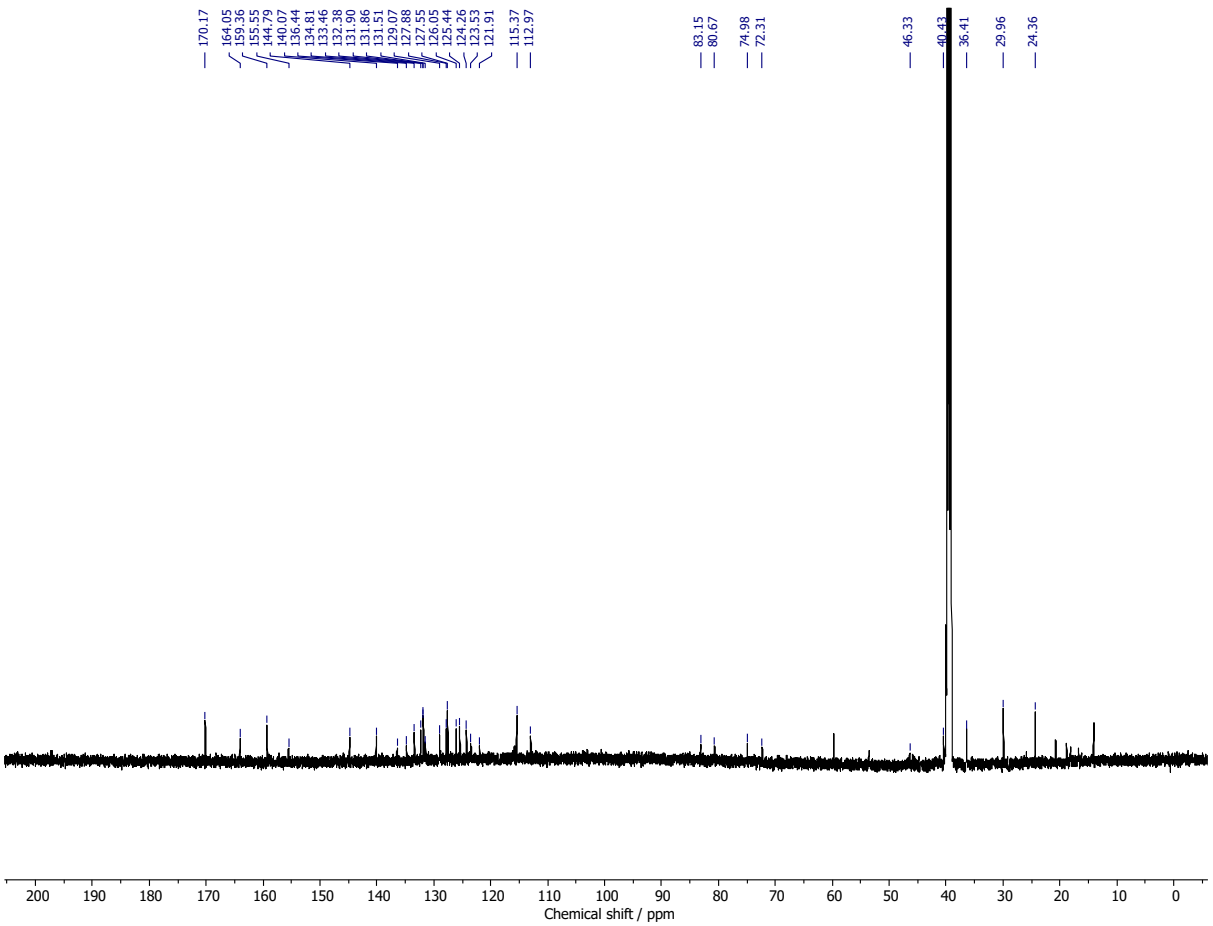
170.17
164.05
159.36
155.55
144.79
140.07
136.44
134.81
133.46
132.38
131.90
131.86
131.51
129.07
127.88
127.55
126.05
125.44
124.26
123.53
121.91
115.37
112.97
83.15
80.67
74.98
72.31
46.33
40.43
36.41
29.96
24.36
200 190 180 170 160 150 140 130 120 110 100 90 80 70 60 50 40 30 20 10 0
Chemical shift / ppm

26h

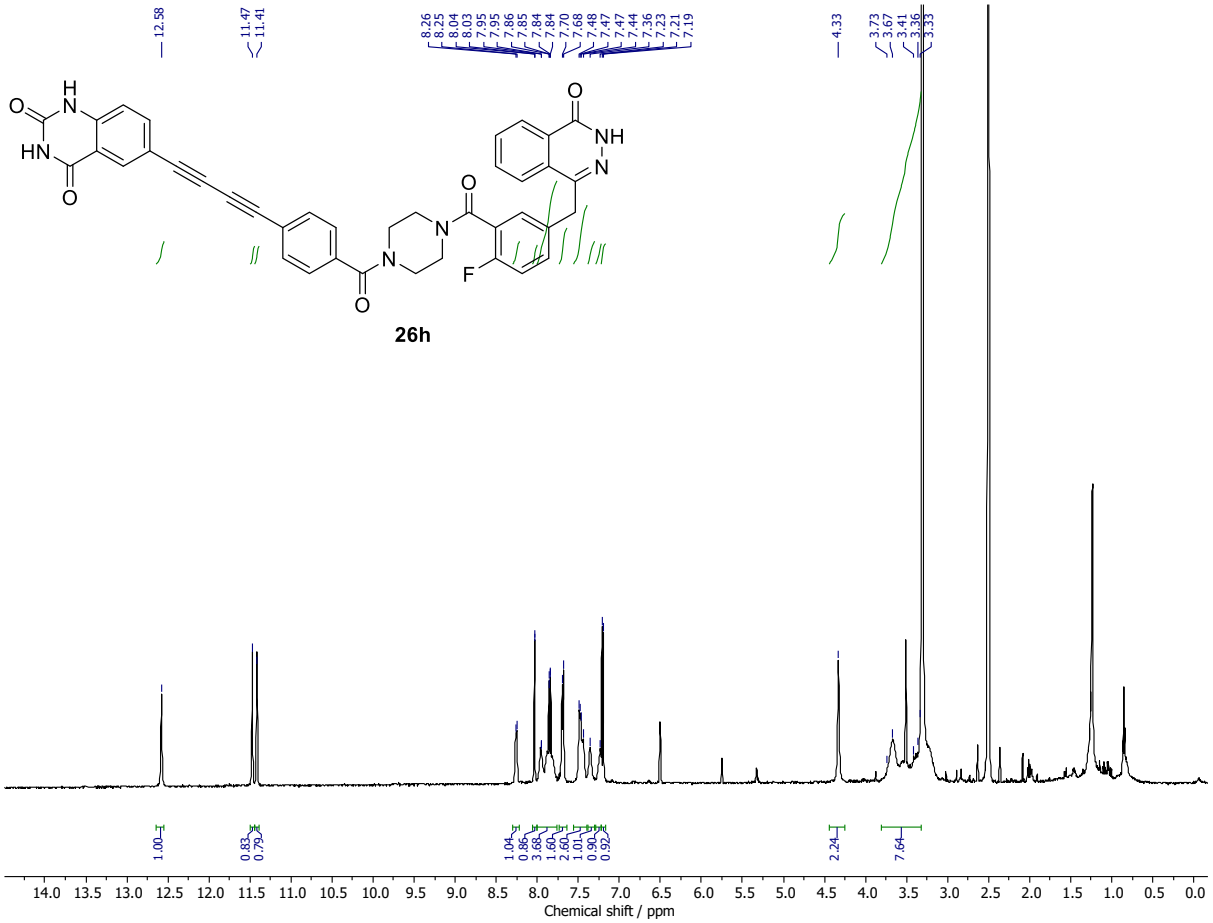
12.58
11.47
11.41
8.26
8.25
8.04
8.03
7.95
7.95
7.86
7.85
7.84
7.84
7.70
7.68
7.48
7.47
7.47
7.44
7.36
7.23
7.21
7.19
4.33
3.73
3.67
3.41
3.36
3.33
1.00
0.83
0.79
1.04
0.86
3.68
1.60
2.60
1.01
0.90
0.92
2.24
7.64
Chemical shift / ppm

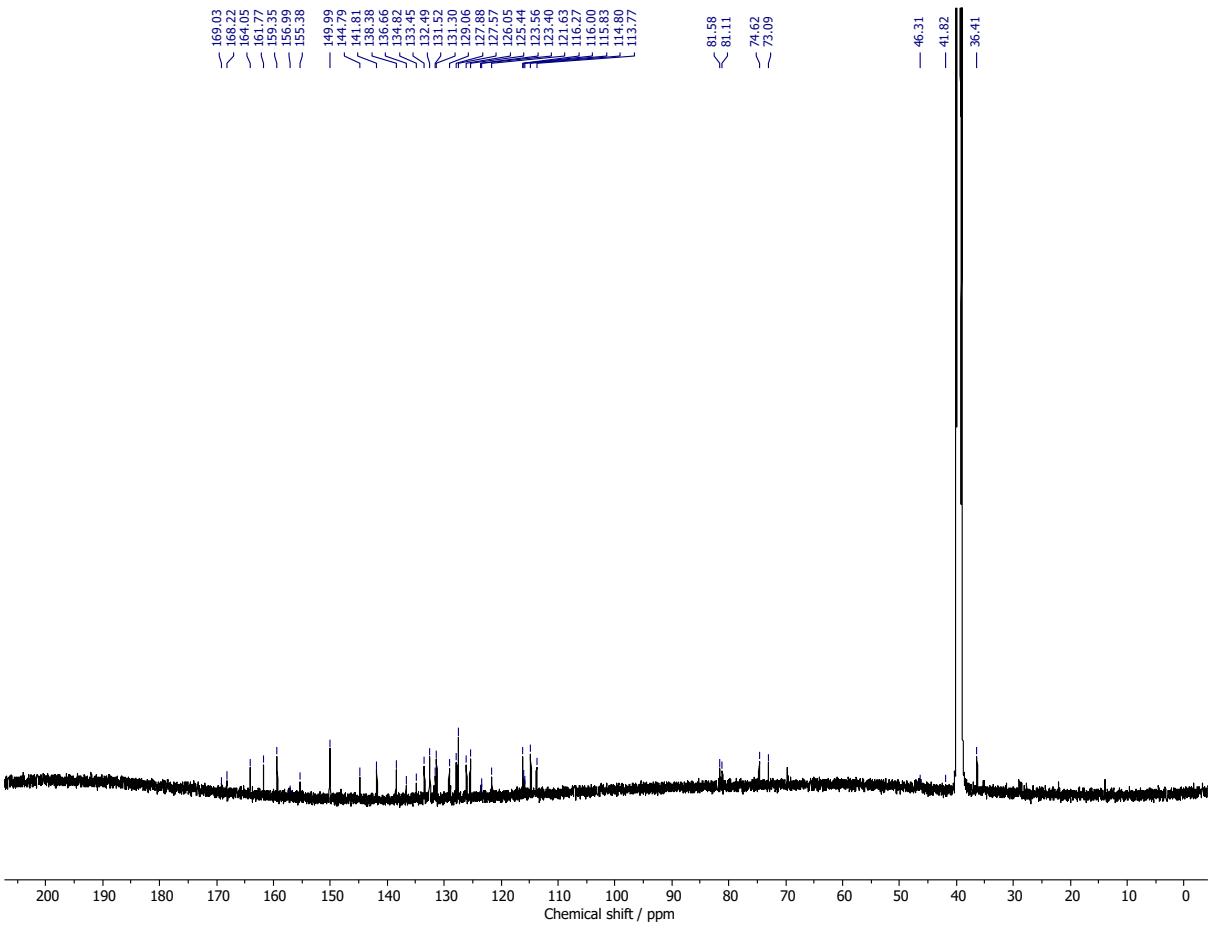
169.03
168.22
164.05
161.77
159.35
156.99
155.38
149.99
144.79
141.81
138.38
136.66
134.82
133.45
132.49
131.52
131.30
129.06
127.88
127.57
126.05
125.44
123.56
123.40
121.63
116.27
116.00
115.83
114.80
113.77
81.58
81.11
74.62
73.09
46.31
41.82
36.41
Chemical shift / ppm

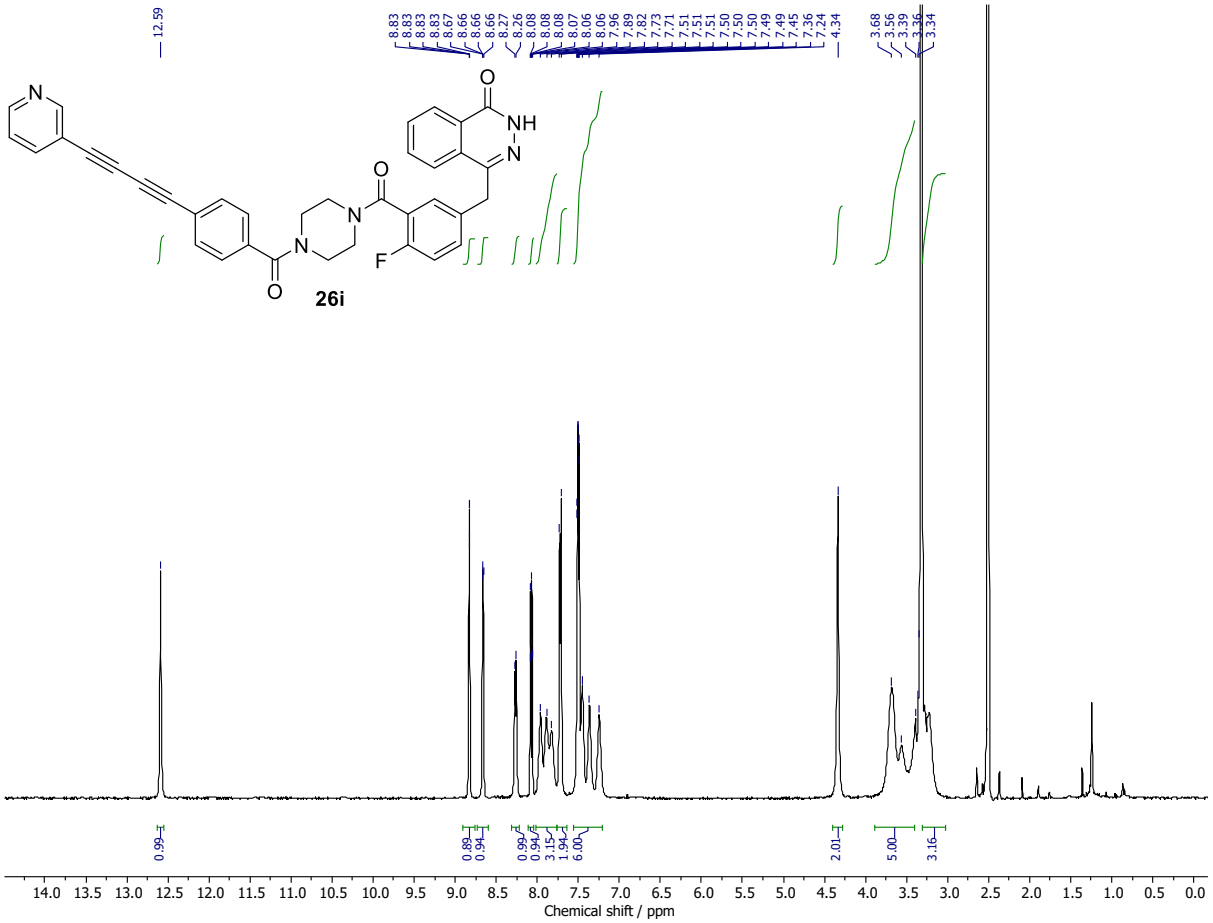
12.59
8.83
8.83
8.83
8.83
8.67
8.66
8.66
8.66
8.66
8.27
8.26
8.08
8.08
8.08
8.08
8.07
8.06
8.06
8.06
7.96
7.89
7.82
7.73
7.71
7.51
7.51
7.51
7.50
7.50
7.50
7.50
7.49
7.49
7.45
7.36
7.24
4.34
3.68
3.56
3.39
3.36
3.34
O
NH
N
N
O
N
N
F
O
26i
0.99
0.89
0.94
0.99
0.94
3.15
1.94
6.00
2.01
5.00
3.16
14.0 13.5 13.0 12.5 12.0 11.5 11.0 10.5 10.0 9.5 9.0 8.5 8.0 7.5 7.0 6.5 6.0 5.5 5.0 4.5 4.0 3.5 3.0 2.5 2.0 1.5 1.0 0.5 0.0
Chemical shift / ppm

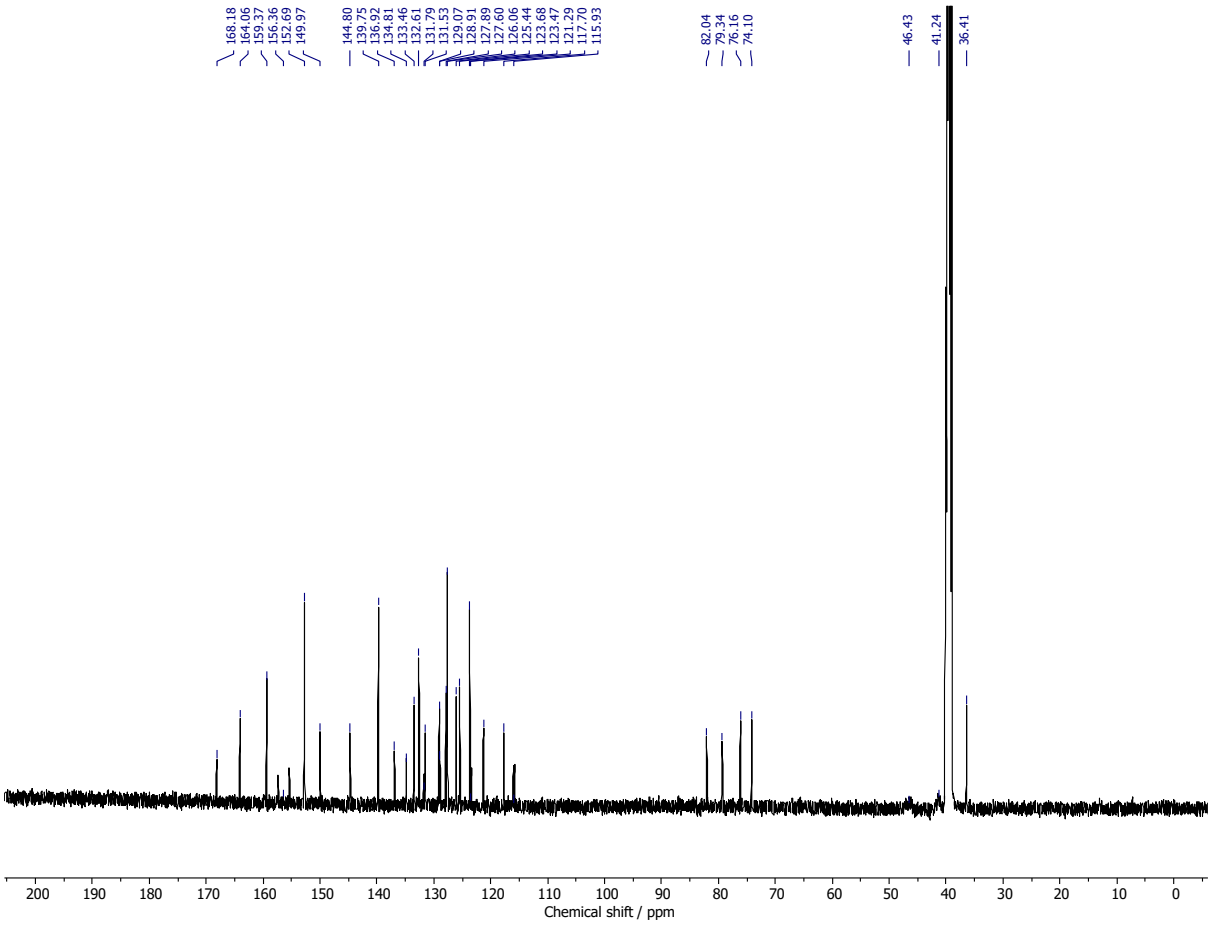
168.18
164.06
159.37
156.36
152.69
149.97
144.80
139.75
136.92
134.81
133.46
132.61
131.79
131.53
129.07
128.91
127.89
127.60
126.06
125.44
123.68
123.47
121.29
117.70
115.93
82.04
79.34
76.16
74.10
46.43
41.24
36.41
200 190 180 170 160 150 140 130 120 110 100 90 80 70 60 50 40 30 20 10 0
Chemical shift / ppm

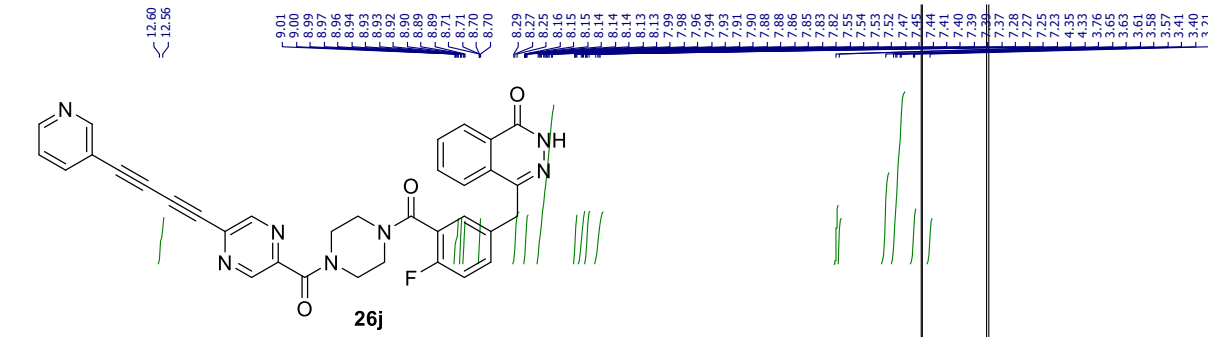
12.60
12.56
9.01
9.00
8.99
8.97
8.96
8.94
8.93
8.93
8.92
8.90
8.89
8.89
8.71
8.71
8.70
8.70
8.29
8.27
8.25
8.16
8.15
8.15
8.14
8.14
8.14
8.13
8.13
7.99
7.98
7.96
7.94
7.93
7.91
7.90
7.88
7.88
7.86
7.85
7.83
7.82
7.55
7.54
7.53
7.52
7.47
7.45
7.44
7.41
7.40
7.39
7.39
7.37
7.28
7.27
7.25
7.23
4.35
4.33
3.76
3.65
3.63
3.61
3.58
3.57
3.41
3.40
N
N
N
N
N
NH
N
O
O
O
F
26j

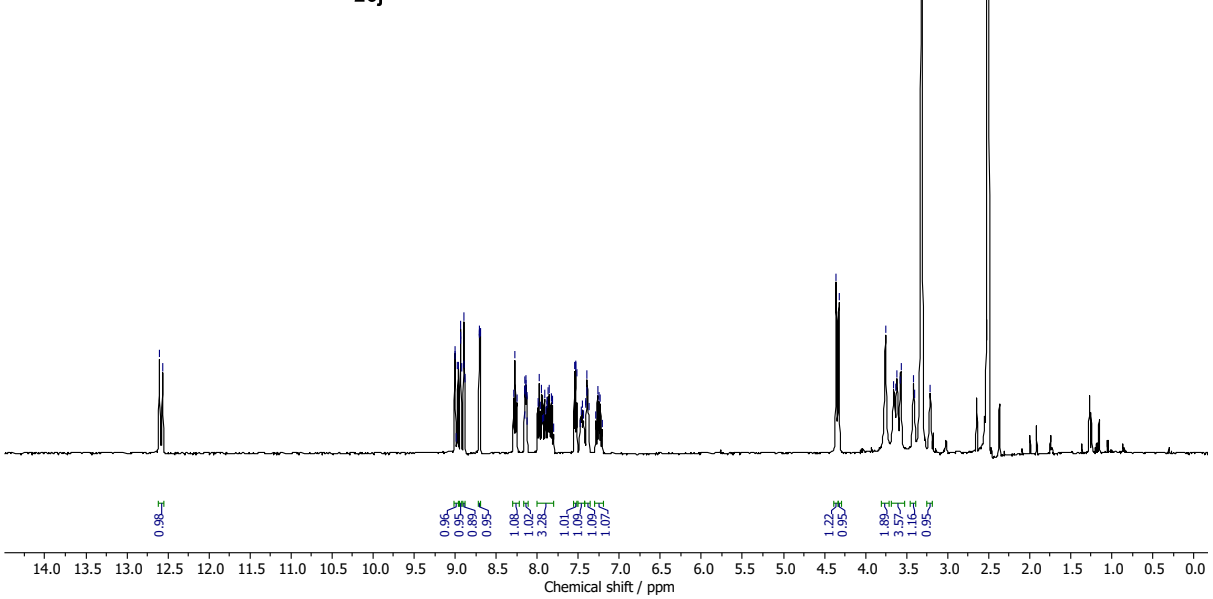
0.98
0.96
0.95
0.89
0.95
1.08
1.02
3.28
1.01
1.09
1.09
1.07
1.22
0.95
1.89
3.57
1.16
0.95
14.0 13.5 13.0 12.5 12.0 11.5 11.0 10.5 10.0 9.5 9.0 8.5 8.0 7.5 7.0 6.5 6.0 5.5 5.0 4.5 4.0 3.5 3.0 2.5 2.0 1.5 1.0 0.5 0.0
Chemical shift / ppm

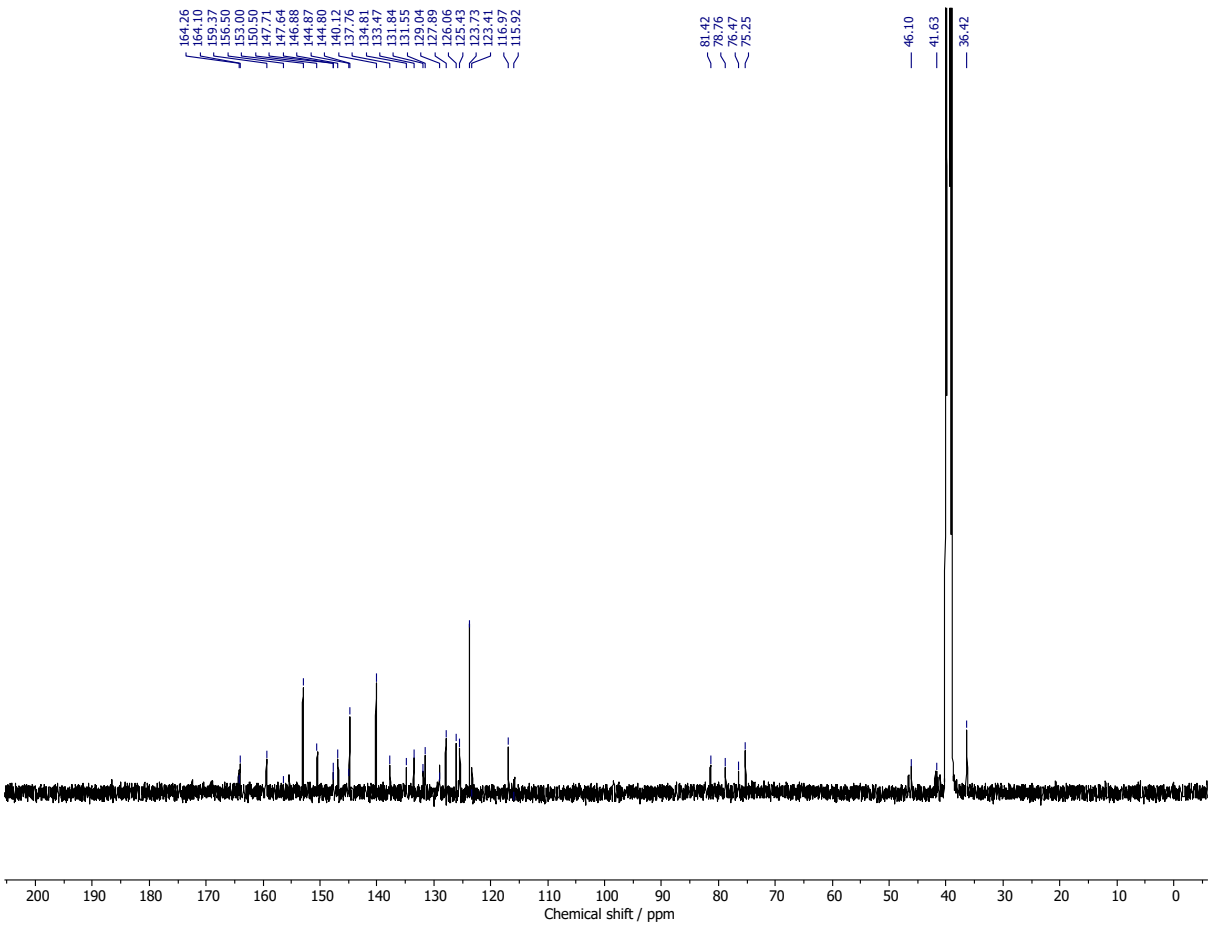
164.26
164.10
159.37
156.50
153.00
150.50
147.71
147.64
146.88
144.87
144.80
140.12
137.76
134.81
133.47
131.84
131.55
129.04
127.89
126.06
125.43
123.73
123.41
116.97
115.92
81.42
78.76
76.47
75.25
46.10
41.63
36.42
200 190 180 170 160 150 140 130 120 110 100 90 80 70 60 50 40 30 20 10 0
Chemical shift / ppm

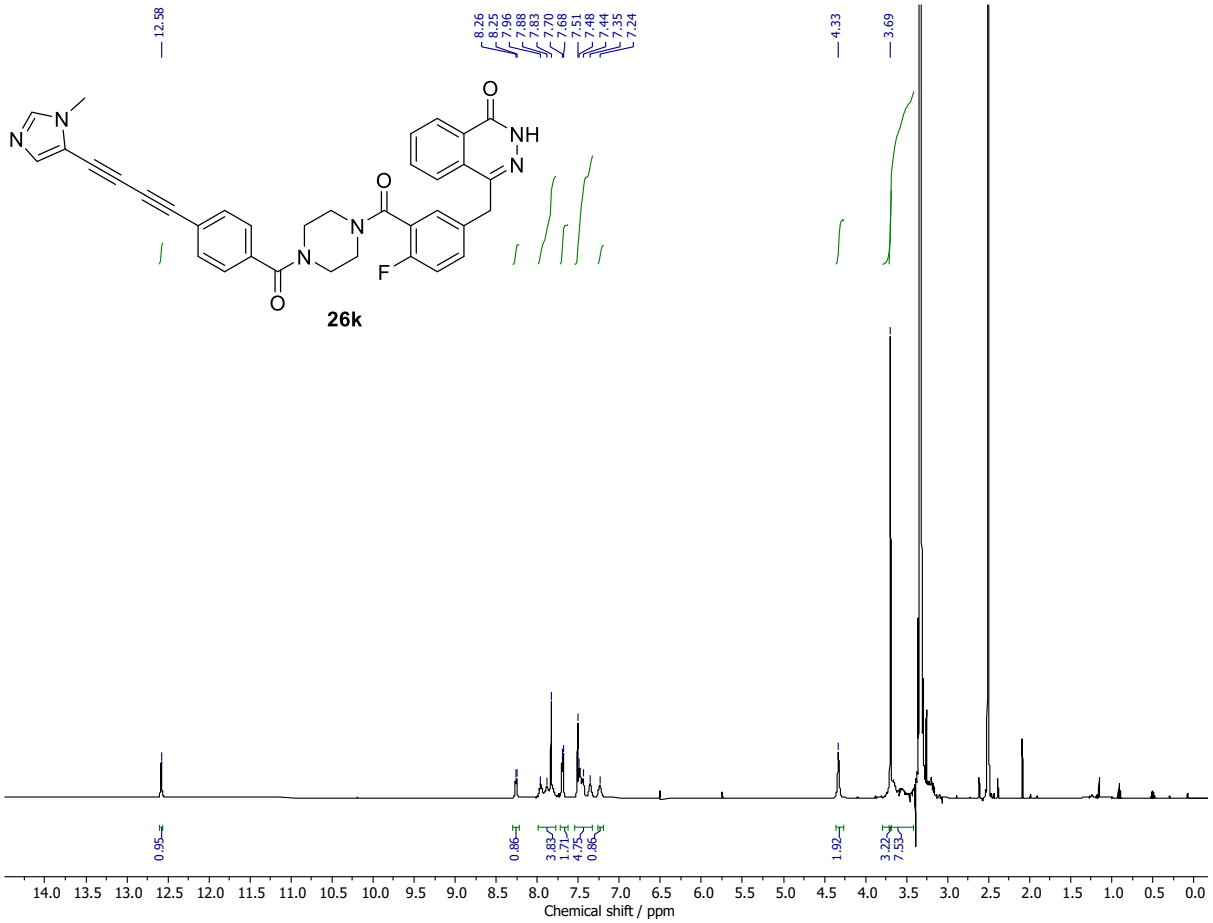
12.58
8.26
8.25
7.96
7.88
7.83
7.70
7.68
7.51
7.48
7.44
7.35
7.24
4.33
3.69
O
NH
N
N
O
N
N
F
O
26k
0.95
0.86
3.83
1.71
4.75
0.86
1.92
3.22
7.53
14.0 13.5 13.0 12.5 12.0 11.5 11.0 10.5 10.0 9.5 9.0 8.5 8.0 7.5 7.0 6.5 6.0 5.5 5.0 4.5 4.0 3.5 3.0 2.5 2.0 1.5 1.0 0.5 0.0
Chemical shift / ppm

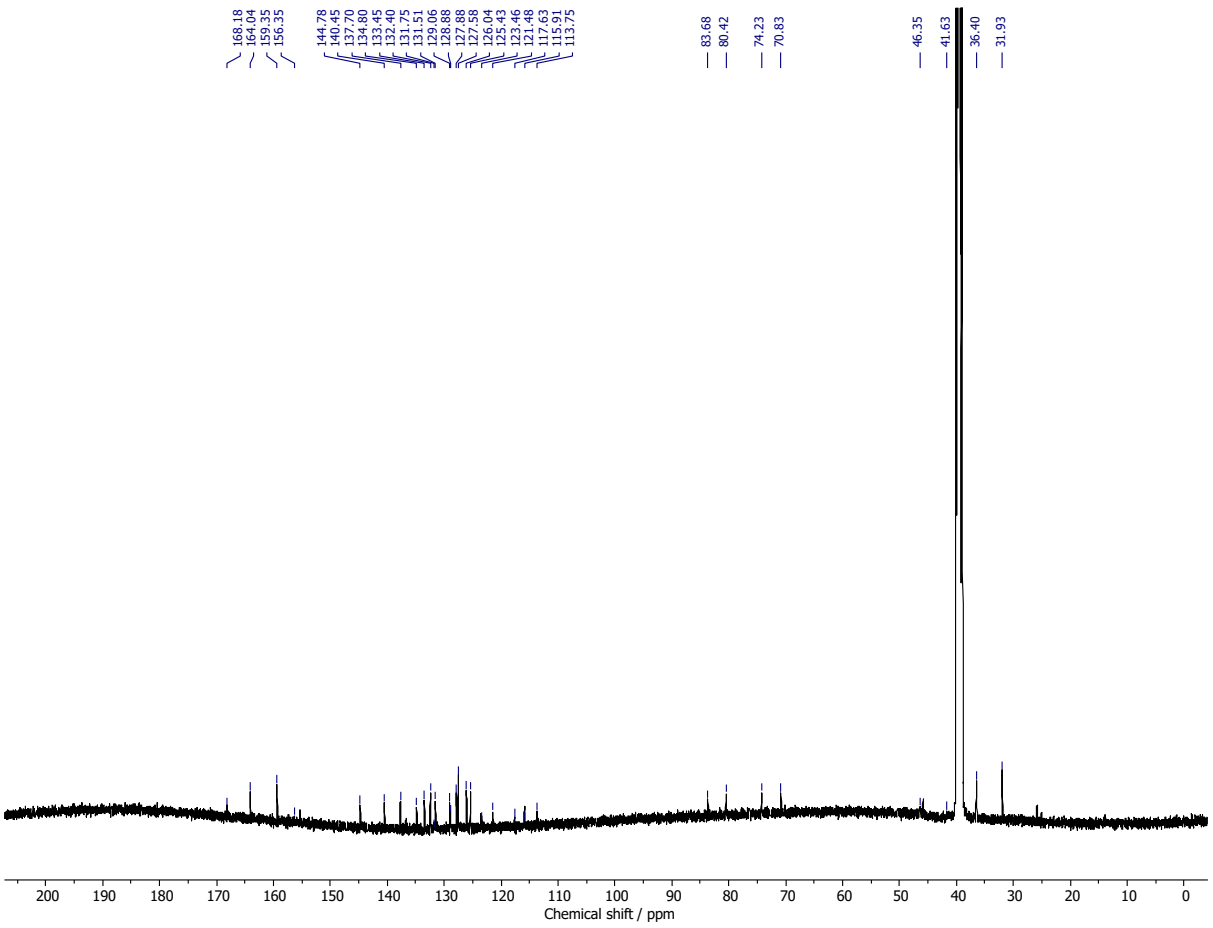
168.18
164.04
159.35
156.35
144.78
140.45
137.70
134.80
133.45
132.40
131.75
131.51
129.06
128.88
127.88
127.58
126.04
125.43
123.46
121.48
117.63
115.91
113.75
83.68
80.42
74.23
70.83
46.35
41.63
36.40
31.93
200 190 180 170 160 150 140 130 120 110 100 90 80 70 60 50 40 30 20 10 0
Chemical shift / ppm

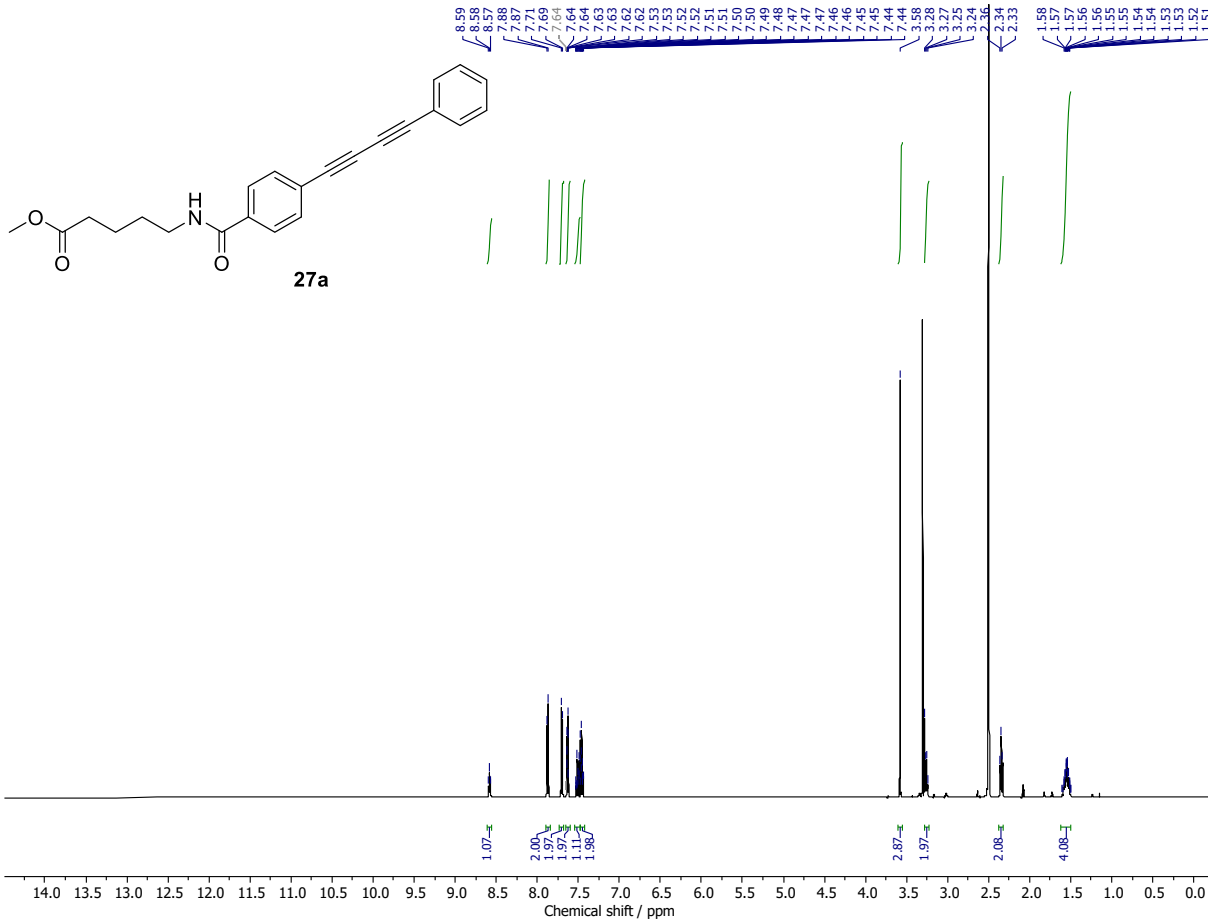
27a
Chemical shift / ppm

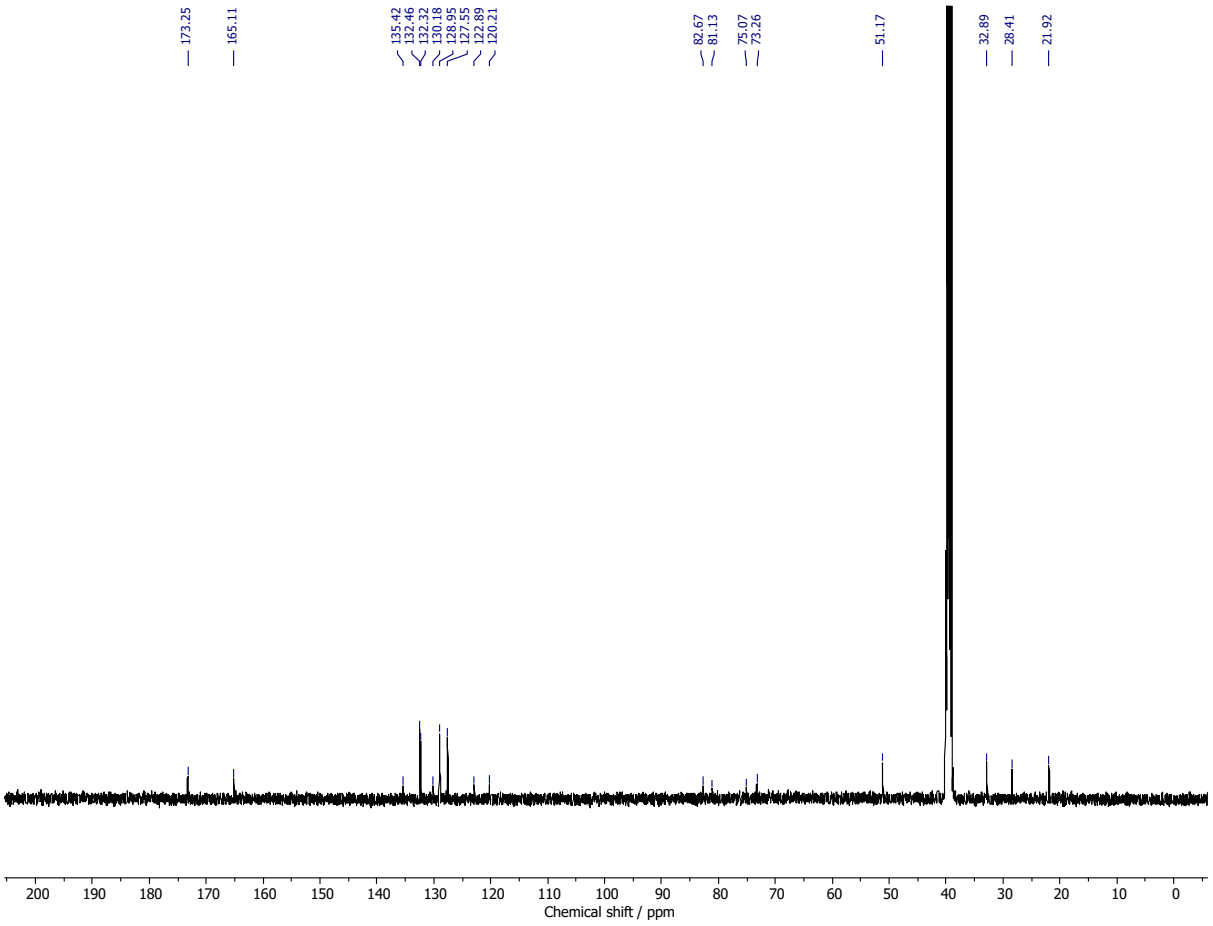
Chemical shift / ppm

27b

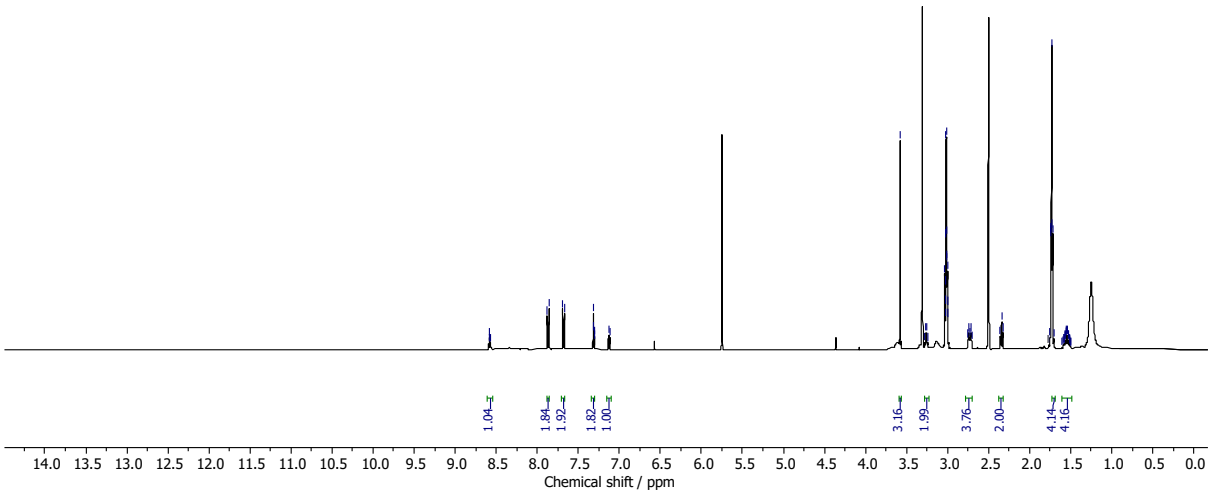
1.04
1.84
1.92
1.82
1.00
3.16
1.99
3.76
2.00
4.14
4.16
Chemical shift / ppm

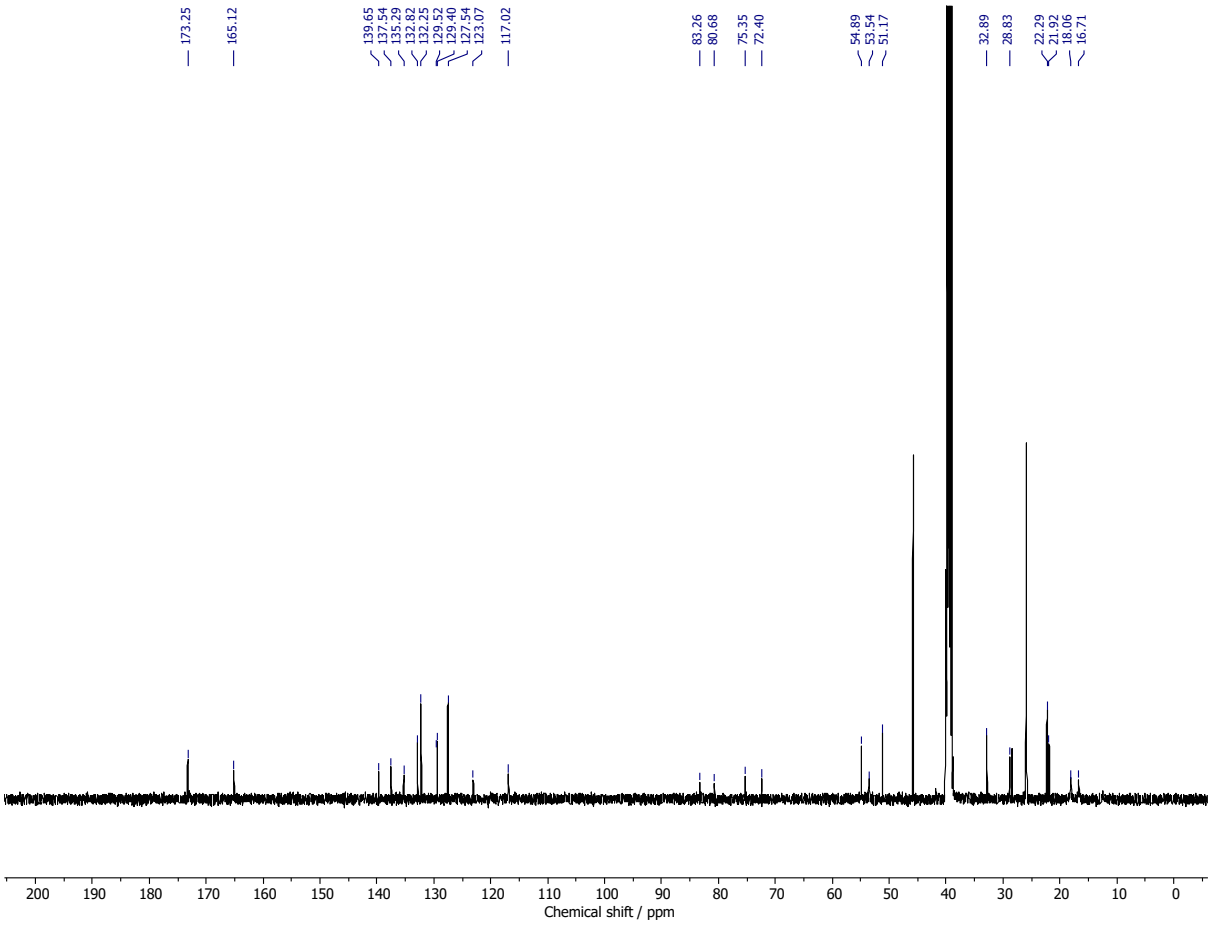
173.25
165.12
139.65
137.54
135.29
132.82
132.25
129.52
129.40
127.54
123.07
117.02
83.26
80.68
75.35
72.40
54.89
53.54
51.17
32.89
28.83
22.29
21.92
18.06
16.71
Chemical shift / ppm

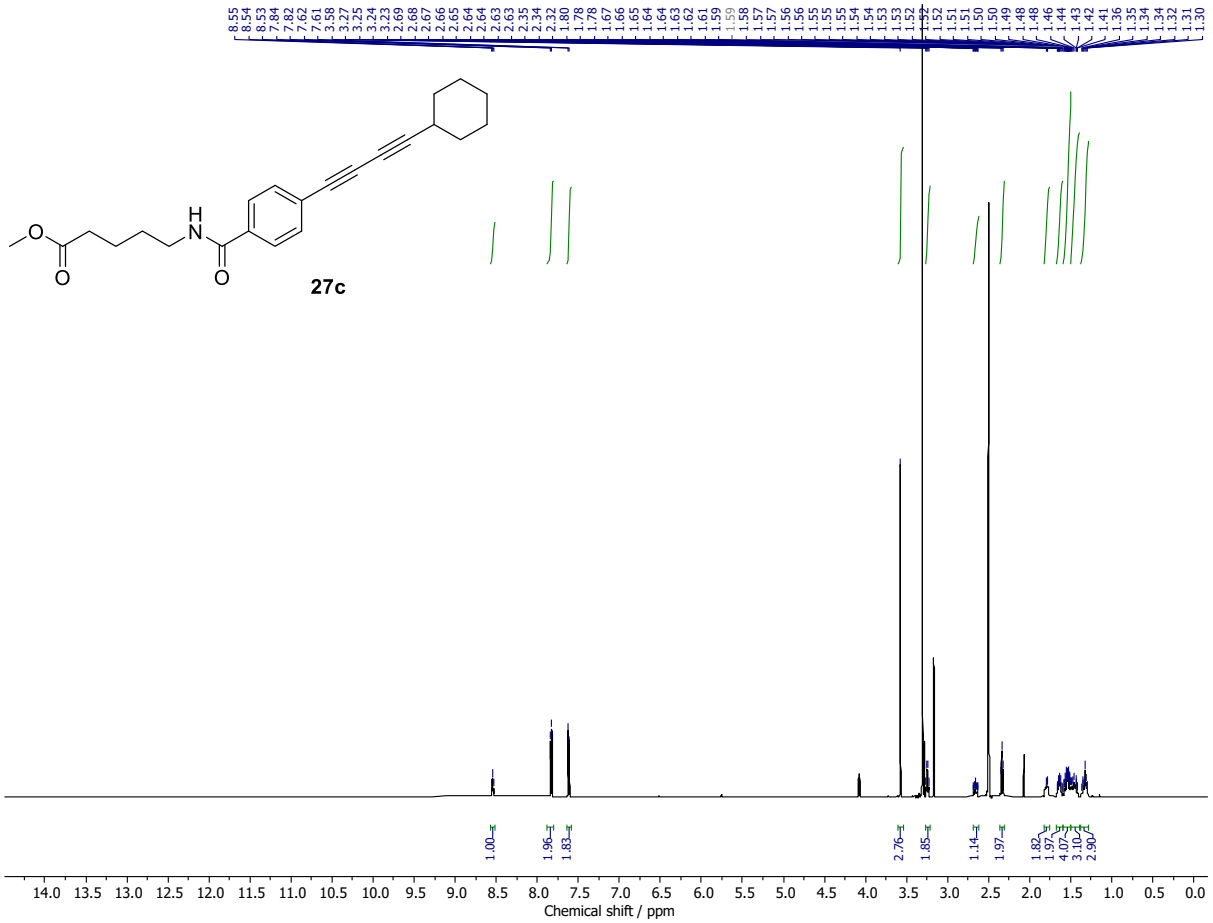
27c
Chemical shift / ppm

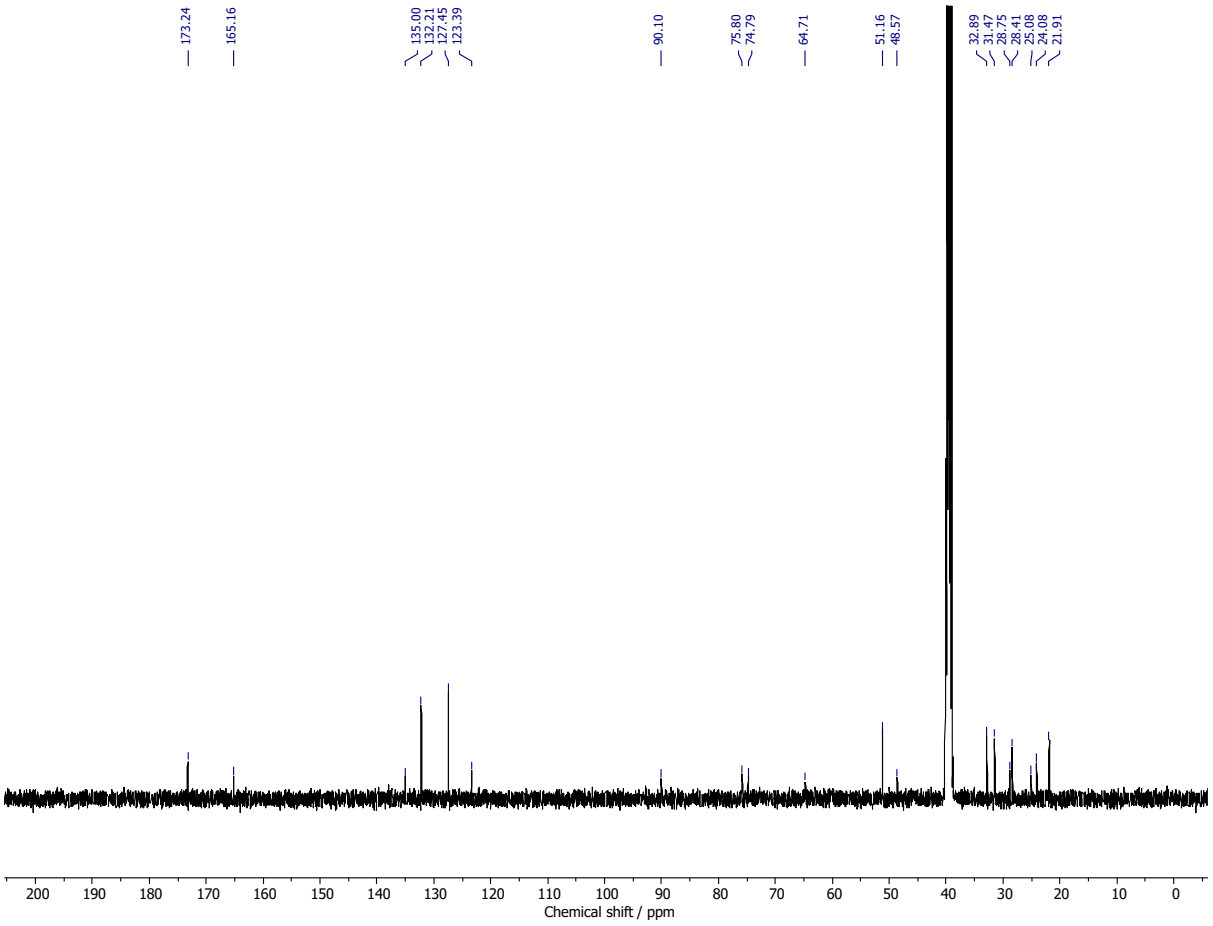
Chemical shift / ppm

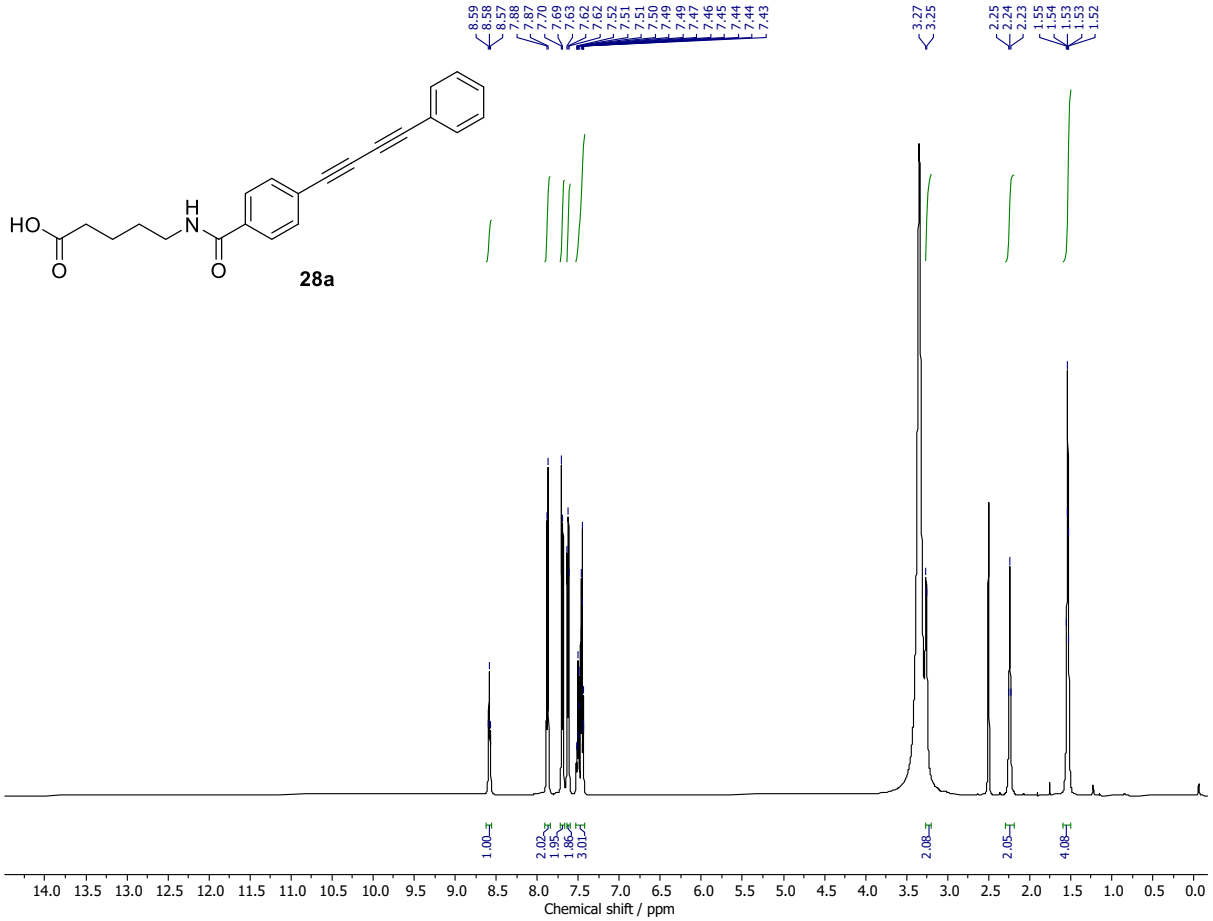
8.59
8.58
8.57
7.88
7.87
7.70
7.69
7.63
7.62
7.62
7.52
7.51
7.51
7.50
7.49
7.49
7.47
7.46
7.45
7.44
7.44
7.43
3.27
3.25
2.25
2.24
2.23
1.55
1.54
1.53
1.53
1.52
HO
O
H
N
O
28a
1.00
2.02
1.95
1.86
3.01
2.08
2.05
4.08
14.0 13.5 13.0 12.5 12.0 11.5 11.0 10.5 10.0 9.5 9.0 8.5 8.0 7.5 7.0 6.5 6.0 5.5 5.0 4.5 4.0 3.5 3.0 2.5 2.0 1.5 1.0 0.5 0.0
Chemical shift / ppm

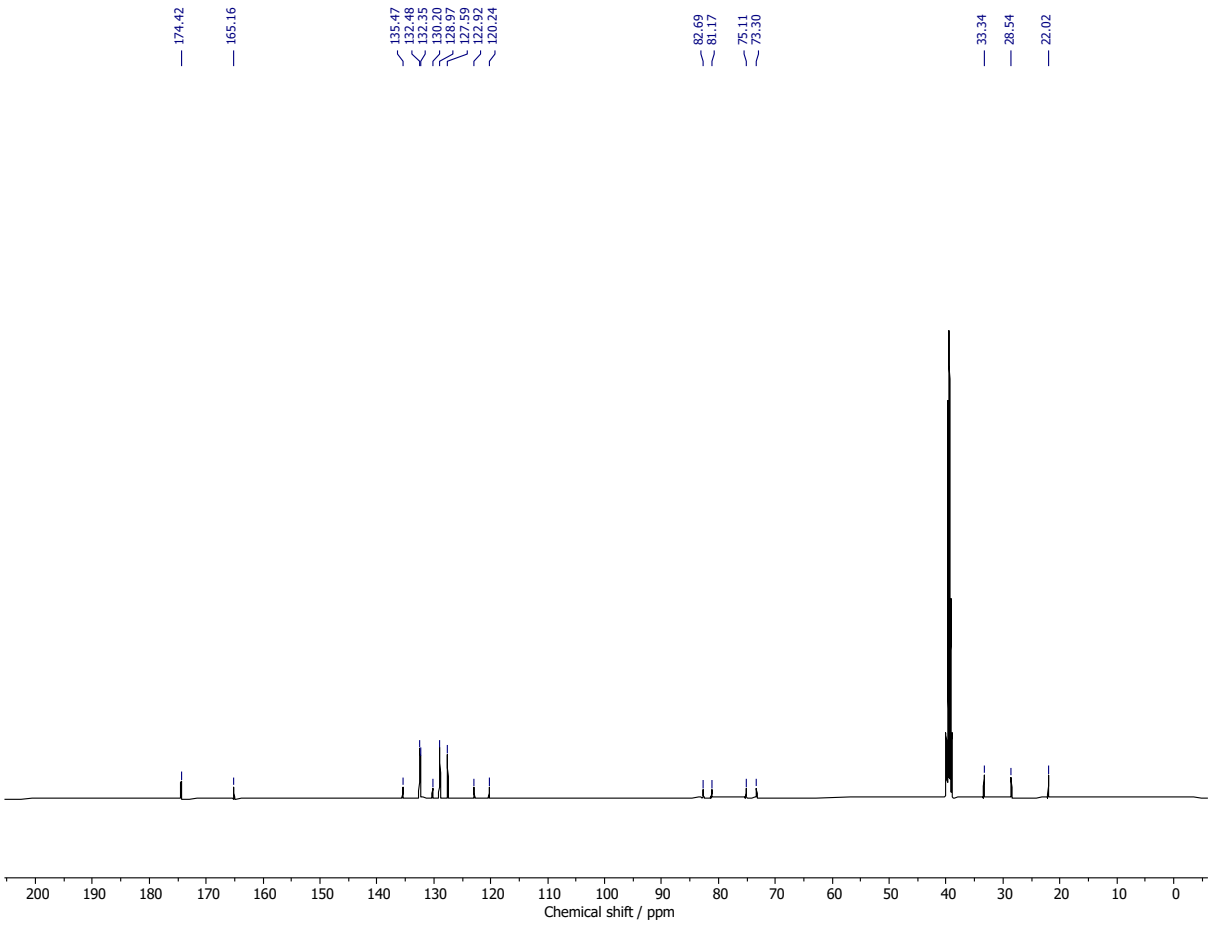
174.42
165.16
135.47
132.48
132.35
130.20
128.97
127.59
122.92
120.24
82.69
81.17
75.11
73.30
33.34
28.54
22.02
200 190 180 170 160 150 140 130 120 110 100 90 80 70 60 50 40 30 20 10 0
Chemical shift / ppm

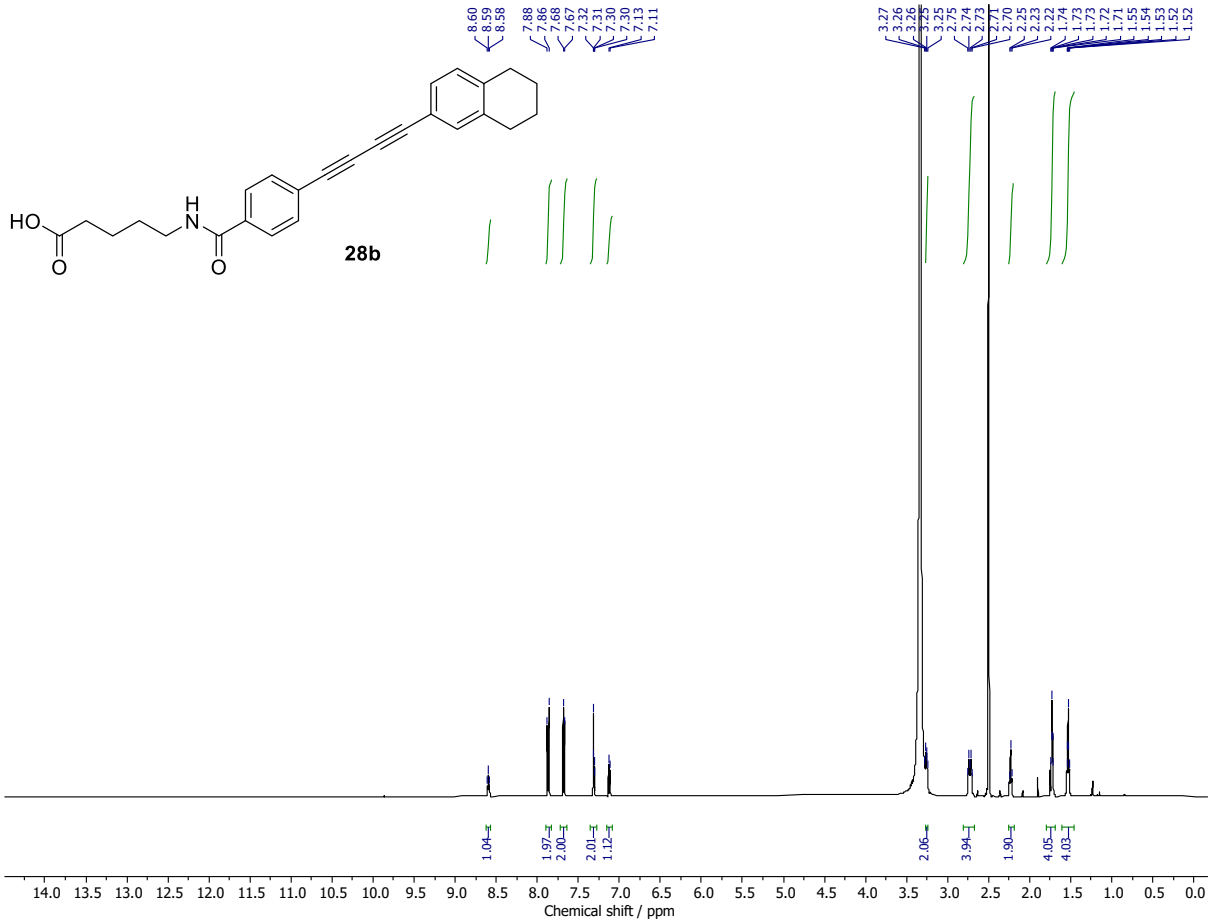
8.60
8.59
8.58
7.88
7.86
7.68
7.67
7.32
7.31
7.30
7.30
7.13
7.11
3.27
3.26
3.26
3.25
3.25
2.75
2.74
2.73
2.71
2.70
2.25
2.23
2.22
1.74
1.73
1.73
1.72
1.71
1.55
1.54
1.53
1.52
1.52
HO
O
H
N
O
28b
1.04
1.97
2.00
2.01
1.12
2.06
3.94
1.90
4.05
4.03
14.0 13.5 13.0 12.5 12.0 11.5 11.0 10.5 10.0 9.5 9.0 8.5 8.0 7.5 7.0 6.5 6.0 5.5 5.0 4.5 4.0 3.5 3.0 2.5 2.0 1.5 1.0 0.5 0.0
Chemical shift / ppm

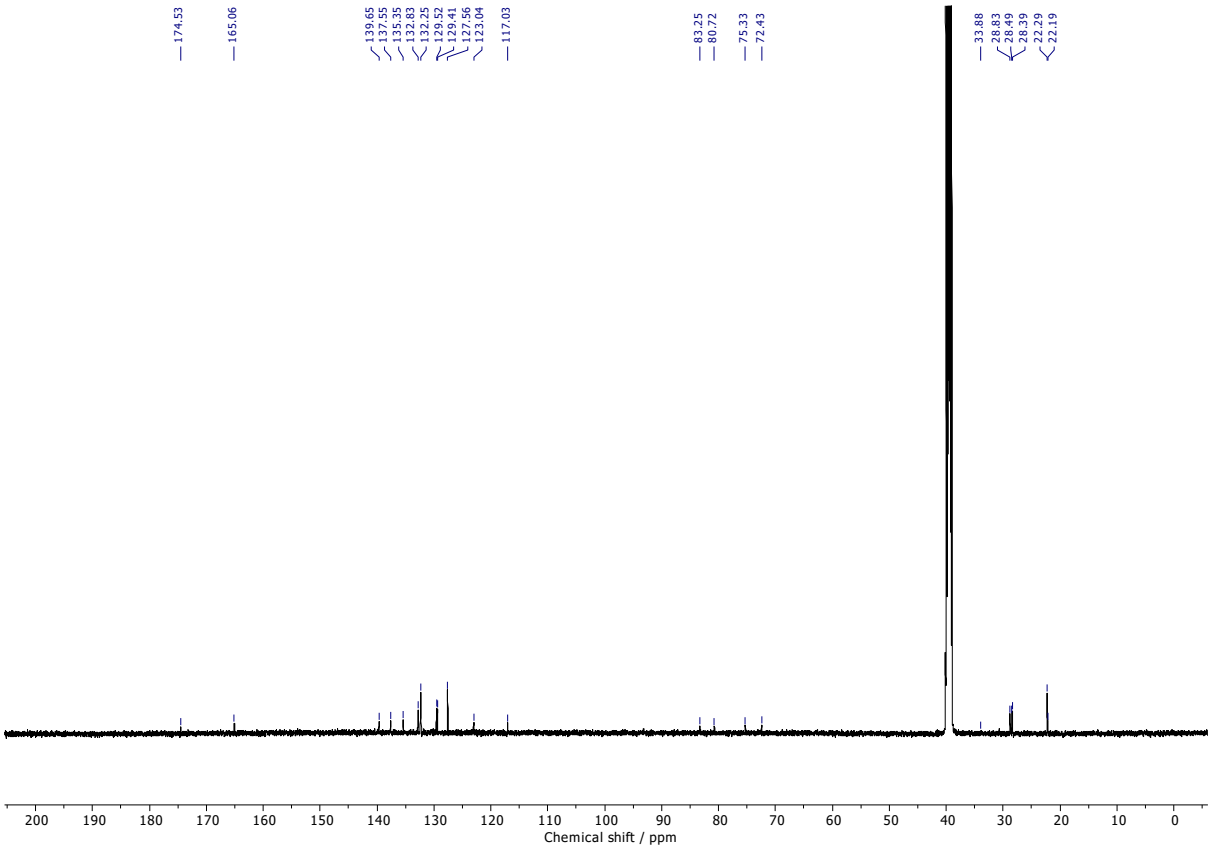
174.53
165.06
139.65
137.55
135.35
132.83
132.25
129.52
129.41
127.56
123.04
117.03
83.25
80.72
75.33
72.43
33.88
28.83
28.49
28.39
22.29
22.19
200 190 180 170 160 150 140 130 120 110 100 90 80 70 60 50 40 30 20 10 0
Chemical shift / ppm

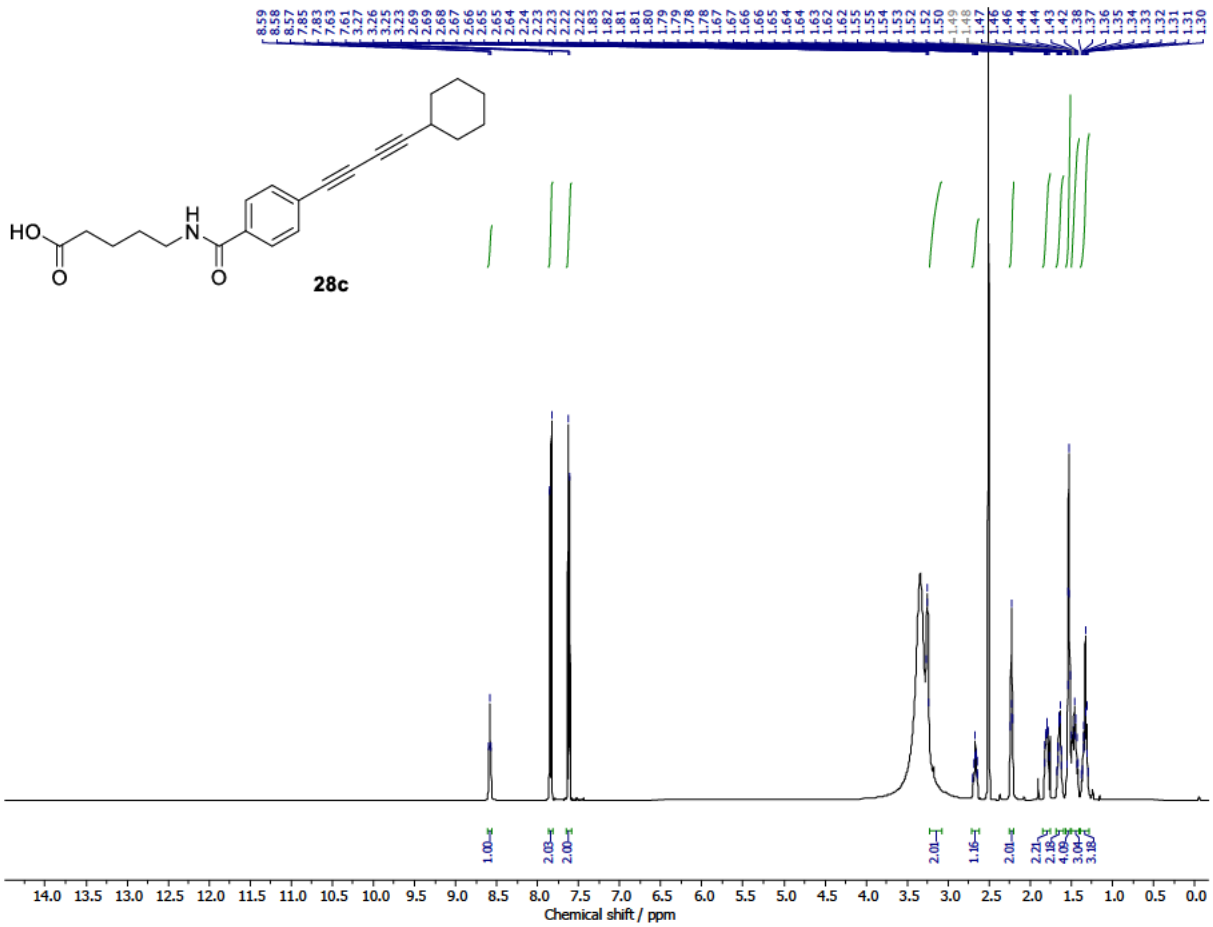
HO
O
H
N
O
28c
Chemical shift / ppm

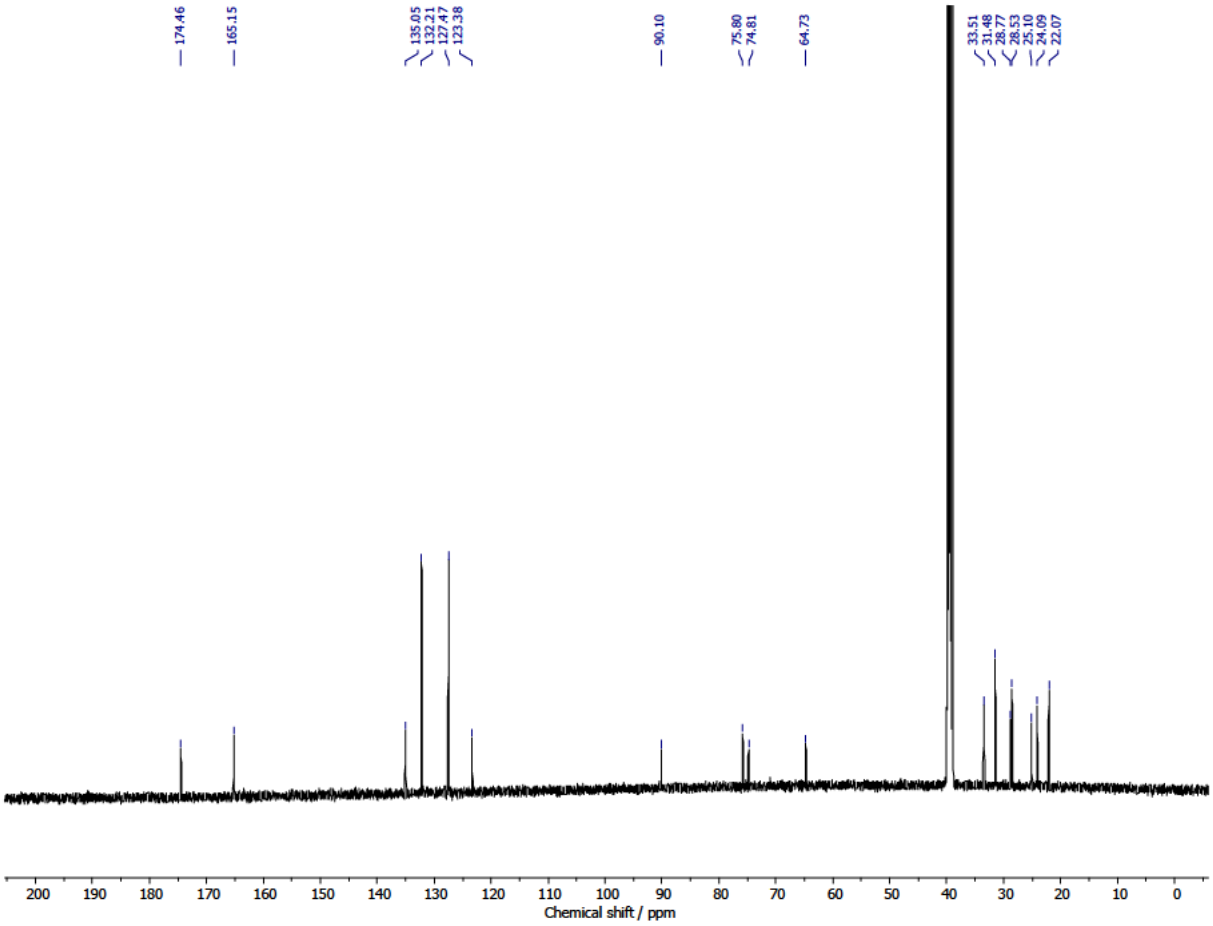
174.46
165.15
135.05
132.21
127.47
123.38
90.10
75.80
74.81
64.73
33.51
31.48
28.77
28.53
25.10
24.09
22.07
Chemical shift / ppm

29a

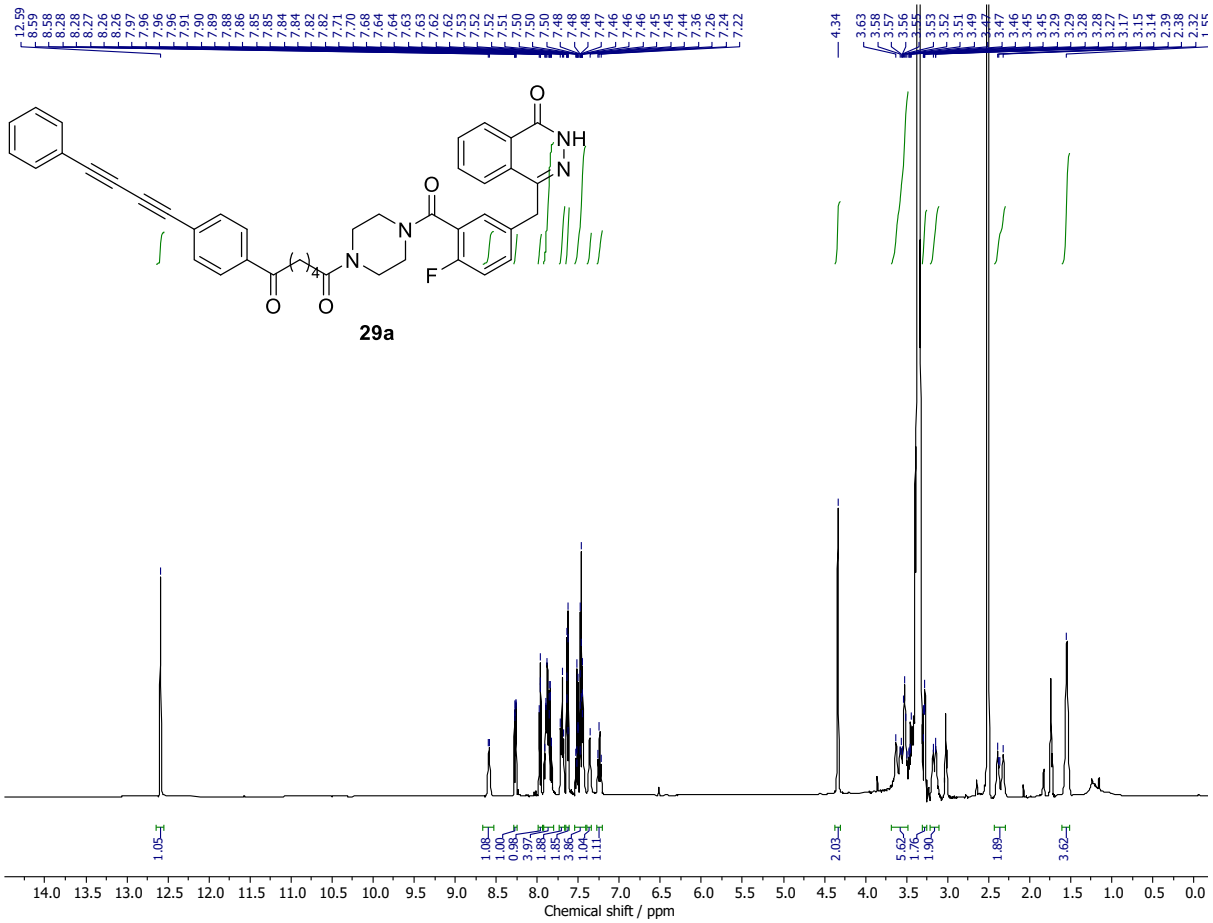

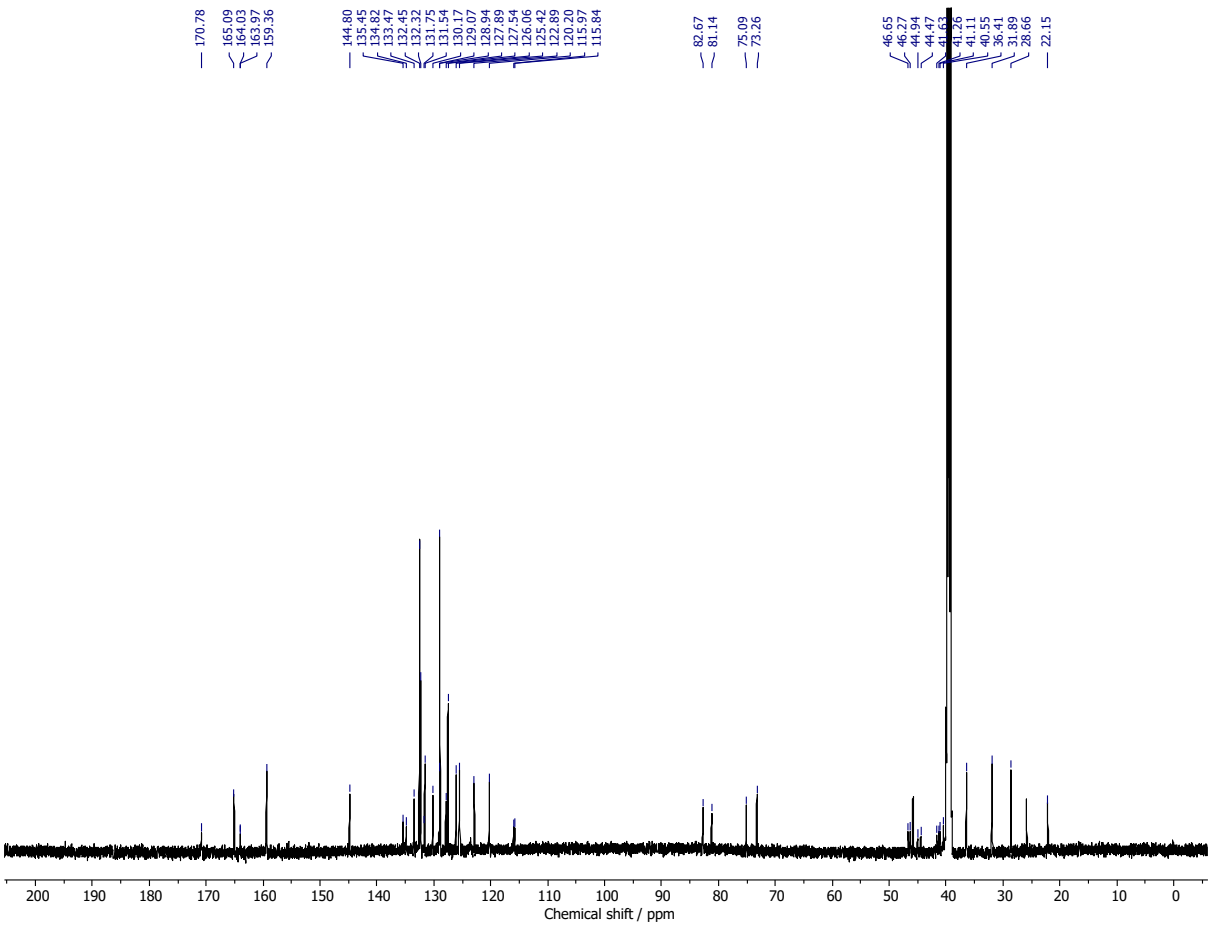

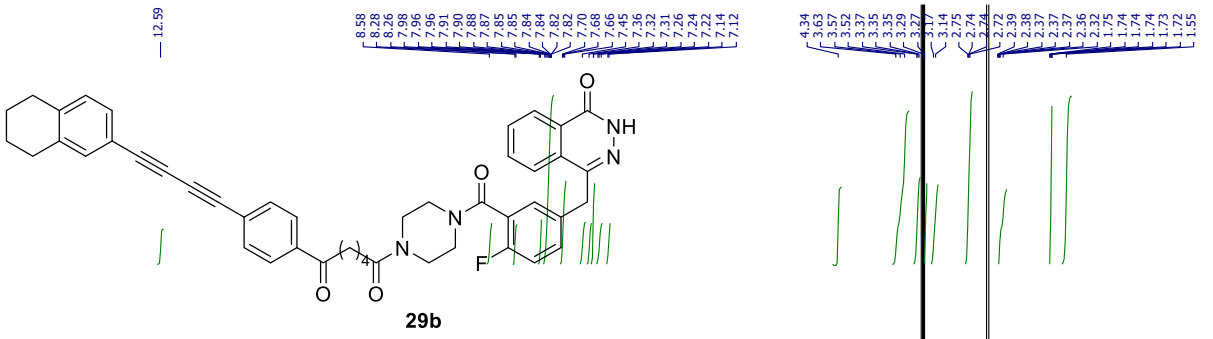
12.59
8.58
8.28
8.26
7.98
7.96
7.91
7.90
7.88
7.87
7.85
7.84
7.82
7.70
7.68
7.66
7.45
7.35
7.32
7.31
7.26
7.24
7.22
7.14
7.12
4.34
3.63
3.57
3.52
3.37
3.35
3.29
3.27
3.17
3.14
2.75
2.74
2.72
2.39
2.38
2.37
2.37
2.36
2.32
1.75
1.74
1.74
1.74
1.73
1.72
1.55
O
NH
N
O
N
N
F
O
O
4
29b

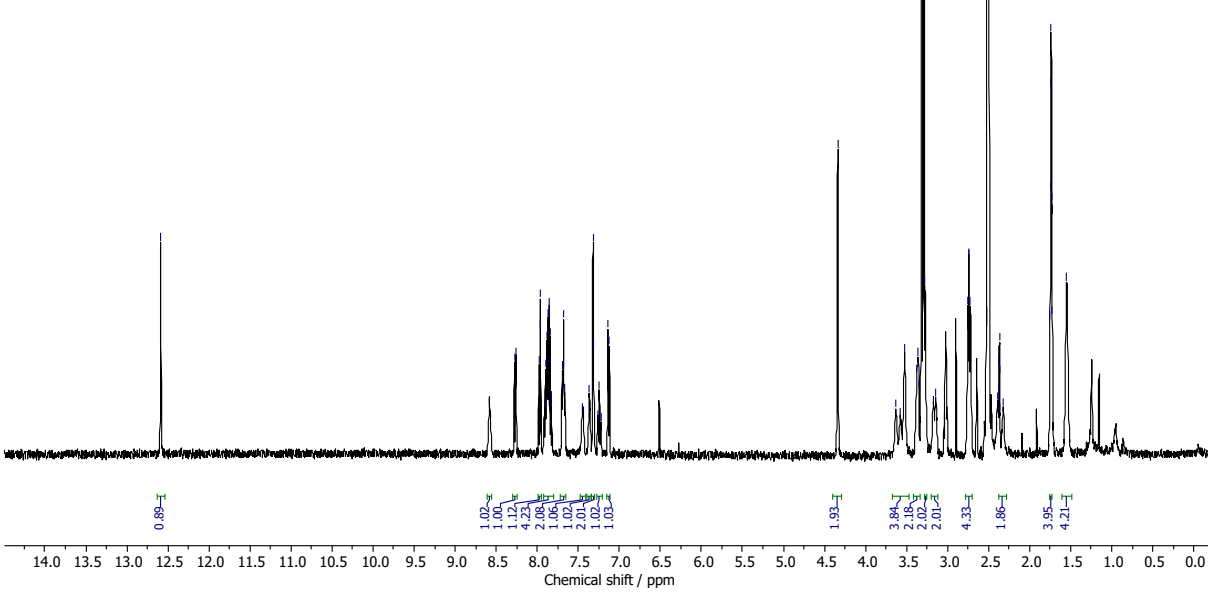
0.89
1.02
1.00
1.12
4.23
2.08
1.06
1.01
2.02
1.03
1.93
3.84
2.18
2.02
2.01
4.33
1.86
3.95
4.21
14.0 13.5 13.0 12.5 12.0 11.5 11.0 10.5 10.0 9.5 9.0 8.5 8.0 7.5 7.0 6.5 6.0 5.5 5.0 4.5 4.0 3.5 3.0 2.5 2.0 1.5 1.0 0.5 0.0
Chemical shift / ppm

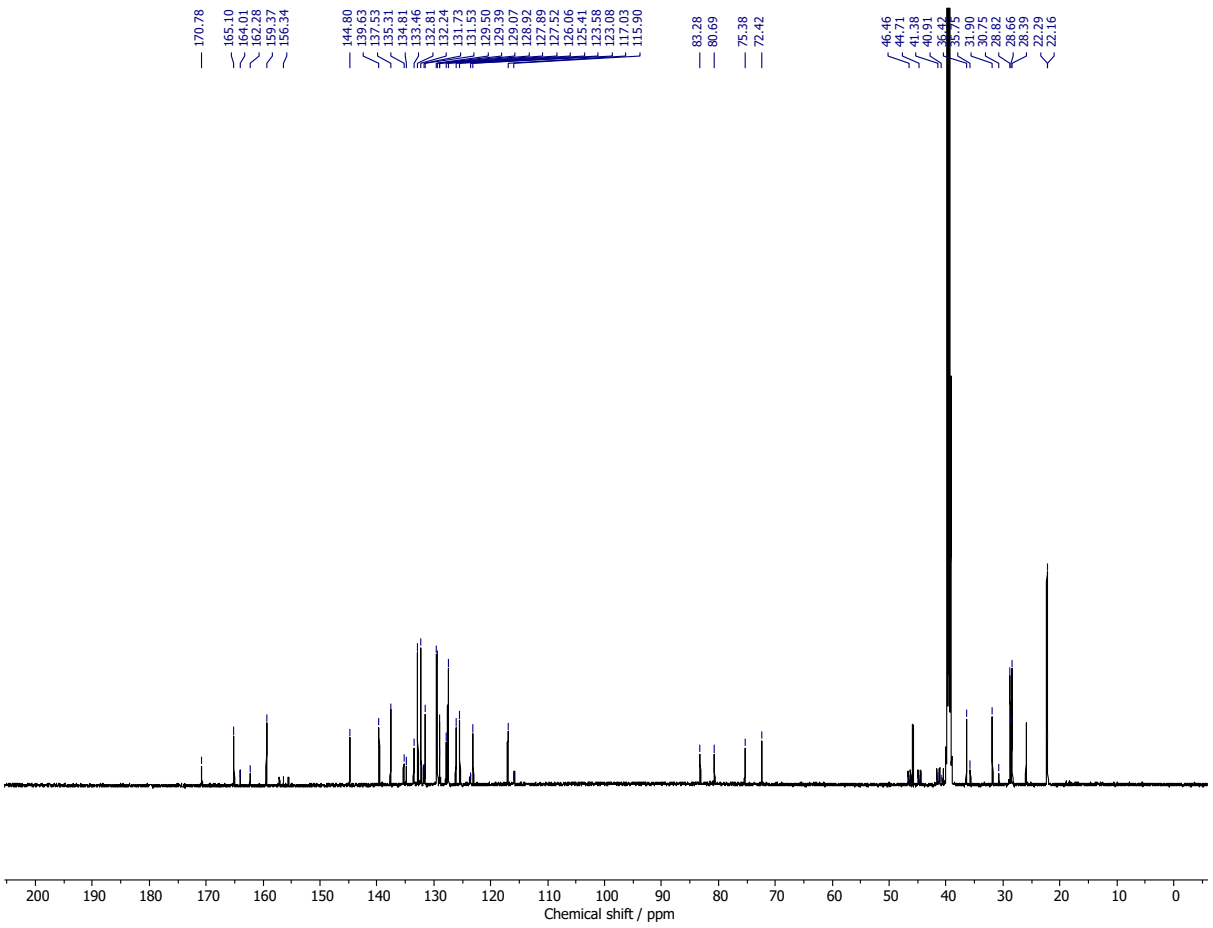
170.78
165.10
164.01
162.28
159.37
156.34
144.80
139.63
137.53
135.31
134.81
133.46
132.81
132.24
131.73
131.53
129.50
129.39
129.07
128.92
127.89
127.52
126.06
125.41
123.58
123.08
117.03
115.90
83.28
80.69
75.38
72.42
46.46
44.71
41.38
40.91
36.42
35.75
31.90
30.75
28.82
28.66
28.39
22.29
22.16
200 190 180 170 160 150 140 130 120 110 100 90 80 70 60 50 40 30 20 10 0
Chemical shift / ppm

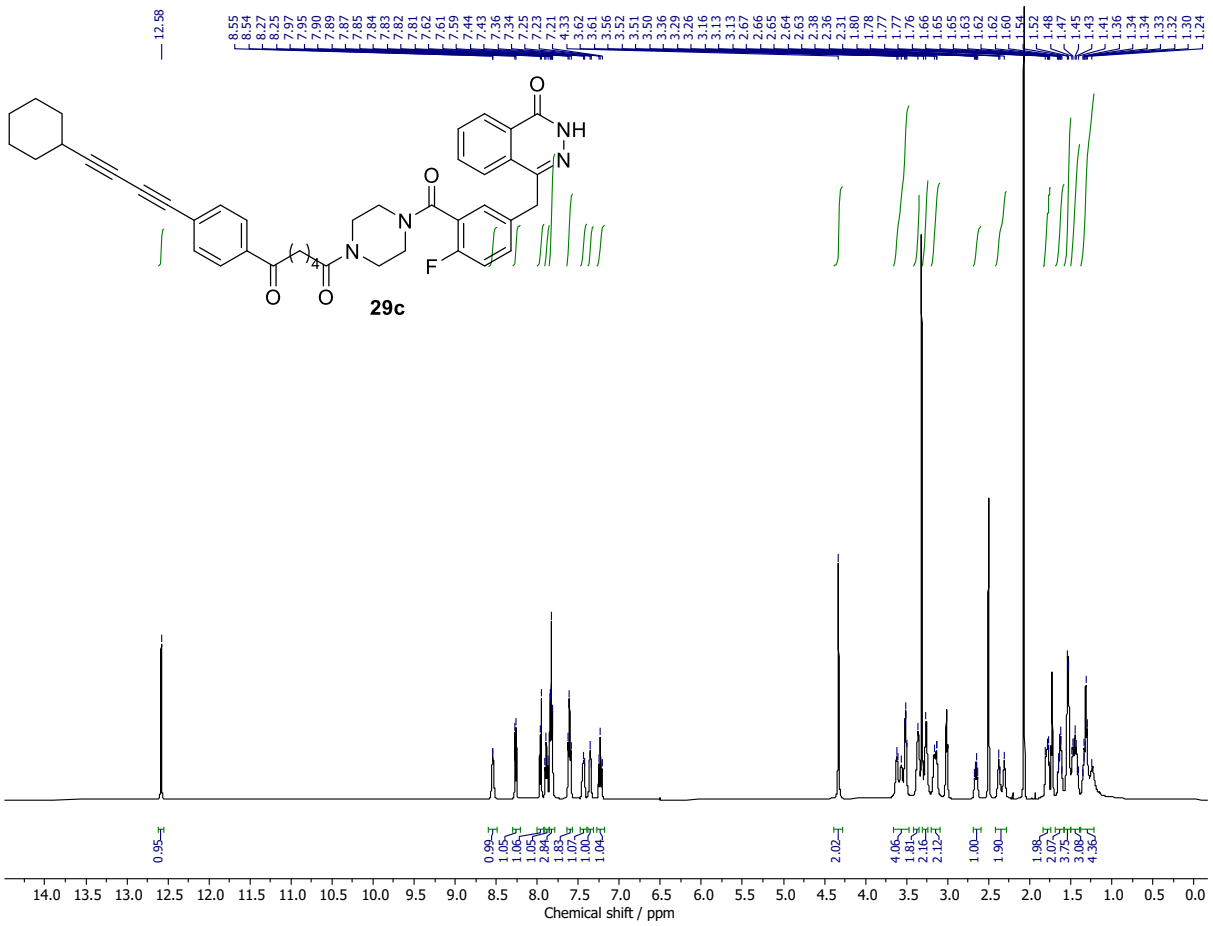
12.58
8.55 8.54 8.27 8.25 7.97 7.95 7.90 7.89 7.87 7.85 7.84 7.83 7.82 7.81 7.62 7.61 7.59 7.44 7.43 7.36 7.34 7.25 7.23 7.21 4.33 3.62 3.61 3.56 3.52 3.51 3.50 3.36 3.29 3.26 3.16 3.13 3.13 2.67 2.66 2.65 2.64 2.63 2.38 2.36 2.31 1.80 1.78 1.77 1.77 1.76 1.66 1.65 1.65 1.63 1.62 1.62 1.60 1.54 1.52 1.48 1.47 1.45 1.43 1.41 1.36 1.34 1.34 1.33 1.32 1.30 1.24
NH
N
O
N
N
F
O
O
29c
0.95 0.99 1.05 1.06 1.05 2.84 1.83 1.07 1.00 1.04 2.02 4.06 1.81 2.16 2.12 1.00 1.90 1.98 2.07 3.75 3.08 4.36
14.0 13.5 13.0 12.5 12.0 11.5 11.0 10.5 10.0 9.5 9.0 8.5 8.0 7.5 7.0 6.5 6.0 5.5 5.0 4.5 4.0 3.5 3.0 2.5 2.0 1.5 1.0 0.5 0.0
Chemical shift / ppm

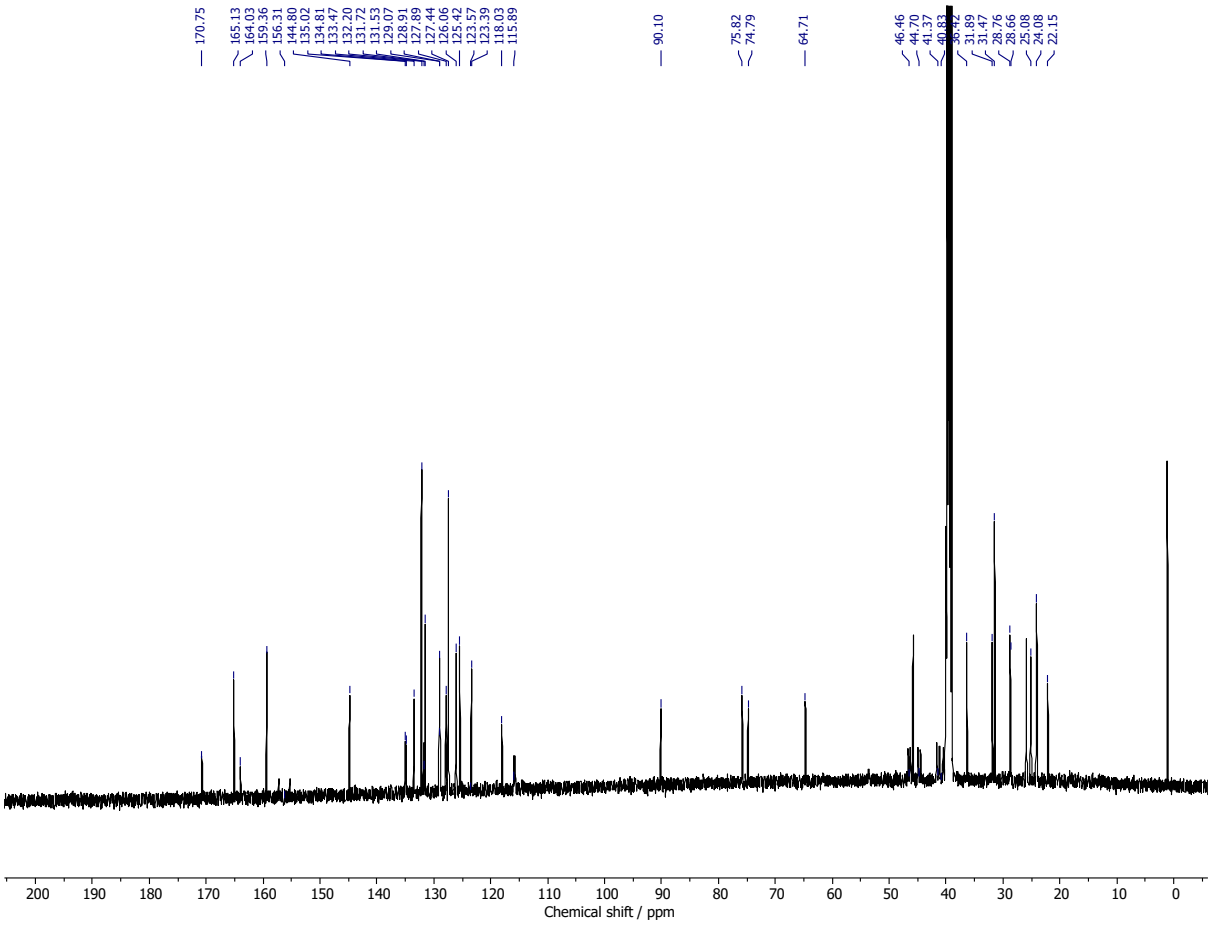
170.75
165.13 164.03 159.36 156.31 144.80 135.02 134.81 133.47 132.20 131.72 131.53 129.07 128.91 127.89 127.44 126.06 125.42 123.57 123.39 118.03 115.89
90.10
75.82 74.79
64.71
46.46 44.70 41.37 40.83 38.42 31.89 31.47 28.76 28.66 25.08 24.08 22.15
200 190 180 170 160 150 140 130 120 110 100 90 80 70 60 50 40 30 20 10 0
Chemical shift / ppm

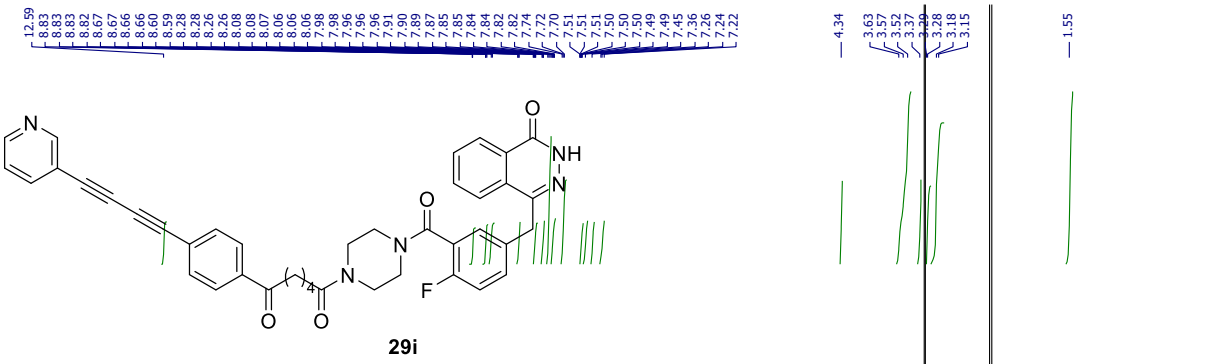

29i

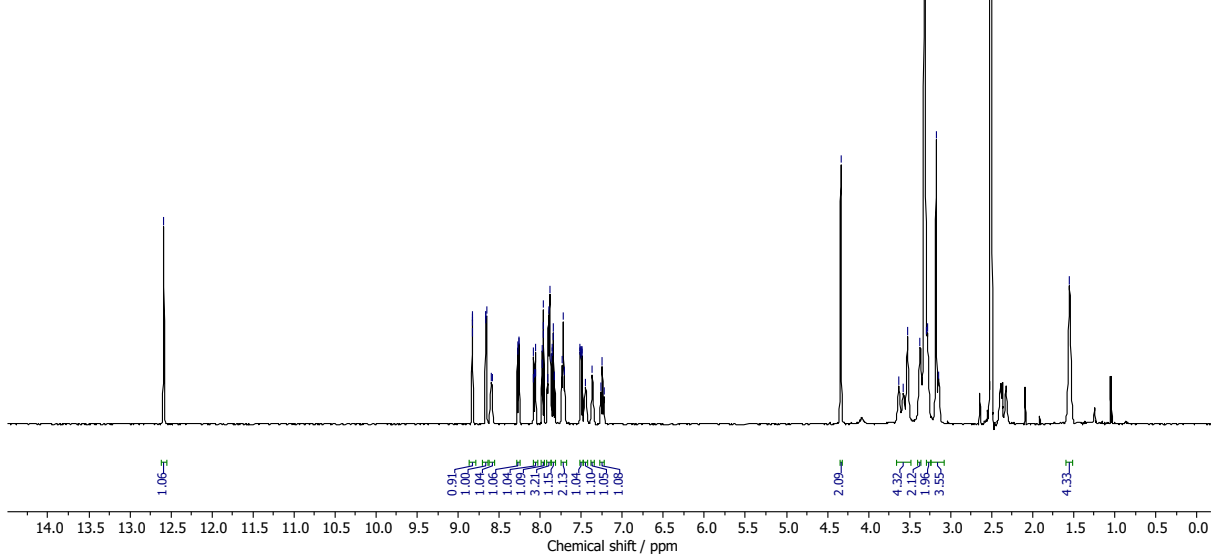

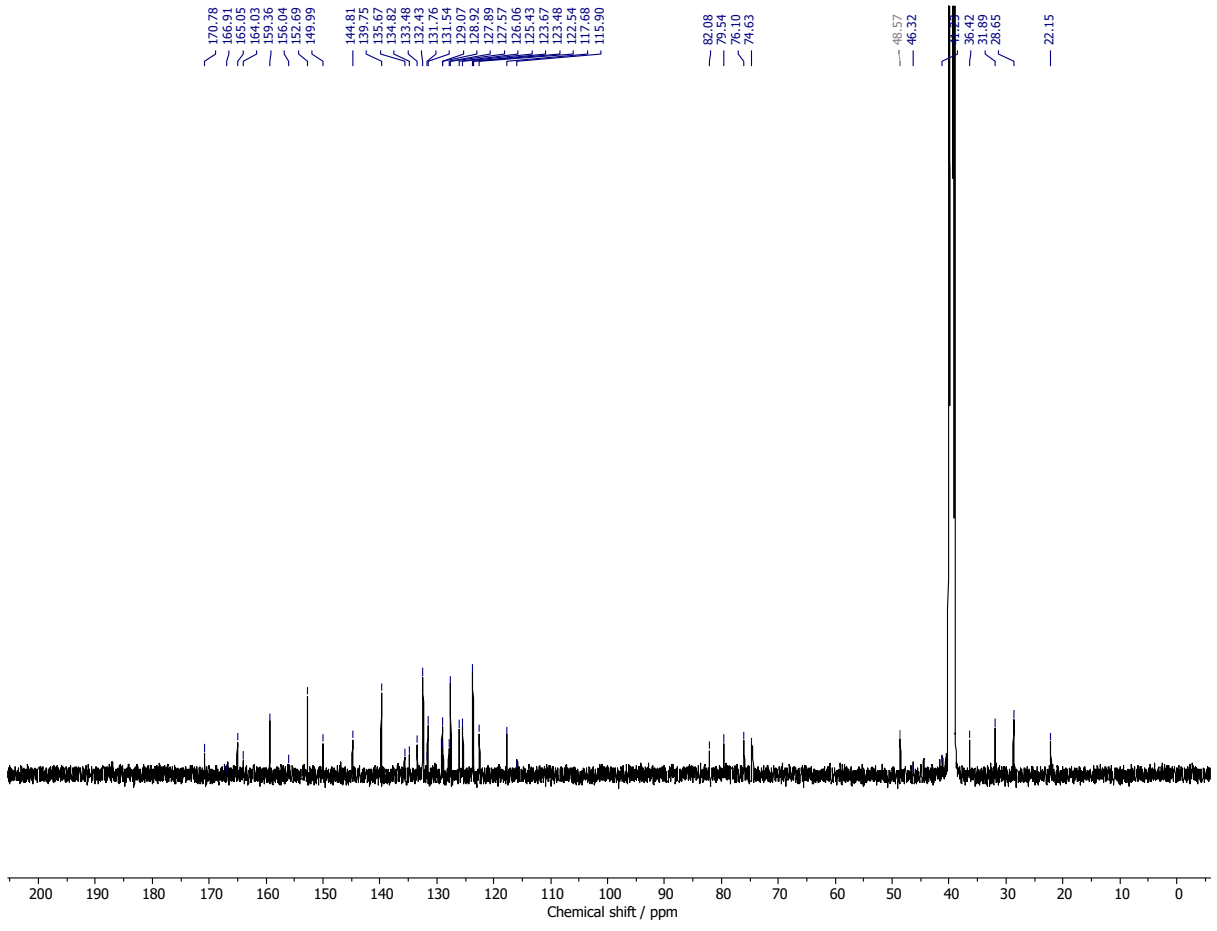

Appendix D. Permissions

This Agreement between University of Edinburgh -- Craig Steven ("You") and Elsevier ("Elsevier") consists of your license details and the terms and conditions provided by Elsevier and Copyright Clearance Center.

License Number	5767681407750
License date	Apr 14, 2024
Licensed Content Publisher	Elsevier
Licensed Content Publication	Elsevier Books
Licensed Content Title	Neurophotonics and Biomedical Spectroscopy
Licensed Content Author	Martin Lee,William J. Tipping
Licensed Content Date	Jan 1, 2019
Licensed Content Pages	25
Start Page	401
End Page	425
Type of Use	reuse in a thesis/dissertation
Portion	figures/tables/illustrations
Number of figures/tables/illustrations	1
Format	both print and electronic
Are you the author of this Elsevier chapter?	No
Will you be translating?	No
Title of new work	Raman-Active Chemical Probes for Cancer Cell Imaging and Medicinal Chemistry
Institution name	University of Edinburgh
Expected presentation date	Jun 2024
Order reference number	CFS140424
Portions	15.8
Requestor Location	University of Edinburgh Joseph Black Building David Brewster Road Edinburgh, other United Kingdom Attn: University of Edinburgh
Publisher Tax ID	GB 494 6272 12
Total	**0.00 USD**

This Agreement between University of Edinburgh -- Craig Steven ("You") and Elsevier ("Elsevier") consists of your license details and the terms and conditions provided by Elsevier and Copyright Clearance Center.

License Number	5766660654036
License date	Apr 12, 2024
Licensed Content Publisher	Elsevier
Licensed Content Publication	Journal of Investigative Dermatology
Licensed Content Title	Label-Free Quantification of Pharmacokinetics in Skin with Stimulated Raman Scattering Microscopy and Deep Learning
Licensed Content Author	Amin Feizpour,Troels Marstrand,Louise Bastholm,Stefan Eirefelt,Conor L. Evans
Licensed Content Date	Feb 1, 2021
Licensed Content Volume	141
Licensed Content Issue	2
Licensed Content Pages	9
Start Page	395
End Page	403
Type of Use	reuse in a thesis/dissertation
Portion	figures/tables/illustrations
Number of figures/tables/illustrations	1
Format	both print and electronic
Are you the author of this Elsevier article?	No
Will you be translating?	No
Title of new work	Raman-Active Chemical Probes for Cancer Cell Imaging and Medicinal Chemistry
Institution name	University of Edinburgh
Expected presentation date	Jun 2024
Order reference number	cfs120424
Portions	figure 1
Requestor Location	University of Edinburgh Joseph Black Building David Brewster Road Edinburgh, other United Kingdom Attn: University of Edinburgh
Publisher Tax ID	GB 494 6272 12
Total	**0.00 USD**

This Agreement between University of Edinburgh -- Craig Steven ("You") and Elsevier ("Elsevier") consists of your license details and the terms and conditions provided by Elsevier and Copyright Clearance Center.

License Number	5764930282249
License date	Apr 09, 2024
Licensed Content Publisher	Elsevier
Licensed Content Publication	Elsevier Books
Licensed Content Title	Stimulated Raman Scattering Microscopy
Licensed Content Author	Craig F. Steven,Elisabetta Chiarparin,Alison N. Hulme,Valerie G. Brunton
Licensed Content Date	Jan 1, 2022
Licensed Content Pages	17
Start Page	403
End Page	419
Type of Use	reuse in a thesis/dissertation
Portion	figures/tables/illustrations
Number of figures/tables/illustrations	2
Format	both print and electronic
Are you the author of this Elsevier chapter?	Yes
How many pages did you author in this Elsevier book?	17
Will you be translating?	No
Title of new work	Raman-Active Chemical Probes for Cancer Cell Imaging and Medicinal Chemistry
Institution name	University of Edinburgh
Expected presentation date	Jun 2024
Order reference number	CFS090424
Portions	Figure 1 and 3
Requestor Location	University of Edinburgh Joseph Black Building David Brewster Road Edinburgh, other United Kingdom Attn: University of Edinburgh
Publisher Tax ID	GB 494 6272 12
Total	**0.00 USD**

This Agreement between University of Edinburgh -- Craig Steven ("You") and Springer Nature ("Springer Nature") consists of your license details and the terms and conditions provided by Springer Nature and Copyright Clearance Center.

License Number	5774770146809
License date	Apr 23, 2024
Licensed Content Publisher	Springer Nature
Licensed Content Publication	Nature Methods
Licensed Content Title	Supermultiplexed optical imaging and barcoding with engineered polyynes
Licensed Content Author	Fanghao Hu et al
Licensed Content Date	Jan 15, 2018
Type of Use	Thesis/Dissertation
Requestor type	academic/university or research institute
Format	print and electronic
Portion	figures/tables/illustrations
Number of figures/tables/illustrations	1
Would you like a high resolution image with your order?	no
Will you be translating?	no
Circulation/distribution	1 - 29
Author of this Springer Nature content	no
Title of new work	Raman-Active Chemical Probes for Cancer Cell Imaging and Medicinal Chemistry
Institution name	University of Edinburgh
Expected presentation date	Jun 2024
Order reference number	CFS203424
Portions	figure 3
Requestor Location	University of Edinburgh Joseph Black Building David Brewster Road Edinburgh, other United Kingdom Attn: University of Edinburgh
Total	**0.00 USD**